Dissertation

submitted to the
Combined Faculties of the Natural Sciences and Mathematics
of the Ruperto-Carola-University of Heidelberg, Germany,
for the degree of
Doctor of Natural Sciences

Put forward by

Sven Buder
born in: Cottbus, Germany

Oral examination: July 16, 2019

Spectroscopic Analysis and Chemodynamic Exploration of the Milky Way with Million-Star Surveys

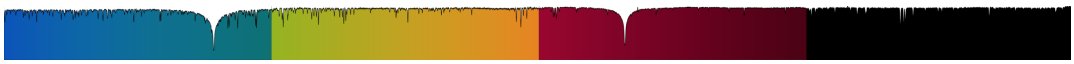

— Dissertation —

Sven Buder

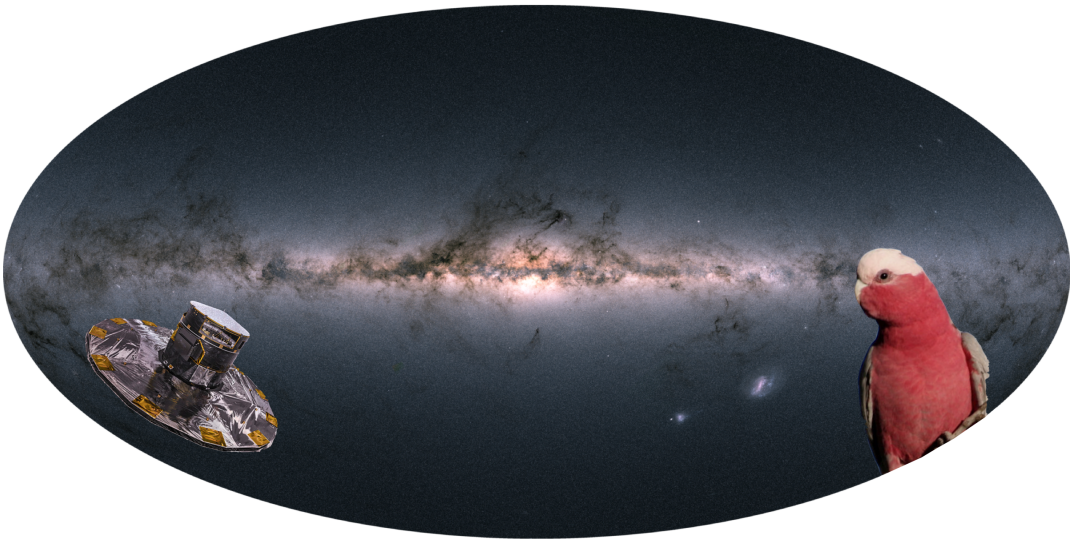

Figure Credit: *Gaia* and DR2 skymap: ESA/*Gaia*/DPAC/Gaia Collaboration et al. (2018b), Galah bird: http://cockatoo-info.com

Supervisors:	Dr Karin Lind
	Prof Dr Melissa Ness
Referees:	Dr Karin Lind
	Dr Andreas Koch
Additional Examiners:	Prof Dr Hans-Walter Rix
	Prof Dr Johanna Stachel

ABSTRACT

The Milky Way is traditionally depicted as a composite of three main stellar components: the halo, disk, and bulge. The closer we look and the more information we gather, this picture becomes more complicated. The components are in fact overlapping in stellar properties, such as positions, kinematics, ages, and chemical composition.

The most promising way to further our understanding of the formation of the Milky Way, the main aim of Galactic Archaeology, is to explore chemical information and stellar ages with large stellar surveys. In Chapter 1, we motivate this exploration in more detail and describe the challenges that come with the collection of big data from spectroscopic surveys.

In Chapter 2, we introduce the large-scale spectroscopic 'Galactic Archaeology with HERMES' (GALAH) survey, whose spectra were analysed in the course of this Thesis in order to estimate stellar properties. The very large data flow of stellar surveys has been referred to as the industrial revolution of Galactic archaeology and the analysis requires new efficient and automated techniques. This Thesis describes the spectroscopic analyses of the more than 650,000 stars in the GALAH survey, which deliver up to 30 abundances with unprecedented accuracy on such scales, based on the papers by Buder et al. (2018) and Buder et al. (in prep. b).

In Chapter 3, we use the chemical information from GALAH together with dynamical information and stellar ages to analyse the Galactic disk in the solar neighborhood, which has shown to be assembled from two populations. This work is published by Buder et al. (2019) and we find that the two populations of the disk can be separated more clearly when using stellar chemical composition and age, rather than phase-space information.

In Chapter 4, we use chemodynamic information and stellar ages to analyse the transition between the disk and halo. This work will be submitted by Buder et al. (in prep. a) and we confirm that the old disk overlaps significantly with the halo. With our performed chemodynamic decompositions we are able to link the disk population that is enhanced in α-element abundances with the high-α halo population identified by Nissen & Schuster (2010). We further show that the accreted halo population of the 'Sausage', identified by Belokurov et al. (2018), is strongly correlated with the low-α halo population identified by Nissen & Schuster (2010). Our stellar age estimates suggest

that the halo components and the oldest high-α disk stars are coeval and show no strong age gradient, which would rule out several formation scenarios of the Milky Way.

In Chapter 5, we conclude the work of this Thesis and outline further ways to continue the research in the field of Galactic archaeology with large stellar surveys.

ZUSAMMENFASSUNG

Die Milchstraße wird traditionell als die Zusammensetzung dreier stellar Hauptkomponenten gesehen: der Halo, der Scheibe und der zentralen Verdickung. Je genauer wir jedoch hinschauen und je mehr Informationen wir sammeln, desto komplizierter wird dieses Bild jedoch. Die Komponenten überlappen genau genommen in ihren Eigenschaften, wie etwa räumlicher Verteilung, Kinematic, Alter und chemischer Zusammensetzung.

Der vielversprechendste Weg unser Verständnis über die Entstehung der Milchstraße zu erweitern, dem Hauptziel Galaktischer Archäologie, ist die Erforschung von chemischen Informationen und dem Alter von Sternen mittels großer Sternendurchmusterungen. In Kapitel 1 motivieren wir diese Erforschung tiefergehender und beschreiben die Herausfordergungen, die das Sammeln großer Daten mittels spektroskopischer Durchmusterungen mit sich bringt.

In Kapitel 2 stellen wir die groß angelegte spectroskopische Durchmusterung "Galactic Archaeology with HERMES"(GALAH) vor, deren Spektren im Rahmen dieser Dissertation zur Bestimmung von stellaren Eigenschaften benutzt wurden. Der große Fluss an Daten im Rahmen von Sterndurchmusterungen wird dabei als industrielle Revolution der Galaktischen Archäologie angesehen und die Analyse erfordert neue, effiziente und automatisierte Techniken. Diese Dissertation beschreibt, basierend auf den Veröffentlichungen von Buder et al. (2018) sowie Buder et al. (in prep. b), die spektroskopischen Analysen von mehr als 650 000 Sternen der GALAH Durchmusterung, welche bis zu 30 Elementhäufigkeiten mit beispielloser Genauigkeiten für solche Größenordnungen bereitstellen.

In Kapitel 3 nutzen wir diese chemischen Informationen der GALAH Durchmusterung zusammen mit dynamischen Informationen und Sternenaltern, um die Galaktische Scheibe in der Nachbarschaft der Sonne zu untersuchen, die sich nachweislich aus zwei Populationen zusammensetzt. Diese Arbeit ist durch Buder et al. (2019) veröffentlicht und wir finden, dass die zwei Komponenten der Galaktischen Scheibe sich eindeutiger mittels chemischer Zusammensetzung und Sternenaltern unterscheiden lassen, als mittels Phasenrauminformationen.

In Kapitel 4 nutzen wir chemisch-dynamische Informationen und Sternalter, um den Übergang von Scheibe und Halo zu analysieren. Diese Arbeit wird von Buder et al. (in prep. a) eingereicht und wir bestätigen, dass die alte Schreibe signifikant

mit der Halo überlappt. Mit der von uns durchgeführten Zerlegung können wir die Scheibenpopulation, deren α-Elementhäufigkeiten erhöht sind, mit der von Nissen & Schuster (2010) identifizierten Halo-Population mit erhöhten α-Elementhäufigkeiten, verknüpfen. Desweiteren zeigen wir, dass die von Belokurov et al. (2018) identifizierte akkretierte Halo-Population der 'Sausage' (Wurst), stark mit der von Nissen & Schuster (2010) gefundenen Population mit niedriegen α-Elementhäufigkeiten korreliert. Unsere Daten deuten darauf hin, dass die Halo-Komponenten und die ältesten, α-erhöhten Scheibensterne gleichaltrig sind und zeigen keinen starken Altersgradienten, was mehrere Erklärungen der Entstehung der Milchstraße ausschließen würde.

In Kapitel 5 fassen wir die Arbeit dieser Dissteration zusammen und zeigen Wege auf, auf denen die Forschung im Feld der Galaktischen Archäologie mit großen Sterndurchmusterungen weitergeführt werden kann.

CONTENTS

List of Figures

LIST OF TABLES

Chapter 1

Introduction

1.1 Motivation and structure

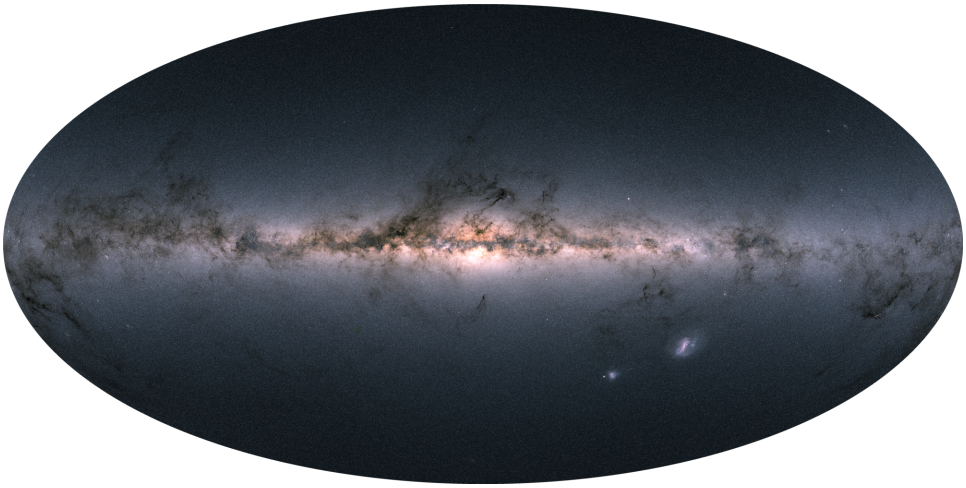

Figure 1.1: The Milky Way as seen from stellar flux measurements by the *Gaia* satellite. Map of the total flux measured in the $G_{\rm RP}$, G, and $G_{\rm BP}$ bands, where the flux in these bands is encoded in the red, green, and blue channel, respectively. **Figure Credit:** Gaia Collaboration et al. (2018b).

Looking up at the night sky, we might be lucky to see hundreds or even thousands of stars with the naked eye, but millions, even billions, that are hiding in the dark can be seen with instruments such as telescopes. Many of these luminous time capsules have survived a significant fraction of the age of the Universe and are part of the large structure that we call our Galaxy, the Milky Way (MW). During their lifetime, these stars have witnessed significant changes, may it be in their own evolution or the evolution of the Galaxy and the Universe. About half the stars in the MW are believed to have formed before ~ 8 Gyr, corresponding to a redshift of $z \sim 1$ (Lineweaver, 1999). While these stars are certainly out of reach for us to perform hands-on experiments, their light contains a vast amount of information that astronomers have used to not only analyse individual stars, but the Galaxy itself with the aim to understand how it formed and evolved.

Most stars are centered along a bright, 'milky' ($\gamma\alpha\lambda\alpha\xi\acute{\iota}\alpha\varsigma$ / galaxias in Greek) band on the night sky, which gave the our Galaxy its name. From star counts and comparison

with external galaxies we have also inferred that the Milky Way is a typical barred spiral galaxy of approximate stellar mass $6.4 \cdot 10^{10}\,\mathrm{M}_\odot$ (see e.g. McMillan, 2011).

Up until now, the MW is the only galaxy for which we can resolve a significant amount of stars and its study, which underlies our understanding of universal processes over cosmic time, is a fundamental cornerstone of contemporary astrophysics, sometimes referred to as near-field cosmology (Freeman & Bland-Hawthorn, 2002; Bland-Hawthorn & Gerhard, 2016).

A major goal that we are aiming for is to estimate the stellar distribution function for the MW, which contains the most important parameters of stars. In general, we can describe stars as spheres with radius $R_\star$ containing a certain mass $M_\star$ that have formed at a certain time $\tau_\star$ ago. To prevent the star from gravitational collapse, their core temperatures must be high enough to sustain nuclear fusion, starting with hydrogen into helium. Increasingly heavy elements are created inside stars during their lives and often explosive deaths. Through these and other processes in the course of Galactic chemical evolution, the chemical compositions in the cores of stars are changing over time. However, the surface abundance of a star is to first order a birth property (with the exception of chemical elements subject to dredge up, atomic diffusion, and other stochastic events like binary transfer and planet engulfment). Therefore, each star has a certain chemical composition made up of a set of elements, X, which are approximately representative of the birth properties of the star forming material. These abundances which make up the chemical composition of stars are defined as the logarithmic ratio of the number density of this element relative to the most abundant element H. We can then compare this ratio to the solar one and describe the abundance in the bracket notation, such that

$$[\mathrm{X/H}] = \log \frac{N_\mathrm{X}}{N_\mathrm{H}} - \log \frac{N_{\mathrm{X},\odot}}{N_{\mathrm{H},\odot}}. \tag{1.1}$$

In combination with the orbit information of the stars, we can then try to study the MW as a compilation of stars, as reviewed by Rix & Bovy (2013):

$$MW(\star) = P_\star\,(M_\star, R_\star, \tau_\star, [\mathrm{X/H}], \mathrm{orbit}(\boldsymbol{r}, \boldsymbol{v}), \dots) \tag{1.2}$$

with
- $M_\star$ ... stellar mass,
- $R_\star$ ... stellar radius,
- $\tau_\star$ ... stellar age,
- [X/H] ... element abundances of element X relative to hydrogen, and
- orbit($\boldsymbol{r}$,$\boldsymbol{v}$) ... orbit information obtained from positions $\boldsymbol{r}$ and velocities $\boldsymbol{v}$

To gather this information, we strongly rely on observations. The vast amount of fossil information like chemical composition, and kinematics can be inferred from photometric and spectroscopic observations of stars (e.g. Rix & Bovy, 2013). We describe this in detail for all parameters of Eq. 1.2 in Sec. 1.3.

A major limitation for the observation of stars is the the light-collecting power of telescopes. Although we have gathered a lot of photometric information of stars in our Galaxy through dedicated observations like the Two Micron All-Sky Survey (Skrutskie et al., 2006, 2MASS) or *Gaia* (see Fig. 1.1, Gaia Collaboration et al., 2018b), the vast

majority of stars has not been analysed spectroscopically. In particular, high-resolution spectroscopic observations, for example by the GALAH survey, that are able to resolve spectral lines, as far or even beyond their natural line width, are so far limited to $\sim 0.001\%$ of the estimated total set of stellar observations[1].

The estimation of the parameters of Eq. 1.2 also relies on our understanding of stellar evolution (to convert e.g. magnitudes and colours into stellar parameters or stellar ages), stellar physics (to convert e.g. measurements of stellar spectra into element abundances) as well as MW dynamics (to convert e.g. spatial information over time into orbit properties).

The collection of orbit information is part of another important discipline, Galactic dynamics, because we will only be able to convert information of the present-day stellar Distribution Function (DF), $\mathrm{DF}(\boldsymbol{r}, \boldsymbol{v})$ (Binney, 2013; Sanders & Binney, 2015) into orbit information, if we can understand and model the gravitational potential $\Phi(\boldsymbol{r})$ of the MW, which encompasses the total matter distribution, including not only baryonic but also dark matter (see e.g. Rix & Bovy, 2013). Until recently, our inference tools had to use a large variety of approximations and assumptions due to limited computational power and understanding.

This thesis is written in a time, when a lot of observational and theoretical effort is put into improving these short-comings and advance our understanding of the MW. Some of the open questions in this context are:

- Can we describe the MW with a set of distinct populations or large-scale structures and how would those be characterised?
- How much formation memory does the Galaxy retain, that is, can we link stars that have been born together via age and/or their chemical and dynamical properties?
- Which processes shaped the MW's present structure and at what stages in the evolution are its properties defined?
- Which processes shape the chemical composition of the Galaxy and the stars?
- Can we distinguish between stars born in-situ in the Galaxy and in smaller galaxies cannibalised by our Milky Way?
- What is the baryonic and dark matter mass?

This chapter is structured in the following way: In Sec. 1.2, we give an overview of the our current understanding of the Milky Way and the components that it can be considered to be divided into. Starting from the observational perspective with respect to the major stellar components in Sec. 1.2.1, we explain how the formation of these components and the MW itself is currently viewed in Sec. 1.2.2. In Sec. 1.2.3 we elaborate on the currently used methods to decompose the components and stars of the MW with chemical, kinematic, and temporal information, whereas Sec. 1.2.3 focusses purely on the chemical aspect and the variety of elements and their production in the

[1] This number can be approximated if we assume that *Gaia* has observed around more than 1.5 billion stars, that is, 1% of all MW stars (Brown et al., 2016), and of these, we have targeted ~ 1.5 million stars with high-resolution spectrographs ($R > 20,000$), see Table. 1.1.

astronomical context. This information is important for being able to trace back stars that were born together via their chemical composition, an idea called chemical tagging. Practical considerations for the quality of the data that is used for the decomposition of components and chemical tagging are discussed in Sec. 1.2.5. Sec. 1.2.6 gives an overview of the past, on-going, and future stellar surveys.

Sect. 1.3 focusses on how the parameters for Eq. 1.2 can be estimated, that is, stellar parameters (Sec. 1.3.1), (primarily chemical) information from spectra (Sec. 1.3.2) and the challenges that the extraction brings with it (Sec. 1.3.3) as we all dynamical and temporal information (Secs. 1.3.4 and 1.3.5, respectively).

Parts of this chapter are inspired by the reviews by Freeman & Bland-Hawthorn (2002), Rix & Bovy (2013), and Bland-Hawthorn & Gerhard (2016) as well as the introductions to the papers by Buder et al. (2019) and Buder et al. (in prep. a).

1.2 THE THEORETICAL AND PRACTICAL BACKGROUND OF GALACTIC ARCHAEOLOGY

"The goal of Galactic archaeology is to put together enough facts about the Galaxy to build a reliable narrative of how the Galaxy was assembled."

— Ken Freeman, Introduction talk to conference Galactic Archaeology & Stellar Physics 2016

1.2.1 THE STELLAR COMPONENTS OF THE MILKY WAY

As a first step to describe the complex distribution of stars in our Galaxy, astronomers have attempted to define discrete components or populations and their inter-relationships. From observations of the MW (see e.g. Fig. 1.1) and similar galaxies, we have inferred that our Galaxy is a luminous barred spiral galaxy with a central box/peanut bulge, a dominant disk, and a diffuse stellar halo (Bland-Hawthorn & Gerhard, 2016). These large scale structures are encompassed by smaller stellar overdensities like open clusters in the Galactic plane as well as globular clusters and stellar streams, which are found mainly in the outer regions of the MW. A sketch in Fig. 1.2 shows how these stellar components can be connected with Fig. 1.1 (although not to scale).

In reality however, these large-scale components overlap strongly and their historical definition (e.g. spatial separation) may not be appropriate in another context (e.g. chemical). Especially the influence of the same evolving Galactic potential (e.g. Guedes et al., 2013) will have a strong effect on the dynamical properties and stars may even migrate far from their formation sites (Sellwood & Binney, 2002; Minchev & Famaey, 2010). This might lead to the conclusion that some historical sub-populations may overlap so strongly today, that they are no longer distinct in several properties, for example because they now share a coherent motion (see e.g. Bovy et al., 2012a). Binney (2013) has argued that the Galaxy's stellar populations are better described by

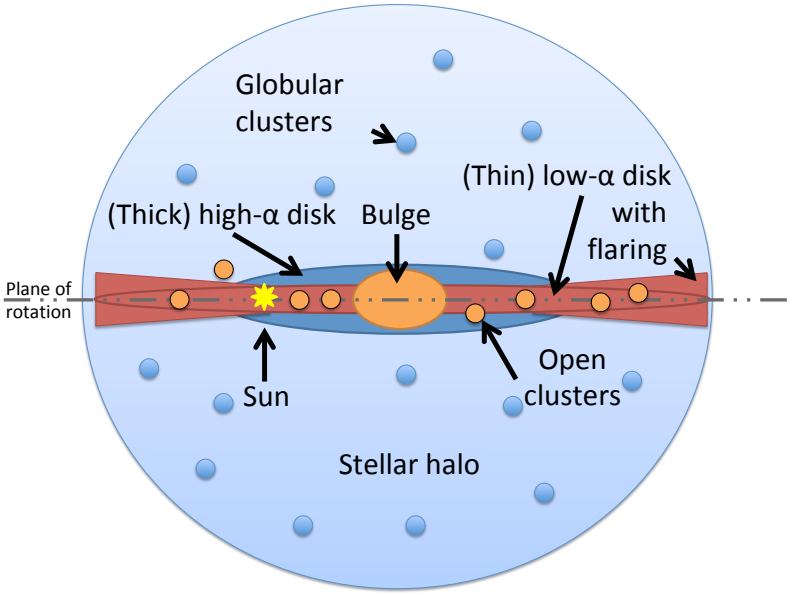

Figure 1.2: A simplified sketch of the stellar components of our Galaxy (not to scale). Contrary to Fig. 1.1, both dust and the extra-Galactic Large and Small Magellanic Clouds are not shown.

self-consistent phase-space distribution functions. This controversy of clear populations versus distribution functions certainly motivates parts of this thesis and throughout this work and we go into more details in Sec. 1.2.3, when we discuss the decomposition of the Galactic components.

Because the discussion of stars as part of these components is still often done, we will review each of the stellar components independently, except for the bulge and bar since they are not covered in this Thesis. For a review of all components, the reader is referred to Majewski (1993); Freeman & Bland-Hawthorn (2002); Ivezić et al. (2012); Bland-Hawthorn & Gerhard (2016) and references therein.

1.2.1.1 THE STELLAR DISK AND OPEN CLUSTERS

The stellar disk The disk is the most massive stellar component of the MW with $5.8 \cdot 10^{10}\,M_\odot$ (McMillan, 2011). The pioneering studies by Yoshii (1982) and Gilmore & Reid (1983) found that the number density of stars along the vertical axis follows two exponentials with two different scaleheights of ~ 300 and ~ 1350 pc, respectively, which lead to the introduction of a separation of the disk into thick and thin disk.

The historical thin and thick disk Estimates of parameters like the ratio of surface densities in the solar vicinity, $f_\Sigma(R_\odot) = 12\% \pm 4\%$ (thick/thin) (Bland-Hawthorn & Gerhard, 2016), have shown that the thin disk is the more massive component of the disk. It is not only vertically thinner, i.e. has a lower scaleheight, but has a larger radial scalelength (2.6 ± 0.5 kpc) than the thick disk (2.0 ± 0.2 kpc) (Bland-Hawthorn & Gerhard, 2016). Kinematic analyses (e.g. Edvardsson et al., 1993; Pasetto et al., 2012) showed that thin disk stars are typically on near-circular, co-rotational orbits with low

velocity dispersions (radially $35 \pm 5\,\mathrm{km\,s^{-1}}$ and vertically $25 \pm 5\,\mathrm{km\,s^{-1}}$), while thick disk stars show significantly larger velocity dispersions (radially $50 \pm 5\,\mathrm{km\,s^{-1}}$ and vertically $50 \pm 5\,\mathrm{km\,s^{-1}}$, Bland-Hawthorn & Gerhard, 2016).

Analyses of the chemical composition of these components (e.g. the seminal paper series starting with Fuhrmann, 1998) further identified distinct differences for the majority of the thin and thick disk stars. For the nearby sky, Fuhrmann et al. (2017) found in their volume-complete study, that stars of the thick disk are enhanced in α-process elements (relative to the Sun), and well separated from those of the thin disk, which typically have a similar ratio of α to iron abundance as the Sun. In their study, only an insignificant number of 9 out of 473 stars (1.9%) are found between the sequences in chemical space.

Several important papers (e.g. Reddy et al., 2003; Fuhrmann, 2011; Adibekyan et al., 2012; Bensby et al., 2014; Hayden et al., 2015) have since established that the stellar disk consists of (at least) two major components in chemical space and age. With the growing number of stars that have been shown in the [α/Fe] vs. [Fe/H], it became however evident, that the component dubbed as thick disk has an extension that overlaps with the thin disk in this plane, see Fig. 1.3. Analyses of the stellar age of the disk stars have further led to the conclusion, that stars of the α-enhanced sequence are very old ($> 8\,\mathrm{Gyr}$), whereas stars of the low-α sequence are younger than 10 Gyr. These arguments and the spatial and kinematical overlap of stars with these chemical and temporal properties (Bovy et al., 2012b,a) led to a rethinking of the disk as a composition of an old, high-α sequence and a young, low-α one, rather than the historical thick and thin disk (see e.g. Bland-Hawthorn et al., 2019).

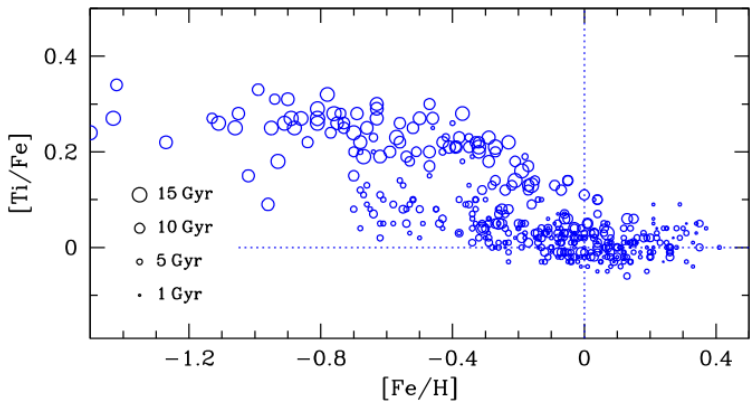

Figure 1.3: α-enancement, traced by [Ti/Fe], versus [Fe/H] for 714 dwarfs of the Solar neighborhood. The sizes of the circles are scaled with the ages of the stars as indicated in the figure. **Figure Credit:** Bensby et al. (2014).

The old, high-α disk and the young, low-α disk The low-α disk extends over a metallicity range of $-0.7 \leq$ [Fe/H] ≤ 0.5 dex with α-enhancement around 0 ± 0.1 dex. The metallicity of the high-α disk, however, extends well below [Fe/H] < -1 dex (Beers et al., 2002). The high-α disk shows an age-dependent sequence with the oldest stars at a plateau of [α/Fe] ~ 0.3 for metallicities below -0.3 dex and a decreasing α-enhancement

towards solar values for its younger stars, which are then overlapping chemically with the low-α sequence. These unique trends of the high-α sequence is constrained by several parameters, as outlined by McWilliam (1997): The initial mass function determines the α-abundance plateau of the oldest stars, whereas the evolution of [α/Fe] depends on the star formation rate. The position of the 'knee', where the α-enhancement decreases for younger stars, depends on the onset of a special enrichment channel, supernovae Ia (see e.g. Maoz et al., 2010).

Hayden et al. (2015) and Bovy et al. (2016) have further shown that the (surface) density of stars in both sequences change as a function of position, as can be seen in Fig. 1.4. The high-α sequence dominates only at large heights z and for the inner disk ($R < 9$ kpc), whereas the low-α sequence can be seen at all radii and heights, but with changing morphology. In the inner disk, only the metal-rich regime of the low-α sequence is populated and we see a gradual change of [Fe/H] towards the outer disk with the population of the full low-α sequence in the Solar vicinity, towards only metal-poor stars in the outer disk ($R > 11$ kpc). The presence of low-α stars in the outer disk at larger vertical heights has been found to be caused by strong disk flaring (see Fig. 1.2 and e.g. Bovy et al., 2016; Xiang et al., 2018).

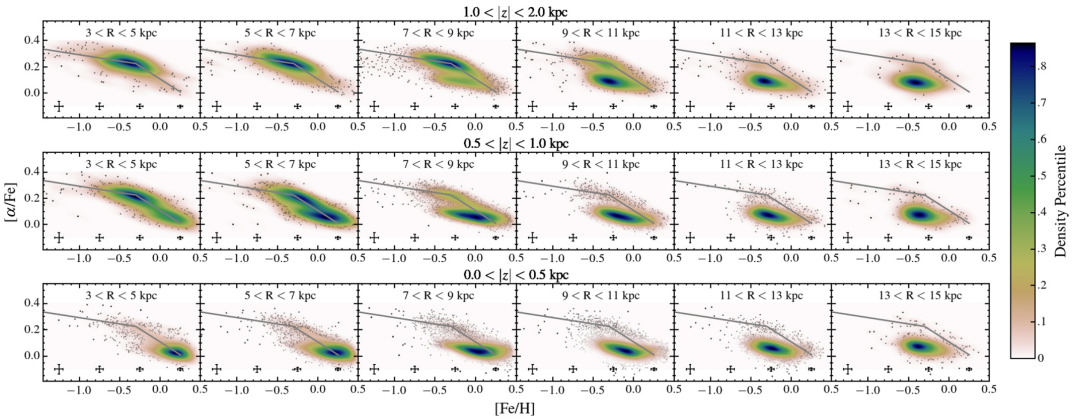

Figure 1.4: Stellar distribution of stars in the [α/Fe] vs. [Fe/H] plane as a function of R and $|z|$. Typical abundance uncertainties are shown as a function of metallicity across the bottom of each panel. The size of individual points is inversely related to the density at that location. **Figure Credit:** Hayden et al. (2015).

As mentioned before, the low-α stars are typically young (< 10 Gyr) and the high-α stars are typically old (> 8 Gyr). We note that due to the still quite large uncertainties of stellar age estimates, it is not yet clear if the sequences were both actively star-forming 8 – 10 Gyr ago or if the young sequence only started forming stars after the star formation of the old sequence came to a complete end. The reason of this abrupt change in chemical composition of the interstellar medium is still an open problem of our understanding of the MW formation (see Sec. 1.2.2).

Open clusters Almost all stars are believed to be born in clusters. Individual clusters have formed from the same giant molecular cloud at roughly the same time and should share the same birth material composition (see e.g. Friel, 1995), but walk a knife edge between survival and disruption (see e.g. King, 1958) and most of them have dispersed

and build up the field population. The presence of open clusters up to ages of 10 Gyr and across a large range of Galactocentric radii and sometimes high above plane (Dias et al., 2002; Salaris et al., 2004), but allows us to study processes such as heating, migration, and cluster disruption over time (see e.g. Bergh, 1980).

Open clusters allow us to study the relationship between stellar distributions in chemical and physical space (see e.g. Armillotta et al., 2018). They provide a direct time line for investigating change, both intrinsic as the a result of stellar evolution (see e.g. Dotter et al., 2017; Souto et al., 2018; Gao et al., 2018; Liu et al., 2019) as well as extrinsic in terms of the enrichment of cluster birth material over time. Before the era of large-scale astrometric measurements, their ensemble with same age and distance allowed some of the most accurate 3D positions and allowed to study the abundance gradients within our Galaxy (see e.g. Cunha et al., 2016). They are widely used as benchmarks for the calibration of ages (see e.g. Fu et al., 2018; Randich et al., 2018) as well as the internal precision estimates of abundances (see e.g. Holtzman et al., 2018).

1.2.1.2 THE STELLAR HALO AND GLOBULAR CLUSTERS

The stellar halo The stellar halo is significantly less massive than the disk, with only about 1% of the total stellar mass (see e.g. Morrison, 1993). It follows a power law density distribution $\rho \sim r^{-3.5}$ and extends out to 100 kpc (Helmi, 2008; Freeman & Bland-Hawthorn, 2002). Contrary to the disk, halo stars do typically not rotate coherently or are even on slightly retrograde orbits with respect to the disk (e.g. Freeman, 1987). Halo stars can be on very energetic orbits, reaching up to 100 kpc from the Galactic center (see e.g. Carney et al., 1990; Mackereth et al., 2019b). Their total velocity is very different from the disk with values above $180 < v_{\rm tot} < 220$ km/s (see e.g. Venn et al., 2004).

Most halo stars are very old (> 8 Gyr), that is as old or older than the thick disk (see e.g. Jofré & Weiss, 2011; Hawkins et al., 2014; Das et al., 2019), and predominantly metal-poor (see e.g. Schlesinger et al., 2012). The metallicity distribution of the halo is however still not well explored due to our limited means to study stars at large distances. It is therefore still contentious as to whether or not the halo can be separated into an metal-rich, prograde, inner ($R < 15$ kpc) and metal-poorer, retrograde, outer halo. This separation was proposed by Carollo et al. (2007, 2010) based on identified variations in metallicity and kinematics, but opposed by Schönrich et al. (2011) and Schönrich & Bergemann (2014) due to systematic shortcomings of the data analyses.

Past and on-going accretion events, like the on-going merging of the Sgr dwarf (Ibata et al., 1995), additionally complexify the characterisation of the halo. We are still only beginning to disentangle the accreted from the in-situ MW stars in the stellar halo. First estimates suggest 60% of stars are accreted, for metallicities [Fe/H] < -1 dex (Di Matteo et al., 2018). It is yet to be understood if there is in fact an in-situ component of the halo from an early dissipational gas collapse or if the halo is formed fully from assembly from accreted stellar systems at early times. Part of this problem is that the transition of the (high-α) disk to the halo is rather smooth both dynamically and chemically (see Chapter 4).

The pioneering analyses of a small set of nearby stars with halo-like kinematics by Nissen & Schuster (2010, 2011, 2012), Ramírez et al. (2012), and Nissen et al. (2014) showed that the halo has at least two rather distinct populations in chemical space. While one of the components resembles the chemical composition of the high-α disk, the second component shows strong differences in several elements like the α-elements, Na, and Ni, see Fig. 1.5. A decrease of α-enhancement at these metallicities would be typical for stars with a different star formation history than the MW, like dwarf galaxies (Koch et al., 2006; Tolstoy et al., 2009). These stars were therefore believed to be accreted in origin.

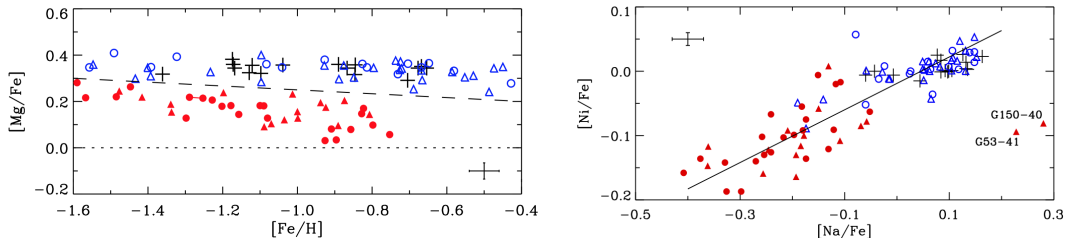

Figure 1.5: Left: [Mg/Fe] versus [Fe/H] for kinematically selected halo stars. Right: [Ni/Fe] versus [Na/Fe] with the same symbols. Crosses refer to thick-disk stars and circles to halo stars observed with UVES. Triangles indicate halo stars with FIES spectra. Halo stars above the long-dashed line in the [Mg/Fe] diagram are defined as belonging to the high-α population and are indicated by open (blue) symbols. **Figure Credit:** Nissen & Schuster (2010).

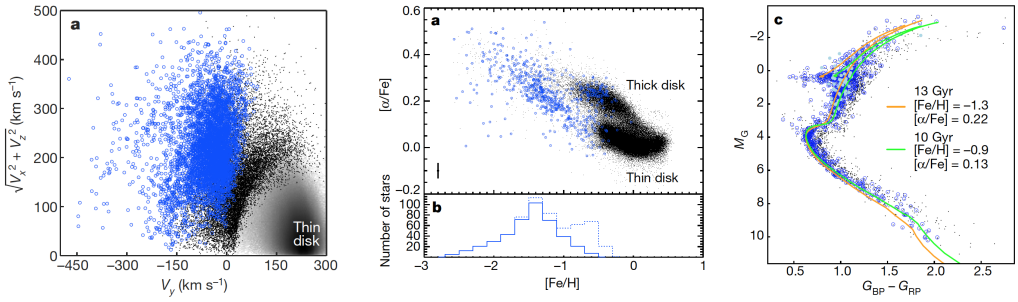

Figure 1.6: Kinematic, chemical, and observational representation of *Gaia*-Enceladus. Left: Toomre diagram, showing the kinematics (from *Gaia* data) of stars with the disk (grey), halo (black) and selected stars with slightly retrograde motion and high orbit energies, attributed to *Gaia*-Enceladus. Middle: α-enhancement vs. iron abundance for APOGEE DR14 (black) and the overlap of the latter with *Gaia*-Enceladus. Right: CMD of kinematically selected halo stars (black) from the left panel and *Gaia*-Enceladus stars (blue) and isochrones from Hawkins et al. (2014). **Figure Credit:** Helmi et al. (2018).

With the recent advent of large scale stellar surveys and their data releases, most notably *Gaia* DR2 (Gaia Collaboration et al., 2018b), the stellar halo came into the focus of both the Galactic dynamics as well as spectroscopic communities. With the precise astrometric and photometric information of *Gaia* for an unprecedented number of stars with halo kinematics, Gaia Collaboration et al. (2018a) confirmed at least two overdensities with distinct metallicities. Data from large stellar spectroscopic surveys like

APOGEE (Hayes et al., 2018) as well as LAMOST (Liu et al., 2018) have subsequently been used to confirm the metallicity bimodality of kinematically defined halo stars, which now appears to have a slightly different shape than claimed by Nissen & Schuster (2010) based on α-abundance, with overdensities around [Fe/H] ~ -0.6 and ~ -1.4 dex. Combining the information, chemodynamic studies (e.g. Schuster et al., 2012; Haywood et al., 2018) in combination with simulations (e.g. Belokurov et al., 2018; Helmi et al., 2018) have been used to assign preferentially low [Fe/H] and low [α/Fe] halo stars to a large precursor of a major merger, dubbed Sausage or *Gaia*-Enceladus. This is visible as a large blue overdensity in kinematic and chemical space in the left and middle panel of Fig. 1.6, respectively. The typically high eccentricity of these stars, as found by Schuster et al. (2012) and Mackereth et al. (2019b), underline that these low-α halo stars are likely accreted.

As pointed out in the review by Nissen & Gustafsson (2018), the origin of the low-α halo is still debated. Were all the stars of this population accreted during the merger with *Gaia*-Enceladus or do we see a superposition of many accretion events of dispersed massive clusters, as the simulations by Kruijssen et al. (2018) would suggest? Previous studies (e.g. Liu et al., 2018) have shown overdensities for even lower metallicities than those analysed by Nissen & Schuster (2010), that is close to the iron abundance of the most metal-poor globular clusters. The chemical pattern of low-α halo stars seems to resemble both globular clusters like ωCen (Myeong et al., 2018a) as well as dwarf spheroidal (dSph) galaxies such as as Fornax and Sculptor (e.g. Shetrone et al., 2001, 2003; Koch et al., 2006; Tolstoy et al., 2009; Kirby et al., 2009; Letarte et al., 2010; Skúladóttir et al., 2017). Different scenarios for mergers of these galaxies with the Milky Way have been discussed by McWilliam et al. (2013) and Fernández-Alvar et al. (2018) but remain inconclusive.

Globular clusters Globular clusters are dense, spherical collections of stars. In the MW, we have so far identified $\sim$ 160 globular clusters (Harris, 1996) with typically $10^5 - 10^6$ stars. ω Cen is one of the (if not the) most massive globular clusters with an estimated mass of $(4.55 \pm 0.1) \cdot 10^6 M_\odot$ (D'Souza & Rix, 2013). Many of the globular clusters are believed to be remnants of early satellite galaxies who experienced a different chemical evolution before their accretion onto the Galaxy (Freeman & Bland-Hawthorn, 2002). The globular cluster M54 for example is believed to be the nucleus of the Sagittarius dSph galaxy (Carretta et al., 2010b).

Contrary to open clusters, globular clusters are currently not being formed in the MW (Lada & Lada, 2003). Almost all of them are older than 10 Gyr, typically 12 – 13 Gyr (Kharchenko et al., 2013). However, we see that their range of metallicity from $-2.2 <$ [Fe/H] < 0.5, their abundance ranges as well as their old age are similar to the thick disk (Freeman & Bland-Hawthorn, 2002). There is also ample evidence that numerous globular clusters have been disrupted and their stars are now contributing around $10 \pm 1\%$ to the field halo stars (see e.g. Koch et al., 2019).

The study of elements within globular clusters have helped to study stellar evolution, like the occurence of dredge-up and thermohaline mixing through studies of Li abundances (see e.g. Lind et al., 2009). The identification of element abundances

variations for CN (see e.g. Popper, 1947), light elemens like Na and Al (see e.g. Grundahl et al., 2002; Marino et al., 2008), but also neutron-capture elements like Ba and La (see e.g. Marino et al., 2011). This has lead to the discovery of several distinct atypical anti-correlations in element abundances, like Na-O (see e.g. Carretta et al., 2009) and which puts in doubt the historical explanation of clusters as simple stellar populations. Through photometric studies it has been shown that most globular clusters actually are home to multiple populations (see e.g. Milone et al., 2017; Bastian & Lardo, 2018). Because no open clusters have so far shown signs of multiple populations, the cluster mass seems to be important for their formation (Carretta et al., 2010a; Milone et al., 2017), as they may be able to retain stellar ejecta from a first generation of stars and form new generations of stars from this enriched material. The current census of globular clusters (see e.g. Bastian & Lardo, 2018) shows that the youngest (< 2.5 Gyr) and most metal-rich ($[Fe/H] > -0.5$ dex) globular clusters are not hosting multiple populations . The origin of multiple stellar populations remains unknown (see the review by Bastian & Lardo (2018)). There are several competing yet incomplete theories to explain the multiple populations, including the internal pollution from Asymptotic Giant Branch (AGB) stars (see e.g. Cottrell & Da Costa, 1981), fast-rotating massive stars and interacting binaries as well as differences in the composition and cloud physics of young molecular cloud.

1.2.2 OUR CURRENT UNDERSTANDING OF MILKY WAY FORMATION

How did the structure of the MW and its components assemble, from the beginning of the Universe with the Big Bang to now? In the last century, several formation scenarios have been proposed. Eggen et al. (1962) proposed a top-down scenario, in which the Galaxy formed through a dissipative collapse of a large isolated protogalactic gas cloud, that first formed a spherical halo and later settled into the now observed, rotationally supported disk under specific angular momentum conservation. In stark contrast to this scenario is the suggested bottom-up scenario (see e.g. Peebles, 1971; Press & Schechter, 1974; Searle & Zinn, 1978) of a hierarchical aggregation of smaller elements, like high-angular momentum gas onto a dark matter halo, which then settled to the disk. The idea of hierarchical accretion over billions of years from small to large scales is also embedded in the most popular cosmological framework of the (λ-) cold dark matter model. This physically motivated model encompasses information about the initial conditions of our Universe in terms of baryonic and dark matter as well as dark energy and under this model small dark matter halos form and later merge via dissipationless gravitational processes (White & Rees, 1978). In this picture we believe that shortly after the Big Bang, baryons and photons were decoupled and dark matter started to drive the baryons towards local density enhancements caused by primordial fluctuations and enhanced by inflation.

These baryons started forming the now observed Galactic structures like bulge and disk, but the exact formation is still not explained. It is possible that a first collapse of the central regions of the protogalaxy or the merging of clumps early on (Noguchi, 1999) may have seeded the early stages of a massive black hole and giving rise to what we see as a significant overdensity of stars in the center of the Galaxy, which accreted

more and more stars and is now the seen as the stellar bulge. In spiral galaxies like the MW which have a boxy/peanut bulge (the vertically extended part of the bar in the inner-most region) a primary mechanism of formation is internal evolution from the disk (see Kormendy & Kennicutt, 2004; Gonzalez & Gadotti, 2016, for a review). There is overwhelming evidence that the Milky Way has a boxy/peanut bulge which is consistent with secular evolution, for example when looking at the metallicity distributions and kinematic properties of stars in the bulge (see e.g. Ness et al., 2013; Bensby et al., 2013; Ness et al., 2015; Bensby et al., 2017).

The formation of the Galactic disk is another complex puzzle, that seems to have had at least two major epochs, giving rise to two distinct populations in phase space, the classical thin and thick disk. Due to the evolution of the MW, these populations are however extensively overlapping both in configuration and velocity space, but seem to be rather distinct in chemistry and age (see Sec. 1.2.1.1). The preferred option of dissection is by chemistry (e.g. Bland-Hawthorn et al., 2019) and age (see e.g. Buder et al., 2019), that is into a young low-α disk (instead of the thin disk) and the old high-α disk (instead of the thick disk). Several studies (see e.g. Haywood et al., 2013; Buder et al., 2019; Haywood et al., 2019) found evidence, that the vast majority of the low-α stars are younger than the youngest high-α disk stars. However, the uncertainties in estimated stellar ages are not yet allowing to disentangle if the low-α disk formed entirely after the high-α one.

A popular theory to explain the formation of the a two-component disk is the two-infall model (see e.g. Chiappini et al., 1997, 2001), where one main infall episodes explain first the formation of the halo and high-α disk on a short gas consumption time scale (roughly 1 Gyr), and continues to evolve until a hiatus in star formation rate. In this model, the formation of the low-α disk is detached from the high-α disk, because during the second infall epoch, the inside-out formation, slowly infalling primordial gas gives rise to the disk where gas accumulates faster in the inner regions than the outer ones on timescales of 8 Gyr in the Solar vicinity. Clarke et al. (2019) showed that two different modes in star formation history, a distributed one and a clumpy one at early times, that is high redshifts, naturally give rise to an α-abundance dichotomy. In their simulations, a considerable amount of star formation occurs in clumps that dominates within the first 3 Gyr over a more distributed ('smooth') one with lower star formation throughout the rest of the disk. The clumps form on the low-α sequence and self-enrich up to the high-α sequence. When the gas mass fraction drops, the distributed star formation becomes dominant and is the main producer of the low-α disk. Decreasing the uncertainty of stars at the age gap between high- and low-α sequence is the most promising way to test both scenarios.

Other scenarios of the disk evolution to explain the exponential density profile of the disk include vertical heating through gradual secular evolution (Schönrich & Binney, 2009; Loebman et al., 2011; Minchev et al., 2015) or minor merger events (Quinn et al., 1993; Villalobos & Helmi, 2008). The presence of a massive thin disk with low velocity dispersions suggests, that the last massive merger/accretion events happened before the formation of the thin disk (Freeman & Bland-Hawthorn, 2002). Dynamically the

low- and high-α sequences are distinct at all ages which is strong evidence for separate formation scenarios (Mackereth et al., 2019a; Gandhi & Ness, 2019). The high-α disk may have formed with stars that are now seen on dynamically hotter orbits than those of the low-α disk for example during the dissipational collapse of the primordial gas cloud out of early turbulent gas (Gilmore et al., 1989; Bournaud et al., 2009) or from the debris of accreted satellites that deposited their stars high above the Galactic plane (Abadi et al., 2003).

The formation of the stellar halo surrounding the MW in a significantly larger volume remains enigmatic, with suggestions of a formation at the same time as the thick disk or a different build-up through progressive accretion of material. Recent simulations (e.g. Abadi et al., 2006; Font et al., 2011; McCarthy et al., 2012; Tissera et al., 2013; Pillepich et al., 2015; Cooper et al., 2015) suggest that a fraction of stars that reside in the halo today could have formed in-situ in the Galaxy, either in the early Galactic disk and subsequently ejected/heated into the halo, or directly in the halo from gas stripped from infalling satellites. Observational data (see e.g. Bonaca et al., 2017) suggests that at least the high-α halo was formed in-situ. An important fraction were formed ex-situ in other galaxies and accreted by the Milky Way (see e.g. Bell et al., 2008) and we still see evidence of on-going accretion through substructures like stellar streams. Such streams and severe structure changes are also seen in other galaxies like M31 (see e.g. Ibata et al., 2001) and suggest a high degree of infall and stochastic accretion (see e.g. Koch et al., 2008).

1.2.3 CHEMOKINEMATIC DECOMPOSITION OF GALACTIC COMPONENTS

To understand the formation of the MW, we clearly have to understand its components individually and also their interplay and temporal correlation. Currently, the techniques to achieve the description of the MW in a statistical way, for example via stellar distribution functions (see Eq. 1.2), are still under development. We will for practical reasons use the simplified view of stars as parts of the aforementioned Galactic components for now.

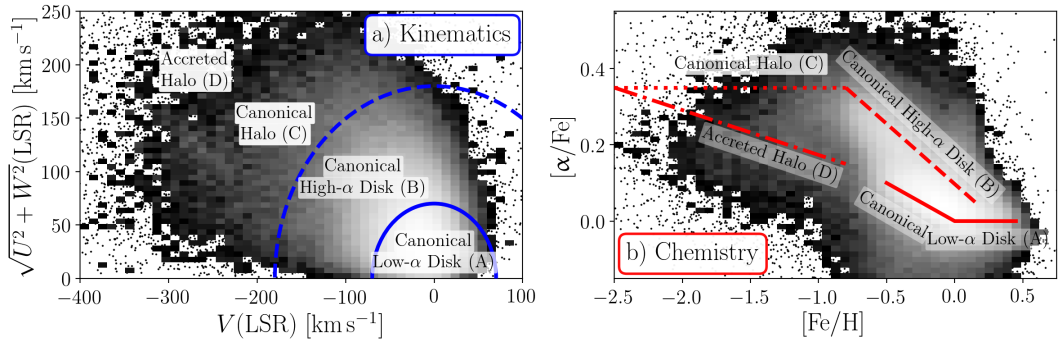

Figure 1.7: A cartoon illustration of the decomposition of the Galactic components via kinematical and chemical information in the right and left hand panels, respectively. In the kinematic view (with the velocity of the LSR as point of origin), blue lines separate the components. In the chemical view, the red lines trace the stars of the particular components. This figure is inspired by Fig. 1 from Hawkins et al. (2015). The gray contours show densities of stars observed by the GALAH survey (**Paper IV**).

In this section, we will review the currently most popular means to separate the Galactic components with chemical, kinematical/dynamical as well as temporal information. Fig. 1.7 shows two diagrams that are largely used to separate the Galactic components. The left panel shows a Toomre diagram as a combination of the three Galactocentric space velocities, where stars of the canonical low-α disk have a similar total motion as the LSR (within 70 km/s) and halo stars are kinematically hotter than 180 km/s with respect to the LSR. For the chemical separation, the [α/Fe]-[Fe/H] plane in the right panel of Fig. 1.7 is used to attribute stars to the components (with most stars along the red lines for the particular components). In numerous studies, discrete cuts are used to separate the individual components. As we have already discussed in Sec. 1.2.1, the transition between the components has proven to be smooth and calls for both studies of the transitions as well as the development of new techniques to separate the components or describe stars in DF. Therefore, we will outline possible shortcomings of hard limits on the assignment of stars to components with kinematical and chemical criteria. For practical reasons, we will discuss the decomposition of the components as before, that is, the intra-disk decomposition and the disk-halo decomposition. For a review on the tracing of components (mostly via chemistry) following the same methodology, the reader is referred to Nissen & Gustafsson (2018).

DECOMPOSITION OF THE DISK COMPONENTS

- **Separation via vertical height** Because of the different scaleheights of the disk components (see Sec. 1.2.1.1), a rough decomposition of stars into 'thin' and 'thick' component can be achieved via the vertical height. Due to the spatial overlap of the components, this selection is however not very reliable.

- **Separation via kinematics** Based on the different velocity dispersions and the typically hotter orbits of high-α stars (in this context similar to the thick disk, see Sec. 1.2.1.1), kinematic properties have been suggested to separate the disk components, as shown in the left panel of Fig. 1.7, where the canonical disk components (A and B) can be separated via lines of total velocities above or below $\sim 75\,\mathrm{km\,s^{-1}}$. A more sophisticated separation was proposed by Bensby et al. (2003) and assumes that the components can be modelled with Gaussian velocity distributions, which allow calculation of probabilities of membership assignment given these distributions. Because of the structural continuity in thickness and kinematics (e.g. Bovy et al., 2012b, 2016) however, such assignments have been shown to be a rather unreliable tracer of the disk sub-populations (see e.g. Bensby et al., 2014).

- **Separation in the [α/Fe]-[Fe/H] plane** The studies by Fuhrmann (1998) suggested that the two disk components can be clearly separated in [α/Fe]-[Fe/H] plane. Taking more and distant stars into account, Bensby et al. (2014) found significantly more stars in the previously apparent gap, see Fig. 1.3. In the Solar neighbourhood, the bimodality between these two populations in the high-α metal-rich regime has been shown to become less or not significant and is still

contentious, based on the chosen approaches and population cuts used for the definition of disk populations, see components A and B in Fig. 1.7. Adibekyan et al. (2011) even claim a third sub-population in this regime, which is not confirmed by other data sets (see e.g. Buder et al., 2019). Some of the recent studies using chemistry assume the existence of two distinct populations in α-enhancement up to the most metal-rich stars. In these studies, the metal-rich stars are cut into high and low sequence memberships rather arbitrarily; either by eye or with rather fiducial straight lines, for example Fig. 7 from Adibekyan et al. (2012) , Fig. 12 from Recio-Blanco et al. (2014) Fig. 1 from Hayden et al. (2017). A consistent measure or definition to separate the two α-sequences in the [α/Fe]-[Fe/H] (especially in the metal-rich regime) remains elusive. Elements other than [α/Fe] have so far not been found to show more distinct separations for the disk (see e.g. Bensby et al., 2014; Battistini & Bensby, 2015, 2016), although some are just as as powerful, for example Al.

- **Separation in stellar age** With the advances in estimating ages for larger samples of stars, we are now in the position to test if stellar age, which of course is an intrinsic property unaffected by environmental effects (contrary to its kinematic properties), can help to reliably separate stars in the disk, especially in the metal-rich regime. First analyses by Haywood et al. (2013) suggest that the combination of age and [α/Fe]-[Fe/H] can indeed help to separate the disk components, tying old stars (> 8 Gyr) to the (thick) high-α disk and young stars (< 10 Gyr) to the (thin) low-α disk, but need further confirmation from other data sets. In particular, more data are needed to study the intermediate regime at $8 - 10$ Gyr as well as the contentious high-α metal-rich population.

DECOMPOSITION OF THE HALO AND THE DISK

The properties of the Galactic halo are significantly less well understood than the disk. Because most of our knowledge on the halo is still based on the analyses of small samples, we have not yet understood the transition between the high-α disk and halo. In particular, we still have to find the answer to the question, if the high-α-halo is only the kinematically hotter, metal-poorer and/or older extension of the high-α-disk. For completion, we will however briefly describe recent studies that analyse the disk-halo transition.

- **Separation via Galactic height** Stars of the spherical halo can in principle be selected, if one looks far enough away from the plane, such that the halo is dominating the exponential decline in number density found for the disks (see Sec. 1.2.1.1). Chen et al. (2019) showed that the disk becomes an insignificant contributor to the stellar density above $|z| > 8$ kpc. Such a selection also neglects the presence of local halo stars, currently passing by the disk and it is non-trivial to accurately infer distances to individual object so far away (from astrometry, photometry and/or spectroscopy see Sect. 1.3). Although we might still be able to collect such information in the current era of large and extremely large telescopes, different selections have proven to be more efficient.

- **Separation via kinematics** Before the *Gaia* era, not many stars could be placed in the Toomre diagram due to missing kinematic information. With the small numbers of analysed stars, the kinematic characterisation of halo stars led to the conclusion, that these stars do not have a coherent motion with respect to the centre of the Galaxy (i.e. individual stars can be non-rotating or even counter-rotating in vertical direction), i.e. their vertical angular momentum is close or below $0\,\mathrm{kpc\,km\,s^{-1}}$. In the Toomre diagram, this corresponds to an azimuthal velocity V of below -180 to $-230\,\mathrm{km\,s^{-1}}$ (depending on the circular velocity of the reference system). Including the uncertainties in the reference frame and the velocity dispersion of the disk and halo, a separation of $v_{\mathrm{tot}} \sim 180 - 220\,\mathrm{km\,s^{-1}}$ (Venn et al., 2004; Nissen & Schuster, 2010) or similar values in the transversal velocity were proposed for the disk-halo transition, see components B and C in Fig. 1.7. With the new kinematic data from *Gaia*, such a sharp cut appears to be however not reasonable. Di Matteo et al. (2018) were for example able to reconstruct kinematic characteristics of the high-α halo as a composite of high-α disk and low-α halo stars, which they interpret as evidence that no in-situ halo component is present.

- **Separation via chemistry** Among others, Hawkins et al. (2015) tried to analyse if we can chemically identify Galactic disk and halo stars. They found however, that the canonical halo and canonical thick disc are not chemically distinct in any of the elements they studied, that is components B and C overlap in panel b) of Fig. 1.7. Several studies (see e.g. Beers et al., 2002; Carollo et al., 2019) have estimated that the metal-weak thick disk extends down to [Fe/H] ~ -2.

DECOMPOSITION OF THE LOW-α (ACCRETED) AND HIGH-α CANONICAL HALO COMPONENTS

Contrary to the disk-halo transition, the low-α (accreted) and high-α canonical halo components appear to be very different in many aspects.

- **Separation via kinematics** First hints of distinct orbit parameters of the two components were found by Nissen & Schuster (2010); Schuster et al. (2012), who showed that the accreted and canonical halo separate in the Toomre diagram as shown in Fig. 1.7 with components C and D. They also found that the accreted stars show significantly higher eccentricities close to 1, a result now backed up with larger samples (see e.g. Mackereth et al., 2019b).

- **Separation via chemistry** The seminal study by Nissen & Schuster (2010) found a clear separation in several abundance planes like [α/Fe]-[Fe/H] (see components C and D in Fig. 1.7), [Ni/Fe]-[Na/Fe] within a limited metallicity range. Hawkins et al. (2015) later confirmed further bimodalities of abundance ratios like [C+N/Fe] or [Mg/Mn]. While Das et al. (2019) already used Gaussian Mixture Models for separating canonical and accreted halo stars in the [Mg/Mn] vs. [Al/Fe] plane, the use of even more elements, like Cu, Y, or Ba with found spreads by Nissen & Schuster (2011) could be included. These might also prove to be useful for the

most metal-poor halo stars, as the α-enhancement of the accreted and canonical halo overlaps below -1.6 dex (see e.g. Reggiani et al., 2017; Matsuno et al., 2019).

- **Separation via stellar age** If determined accurately for large samples, stellar age is the most useful piece of information to understand their origin and the overall evolution of the Galaxy. Contrary to the disk, where the low-α disk consists of young stars and the high-α disk of old ones, the ages of both the high- and low-α populations in the halo are expected to be rather similar and high precision on the age estimates is needed. However, Hawkins et al. (2014) found that in the high-metallicity regime of the halo, α-rich stars are older than α-poor ones, while for the low-metallicity regime, stars appear to be mostly coeval. New insights on the age distribution of the halo stars, and our ability to attribute stars to different populations will be gained by the analyses of the newly published data from *Gaia* and large stellar surveys. A first analyses via CMD isochrone fitting by Gallart et al. (2019) suggested, that the high-α halo stars are older than the typical high-α disk stars, but coeval with the low-α halo stars. Due to the uncertainties on their age distributions, which is using the still uncertain calibrations of the *Gaia* passbands and extinctions, further studies are however needed to confirm their contentious findings.

In this section, we have discussed how stars can be assigned to one of the major components or subpopulations found in the Galaxy. Going one step further, we would ideally also like trace stars back in time to a more well-defined birth location, for example exact birth radius in the disk, or even find stellar siblings and parent clusters, an idea suggested by Freeman & Bland-Hawthorn (2002) and called chemical tagging.

1.2.4 CHEMICAL SPACE AND CHEMICAL TAGGING

Given that we can use stars as time capsules of their birth conditions, studying their present-day composition ideally allows us to reconstruct the past. These kinds of studies provide clues to the assembly of different Galactic structures from stellar moving groups (see e.g. Eggen, 1974), dispersed open and globular clusters (Searle & Zinn, 1978) and dwarf galaxies (Eggen et al., 1962).

The pioneering studies by Edvardsson et al. (1993), Reddy et al. (2003), Bensby et al. (2014) and Hayden et al. (2015) - to name a few - have promoted the idea that by probing large samples of stars, we also should be able to reconstruct the chemical pattern and substructure in the protogalactic disk.

Before collapsing to form the stars that we observe now, the gas experienced events that imprinted a certain chemical pattern. In a closed parcel of gas only a few Supernova(e) (SNe) events would be required to reach [Fe/H] ~ -3, and 30 to 100 events to enrich the material to [Fe/H] ~ -1.5. To reach solar metallicities, that is [Fe/H] ~ 0, maybe a thousand events would be needed (Freeman & Bland-Hawthorn, 2002).

In addition to supernovae, other enrichment channels could have altered the element abundances as well (see e.g. Burbidge et al., 1957), as will be outlined in this section. If

the type and number of enrichment events would then be sufficiently different, stars born from different birth material should show different chemical patterns.

THE DIMENSIONALITY OF CHEMICAL SPACE C

The chemical space that we want to explore is spanned by all the elements that are formed and are readily detectable in stellar spectra of large-scale surveys. These elements are highlighted in the periodic table in Fig. 1.8. Such tables are used to demonstrate different chemical groups and the one in Fig. 1.8 is additionally highlighted by color for the element groups that are detected in spectra of the HERMES spectrograph. The elements that can be observed with current ground-based large-scale spectroscopic surveys are indicated at the bottom of each element box. We note that boutique analyses (see e.g. Hansen et al., 2012; Roederer et al., 2014) allow the collection of even more elements and abundance measurements (Hinkel et al., 2014).

Ting et al. (2012), investigated the dimensionality of the C-space (Cspace) from a data-driven aspect via principal component analyses of element abundances from catalogues of metal-poor stars, metal-rich stars, open clusters as well as stars in the Fornax dSph galaxy and estimated that a survey that measures up to 30 different elements of the various nucleosynthesis groups, will explore a Cspace with $7 < n < 9$ dimensions.

The seminal paper by Burbidge et al. (1957) has reviewed the synthesis of these elements in stars and demonstrated that a large variety of elements are produced in different sites and under different conditions. In the current literature, a common way to group different elements is the following chemical 'families':

- **Lithium** is produced during the Big Bang nucleosynthesis with an initial abundance of $A(\mathrm{Li}) = 2.75 \pm 0.02$ (Pitrou et al., 2018), but the measurements of surface abundance in stars typically deviate strongly from this value, especially for metal-poor main sequence stars, for which a plateau-like abundance of $A(\mathrm{Li}) \sim 2.2$ was discovered by Spite & Spite (1982). Li abundances in most other stars even span the range of solar $A(\mathrm{Li}_\odot) \sim 1.05$ (Asplund et al., 2009) to meteoric values with $A(\mathrm{Li}) \sim 3.26$ (Lodders et al., 2009) and we need both additional production but also depletion channels to explain this large abundance range. Several production mechanisms and sites have been proposed, such as cosmic ray spallation (Reeves et al., 1970), novae and core-collapse supernovae (Arnould & Norgaard, 1975), Red Giant Branch (RGB) and AGB stars (Sackmann & Boothroyd, 1999, 1992), but are not contributing sufficiently to explain the observations (Prantzos, 2012). The Li surface abundance of a star is strongly depending on the physical conditions throughout its atmosphere. Effects like convective and non-convective (e.g. rotation-induced) mixing combined with atomic diffusion (see e.g. Talon & Charbonnel, 1998, 2004) are believed to govern the abundance of Li in main sequence stars, whereas the first dredge-up after the turn-off dilutes Li (Lind et al., 2009). Because Li is depleted by the proton bombardment processes at temperatures higher than $2.5 \cdot 10^6$ K (Pinsonneault, 1997), other processes that either create low-temperature layers or drive Li production and subsequent mixing of these layers with the photosphere could explain high values. Casey et al. (2019) suggested for

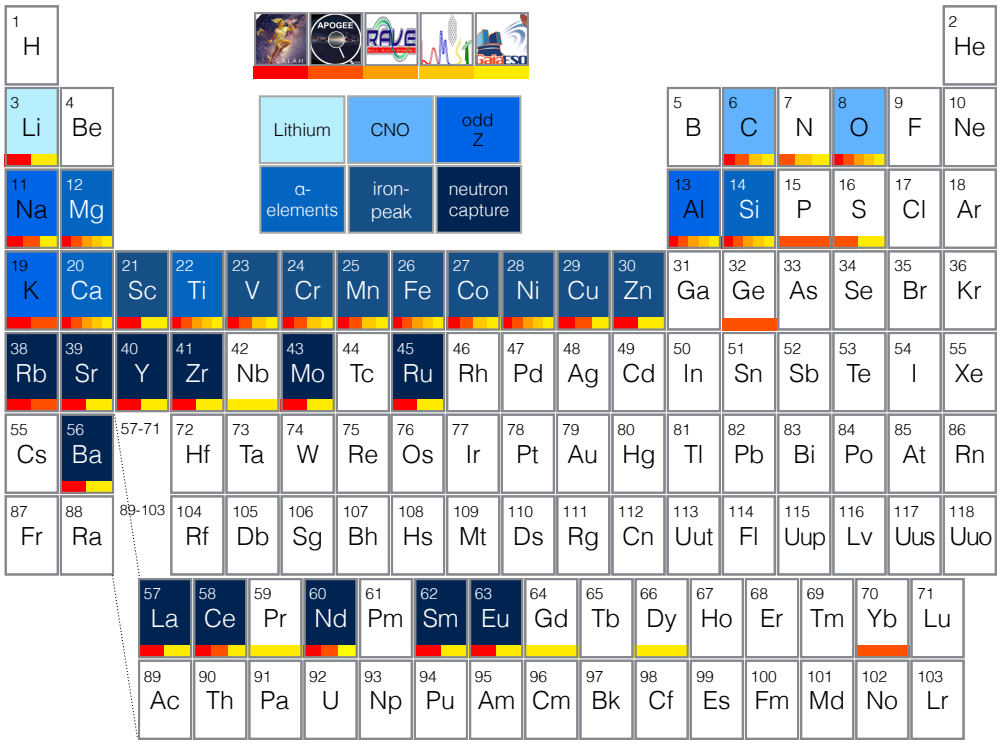

Figure 1.8: Periodic table of elements annotated with current knowledge of their nucleosynthetic channels (colored area) and their detectability of large stellar surveys (colored bars at bottom of each element). The boxes of those elements observed by the GALAH survey are colored by the main group/family of the primary isotope.

example Li production and fast mixing in the course of binary evolution to explain the occurrence of Li-rich giant stars, whereas for example Kumar et al. (2011) argue that these stars are predominantly clump stars, involved in core He burning after Li production at the tip of the giant branch at the core flash.

- **The CNO-elements** C and O are convective and non-convective (e.g. rotation-induced) mixing combined with atomic diffusion produced by a large variety of processes. Carbon is produced during hydrostatic burning inside massive stars via the triple α process, but also in low mass stars, core-collapse Supernovae type II (SNe II), as well as AGB stars (see e.g. Nomoto, 1984). While the relative importance and yields of these processes are still uncertain for C (Nissen et al., 2014), for O it is more clear that it is mainly produced during hydrostatic burning in massive stars and then dispersed by SNe II into the interstellar medium (Kobayashi et al., 2006). Because C and O are part of the H-burning CNO cycle, the C abundance can be depleted, while O (and N) are created. Because those elements are only catalysts in the CNO cycle, their total abundance remains constant, with their relative abundances driven to equilibrium values . Although the CNO cycle

is happening in deeper layers of the atmosphere, CNO-processed material can be brought up to the surface during the a mass-dependent dredge-up after the turn-off (see e.g. Iben, 1965; Martig et al., 2016).

- **The α-elements** Mg, Si, Ca, Ti are created inside massive stars, by α-particle capture on increasingly heavy nuclei in shell-structures surrounding the core. The elements are predominantly released to the interstellar medium during core-collapse supernovae SNe II. Formally, C and O are part of the family of alpha-elements, but are typically separated from them because of secondary production channels (see above) and because they are produced at shallower layers in massive stars, resulting in higher yields (Nomoto et al., 2013).
- **The odd-Z elements** Na, Al, and K are produced during Supernovae type Ia (SNe Ia) and SNe II as well as hydrostatic and explosive C, O, and Ne burning. According to Kobayashi et al. (2006), the production of Na and Al is expected to be similar but depending on the C+N abundance.
- **The iron-peak elements** Sc, V, Cr, Mn, Fe, Co, Ni, Cu, and Zn all have large binding energies and are mainly produced during supernovae. While at early times mainly SNe II increase their abundance (and the ratio of α to iron abundance stayed rather constant), more and more low mass stars evolved and died in SNe Ia after after a certain delay time and enriched iron significantly more than the α-elements (see e.g. Iwamoto et al., 1999; Maoz et al., 2010). Due to the similarly high binding energies, the iron-peak elements are expected to roughly follow the trend of Fe, although chemical evolution models still struggle with the reproduction of these observations for several elements (see e.g. Kobayashi et al., 2011).
- **The s-process elements** Rb, Sr, Y, Zr, Ba, and La are produced by neutron-capture and decay processes with typically low neutron fluxes, most likely within thermally pulsating AGB stars (see e.g. Herwig, 2005; Karakas et al., 2012) or massive star winds (Prantzos et al., 2018).
- **The r-process elements** Ru, Ce, Nd and Eu are produced by neutron-capture and decay processes with typically high neutron fluxes. While their production sites are still under investigation, the follow-up of gravitational wave detections from double neutron star mergers suggest that r-process elements are formed during these so called kilonovae (see e.g. Pian et al., 2017). Comparisons with observations (see e.g. Côté et al., 2018a) show, however, discrepancies for r-process abundances in the MW disk. It is plausible that an additional site, such as massive stars and their associated core-collapse supernovae create high neutron fluxes and contribute to the r-process production. Further investigations are needed to pin down the importance of each possible production site for the r-process (see e.g. Arnould et al., 2007; Côté et al., 2018b).

With the on-going investigation of production sites and channels (see e.g. Hampel et al., 2016, for the i-process), our understanding of the creation of elements and their yields during nucleosynthesis processes is constantly increasing. For a review of the

production sites of the individual isotopes, the reader is referred to to works by Woosley & Weaver (1995); Samland (1998); McWilliam (1997); Kobayashi et al. (2006); Nomoto et al. (2013); Karakas & Lattanzio (2014).

THE IDEA OF CHEMICAL TAGGING

Freeman & Bland-Hawthorn (2002) proposed the idea of chemical tagging that uses the chemical patterns to identify stars that are born from the same birth material. A necessary condition according to Freeman & Bland-Hawthorn (2002) is that the progenitor cloud has to be uniformly mixed in key chemical elements before the stars are formed or a few high-mass stars enrich the cloud uniformly before the formation of the low-mass ones. Studies of open clusters and young embedded clusters (see e.g. Bica et al., 2003; Porras et al., 2003; Koposov et al., 2008; Borissova et al., 2011) suggest, that these conditions are met to a certain degree, but the importance of mechanisms like dust-cleansing still has to be further explored (Gustafsson, 2018). Additionally we have to follow up the intrinsically small dispersions in clusters for stars with same evolutionary stage (Bovy et al., 2016; Liu et al., 2018; Ness et al., 2018) down to a level of ~ 0.02 dex, but larger inhomogeneities across different evolutionary stages (see e.g. Gao et al., 2018; Liu et al., 2019).

Simulations by Bland-Hawthorn & Freeman (2004) as well as Bland-Hawthorn et al. (2010) suggest, that we should be able to detect about 20 thick disc dwarfs with a common origin, if we assume 3,000 star formation sites and about 10 thin disc dwarfs if we assume 30,000, if we were to observe a sample of 1 million stars with $V < 14$ in the solar vicinity. These numbers depend, however, on assumptions of the initial cluster mass function and the success of a chemical tagging experiment will rely both on the initial conditions and sites as well as our capability to recover them (De Silva et al., 2015), especially as they might change over time.

With simulations of star cluster formation, Armillotta et al. (2018) analysed the relationship between stellar distributions and their birth cloud in chemical and physical space and found that chemically homogeneous star clusters must have formed within ~ 1 pc of one another, because stellar abundances are only highly correlated below a few pc. However their simulations suggests that this correlation is stable regardless of the spatial structure of the metals right before the collapse.

Given that most stars are born in large clusters with hundreds or thousands of stars (Clarke et al., 2000; Carpenter, 2000), this idea should be feasible. In practise, the star formation efficiency however influences if clusters stay together or become unbound shortly after the initial star burst, with each star experiencing a random kick superimposed on the birth cloud's motion (Freeman & Bland-Hawthorn, 2002). The majority of stars are currently however not found in star clusters, because even if stars are formed in clusters, most of these clusters tend to evaporate naturally, aided by tidal disruption, within 10 Myr (Lada & Lada, 2003) and almost immediately unbound upon formation by expulsion of gas (e.g., Kroupa & Boily 2002; Baumgardt & Kroupa 2007; Fall et al. 2010; Murray et al. 2010; Kruijssen 2012 – see Krumholz et al. 2014 for a

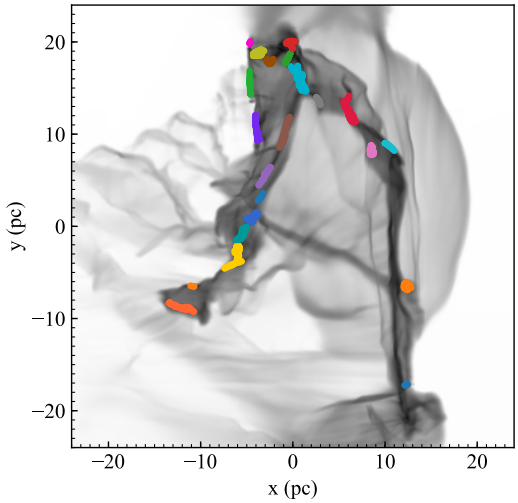

Figure 1.9: Map of the clusters identified at the end of a star cluster formation simulation by the minimum spanning tree algorithm overlapping the projected gas density distribution. Different colours indicate different star clusters. **Figure Credit:** Armillotta et al. (2018).

review). In addition, stars can be also scattered by spiral arm interactions and star-cloud encounters, allowing stars to migrate in integral space.

Following on from this, a major question of chemical tagging is, if it is possible to detect the debris of star formation sites and if there are enough independent cells in Cspace to make this possible with chemical information only.

STRONG AND WEAK CHEMICAL TAGGING

With the large amount of chemical and other types of information at hand, two different chemical tagging approaches have been defined - strong and weak chemical tagging.

Strong chemical tagging refers to the tagging based purely on chemical information. The term weak chemical tagging refers to a chemical tagging that involves additional non-chemical information. This information can be spatial, kinematical (e.g. radial velocities), dynamical (e.g. orbits), or temporal (i.e. via same stellar age).

Whereas strong chemical tagging is what Freeman & Bland-Hawthorn (2002) initially imagined in their review, studies within the last decade have shown that this approach is very hard in practice and several requirements have to be met in order to perform chemical tagging on large scales.

Hogg et al. (2016) have shown that chemical tagging can work when applying k-mean algorithms to find overdensities in chemical space of the APOGEE survey data. They were able to identify the halo globular cluster M31, the globular cluster M5, and Sagittarius dwarf spheroidal galaxy, as well as some unrecognised stellar structures when using 15 element abundances. Kos et al. (2018) were able to find new members of the Pleiades based on the chemical information from the GALAH survey data. Other first attempts of chemical tagging identified field stars that have chemical patterns similar to globular clusters both in the halo (Martell et al., 2016; Lind et al., 2015) and in the inner

Galaxy (Schiavon et al., 2017), but could not yet link them to their birth clusters with confidence.

Other studies, however found that chemical tagging is (still) not possible with the data at hand (see e.g. Smiljanic & Gaia-ESO Survey Consortium, 2018) as the stars they use for tagging are not separating significantly from other stars in their data sets. Blanco-Cuaresma et al. (2015) have gathered chemical information of 31 open clusters and have found several differences within the clusters, which are possibly driven by NLTE effects, atomic diffusion, mixing, and biases. When looking at cluster stars at the same evolutionary stage, they find that only few open clusters show distinct chemical patterns, while the chemical patterns of the majority of the clusters overlap. Ness et al. (2018) further found that 1 in 100 field stars are as chemically indistinguishable as stars within a single cluster. This is a contamination rate of at least $10^2 - 10^4$ times the expected true sibling rate in the field. A rate which is fatal to the prospect of chemical tagging using abundances alone. They were however able to show that chemo-orbital modelling with the additional use of stellar velocities is extremely useful to identify new cluster members.

1.2.5 DATA REQUIREMENTS FOR STELLAR SPECTROSCOPIC SURVEYS

Ting et al. (2015) analysed the prospects of chemical tagging as a function of several key parameters. They identified that the most limiting factors for chemical tagging with a stellar survey are likely to be the number of chemical cells in the chemical space and the sampling rate of the underlying stellar populations by the survey. We can split this problem into physical limitations that are caused by the true spread of elements in the chemical dimension as well as the true sizes and numbers of star clusters, and measurement limitations that are caused by uncertainties in the data and the analysis. For a spectroscopic survey, we can identify four key parameters that influence its use for chemical tagging of stars and populations:

- **Sample size** Ting et al. (2015) estimated that for a fiducial case of 10^4 distinct cells in chemical space, a survey would need to observe on the order of $10^5 - 10^6$ stars to find $\sim 10^2 - 10^3$ stellar groups with more than 5σ significance. De Silva et al. (2015, see their Fig. 6) estimated the number of clusters that can be recovered depending on the initial cluster mass and the number of observed stars.
- **Chemical dimensionality** Identifying groups of chemically homogenous stars will be challenging if the abundances are not significantly different from the majority of the stars. Based on the studies by Ting et al. (2016) it seems likely that chemical tagging will best be possible at the peripheral regions in abundance space, that is, where one of more abundances are significantly different from the average composition. Increasing the dimensionality of a data set with given size is the best way to create many of these peripheral regions - where chemical dimensionality is key for strong chemical tagging, but also dynamical information and ages can be used for weak chemical tagging. Increasing the number of observed element lines and especially the coverage of elements from the different element groups (see

Sec. 1.2.4) is a vital success factor for a survey that aims to provide information for chemical tagging.

- **Abundance precision** Lindegren & Feltzing (2013) analysed the correlation of the minimum sample size $N_{\rm min}$ that has to be analysed to resolve a minimum separation r (scaling with the measurement error) in abundance space, which can for example be the separation in Fe and Mg abundances for stars in the solar neighbourhood, as used in their study. Assuming that two equal Gaussian populations are the underlying sample, they found a functional form of

$$N_{\rm min} \simeq {\rm e}^{0.6+13r^{-0.8}} \tag{1.3}$$

  If the uncertainty of the estimated abundance is for example a third of the population distance ($r = 3$), the minimum sample size would be $N_{\rm min} \sim 400$. With only half the precision ($r = 1.5$), $N_{\rm min}$ would increase drastically to 22,000. While this is a theoretical exercise, it illustrates that an increase in abundance precision has a significant influence on the needed sample size and shows that it will almost be impossible to resolve populations that separated by less than the measurement error when only considering one component.

- **Abundance accuracy** Whenever we are comparing stars that are not identical and analysed identically, the same arguments can be made for abundance accuracy as for abundance precision. If we want to collect as many elements as possible, a possible way might to be to combine several studies or surveys. Comparisons of stars analysed by two surveys (see e.g. Kunder et al., 2017, for the comparison of RAVE DR5 and other surveys) have shown that several large scale stellar surveys differ significantly and beyond the precision limits in the estimated stellar properties. Although serious efforts have been invested, for example by Hinkel et al. (2014), to post-process abundances and combine different spectroscopic studies, significant improvements have to be made to already estimate accurate abundances within from the spectral analysis, demanding for example a better knowledge of model atmospheres, shortcomings of of the analyses and line information used.

While the first two parameters are typically only adjusted in the preparation of the survey, the last two can also be improved after the data collection has been finished and make improvements of spectroscopic analyses also powerful important for the re-analyses of already acquired data. It is important to note that not only the data has to be of good quality, but we also have to understand how to exploit it and interpret it in terms of the underlying stellar physics.

While this is beyond the scope of this thesis, it should be mentioned that we are still only at the beginning of finding appropriate means to analyse high-dimensional data in the context of chemical tagging. Several studies have made important contributions to the advance of group finding. Mitschang et al. (2013, 2014) were among the first to explore possible metrics to identify groups in Cspace. Ting et al. (2015) and Hogg et al. (2016) later applied k-means algorithms for group finding. Kos et al. (2018) were able to find chemically similar stars with a combination of the t-disctributed stochastic

neighbor embedding t-SNE and the grouping algorithm DBSAN. Later, Price-Jones & Bovy (2019) applied DBSCAN for grouping. Jofré et al. (2017) and Blanco-Cuaresma & Fraix-Burnet (2018) showed that one can use tools typically used in biology to group stars via phylogenetic trees.

1.2.6 CURRENT LARGE SCALE STELLAR SURVEYS

ASTROMETRIC SURVEYS

HIGH PRECISION PARALLAX COLLECTING SATELLITE (HIPPARCOS) (ESA, 1997) was the first satellite mission to estimate 3Dpositions (right ascension, declination, and the distance-related parallax) for almost 120,000 stars, two-thirds of them in the solar vicinity of < 350 pc. The latest reduction of this mission (van Leeuwen, 2007) provided parallax estimates with uncertainties below 30% for two-thirds of the sample and allowed us to explore the local stellar volume for the first time in 3 dimensions. The satellite also collected photometric measurements of more than 2.5 million sources over the course of 3.5 years, which could later be combined to a collection of magnitudes, positions (at a mean epoch J1991.25) and proper motions in the Tycho-2 catalog (Høg et al., 2000).

The *Gaia* space mission is the successor of HIPPARCOS and will provide the 3D position (right ascension, declination and distances/parallaxes) and proper motions as well as three photometric measurements in the visual range for more than a billion stars. The latest release, *Gaia* DR2 (Gaia Collaboration et al., 2018b), includes approximately 1.7 billion sources down to magnitude $G \leq 21$, and 5D information (right ascension, declination, parallaxes and proper motions in the directions of right ascension and declination) for more than 1.3 billion sources. Prior to this, the first release (Brown et al., 2016) already provided this 5D information for the overlap of *Gaia* sources with the Tycho-2 catalog (Høg et al., 2000) by using the positions of Tycho-2 (with mean observation date around spring 1991) as baseline (see Michalik et al., 2015; Lindegren et al., 2016). For the brightest of the *Gaia* sources, an additional spectrograph, the ***Gaia* Radial Velocity Spectrometer** (*Gaia* RVS), is used to obtain medium resolution ($R \sim 11,200$) spectra in order to estimate radial velocities and some element abundances around the Ca II triplet lines in the near-infrared (see Perryman et al., 2001; Gaia Collaboration et al., 2016). *Gaia* DR2 already provided 7,224,631 radial velocity estimates.

The *Gaia* satellite will continue to observe at least until 2020, but likely even beyond 2022. With this extended observing time beyond the official end of mission, the number of stars as well as the quality and time-coverage of their observations are increased, which will lead to an almost complete observation of stars down to the 21st magnitude in the visual.

The unprecedented volume observed by the *Gaia* satellite is sometimes referred to as the *Gaia*verse (Freeman & Bland-Hawthorn, 2002) and for stars in this volume, which will also be observed by stellar spectroscopic surveys, a large variety of chemodynamic information will be provided. Especially beyond the faint magnitude limit of *Gaia* RVS, ground based surveys will complement *Gaia* with their radial velocity estimates in addition to the estimated chemical compositions.

PHOTOMETRIC SURVEYS

Throughout the centuries, numerous photometric observations all across the world and in space have been gathered. The most notable and large-scale ones include the photometric part of the *Gaia* mission (see e.g. Evans et al., 2018), **Two Micron All-Sky Survey** (2MASS), PanSTARRS1 (see e.g. Chambers et al., 2016), and SkyMapper (see e.g. Keller et al., 2007; Wolf et al., 2018). For the work carried out in this Thesis, the most important one is 2MASS.

2MASS observed 99.998% of the celestial sphere with three filters (see Fig. 1.11) in the near-infrared, namely the filters J (with central wavelength 1.25 µm), H (1.65 µm), and K_S (2.16 µm) in Chile and the USA (Skrutskie et al., 2006). The observations are $> 99\%$ complete up to magnitudes 15.8, 15.1, and 14.3 mag for the filters J, H, and K_s, respectively, and have typical 1σ uncertainties of < 0.03 mag with a positional accuracy of $\sim$ 0.1arcsec. This combination of completeness, precision and accuracy for 471 million sources made it one of the most used catalogs for stellar astronomy in the last decades, for example for target selection and pointing.

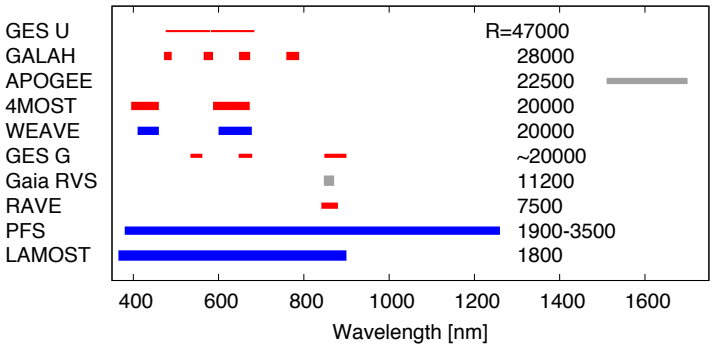

Figure 1.10: Wavelength coverage of a selection of on-going and future spectroscopic surveys from Table 1.1, sorted by resolution. Northern, southern, and all-sky surveys are represented by blue, red, and grey colours, respectively. Broader lines indicate larger numbers of target stars. GES U stands for *Gaia*-ESO UVES, GES G stands for *Gaia*-ESO GIRAFFE. **Figure Credit:** Jofré et al. (2018).

SPECTROSCOPIC SURVEYS

A selection of past, on-going and future spectroscopic surveys is listed in Table 1.1 and their wavelength coverages are shown in Fig. 1.10. The **Geneva-Copenhagen Survey** (GCS) and **Sloan Extension for Galactic Understanding and Exploration** (SEGUE) were the first large scale surveys, which provided radial velocities, stellar parameters and partially even α-process abundances for a significant amount of stars (see e.g. Yanny et al., 2009). While GCS (using also narrow-band photometry, see e.g. Nordström et al., 2004) focussed more on the solar vicinity exploration, SEGUE aimed to study the structure of the MW, by mapping stars as far as 60 kpc away from the Sun, including the observation of stellar streams (see e.g. Belokurov et al., 2006).

The currently on-going large-scale surveys, namely **Radial Velocity Experiment** (RAVE), **Apache Point Observatory Galactic Evolution Experiment** (APOGEE),

Gaia-ESO, **Large Sky Area Multi-Object Fiber Spectroscopic Telesope** (LAMOST), GALAH, and *Gaia* RVS, largely complement each other in terms of targeted stars. Their different wavelength ranges lead to a mix of both overlapping and complementary abundance information, as can be seen in Fig. 1.8. Each survey follows a unique observation strategy with different achievable abundance precisions. Currently, APOGEE and GALAH achieve the highest overall precisions down to typically 0.05 dex (Holtzman et al., 2018; Buder et al., 2018). The current large-scale surveys are observing on the order of 10^5-10^6 stars and next generation surveys will even target several tens of 10^6.

The **William Herschel Telescope Enhanced Area Velocity Explorer** (WEAVE), **Subaru Prime Focus Spectrograph** (PFS), **Dark Energy Spectroscopic Instrument** (DESI), **Multi-Object Optical and Near-infrared Spectrograph** (MOONS), **4-metre Multi-Object Spectroscopic Telescope** (4MOST), **Sloan Digitial Sky Survey** (SDSS)-V and **Maunakea Spectroscopic Explorer** (MSE) are the next generation of large scale surveys that will be starting operations within the next years and aim to achieve similar precisions with even higher multiplexing capabilities. GALAH is a main focus of this Thesis and is presented in more detail in Chapter 2.

Table 1.1: Stellar Spectroscopic Surveys of the Milky Way. The table is based on the collection by Rix & Bovy (2013) and Kollmeier et al. (2017) but was updated and extended. VIS stands for visible range, NIR for near-infrared and IR for infrared.

Survey	Magnitudes	Nr. Spectra	Resolution	Spectrograph
GCS (1)	$m_V \sim 10$	$2 \cdot 10^4$	20,000	CORAVEL (VIS)
SEGUE (2)	$15 \leq m_g \leq 20$	$4 \cdot 10^5$	2,000	SDSS-I/II (VIS)
RAVE (3)	$9 \leq m_i \leq 12$	$5 \cdot 10^5$	7,500	6dF (NIR)
LAMOST (4)	$m_G \leq 16$	$9 \cdot 10^6$+	1,800	LAMOST (VIS+NIR)
APOGEE (5)	$m_H \leq 12.2$	$4 \cdot 10^5$+	22,500	APOGEE (IR)
Gaia-ESO (6)	$m_V \leq 18$	$2 \cdot 10^5$	20,000	GIRAFFE (VIS+NIR)
			47,000	UVES (VIS)
Gaia RVS (7)	$m_G \leq 12$	$8 \cdot 10^6$	11,200	*Gaia* RVS (NIR)
GALAH (8)	$9 \leq V \leq 14$	$8 \cdot 10^5$+	28,000	HERMES (VIS+NIR)
WEAVE (9)	$m_G \leq 15.5$	$1 \cdot 10^6$+	5,000	WEAVE (VIS+NIR)
			20,000	WEAVE (VIS)
PFS (10)	$m_i \leq 23$	$1 \cdot 10^6$+	3,000	PFS (VIS+NIR)
DESI (11)	$m_r \leq 23$	$1 \cdot 10^6$+	5,000	DESI (VIS+NIR)
MOONS (12)	$m_g \leq 22$	$2 \cdot 10^6$	5,000	VIS+NIR+IR)
	$m_H \leq 17$		20,000	WEAVE (VIS)
4MOST (13)	$m_G \leq 20.5$	$16 \cdot 10^6$+	6,500	LRS (VIS+NIR)
		$3 \cdot 10^6$+	20,000	HRS (VIS)
SDSS-V (14)	$m_H \leq 13.4$	$7 \cdot 10^6$	22,000	APOGEE (IR)
	$m_i \leq 20$		2,000	BOSS (VIS+NIR)
MSE (15)	$m_g \leq 24$	10^6++	$\leq 40,000$	MSE (VIS+NIR)

Notes: (1) see e.g. Nordström et al. (2004), (2) see e.g. Yanny et al. (2009), (3) see e.g. Steinmetz et al. (2006), (4) see e.g. Cui et al. (2012), (5) see e.g. Allende Prieto et al. (2008); Majewski et al. (2016), (6) see e.g. Gilmore et al. (2012), (7) see e.g. Cropper et al. (2018); Katz et al. (2019) (8) see e.g. De Silva et al. (2015), (9) see e.g. Dalton et al. (2016), (10) see e.g. Takada et al. (2014), (11) see e.g. DESI Collaboration et al. (2016), (12) see e.g. Cirasuolo et al. (2014), (13) see e.g. de Jong et al. (2019), (14) see e.g. Kollmeier et al. (2017), (15) see e.g. Bergemann et al. (2019)..

1.3 CHEMODYNAMIC INFORMATION FROM LARGE STELLAR SURVEYS

"Data! Data! Data!" he cried impatiently.
"I can't make bricks without clay."

— Arthur Conan Doyle, The Adventures of Sherlock Holmes

In Sec. 1.2, we have outlined the broad goals of Galactic archaeology; characterising the Galactic components and understanding their formation and interrelationships. To achieve such ambitious goals, we need precise chemical (see Sec. 1.2.4), dynamic, and temporal information (see Sec. 1.2.3) for large samples of stars, which are our tracers of this information.

In this section, we will describe how we can estimate this information from large stellar surveys, that is chemical information from stellar spectra in Sec. 1.3.2 and dynamic information from both a combination of spectroscopic and astrometric information in Sec. 1.3.4. To estimate stellar ages, we need a multitude of information, as will be explained in Sec. 1.3.5.

1.3.1 STELLAR PARAMETERS

When we observe stars by eye, we can see that stars appear in a variety of colours, some white, some red, and others bluish. The reason for this is their surface temperature, which influences the wavelengths λ or frequencies ν at which they emit most photons. To first approximation, stars emit electromagnetic radiation like black-bodies, that is with a spectral radiance that follows Planck's law:

$$B_\nu(\nu, T) = \frac{2h\nu^3}{c^2} \frac{1}{\mathrm{e}^{\frac{h\nu}{kT}} - 1}, \tag{1.4}$$

with Planck's constant h, speed of light c and Boltzmann constant k. The frequency peak of this distribution is a linear function of temperature ($\mathrm{d}B/\mathrm{d}\nu \propto \text{const.} \cdot T$) and is known as Wien's displacement law, which basically states that hotter stars to appear bluer than colder ones. We can quantify this effect by observing a star in different wavelength ranges or filters. By quantifying the amount of photons emitted in a bluer versus a redder wavelength range via photometric measurements, we can estimate the temperature of a star.

Stars contain an unbelievable amount of mass within them. The Sun, a so called low-mass star, contains a mass of $M_\odot = 1.98 \cdot 10^{30}$ kg within the Solar radius of $R_\odot = 6.957 \cdot 10^8$ m (Prša et al., 2016). A gravitational collapse of the Sun is however avoided by the nuclear fusion processes in its core which generate an enormous radiation pressure. A commonly used parameter to describe a star's atmosphere as a function of mass and radius is the surface gravity, linked through the gravitational constant G

$$g = G\frac{\mathcal{M}}{R^2} \qquad \text{or} \qquad \log g = \log g_\odot + \log \frac{M}{M_\odot} - \log \frac{R^2}{R_\odot^2} \tag{1.5}$$

During the life of a star, it emits a lot of energy or flux F_ν across different frequencies ν (for example also as visible light). The total amount of energy emitted per unit of time is referred to as its (bolometric) luminosity and defined by

$$L_{\rm bol} = 4\pi R^2 \int_0^\infty F_\nu {\rm d}\nu = 4\pi R^2 \sigma T_{\rm eff}^4, \tag{1.6}$$

where $T_{\rm eff}$ is the temperature corresponding to the same luminosity of a black-body (see Eq. 1.4). In a similar fashion, we can count (or integrate) the flux not throughout the whole electromagnetic spectrum, but in a spectral window with transmission $T(\nu)$ and define a so called magnitude[2] m, which is the standard logarithmic luminosity scale used in astronomy:

$$m = -2.5 \log \int_0^\infty F_\nu T(\nu) {\rm d}\nu + \text{constant}. \tag{1.7}$$

For a flat and infinitely wide filter, $T(\nu)$=1 and Eq. 1.7 will deliver the bolometric magnitude. Different photometric broadband filters, as shown in Fig. 1.11, will have a characteristic response (or transmission) function $T(\nu)$ and when observing a star through such a filter, Eq. 1.7 will deliver a magnitude for a specific filter. If we observe a star with a clever choice of two or more filters at regions where Planck's distribution changes significantly, we can sample the color of stars (literally the difference of two filter magnitudes) and (mostly empirically) estimate a stars effective temperature. Several photometric surveys, like the 2MASS, have gathered such magnitudes and several techniques have been developed to estimate temperatures from fluxes and magnitudes (see e.g. Casagrande et al., 2010).

It has to be noted, however, that the flux of a star, which reaches us, is decreasing with distance. In practise, two different magnitudes have been defined. The apparent magnitude m_i is the magnitude that we actually measure with a filter i. Contrary, the so called absolute magnitude, M_I, was introduced to measure of the luminosity at a fixed distance of 10 pc, such that

$$m_I - M_I = 5 \log \frac{d}{10} \tag{1.8}$$

We can compute the distance of a star by observing its apparent displacement angle relative to very far objects as the Earth orbits around the Sun, the so called parallax, and combine with the known distance between Sun and Earth[3].

The aforementioned stellar parameters are linked through fundamental physics, for example $\log g$ and L via Eqs. 1.5, such that 1.6:

$$\log g = \log g_\odot + \log \frac{M}{M_\odot} - 4 \cdot \log \frac{T_{\rm eff}}{T_{\rm eff,\odot}} - \log \frac{L}{L_\odot}. \tag{1.9}$$

[2] Similar to Z and [M/H], a logarithmic scale was introduced for practical reasons because of the immense changes of F_ν.

[3] This method is the most used for stars and the distance of a star is given in parsec (pc), $\sim 3.09 \cdot 10^{16}$ m, and refers to an displacement angle of one arc second. Other methods include the observation of objects with characteristic absolute magnitudes, such as red clump stars or supernovae Ia, or time-varying quantities like periodically changing luminosity of Cepheids.

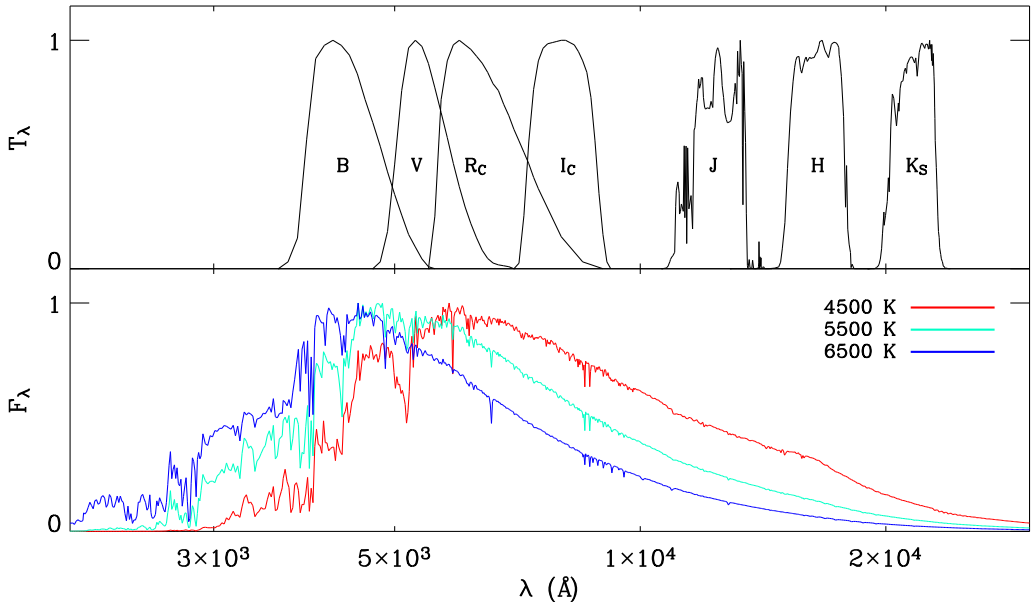

Figure 1.11: Transmission function T_λ of the Johnson-Cousins filters B, V, R_C, and I_C (Bessell, 1990) as well as the 2MASS (Skrutskie et al., 2006) filters J, H, and K_s (top panel) and normalised stellar fluxes (bottom panel) for three example stars as a function of wavelength. **Figure Credit:** Casagrande et al. (2010).

We can also visualise this through the very similar distribution of stars in the two most used diagnostic diagrams, the CMD in the left panel of Fig. 1.12 and its spectroscopic equivalent with $T_{\rm eff}$ and $\log g$ in the right panel of Fig. 1.12 (also known as the Kiel diagram), respectively. In the literature is also common to refer to both diagrams (as well as alterations of them, for example with spectral types on the absissa) as Hertzsprung-Russell Diagram (HRD). Due to the characteristics of their atmospheres and photospheres, stars of different evolutionary phases can be found at rather distinct places in these diagrams, which have similar appearance because color is correlated with surface temperature and surface gravity is correlated with luminosity (but due to the simultaneous $T_{\rm eff}$-dependence of luminosity the morphology of the diagrams is nevertheless different)

For our purposes, low-mass stars with long lifetimes, that is longer the dynamical time scales, are important. Their evolution can be traced from the Pre-Main Sequence (PMS) phase, to the H-core burning Main Sequence (MS) phase (distributed typically at the highest M_G and $\log g$ in Fig. 1.12), to the H-shell burning RGB phase with He-core degeneracies, to core-helium burning phase (also known as Red Clump (RC) and horizontal branch phase) with typical absolute magnitudes around -1 and $\log g \sim 2.5$ after the helium flash, all the way to He-shell burning and/or thermally pulsating AGB phase with the highest luminosities. After this phase, stars evolve towards planetary nebulae and contract rapidly before they cool down as a White Dwarf (WD). For detailed descriptions of stellar evolution (including, but also exceeding low-mass stars), the reader is referred to Karakas & Lattanzio (2014) or the book by Clayton (1983).

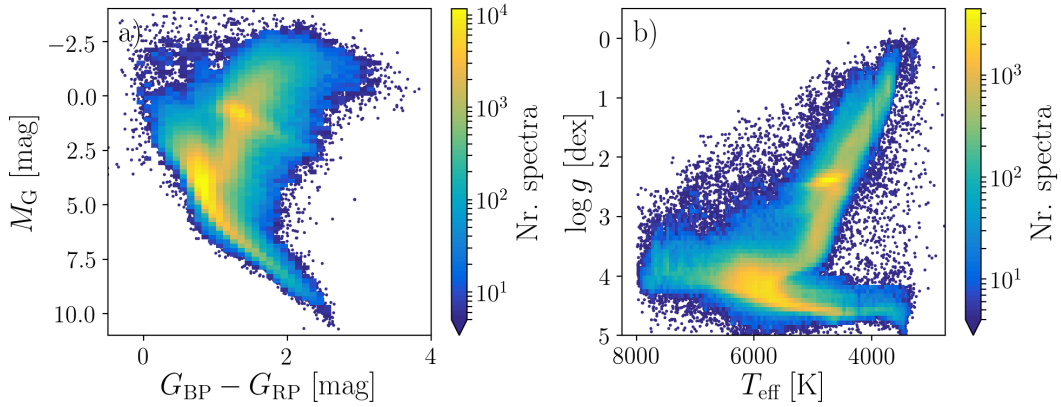

Figure 1.12: The photometric color-magnitude diagram (with color $G_{BP} - G_{RP}$ and absolute magnitude M_G estimated by the *Gaia* satellite) and its spectroscopic version with T_{eff} and $\log g$ (estimated by the GALAH survey) for 650,000 nearby stars, colored by density. Note that extinction by dust changes the color of stars and reddens them (causing a smearing of stars in the CMD towards higher visual magnitudes and colors). **Figure Credit:** Buder et al. (in prep. b).

It should be noted that a star's path along this evolutionary track is significantly influenced by its chemical composition. Although stars mostly consist of H and He, the composition of the other elements (Li and heavier), referred to as metals in stellar astrophysics, play a dominant role for a star. Their mass fraction, often combined as Z (whereas X and Y are used for H and He and $X + Y + Z = 1$) is typically of the order of less than two percent and the number density of metals is typically several orders of magnitudes lower than H and He. It has become standard to describe a metallicity [M/H] on a logarithmic scale via the number density and the solar values as reference, such that

$$[\mathrm{M/H}] = \log \frac{\sum_{i \in \mathrm{Li,\,Be,\,\ldots}} N_i}{N_\mathrm{H}} - \log \frac{\sum_{i \in \mathrm{Li,\,Be,\,\ldots}} N_{i,\odot}}{N_{\mathrm{H},\odot}}. \tag{1.10}$$

Historically, the metallicity has been linked to the element that shows the most lines in stellar spectra, namely Fe, and it is currently still common to approximate [M/H] with the iron abundance [Fe/H], which is strictly speaking

$$[\mathrm{Fe/H}] = \log \frac{N_\mathrm{Fe}}{N_\mathrm{H}} - \log \frac{N_{\mathrm{Fe},\odot}}{N_{\mathrm{H},\odot}} \tag{1.11}$$

These two are however not exactly the same, especially for those stars, where the rest of the metals, that is, the elements other than H, He, and Fe, are not following a scaled solar composition.

1.3.2 EXTRACTING INFORMATION FROM SPECTRA

When dispersing the light of a star into its wavelength constituents, we can study its spectral distribution. Performing this experiment with the Sun, Wollaston and later Fraunhofer (1823) discovered absorptions at specific wavelengths, which the latter

initially named with letters B (at a red wavelength), C (deep red), D (orange) to H (violet). The Heidelberg based scientists Gustav Kirchhoff and Robert Bunsen later connected such absorptions with specific elements, for example the absorption with the letter D with sodium (Kirchhoff & Bunsen, 1860).

With the advances of photometric plate observations, it later became possible to observe thousands of stars and their spectra both simultaneously and quantitatively. Pioneers like Annie Jump Cannon at Harvard discovered that the line strength of various stars differs and transitions in a rather smooth way, which allowed her to classify stars based on characteristic lines and their strengths, in the still used spectral classification O-B-A-F-G-K-M with decimal subdivisions (see e.g. Cannon & Pickering, 1901). Note that this notation is completely independent of Fraunhofer's notation. Throughout her lifetime, she managed to classify up to 395,000 stars by hand (see e.g. the Henry Draper catalog by Cannon & Pickering, 1918b,a, 1919a,b, 1920, 1921, 1922, 1923, 1924).

The fundamental and digital/computational advances in stellar spectroscopy are nowadays enabling us to link hundreds of thousands of absorption lines with elements and link chemical abundances of certain elements with stellar spectra. We can now link the shape of spectra with mechanisms in stellar atmospheres such as radiative and collisional excitations as well as spontaneous and stimulated emissions (see e.g. Gray, 2008, and references therein).

1.3.2.1 SPECTROSCOPIC ANALYSIS

A stellar spectrum is worth a thousand pictures. With the combination of spectral line shapes and positions (or shifts), we can estimate velocities (or redshift), temperatures, densities, chemical composition and abundances, rotation, turbulence and even magnetic fields. From the temporal change of a spectrum we can also infer the presence of stellar or sub-stellar companions and even internal oscillations.

The analysis of spectra is therefore a powerful tool and the basic approach to estimate (chemical) information from stars. The steps in more detail for stellar spectrum analysis are as follows:

1. Obtain the spectrum and prepare it for the spectroscopic analysis
    a) Obtain a stellar spectrum with a telescope by splitting the light of a star via a prism or an échelle grating. Depending on the science case, different wavelength ranges and resolving powers $R = \lambda/\Delta\lambda$ as well as exposure times (to achieve a necessary signal-to-noise ratio) of the Charge-Coupled Device (CCD) can be chosen, see Table 1.1. CCDs are used to convert the signal (photons from the star's photosphere collected and focused through mirrors) physically into electrons within semi-conductor material and then convert those into digital units.
    b) Obtain calibration observations to correct systematics of the observation setup. These can include the observation of pure noise, that is, reading out the CCD without the scientific signal to characterise thermal and readout noise. Because electrons can not only be excited by electrons, but also

are statistically thermally excited with energies above the band gap energy E_{gap} of the semi-conductor material due to thermal motions, the CCD can either be cooled to limit this noise, or the noise has to be monitored via the observation of so called dark frames (without signal for the same exposure time as the scientific observation). The readout noise occurs due to imperfect operation of physical electronic devices and is typically small, but is important if the scientific signal is weak. Additionally, an observation with a well-illuminated flat field should be obtained in order to correct systematics in the throughput along the CCD area and the so called blaze function. The third set of calibration observations is important for the conversion of pixel position to wavelength. This is typically achieved by illuminating the optical path with a lamp with numerous well-known emission lines (like a ThXe lamp) and using it to calculate a wavelength function $f(\lambda|px)$.

c) Extract the 1-dimensional spectrum of each star from the the 2-dimensional information of the CCD, for example by summing over all the pixels in one order orthogonally to the dispersion axis.

d) If the information of absolute flux is needed, the spectrum has to be flux-calibrated. The current best technique is to observe a so called spectrophotometric standard star (see e.g. Oke, 1990) that is nearby and for which a flux-calibrated spectrum are available for reference. Then apply the ratio of observed and reference flux from the standard star onto the flux calibrated spectrum. In large-scale stellar spectroscopy it is however not feasible to achieve this flux calibration and the reduced spectra is not on an absolute flux scale, but the signal depends on the exposure time, and spectra can contain systematics due to imperfect flat fielding. To cancel these effects, the spectrum is being normalised to a (pseudo-)continuum, like shown for spectrum of Arcturus in Fig 1.13, obtained with the HERMES spectrograph with a resolving power of $\sim 28,000$. If the spectra have been obtained with a fiber-fed spectrograph and properly flat-field corrected, this can be achieved by fitting linear or low-order polynomial functions with the help of selected continuum points for sufficiently small wavelength regions.

e) Because the spectrum can be red- or blue-shifted due to the motion of the star relative to us, we have to apply a line-of-sight velocity (or radial) velocity correction to shift the spectrum onto a restframe, where each line wavelength corresponds to a laboratory wavelength.

2. Extract stellar parameters from the spectrum. Different methods can be used, some use selected lines and rely on line strength, whereas other use the full spectrum. But all rely on the strength and shape of absorption lines and their change with parameters of the atmosphere. As we will lay out in the next section, we can utilise several dependencies of how particles distribute in different states of excitation and ionisation and of how wings of broad lines are shaped with parameters like temperature or gravity. In practice, the most used lines for these analyses are

the numerous lines of Fe (with several neutral and ionised Fe I and Fe II lines) and strong lines like the Balmer lines or the Mg I or Ca II triplet, and the most important stellar parameters are $T_{\rm eff}$, $\log g$, $v \sin i$ and [Fe/H]. At this stage it is common to assume that all other elements follow a standard chemical composition, scaled to the solar composition.

3. Use the absorption lines of individual elements to estimate their abundance in the star. A spectrum of a star can contain many strong absorption features, like Arcturus in the visual wavelength range (see Fig. 1.13) or very few (for example very hot stars). In the best case we aim to use as many lines as possible, but want to avoid they have poorly known transition probabiity, are blended by other element lines and too strong or too weak (to have enough information but avoid saturation effects).

A detailed overview of the most used material and tools for spectral analyses can be found in the review by Jofré et al. (2018).

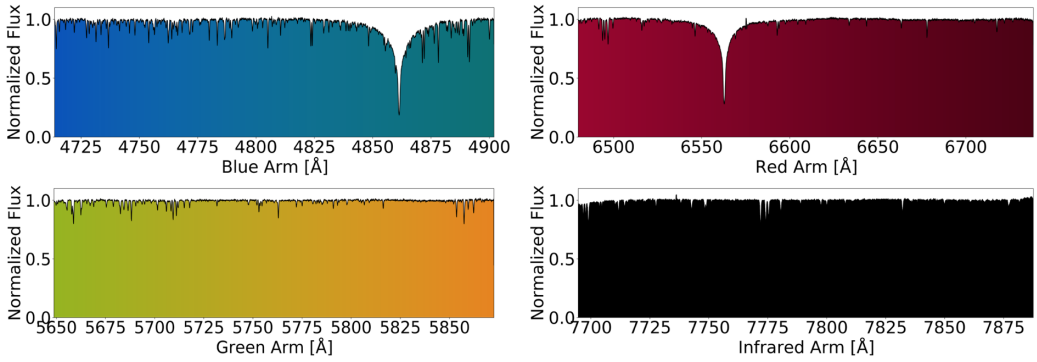

Figure 1.13: Normalised spectrum of Arcturus, taken with the HERMES spectrograph. The color code is for graphical display and correlates with the particular wavelength. In each of the four wavelength bands of the spectrograph, a resolution of $\sim 28,000$ can be reached to resolve individual element lines and alleviate blending.

1.3.2.2 SPECTRUM SYNTHESIS

The bulk of photons emitted from a star originate in the stellar photosphere, a surface layer that is very thin compared to the stellar radius. To predict the emergent shape of a stellar spectrum, we need to characterise the radiative transfer in the photosphere.

If we consider radiation traveling towards us, we can estimate the change in specific intensity $\mathrm{d}I_\nu$ along the path length s as the combined effect of absorption and emission in a medium with given density ρ. When expressing these with the absorption[4] and emission coefficients κ_ν and j_ν, respectively, we can write

$$\mathrm{d}I_\nu = -\kappa_\nu \rho I_\nu \mathrm{d}s + j_\nu \rho \mathrm{d}s \tag{1.12}$$

[4]The absorption coefficient is also known as extinction coefficient α_ν (see e.g. Rutten, 2003), but throughout this section, we will use κ_ν.

In spectroscopy, it is however more common to describe intensity as a function of optical depth $\tau_\nu = \kappa_\nu \rho \mathrm{d}s$ rather than the increment of geometric length $\mathrm{d}s$ and combine the ratio of emission and absorption coefficient to the source function $S_\nu = j_\nu/\kappa_\nu$.

$$\frac{\mathrm{d}I_\nu}{\mathrm{d}\tau_\nu} = -I_\nu + S_\nu \tag{1.13}$$

As we are aiming to calculate the outward directed intensity $I_\nu(\tau_\nu)$, we have to integrate Eq. 1.13, which we can achieve by using an substitution Ansatz (see e.g. Gray, 2008) with the dummy variable t_ν as a point along the path (where $\tau_\nu - t_\nu$ is the optical-depth separation):

$$I_\nu^+(\tau_\nu) = \int_\infty^{\tau_\nu} S_\nu(t_\nu) \mathrm{e}^{-(\tau_\nu - t_\nu)} \mathrm{d}t_\nu. \tag{1.14}$$

With this basic integral form of the transfer equation, we can then estimate the flux as the projected intensity with inclination θ integrated over the solid angle ω

$$F_\nu^+ = \oint I_\nu \cos\theta \mathrm{d}\omega. \tag{1.15}$$

For current spectroscopic analyses, it is common to assume a 1-dimensional plane-parallel geometry, which simplifies the computation to $F_\nu = 2\pi \int \mu I_\nu \mathrm{d}\mu$, with the viewing angle $\mu = \cos\theta$.

To calculate the flux, one needs to know the total source function S_ν, which includes continuous processes and lines

$$S_\nu = \frac{S_\nu^{\mathrm{cont}} \kappa_\nu^{\mathrm{cont}} + \sum S_\nu^{\mathrm{line}} \kappa_\nu^{\mathrm{line}}}{\kappa_\nu^{\mathrm{cont}} + \sum \kappa_\nu^{\mathrm{line}}} \tag{1.16}$$

For a discussion of the continuous absorption coefficients, the reader is referred to the excellent descriptions by Rutten (2003) and Gray (2008). For stars like the Sun, the continuous absorption is dominated by the bound-free H^- ion components, whereas the free-free H^- component and the neutral H component can become important for significantly hotter stars at shorter wavelengths.

For the individual lines, we can estimate a source function (see e.g. Rutten, 2003)

$$S_\nu^{\mathrm{line}} = \frac{2h\nu^3}{c^2} \frac{1}{\frac{g_u n_l}{g_l n_u} - 1}, \tag{1.17}$$

where g_u/g_l is the ratio of the statistical weight of the upper and lower level of a transition and n_l/n_u is the ratio of the populations of lower and upper level.

It is currently common (see e.g. Jofré et al., 2018) to assume local thermodynamic equilibrium, which means that all material energy partitioning, that is, atomic, ionic and molecular level populations are following the Boltzmann distribution, describing the ratio of atoms of an ionisation stage r between a lower and upper level, l and u respectively, as a function of their statistical weights and their excitation energies (χ_u and χ_l) as well as temperature,

$$\frac{n_{r,u}}{n_{r,l}} = \frac{g_{r,u}}{g_{r,l}} \mathrm{e}^{-(\chi_{r,u} - \chi_{r,l})/kT}. \tag{1.18}$$

Additionally, the Saha distribution,

$$\frac{N_{r+1}}{N_r} \propto \frac{1}{N_e}\frac{2U_{r+1}}{U_r}\,(kT)^{3/2}\,\mathrm{e}^{-\chi_r/kT}, \tag{1.19}$$

is fulfilled, which describes the degree of ionisation. In this equation, N_r and N_{r+1} are the total population densities of two successive ionisation stages r and $r+1$, N_e the electron density and U_r the partition function of stage r,

$$U_r = \sum_u g_{r,u}\mathrm{e}^{-\chi_{r,u}/kT} \tag{1.20}$$

By inserting Eq. 1.18 into Eq. 1.17 and combination with the energy of a photon in the line transition $h\nu = \chi_{r,u} - \chi_{r,l}$, the line source function simplifies to

$$S_\nu^{\mathrm{line}} = \frac{2h\nu^3}{c^2}\frac{1}{\mathrm{e}^{\frac{h\nu}{kT}}-1},. \tag{1.21}$$

This means that in LTE, the line source function is simply the Planck function (see Eq. 1.4) and does not depend on the chemical species, but only local temperature and frequency.

To estimate the flux F_ν we however still need the absorption coefficients $\kappa_\nu^{\mathrm{cont}}$ and $\kappa_\nu^{\mathrm{line}}$, which determine the optical depth (Eq. 1.12). Together with the source function, these can be computed, when we know the stellar environment, that is, the thermodynamic quantities characterising the stellar atmosphere.

Classical and widely used 1D model atmospheres are MARCS (Gustafsson et al., 2008) or ATLAS9 (Castelli & Kurucz, 2003). These are built around several assumptions:

- 1D stratification (spherically symmetric or plane-parallel)
- hydrostatic equilibrium, where radiation pressure and thermal as well as the turbulent pressure of the gas are balancing the gravity
- Local Thermodynamic Equilibrium (LTE)
- flux conservation
- energy propagated by radiation and convection
- convection described by the mixing length theory (Böhm-Vitense, 1958), giving rise to free parameters such as mixing length and microturbulence

Although these assumptions are only approximations of actual stellar atmospheres, they have been shown to still deliver surprisingly accurate results. It should be mentioned though, that during recent decades, large (especially computational) efforts have enabled the calculation of 3D, hydro-dynamical models (see e.g. Freytag et al., 2012; Magic et al., 2013) and abundance estimations in Non-Local Thermodynamic equilibrium (non-LTE). The most widely used atmospheres are currently still 1D plane-parallel models and when assuming fixed mixing length parameters, they are fully determined by

- effective Temperature $T_{\rm eff}$
- surface gravity $\log g = \log\left(GMR^{-2}\right)$
- element mixture, usually parametrised by metallicity [Fe/H] (for commonly adopted chemical compositions see e.g. Grevesse et al., 2007; Asplund et al., 2009)
- microturbulence ξ

For a given combination of these parameters, model atmospheres provide (partially redundant) thermodynamic quantities like temperature T, gas and electron pressure P_g and P_e (and/or gas and electron number densities, which can be converted via the gas laws) as well as mass density ρ, as a function of optical depth τ. With these and the chemical composition of the star, it is possible to solve the equation of state and estimate the number density of absorbers and perturbers at every level of the stellar atmosphere. During this procedure, particle and charge conservation as well as chemical and ionisation equilibrium have to be obeyed for the list of atomic and molecular lines. (for a practical implementation of these computations see Piskunov & Valenti, 2017).

In stellar spectroscopy the abundance of an element is typically described on a scale, where $A(\mathrm{H}) = 12$. The abundance of the element X is then

$$A(\mathrm{X}) = \log N_{\mathrm{X}} - \log N_{\mathrm{H}} + 12. \tag{1.22}$$

Further, spectroscopists tend to discuss abundances relative to the solar values with a bracket notation for iron and other abundances, that is similar to Eq. 1.11 for the iron abundance [Fe/H],

$$[\mathrm{X/Fe}] = \log\left(N_{\mathrm{X}}/N_{\mathrm{Fe}}\right)_{\rm star} - \log\left(N_{\mathrm{X}}/N_{\mathrm{Fe}}\right)_{\odot}. \tag{1.23}$$

In LTE, the line absorption coefficient is described by the number density $n^{\rm line}$ (following the Saha-Boltzmann distributions), the classical oscillator strength $f^{\rm line}$ (typically combined to the gf-value by combination with the statistical weight g) and the line profile $\phi(\nu - \nu_0)$ with the central (laboratory) frequency ν_0. Following the conventional description of stimulated emission as negative absorption, we can write

$$\kappa_\nu^{\rm line} \propto n^{\rm line} f^{\rm line} \varphi(\nu - \nu_0)\left(1 - \mathrm{e}^{-h\nu_0/kT}\right). \tag{1.24}$$

The shape of the line profile $\varphi(\nu - \nu_0)$ can be dominated by several processes. The basic mechanisms that govern the shape of the absorption coefficient are described in great detail by Rutten (2003) and include:

- Natural broadening due to the limited lifetime of excited states (given by Lorentz profiles),
- Collisional broadening (including the Stark effect and van-der-Waals broadening mostly given by Lorentz profiles),
- Doppler broadening by thermal motions (given by the Gaussian profile of the Maxwell distribution),

- Doppler broadening by non-thermal motions by small-scale turbulences (compared to the mean free path of photons), that is microturbulence (an additional constant in the Doppler shift profile by thermal motions accounting for shortcomings of hydrostatic atmosphere modelling)
- Fine- and hyperfine structure (e.g. for Mn I, VI, Co I, Cu I), isotope splitting (e.g. for LiI), and Zeeman splitting

The final profile of the emergent spectrum is additionally altered by additional process, which include

- Doppler broadening by non-thermal motions by large-scale turbulence (compared to the mean free paths of photons), that is, macroturbulence (often given by a Gaussian profile)
- Rotational broadening by the rotation of the whole star, typically noted as $v \sin i$ (with a rotation profile described approximately by a half-ellipse)

In summary, most broadening parameters will imprint a superposition of Lorentzian and Gaussian shapes, that is, Voigt profiles or even more complex shapes due to line splitting.

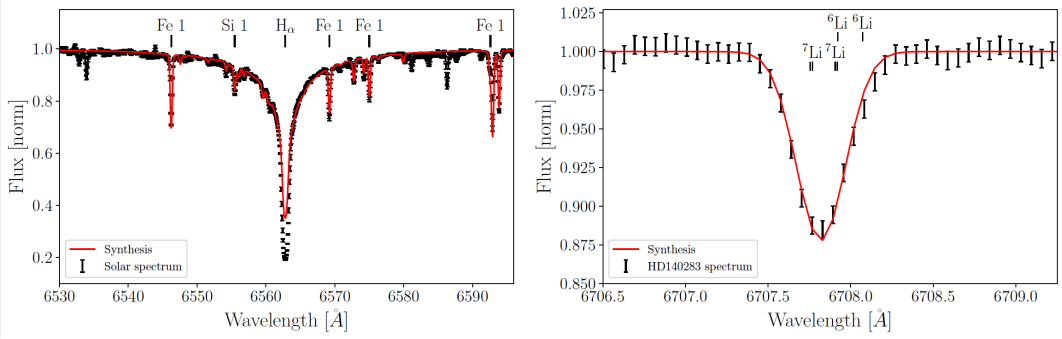

Figure 1.14: Examples of observed and synthesised spectra at different wavelengths. The left panel shows an observed spectrum taken of the sky (mimicking a Solar spectrum) around the strong H_α line in black and a synthesised spectrum overlaid in red. The right panel shows the Li I line of HD 140283, which exhibits fine- and hyperfine structure as well as isotope splitting, causing a slightly asymmetric line shape. The synthetic spectrum for the Li line agrees well with the observation. The synthetic spectrum on the left, however, shows several shortcomings. It does for example not include all lines observed in the spectrum and the line shapes and depths do not agree exactly with the observation, which is a hint of shortcomings of the parameter choices and model assumptions (e.g. the use of a 1D photospheric model atmosphere).

Once all these parameters are known (or at least defined), one can compute the flux F_ν for each given frequency. In stellar spectroscopy, it is however common to compute the flux F_λ for each wavelength point and normalise the spectrum to follow the continuum, as shown in the left and right panels of Fig. 2.12 for a zoom at the region of the H_α and Li I line. From these spectra, especially the synthetic spectrum which is missing numerous lines, it is obvious, that we can only achieve the best results if our line

data is complete and accurate (see example a discussion on wrong Mn line data by Jofré et al., 2017).

For completeness it should be said that finding the best set of stellar parameters, for example via χ^2-minimisation of observed and synthesised flux is a numerical challenge on its own and typically requires a lot of approximations and computational resources (especially if fluxes are synthesised on-the-fly for stars with tens of thousands of absorption lines).

1.3.3 CHALLENGES OF LARGE SCALE SPECTROSCOPIC ANALYSES

The challenges of large scale spectroscopic analyses regarding may appear sheer endless. From the beginning of a scientific idea to the realisation, several milestones have to be passed and with the growing amount of information, analyses techniques have to be improved both in computational ability as well as their performance in terms of accuracy and precision. Subsequently we will discuss these challenges in more detail, but will restrict this section to the Challenges that have been addressed throughout this Thesis. For a further discussion of additional challenges for large scale spectroscopic analyses in the future, we refer to the outlook of this Thesis in Sect 5.2.

1.3.3.1 ANALYSING BIG SPECTROSCOPIC DATA

The analysis of large amounts of spectroscopic data imposes several challenges on standard spectrum analysis methods.

As pointed out before, computational costs for classical spectrum analysis based on stellar physics are typically high (e.g. around 1-2 hours per spectrum observed and analysed by the GALAH survey with the spectrum synthesis method Spectroscopy Made Easy, see Sec. 2.2.7). Because the theoretical prediction of the models should be as close as possible to the observed spectra, such analyses are usually limited to unblended atomic lines with well known line information, for example 15% of the wavelength range for the GALAH survey stellar parameter estimation with Spectroscopy Made Easy.

With the increasing number of observed targets, reaching more than a million for GALAH, and eventually up to 16 million with 4MOST and other future surveys, this would require millions of CPU hours per individual analysis run. In total, this will amount to tens and hundreds of millions of CPU hours over the course of the survey (including runs during the development of the pipeline and production runs for the individual data releases).

In recent years, the development to more data-driven approaches of data analysis has commenced to estimate the spectral flux f_λ of a star as a function of stellar labels $\boldsymbol{\ell}$ (such as stellar parameters, chemical composition) not with a physics-based model approach (as outlined in Sec. 1.3.2.2). The new models are determined by the data itself and a more straightforward approximation (or mapping) of the flux f_λ as a model based on coefficients $\boldsymbol{\theta}_\lambda$, such that

$$f_\lambda \sim P(\text{model}|\text{data}) \approx g\,(\boldsymbol{\ell}|\boldsymbol{\theta}_\lambda) + \text{noise}. \tag{1.25}$$

Recio-Blanco et al. (2006) introduced MATISSE, an algorithm that finds the best combination of stellar labels from weighted linear combinations of theoretical spectra to reproduce the observed spectrum. Ness et al. (2015) introduced *The Cannon*, which approximates Eq. 1.25 with a polynomial spectral model (Rix et al., 2016), such that,

$$f_\lambda = \boldsymbol{\theta}_\lambda^T \cdot \boldsymbol{\ell} + \text{noise} \tag{1.26}$$

In current studies (see e.g. Casey et al., 2016), a quadratic function is most common, but any polynomial form would be possible. Ting et al. (2018b) introduced *The Payne*, which uses an even more flexible functional form of

$$f_\lambda = w \cdot \sigma\left(\tilde{w}_\lambda^i \sigma\left(w_{\lambda i}^k \ell_k + b_{\lambda i}\right) + \tilde{b}\right) + \bar{f} \tag{1.27}$$

with a different combination of coefficients (w, $\tilde{w}_\lambda^i$, b, $\tilde{b}$, and the sigmoid functions $\sigma(x) = 1/(1 + e^{-x})$ for a number of 'neurons' i). Such a combination of simple functions is commonly summarised under the collective term 'neural network' . While *The Payne* uses such a rather simple (fully-connected) convolutional neural network, other programs like the recently developed *AstroNN* (Leung & Bovy, 2019) or *StarNet* (Fabbro et al., 2018) use more complex 'deep' neural networks.

The coefficients of all these approaches are typically found by creating a small, representative training set with both best possible flux information f_λ (with high signal-to-noise) and reliable label information $\boldsymbol{\ell}$ (for example from literature, a prior spectrum synthesis analysis, or *ab initio* models). Once these coefficients are established (that the best fitting model is found or 'trained'), the model can predict stellar labels for any given flux f_λ.

The methods have in common, that they do not need to follow underlying physical laws, but can empirically map the connection of stellar parameters and abundances with the stellar flux. This has several advantages:

- **Lower computational costs** The simplified nature of these models makes these approaches computationally significantly cheaper. *The Cannon* needs for example only $\sim$ 5 s to predict stellar parameters and element abundances for a GALAH spectrum.
- **Use full spectral information** One does not need to restrict the spectrum analysis to the parts of the spectrum with the most reliable line information, that is one can use 100% of the GALAH spectral range rather than just 15% for the stellar parameter estimation. This naturally implies an increased precision for the analysis.
- **Empirical exploration of physical relations** One can directly explore the spectral information beyond the labels necessary for spectrum synthesis, for example the response of spectra to stellar ages, later confirmed to be related to C/N ratios (see e.g. Ness et al., 2016; Ho et al., 2017a) or the evolutionary phase of giant stars via CNO abundances (Hawkins et al., 2018).

These approaches suffer however also from possible shortcomings:

- **Model flexibility** Are data-driven models flexible enough to describe complex physics? A question that still has to be studied extensively is whether data-driven models, like a quadratic model, sufficiently describe the complex connection of stellar composition and flux (see e.g. Ting et al., 2018b).
- **Data does not care about physics** Similar to other data-driven approaches like principal component analyses, the complex ('hidden') nature of the coefficients also makes it hard to understand their underlying physics - if there is any. The first applications of data-driven approaches (see e.g. Ho et al., 2017a; Buder et al., 2018; Ting et al., 2018b) showed that the approaches tend to need guidance to separate true from coincidental correlations for certain abundances, as for example the trends of all α elements are similar and pixels might be mismatched with elements without guidance. Line masks or coefficient priors are however easily implemented and able to solve those degeneracies.
- **Completeness of training set labels** Until now, most data-driven approaches need complete sets of labels for the training set, because they assume that these labels are perfect. Buder et al. (2018) suggested to overcome this problem by creating $N + 1$ models for stellar parameters and N abundances to have the largest possible training set sample for each abundance. Recently, Leung & Bovy (2019) showed that an objective function can be used for their Bayesian neural network to deal with incomplete and noisy training data.
- **The ability to extrapolate** The last and possibly most important concern is related to the training step. Because all these approaches need to be trained on input data, they are expected to be (typically) only as reliable as the training set. Even more important, such networks are not expected to have a high predictive power for spectra with labels outside of their training range and are expected to only propagate information, but not create 'truth' in terms of accurate labels.

1.3.3.2 ACCURACY AND PRECISION

The challenges of large scale spectroscopic analyses regarding accuracy and precision may appear sheer endless. From the subjective view of a member of the scientific community, the aspects outlined in section are currently most discussed in the community.

The compromise between wavelength range, resolution, and signal-to-noise The limited amount of telescope time makes it imperative to find the best setup to achieve science goals in the least amount of time. For stellar spectroscopy this means that the best combination of wavelength range, resolution, and signal-to-noise has to be found. There are several factors to consider with respect to this:

- Which lines and wavelength ranges should be observed? As described above, we need to include lines that carry information for both stellar parameters and element abundances. In the visual range, several strong lines, which are pressure and temperature sensitive, are available, such as the Mg I and Ca II triplet as well as the Balmer lines, respectively. To estimate element abundances, the individual lines of

an element can be used, or molecular lines (such as CN and CH)[5]. Their strengths vary strongly across the parameter space, that is lines can become negligible in strength or saturate for several atmospheric and chemical compositions. A thorough selection has to be performed and it might be advisable to not use all lines for the abundance determination of each star.

- Which resolution is necessary to achieve the science goal? If the resolution of a spectrograph is low compared to the intrinsic line width (typically a few km/s, corresponding to $R \sim 20,000$), a significant fraction of lines become blended due to instrumental broadening, which is super-positioned with the natural line width and blending of lines (see e.g. Ting et al., 2017). The necessary resolution to estimate precise and accurate abundances is however still a contentious value. In theory, it should be possible to estimate a large number of elements even with low resolution $R < 10,000$ if the lower resolution can be counterbalanced with a larger wavelength coverage, that is, having the same information content due to more lines per element (Ting et al., 2017). However, this requires that the line flux changes are not degenerate with (changes of) the chemical composition and our theoretical models of flux as a function of chemical composition are sufficient.
- Which is the necessary signal-to-noise to achieve the science goal? The signal-to-noise has direct implications on our ability to solve spectroscopic degeneracies. If both wavelength range and resolution of a survey are already defined, for example by an already existing spectrograph, this it the last free parameter which can be adjusted to reach a certain precision by the exposure time.

In the past, several surveys, like *Gaia*-ESO, have made use of already existing spectrographs and only needed to find the right signal-to-noise (or exposure time) for their defined science goals. Recently, however, surveys like GALAH, 4MOST, and WEAVE have first studied the necessary element lines that should be estimated and then chosen the wavelength coverage(s), resolution(s), and signal-to-noise-ratio(s) to achieve their science goals. GALAH, in particular, has influenced the design of a high-resolution spectrograph ($R \sim 28,000$) with a wavelength covering atomic lines of up to 30 elements. Furthermore, the GALAH specifications define a requirement on the signal-to-noise of 100 per pixel, with corresponding exposure times set by this requirement.

Spectroscopic degeneracies As a result of the chosen compromise of wavelength range, resolution, and signal-to-noise, but also the partially limited information content in spectra, purely spectroscopic analyses may suffer from inaccuracies due to degeneracies between stellar parameters and chemical abundances.

This is a consequence of simplified assumptions about stellar spectra and the subsequent construction of incomplete stellar models, for example assuming a 1D hydrostatic atmosphere and chemical compositions scaled with solar values and the metallicities, as pointed out by Buder et al. (2019): Previous high-resolution spectroscopic studies

[5]It is worth noting that recent studies (see e.g. Ting et al., 2018a) suggest that due to atomic-molecular equilibria it might even be possible to use more molecular lines than CN and CH (like CO) for abundance determination.

(see e.g. Bensby et al., 2014; Martell et al., 2017) find inconsistencies between purely spectroscopic and photometric/asteroseismic parameter estimates. Furthermore, many studies find that unphysical low surface gravities are estimated for G and K-type MS stars from spectroscopy alone (Sousa et al., 2011; Adibekyan et al., 2012). Cool dwarfs ($T_{\rm eff} < 4500$ K) are particularly challenging to study in the optical regime, because of the weakening of the singly ionised lines that are used to constrain the ionisation equilibrium, and due to the increasing influence of molecular blends as well as the failure of 1D LTE modelling; see for example Yong et al. (2004). Adding further (non-spectroscopic) information may alleviate these problems (see e.g. Bensby et al., 2014).

Binarity Current large-scale spectroscopic analyses assume that the observed flux of a spectrum originates from a single star or identify and typically discard them for the further analysis. However, El-Badry et al. (2018a,b); Čotar et al. (2019, among others) have shown, that the contribution of companions can significantly influence the flux profiles, but can be solved. This can however be modelled as a binary system, if the flux contribution and line-of-sight velocities of the components are reasonably different. The implementation of such algorithms will be a major challenge, because a significant fraction of all stars, that is between a third (Lada, 2006) and almost all stars (Sadavoy & Stahler, 2017), are expected to have formed or still occur in systems of two or more stars.

The shortcomings of model assumptions (including 1D and LTE) In Sec. 1.3.2.2 we described the *ab initio* modelling of flux, but made several assumptions regarding the atmosphere (following a 1D stratification) and the thermodynamic equilibrium (being locally applicable). The comparison with independently estimated stellar parameters (see e.g. Heiter et al., 2015a) suggests that these assumptions still lead to rather accurate stellar parameter results. 3D and non-LTE effects are, however, strongly non-linear and typically hard to predict without modelling, but have serious consequences for Galactic chemical evolution (see e.g. the reviews by Asplund, 2005; Nissen & Gustafsson, 2018). The latter is however computationally extremely expensive and became feasible only within the last two decades. Only recently, 3D and/or non-LTE calculations became available for the the solar abundances (Asplund et al., 2009), as well as abundances for several elements like H (Amarsi et al., 2018), Li (Lind et al., 2009), C (Amarsi et al., 2019a), O (see e.g. Amarsi et al., 2015, 2016a), Na (Lind et al., 2011), Mg (Osorio & Barklem, 2016), Al (Nordlander & Lind, 2017), Si (Amarsi & Asplund, 2017), K (see e.g. Reggiani et al., subm.), Ca (see e.g. Osorio et al., 2019), Ti (Bergemann, 2011), Mn (Bergemann & Gehren, 2008), Co (Bergemann et al., 2010), and Fe (see e.g. Amarsi et al., 2016b). The corrections of 1D LTE to 3D non-LTE abundances have been shown to reach up to 1 dex (see e.g. Nordlander & Lind, 2017) and change measured trends of abundances that are often used as tracers of Galactic chemical evolution (see e.g. the analyses by Amarsi et al., 2018, 2019b, 2016a, for 3D non-LTE for H, C, O, and Fe).

Departures from LTE are especially then large, when radiative rates R are larger or comparable to collisional rates C, that is, when the rate of photon absorptions is significantly larger than the rate of inelastic electron collisions, which is especially the case for high temperatures and low densities. An extreme case of such conditions is the solar chromosphere and corona. In general, populations n_i of an atomic level i in

non-LTE can be computed from the difference of the sum of the incoming rates from every level j to i, and the sum of all outgoing rates from level i to every level j. This difference is time-independent in statistical equilibrium, such that

$$0 = \frac{\mathrm{d}n_i}{\mathrm{d}t} = \sum_{j \neq i} n_j \left(R_{ji} + C_{ji}\right) - n_i \sum_{j \neq i} \left(R_{ij} + C_{ij}\right), \tag{1.28}$$

with the radiative and collisional rates for a transition i to j, that is, R_{ij} and C_{ij} respectively. However, this equation has to be solved iteratively, because the radiative rates depend not only on the atomic transition data (such as frequency-dependent cross sections for each transition), but also the radiation field. In practice, it is common to actually compute departure coefficients (with respect to the LTE case)

$$\beta_i = \frac{n_i^{\mathrm{NLTE}}}{n_i^{\mathrm{LTE}}}, \tag{1.29}$$

which can be inserted into Eq. 1.17, resulting in

$$S_\nu^{\mathrm{line}} = \frac{2h\nu^3}{c^2} \frac{1}{\frac{\beta_i}{\beta_j} \cdot \mathrm{e}^{\frac{h\nu}{kT}} \cdot -1} \overset{h\nu \gg kT}{\approx} B_\nu \cdot \frac{\beta_j}{\beta_i}. \tag{1.30}$$

In the regime where $h\nu \gg kT$, that is, the regime where the Planck function follows Wien's approximation, we can further approximate the source function as a combination of the Planck function and the departure coefficients (see last part of Eq. 1.30). Synthesis codes like Spectroscopy Made Easy (Piskunov & Valenti, 2017) can thus be supplied with grids of departure coefficients in order to synthesise spectra in non-LTE on-the-fly, without added computational costs.

The quality of spectral lines The automated analysis of spectra for a large parameter space is currently still in its early stages. Until the advent of large scale spectroscopic surveys, lines could be carefully selected and analysed by hand. The amount of spectra makes this task now impossible and spectroscopists have written pipelines that using predefined line regions (masks) when estimating element abundances. Starting from all detected lines in a spectrum, the preselection of lines typically includes the following criteria:

- Blending of the line (by neighbouring atomic and molecular, telluric, sky, and interstellar lines)
- Variation of line strength across the parameter space (from being non-detectable to detectable up to saturated with damping wings)
- Accuracy of wavelength and $\log gf$ values and broadening data (including line splitting effects)
- 3D and non-LTE effects for individual lines

The importance of careful line selection for the element abundances was shown for example by Jofré et al. (2014, 2015, 2017), as well as Hawkins et al. (2016, see Figure 1.15). A review on this can be found in Jofré et al. (2018).

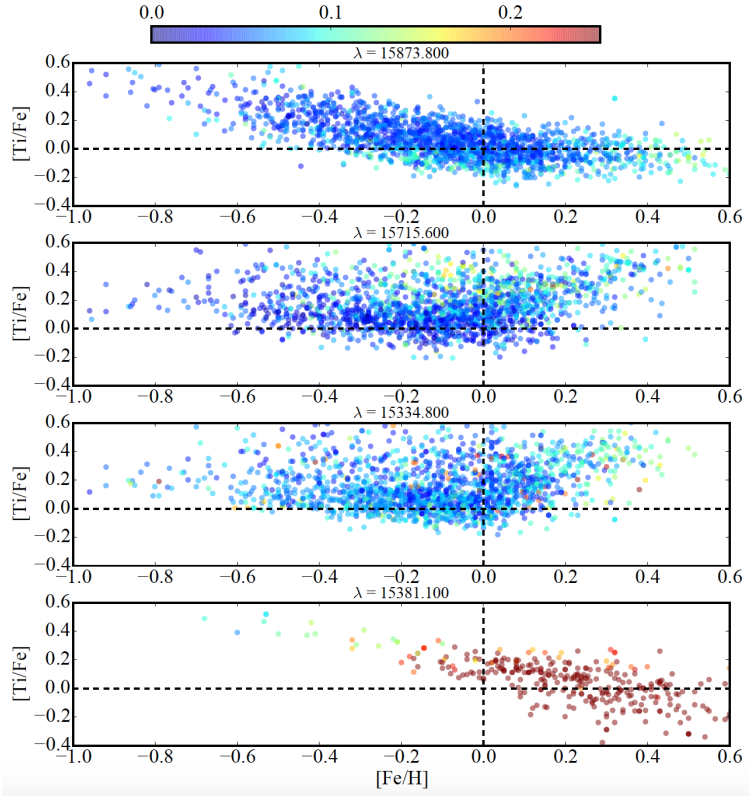

Figure 1.15: [Ti/Fe] as a function of metallicity for the full APOKASC sample for the 15 873.8 Å, 15 715.6 Å, 15 334.8 Å, and 15 381.1 Å lines from top to bottom, respectively. The stars are color-coded by the BACCHUS method-to-method dispersion, which is defined as the standard deviation of the abundance derived from the four procedures. **Figure Credit:** Hawkins et al. (2016).

Data/reduction quality issues With the large amount of observations over a long period of time for large programs, the data and reduction quality becomes very important but is typically hard to achieve in an automated fashion. As outlined for example by Kos et al. (2017), automatic reduction pipelines only reach a certain level of performance, and several issues, like wavelength calibrations, the dependence on line-spread function over the chip, or hot/broken pixels across the CCD as well as the influence of telluric and sky lines can only be corrected to a certain degree. This means that also spectroscopic analysis pipelines have to be able to handle such imperfections, which will otherwise introduce several systematic trends in the analysis.

Including non-spectroscopic information In the era of photo- and astrometric satellite missing like *Gaia*, Kepler, K2, TESS, and Plato in the future, but also ground-based surveys like 2MASS and SkyMapper, non-spectroscopic information is or will become available. On-going surveys will have the possibility (and challenge) to include this information into their analyses and can help to break spectroscopic degeneracies. When considering photometric information, one has to be cautious, that they underly the

influence of reddening, which becomes typically increasingly stronger with distance and is hard to model.

For effective temperature, photometric estimates from the Infrared Flux Method (IRFM) (see e.g. Casagrande et al., 2010) will become available for large parts of the spectroscopically accessible stars (see e.g. Casagrande et al., 2019). They can provide important validation (or flagging) values for spectroscopic surveys and are expected to be very useful for the lowest signal-to-noise spectra, but are not as accurate as temperature estimates from interferometric measurements. The later are however limited to the very brightest objects in the sky (see e.g. Boyajian et al., 2013; Karovicova et al., 2018).

Through the fundamental relations of surface gravity and luminosity it is possible to use trigonometric distances and photometric information to estimate surface gravities (see Sec. 1.3.1). With the precise parallax information provided by *Gaia* (Lindegren et al., 2018), this method is now applicable to a large fraction of the observed stars of past and on-going surveys.

The analysis of time-series photometry from the CoRoT (De Ridder et al., 2009) and Kepler (Bedding et al., 2010) missions has led to the discovery, that virtually all red giants are non-radial oscillators. The properties of the oscillations, such as large frequency spacing $\Delta\nu$ and the frequency of maximum oscillation power $\nu_{\rm max}$ are physically related to the stellar mean density and surface gravity (Kjeldsen & Bedding, 1995; Pinsonneault et al., 2014) and can be estimated from frequency analyses. Asteroseismic values are providing very accurate and precise surface gravities when combined with $T_{\rm eff}$ (see e.g. APOKASC Pinsonneault et al., 2014) through empirical scaling relations (as reviewed by Chaplin & Miglio, 2013). Such values are now also available for the large fraction of K2 targets and will become available for TESS targets.

1.3.4 ESTIMATING DYNAMIC INFORMATION

The estimation of orbits, that is, the paths that stars follow in a collisionless stellar system[6] like our Galaxy under the influence of a gravitational potential, is complex and involves the transformation of parameters in observable space (positions and velocities) into meaningful, say conserved and interpretable, parameters in dynamical space.

With our increasing understanding of the potentials governing the MW (see e.g. Miyamoto & Nagai, 1975; Navarro et al., 1997) and the ability to model the potential and orbits methodologically (see e.g. Binney & McMillan, 2011; Binney, 2012) and computationally (see e.g. Bovy, 2015), we are now able to quantify orbits. It should be noted however, that current dynamic models assume that the MW is in a steady state, that means dynamic properties of the Galaxy do not explicitly depend on time. Another common assumption is that the Galaxy is axisymmetric, such that we can model it without any dependence on the azimuthal angle. We have to keep in mind though, that the Galactic bar and spiral arms are clearly proving these assumptions wrong, which

[6]Observations of the Solar random motion with respect to the Galactic flow and the expected mean free path of stars in an environment with less than 1 star per pc^3, which lead to an average stellar encounter time that is significantly higher than the age of the universe, warrant the assumption that the MW is a collisionless system (Binney & Tremaine, 2008).

means that current Galactic models are still only simplified approximations of the true Galaxy.

An additional challenge of Galactic dynamics is that we can only collect our observables in relative small scales compared to the typical dynamical times scales of stars and our Galaxy. The Sun is for example orbiting the Galactic center at a Galactocentric radius of 8.178 ± 0.035 kpc (Abuter et al., 2019) with a circular velocity of $v_c = 229.0 \pm 0.2\,\mathrm{km\,s^{-1}}$ (Eilers et al., 2019) and needs ~220 million years for one rotation. Although present-day positions and space velocities only represent a snapshot of an orbit, they are powerful for the analysis because large scale structures of our MW are likely to be correlated in positions and velocities over large time scales (see Sec. 1.2.3).

The inventory of observables: position and velocity Before considering any analytical approaches, we will briefly take a look at the observables which can be used to test them. Depending on the physical scales and motivation, different coordinate systems are commonly used. In a Galactic context, it is advantageous to find a coordinate system with the center of the Galaxy at origin, and a set of canonical coordinates with one being perpendicular to the Galactic plane. Here, the Galactocentric cartesian and cylindrical systems have become most common. From an observational point of view, it is however advantageous to find a coordinate system which has either the Sun or our Earth as center. Because of the rotation of the Earth, which dominates the apparent motion of stars on the night sky, the so called equatorial coordinate system has become one of the most commonly used observationally motivated coordinate system, with positions represented by the latitude angle declination δ (with highest and lowest values at the the celestial poles) and longitude angle right ascension α (describing the angular distance along the celestial equator from a fixed starting point at the vernal equinox[7] where the celestial equator intersects the ecliptic) as well as the stars' line-of-sight distance from us. Velocities are then observed aligned to this frame, namely the proper motions μ_δ and μ_α along δ and α, respectively, and the radial velocity along the distance vector. Because of Earth's rotation and its orbit around the Sun at a radius of $\sim 1.5 \cdot 10^{11}$ m within a year, the barycentric equatorial coordinate frame is another version if this systems and requires the correction of the line-of-sight velocity from Earth towards the barycentric radial velocity. As we are however interested in the more global, Galactic motions, the transformation to a Galactocentric frame is favourable and can be performed with certain reference point, namely the position and velocity of the Sun in the Galactocentric frame[8]. Common estimates of the Solar position and velocity in the Galactocentric rest-frame are listed in Table 1.2.

Panels (a) and (b) of Fig. 1.16 show examples of orbits for five different stars, with typical properties of stars in the neighborhood. The green, violet, and orange stars are examples of disk stars on near-circular orbits. The blue star resembles a star that typically

[7]The currently most common definition of the vernal equinox is given by the International Celestial Reference System for the most commonly used equinox epoch "J2000", that is, the Julian date 2451545.0 or 2000 January 1, 11:58:55.816 UTC or "J2015.5" (Lindegren et al., 2018).

[8]Both the Galactocentric cartesian frame with positions X, Y, Z and velocities U, V, W or the Galactocentric cylindrical frame uses R, ϕ, z and v_R, v_ϕ, v_z are commonly used and can be easily transformed, because $R = \sqrt{(X^2 + Y^2)}$, $\phi = \tan(Y/X)$ and $Z = z$.

Table 1.2: Common values for the Solar position and velocity in the Galactocentric rest-frames. Ω_{GC} is the Sun's total angular velocity relative to Sgr A*.

Parameter	Value	Reference
$X_{GC,\odot} = R_\odot$	8.178 ± 0.035 kpc	(1)
$\phi_\odot$	0	(by definition)
$Y_{GC,\odot}$	0	(by definition)
$Z_{GC,\odot}$	0.025 kpc	(2)
$U_{GC,\odot}$	$11.1^{+1.69}_{-1.75}$ km s^{-1}	(3)
$V_{GC,\odot} = \Omega_{GC} \cdot R_\odot$	30.24 ± 0.12km s^{-1} kpc^{-1} $\cdot$ 8.178 ± 0.035 kpc	(4+1)
$V_{GC,\odot} \sim v_{circ}(R_\odot) + V_\odot$	229.0 ± 0.2 km s^{-1} + $12.24^{+2.47}_{-2.47}$ km s^{-1}	(5+3)
$W_{GC,\odot}$	$7.25^{+0.87}_{-0.86}$ km s^{-1}	(3)

Notes: (1) Abuter et al. (2019), (2) Jurić et al. (2008), (3) Schönrich et al. (2010), (4) Bland-Hawthorn & Gerhard (2016), (5) Eilers et al. (2019).

orbits closer to the Galactic center but due to its larger eccentricity and the subsequent large oscillations along R and z, its apocentre overlaps with the Solar neighborhood. The red star is typically located further out but its epicentre overlaps with the Solar neighbourhood. If we were to observe such stars in the Solar neighborhood, we would expect them to show velocities similar to those shown in panel (c) of Fig. 1.16, which can also be drawn in a Toomre diagram, shown in panel (f). While for small volumes U, V, W, these two diagrams are useful diagnostic tools, their interpretation becomes difficult if we want to interpret stars that are tens of kpc away, the reference system of the Toomre diagram around the Sun is expected to become inconvenient. A more convenient choice of parameters to describe orbits is needed. Subsequently, we will introduce the radial, azimuthal, and vertical actions J_R, J_ϕ, and J_z respectively, which are more helpful in the interpretation of orbits, as they intuitively indicate guiding radii and eccentricities of orbits. From panels d) and e) of Fig. 1.16, one can for example directly see that the orbit of the green star does not oscillate radially, and the violet star does not oscillate vertically - as confirmed by the orbits in panel a) and b), whereas this conclusion is not as obvious from the space velocity diagrams in panel c) and f).

Orbit characterisation with action-angle coordinates Similar to the observables, we are looking for a coordinate system to describe orbits, using Binney & Tremaine (2008) as main reference. In the framework of Hamiltonian mechanics, that means that we are looking for a convenient set of canonical conjugate positions $\boldsymbol{q}$ and momenta $\boldsymbol{p}$ to describe the sum of kinetic energy K and potential energy V with the Hamiltonian function

$$\mathcal{H}(\boldsymbol{q}, \boldsymbol{p}) = K + V \tag{1.31}$$

By using our observables, such that $\boldsymbol{q} = \boldsymbol{r}$ and $\boldsymbol{p} = \boldsymbol{v} \cdot m$, we can formulate

$$\mathcal{H}(\boldsymbol{r}, \boldsymbol{v}) = \frac{1}{2}\boldsymbol{v}^2 + \Phi(\boldsymbol{r}) \qquad \dot{\boldsymbol{r}} = \boldsymbol{v} \qquad \dot{\boldsymbol{v}} = \frac{\partial \Phi}{\partial \boldsymbol{r}} \tag{1.32}$$

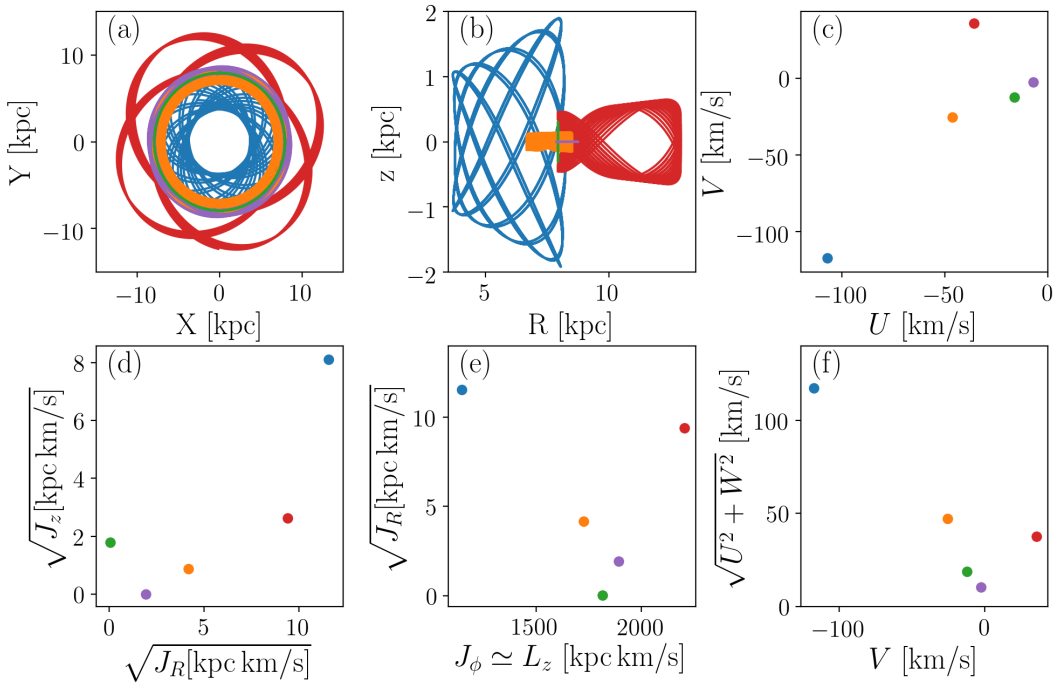

Figure 1.16: Examples of orbits, actions, and velocities for five stars, with the same color applied for all panels. Top left: positions (X, Y) of the stars for a Galactocentric cartesian system for a period of 4 Gyr. Top middle: positions (R, z) of the stars in Galactocentric zylindrical coordinates. Top right: Space velocities (U, W) in the Galactocentric cartesian system at $t = 0$. Bottom left: Actions (J_R, J_z) of the stars. Bottom middle: Actions (L_z, J_R) of the stars. Bottom right: Toomre diagram of the stars at $t = 0$.

In our endeavour to find dynamic parameters that are interpretable, integrals of motion $I(\boldsymbol{r}, \boldsymbol{v}, t)$ are promising quantities, as they are conserved along a stellar orbit, that is,

$$0 = \frac{\mathrm{d}}{\mathrm{d}t} I = \boldsymbol{v} \cdot \frac{\partial I}{\partial \boldsymbol{r}} - \frac{\partial \Phi}{\partial \boldsymbol{r}} \frac{\partial I}{\partial \boldsymbol{v}} \tag{1.33}$$

The search for suitable coordinates and integrals of motions is described in detail by Binney & Tremaine (2008), and we will only briefly introduce those that will be used throughout this Thesis, based on this reference.

Because we assume that our Galaxy is in a steady-state, that is $\mathrm{d}\mathcal{H} = 0$, a first integral that can be found is describing the total (conserved) energy

$$E = \frac{1}{2}\left(v_R^2 + v_\phi^2 + v_z^2\right) + \Phi = \text{const.} \tag{1.34}$$

Depending on the symmetry of our potential, we might also be able to find more integrals of motion. In an axisymmetric potential, where no forces are acting on the stars in tangential direction $\mathrm{d}\phi$, we can also find another constant parameter, the angular momentum in vertical direction

$$L_z = \frac{1}{2\pi} \oint v_\phi \mathrm{d}\phi = \frac{1}{2\pi} \int_0^{2\pi} v_\phi R \mathrm{d}\phi. \tag{1.35}$$

We can understand this integral as a marginalisation of all momenta $v_\phi \cdot R$ along the orbit, which could also be described with a circular orbit with the guiding-centre radius R_G, such that $L_z = R_G \cdot v_{\rm circ}(R_G)$. Finding a third integral in addition to E and L_z has proved to be challenging, as it needs to quantify the distribution of energy in R and z-direction that is not in rotation.

Another approach to describe the periodic movement of a star is to describe its movement as near-circular. With this idea, orbits can be with a set of frequencies and momenta, which characterise a circular orbit (described by the guiding centre radius) and the oscillations from this circular orbit. For this we need to find frequencies and moments of the oscillatory and rotational motion.

Because the Hamiltonian does not explicitly depend on time under our assumptions, we can find such moments as the actions $\boldsymbol{J} = (J_R, J_\phi = L_z, J_z)$ with

$$J_i = \frac{1}{2\pi} \oint_{\rm orbit} v_i {\rm d}i \qquad \text{with} \qquad i \in [R, \varphi, z] \tag{1.36}$$

These actions are also integrals of motion and conserved under our assumptions. Finding appropriate parametrisations for their integrals is however complex and the associated orbit integration is computationally very expensive (Sanders & Binney, 2016). However, the introduction of the so called Stäckel fudge, an approximation of the actual potential with a Stäckel potential (Binney & Tremaine, 2008), that instead of the coupled variables (R, z) is described with separated variables, by Binney (2012) led to a breakthrough and and makes it possible to estimate actions for large data sets (see e.g. Bovy & Rix, 2013; Bovy, 2015).

Trick et al. (2019) have shown that the substructure (for example of moving groups in the left panel of Fig 1.17) is preserved in action space (see right panel of Fig. 1.17) when analysing stars in the Solar neighborhood ($1/\varpi < 200$ pc) with information from *Gaia* DR2 and *Gaia* RVS.

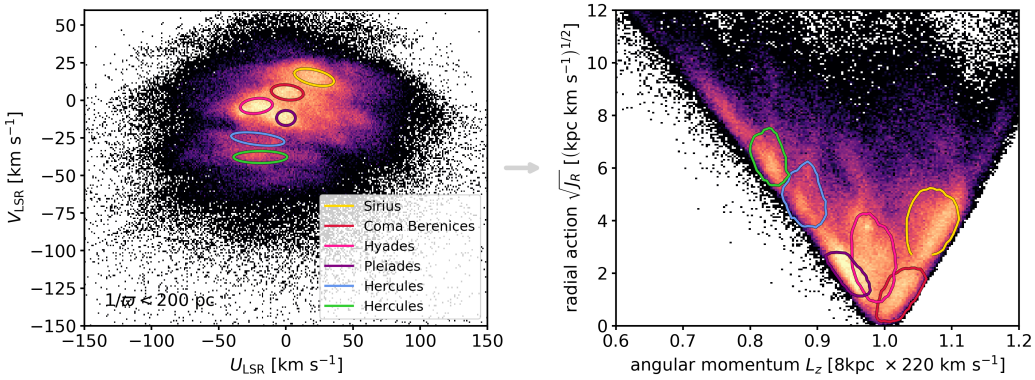

Figure 1.17: Known moving groups in the Solar neighbourhood ($1/\varpi < 200$ pc) identified in the (U, V) velocity plane, and the location of the corresponding stars in the orbital action plane (L_z, J_R). **Figure Credit:** Trick et al. (2019).

1.3.5 ESTIMATING STELLAR AGES AND MASSES

The age of stars is not a direct observable and its estimation involves model-dependent or empirical methods. The review by Soderblom (2010) reviews the plethora of approaches for stellar age dating and the regimes in which they work. This includes age dating stars through the correlation with chromospheric activity or rotation decay or stellar seismology. We will restrict ourselves to the methods that are of practical importance for this Thesis.

The two methods that are explored in this Theses are isochrones fitting and age-abundance correlations. The first method is until now most commonly used for nearby turnoff stars, because its discriminating power is given by the large separation in the $T_{\rm eff}$ - $L_{\rm bol}$ or CMD domain. The red giant branch has until recently been the regime of asteroseismology, which could estimate precise masses to derive stellar ages, but was limited to a small number of stars due to the need for time-series photometry. With the increase of abundance measurements and data-driven algorithms, several age-abundance correlations have been found so provide chemical clocks for certain stellar types.

Isochrone fitting The currently most applied method to estimate stellar ages is isochrone fitting, that is the comparison of observables or estimated stellar parameters, $\{data\}_{\rm obs}$, which can for example include $T_{\rm eff}$, L or $\log g$, and [Fe/H], from a survey with those predicted through isochrone data. The latter is constructed from stellar evolution theory which to first approximation depends essentially only on the model parameters $M_\star$, [Fe/H], and $\tau_{\rm age}$ (see e.g. Dotter et al., 2008; Bressan et al., 2012; Dotter, 2016). Given these models and the observational data, we can estimate the probability of a star's age with (cf. Rix & Bovy, 2013)

$$\mathcal{L}\left(\{data\}_{\rm obs}\,|\tau_{\rm age}\right) = \iint p\left(\{data\}_{\rm obs}\,|M, [\mathrm{Fe/H}], \tau_{\rm age}\right) \cdot p_{\rm prior}\left(M|\tau_{\rm age}\right) p_{\rm prior}\left([\mathrm{Fe/H}]|\tau_{\rm age}\right) \mathrm{d}M\mathrm{d}[\mathrm{Fe/H}] \tag{1.37}$$

by also taking into account possible prior knowledge for the distribution of M and [Fe/H] for given ages, like the stellar mass function. The marginalisation over mass and [Fe/H] can be performed in many ways and several codes are available, like MADE (Das et al., 2019), UNIDAM (Mints & Hekker, 2018), or ELLI (Lin et al., 2018) or the code based on hierachical modelling by Feuillet et al. (2016). Generally speaking, the quality of the age estimate is driven by three components:

- the quality of the observables,
- the quality of the isochrone models (being able to predict the observables), and
- the evolutionary stage.

The latter point can be appreciated by looking again at the color-magnitude and $T_{\rm eff}$-$\log g$ diagrams in Fig. 1.12. The tight distribution of observables of cool MS stars however significantly spreads the age posterior. Red giant branch and RC stars tend to show very

similar observable parameters and the latter are even partially overlapping, which can lead to ambiguous age predictions (with two peaks). The same structure can arise, when the quality of the observables is so bad, that not even the evolutionary stage is well known. However, turn-off stars show a significant spread in the observable space and are those stars, for which isochrone ages are most precise. This is plausible from an evolutionary perspective, because the relatively rapid movement of stars at the turn-off/early subgiant phase marks the end of the MS life time, which has the longest duration of all phases.

Chemical clocks The analysis of correlations of stellar age with abundances in stars has found multiple correlations of those parameters and fuelled the idea that chemical abundances could be used to estimate precise ages if such correlations can be calibrated properly and are valid for the observed samples. While age-metallicity and age-α relations show general trends in the Galactic disk, that is α-enhanced stars tend to be older than those with solar [α/Fe], these relations have shown a large spread throughout the disk (see e.g. Bergemann et al., 2014; Bensby et al., 2014), such that a direct mapping of ([Fe/H], [α/Fe]) $\rightarrow \tau_{\rm age}$ is not promising over a large parameter space.

Studies of Solar twins (Nissen, 2015; Spina et al., 2016), however, have shown that there is an empirical correlation of age and α-enhancement and were even able to find an anti-correlation of age with s-process elements like Y or Ba (due to the delay times of enrichment through low mass AGB stars). The applicability of these correlations onto less restricted samples is currently contentious (see e.g. Feltzing et al., 2017), but recent studies (Slumstrup et al., 2017; Lin et al., 2019) suggest that the ratio of [Y/Mg] can also be used as chemical clock for evolved solar-metallicity stars and turn-off stars, respectively. The actual physical relation and validity beyond the solar neighborhood is however not yet understood.

For evolved stars, (Masseron & Gilmore, 2015; Martig et al., 2016) were able to identify a physical connection of the ratio of C and N abundances with mass (and stellar age). While low-mass stars experience a first-dredge up, that mixes the material in the photosphere with deeper layers where the CNO-cycle processed and altered the chemical composition, higher mass stars ($> 2\,M_\odot$) go through this phase without further mixing within a short timescale and eventually ignite helium, that is, becoming core-helium burning stars like RC. Because the surface abundance of C, N, and O of stars after the first dredge-up depends on the mass-dependent distribution of CNO-processed material within the core of the star (at the end of the MS phase) and the depth reached by the base of the convective envelope during the dredge-up, a true physical relation of mass and surface abundances is present (Martig et al., 2016).

1.4 THIS THESIS

This thesis is devoted to the study of the MW stellar components with chemical, dynamical, and temporal information. The MW has shown incredible substructures in all these dimensions of data. We are just at the beginning of understanding how to explore and interpret the big amount of data that we have collected and will collect in the future with large-scale stellar survey.

Due to my involvement in one of these surveys, GALAH, the selection of stars for my research is mainly given by the survey observations. The focus of the work during my Thesis is two-fold:

As a stellar spectroscopist, I am interested in understanding and improving how we can extract information about stars from stellar spectra in the best possible way. During my Thesis I have developed tools to analyse the spectroscopic data from the GALAH survey under the following key considerations:

- Efficiency, given a very large data set and limited computational and person power.
- Precision and homogeneity, given the limited signal-to-noise ratio of the spectra and the large number of elements with detectable absorption
- Accuracy, given known limitations of traditional spectroscopic models and access to non-spectroscopic information

Chapter 2 describes the research for answers to these questions during the application of spectroscopic analyses for the GALAH survey. I have been a main contributor to all data releases and the accompanying release papers of GALAH, that is GALAH DR1 (Martell et al., 2017), TESS-HERMES DR1 (Sharma et al., 2018), K2-HERMES DR1 (Wittenmyer et al., 2018), and GALAH DR2 (Buder et al., 2018). From this set of GALAH papers, only the latter paper by Buder et al. (2018) (**Paper I**), is included in this work, for several reasons. This paper is the last of the release papers and I was the main contributor to this paper. It includes the most advanced and complete analysis, but the previous analyses have all been performed in a very similar way. With the new data from *Gaia* DR2, the collaboration has decided to change the analysis strategy and the next data release will be following a different approach. I am also the main contributor to the new analysis. The improvements and changes for the analysis of GALAH DR3 will be laid out not only in this Thesis in Sec. 2.4, but also a peer-review journal article, hereafter called **Paper IV**.

As a Galactic archaeologist, I am interested in using the gathered stellar information to understand some of the puzzling questions of the formation of our MW:

- What is the best way to separate the main components of our Milky Way and to which extent are the components actually distinct in the chemical, dynamical, and temporal dimensions?
- Can we find the signatures of accreted and in-situ halo stars also among the stars observed by the GALAH survey? How much substructure is there actually in the

halo? Do all halo stars belong to the populations identified by Nissen & Schuster (2010) and is one of them the large accreted structure identified by Belokurov et al. (2018) and Helmi et al. (2018)?

- Which timescales are spanned by disk and halo stars? Does the age difference between the high- and low-α disk suggest that they formed at different times and if so what caused this? Could the accretion of the low-α halo stars be responsible for this drastic change of disk structure (including the plausibility of age distributions among all the components)?

Chapter 3 describes the research that I performed in Buder et al. (2019) (**Paper II**) with a local sample of stars that have been observed by the GALAH survey and overlap with the first astrometric data set from *Gaia* DR1, Tycho-*Gaia* Astrometric solution (TGAS). In the course of this research I have tried to analyse how the Galactic disk components can be separated with the use of chemical, kinematical and temporal information.

Chapter 4 describes the research that I have performed with the latest internal data of the GALAH survey and astrometric information from *Gaia* DR2 to understand the structures of the stellar halo in light of the aforementioned questions. The obtained results will be presented in Buder et al. (in prep. a) (**Paper III**).

A summary of all research and achievements of this Thesis is given in Chapter 5, where I also put my work in the context of future research.

CHAPTER 2

THE GALACTIC ARCHAEOLOGY WITH HERMES (GALAH) SURVEY

2.1 PREFACE

In the last decade, several large scale stellar spectroscopic surveys, among them APOGEE, RAVE, and LAMOST, have been launched with the aim to collect unprecedented amounts of stellar parameters and chemical information.

In 2013, the GALAH survey and its sister surveys TESS-HERMES and K2-HERMES joined them and have since collect more than 650,000 spectra of stars in the Southern hemisphere with the High Efficiency and Resolution Multi-Element Spectrograph (HERMES) attached to the Anglo-Australian Telescope in Siding Springs (Australia).

In this chapter, I am giving an overview of the survey, including the major science goals, target selection, observations, and data reduction. The focus of this chapter however is the spectroscopic analysis of the GALAH spectra, which were one of the main tasks of my work as member of the spectroscopic analysis working group. Since 2015 I have become the main spectroscopic analyst of GALAH data and have provided all stellar parameters and chemical abundances published in every major Data Release (DR) of the collaboration until now, namely GALAH DR1 (Martell et al., 2017), TESS-HERMES DR1 (Sharma et al., 2018), K2-HERMES (Wittenmyer et al., 2018), and GALAH DR2 (Buder et al., in prep. b).

All aforementioned data releases follow a rather similar analysis routine which will be described in Sec. 2.3. With the publication of astrometric data from the second data release of *Gaia*, exquisite astrometric information became available for almost all stars, including 99.8% of the GALAH DR2 targets. The implementation of this data and several other improvements are currently in process as part of my work for GALAH DR3, as I explain in Sec. 2.4.

The overview in Sec. 2.2 with exceptions of the overview and analysis strategy description of the data releases and Sec. 2.3 on the analyses until *Gaia* DR2 are based on

the published and peer-reviewed paper on GALAH DR2 (**Paper I**). The descriptions of Sec. 2.4 will be included a peer-reviewed paper in a scientific journal **Paper IV**, which is currently in preparation.

The author's contribution to the study presented in this chapter includes:

- Observations:
  - Observing tens of thousands of survey targets during five nights with HERMES/AAT at Siding Spring Observatory
- Analysis and Data Releases:
  - Coordinating the second data release of GALAH together with the survey management group
  - Coordinating the third data release of GALAH together with the survey management group
  - Developing, extending and testing a pipeline that analyses stellar spectra in an automated fashion with the spectrum analysis tool Spectroscopy Made Easy (Piskunov & Valenti, 2017)
  - Extending the data-driven spectrum analysis tool *The Cannon* (Ness et al., 2015) to analyse all GALAH data and provide not only stellar parameters but also element abundances, first for the α-process elements and later for up to 23 element of 342,000 stars
  - Developing tools for an automated quality assessment for these big data sets
  - Providing the stellar parameters and α-process elements for GALAH DR1 (Martell et al., 2017), TESS-HERMES DR1 (Sharma et al., 2018), and K2-HERMES (Wittenmyer et al., 2018)
  - Extending the pipeline so that it can take into account external information such as parallaxes and asteroseismic information
- Manuscripts:
  - Producing the text of the data analysis sections of the accompanying release papers for these all GALAH and TESS-HERMES data releases
  - Producing the text of the original manuscript of the second data release paper
  - Producing the text of the original manuscript of the third data release paper

The contribution of my co-authors have been related to the collaboration work in terms of application for observation time, selection of targets, observation of most targets, reduction of the spectroscopic data or other contribution to the GALAH survey as builders. M. Asplund and K. Lind selected the lines used for the spectroscopic analysis. K. Lind and T. Nordlander gave valuable advice regarding the use, shortcomings, and improvement of SME. M. Ness gave important guidance regarding the initial use of *The Cannon*. Sec. 2.2.2 was written in cooperation with G. de Silva, K. Freeman, and J. Bland-Hawthorn, Sec. 2.2.3 was written in cooperation with J. Kos and Sec. 2.2.4 was

written in cooperation with S. Martell. S. Sharma provided information and figures for the comparisons with the asteroseismic results and L. Casagrande provided information and figures for the comparison with infrared flux method temperatures. I want to stress that the majority of text was written by me and my co-authors mainly gave valuable comments regarding the figures or passages of the text of the data release paper.

2.2 OVERVIEW OF THE GALAH SURVEY

2.2.1 INTRODUCTION

The last decade has seen a revolution in Galactic astronomy. This is particularly evident in the domain of spectroscopic studies where sample sizes have grown from tens or hundreds of stars to several hundred thousands of stars, enabled by the availability of multi-object spectrographs. We now live in an extraordinary era of interest and investment in stellar surveys of the Milky Way. At optical and infrared wavelengths, large-scale photometric surveys have delivered accurate photometric magnitudes and colours for several hundred millions of stars (e.g., Skrutskie et al., 2006; Saito et al., 2012; Chambers et al., 2016; Wolf et al., 2018).

Spectroscopic surveys of stars in our Galaxy are fundamental to astrophysics because there are important measurements that can only be made in the near-field and through stellar spectroscopy. This is especially true for the measurement of detailed chemical compositions of stars. The determination of accurate stellar ages continues to be a challenge but there is cautious optimism that the situation will improve in the decades ahead. Asteroseismic surveys from NASA's *Kepler* and K2 missions are providing reliable estimates of stellar surface gravities and masses (e.g. Stello et al., 2015; Sharma et al., 2016) and this is expected to continue with missions like TESS (Ricker et al., 2015; Sharma et al., 2018) and PLATO (Rauer et al., 2014; Miglio et al., 2017). The ESA *Gaia* astrometric mission will measure accurate distances for billions of stars belonging to most components of the Galaxy (Perryman et al., 2001; Lindegren et al., 2016).

The Galactic Archaeology with HERMES (GALAH) survey[1] brings a unique perspective to the outstanding problem of understanding the Galaxy's history (De Silva et al., 2015; Martell et al., 2017). The survey makes use of the High Efficiency and Resolution Multi-Element Spectrograph (HERMES) at the Anglo-Australian Telescope (Barden et al., 2010; Sheinis et al., 2015). This unique instrument employs the Two Degree Field (2dF) fibre positioner on the Anglo-Australian Telescope to provide multi-object ($n \sim 392$), high-resolution ($R \sim 28,000$) spectra optimized for elemental abundance studies for up to 30 elements in four optical windows. The HERMES instrument was built specifically for the GALAH survey and is largely achieving its original design goals.

2.2.2 MOTIVATION

The overarching goal of the GALAH survey is to acquire high-resolution spectra of a million stars for chemical tagging, in order to investigate the assembly history of the Galaxy (Freeman & Bland-Hawthorn, 2002; De Silva et al., 2009; Bland-Hawthorn et al., 2010). The GALAH selection criteria are simple, with the baseline selection being a magnitude cut of $12 < V < 14$ with Galactic latitude $|b| > 10\,\mathrm{deg}$. As such, GALAH probes mainly FGK stars of the thin and thick disc of the Galaxy. However, due to the unprecedented sample size, the survey also includes a substantial number of halo stars, as

[1] https://galah-survey.org/

well as other stellar populations serendipitously along the GALAH stars the line of sight, such as stars in the Magellanic clouds. In addition, complementary programs with the same instrument targeting the Milky Way bulge (Duong et al., 2019) and open clusters (De Silva et al., in preparation) are underway. For the main GALAH survey, roughly two-thirds of the sample are dwarf stars, whilst the rest are predominantly red giant branch stars located at distances up to several kpc from the solar neighbourhood.

Whilst the volume and wealth of detail contained within the GALAH dataset present a broad range of science opportunities in Galactic and stellar astrophysics, such work is beyond the scope of this publication. The key science questions that motivated the GALAH survey are as follows:

- What were the conditions of star formation during early stages of Galaxy assembly?
- When and where were the major episodes of star formation in the disc, and what drove them?
- To what extent are the Galactic thin and thick discs composed of stars from merger events?
- Under what conditions and in what types of systems did accreted stars form?
- How have the stars that formed in-situ in the disc evolved dynamically since their formation?
- Where are the solar siblings that formed together with our Sun?

The above science questions can be presented as specific delivery goals for the survey. It is these delivery goals that are the highlight of this Data Release. The goals can be summarised as follows:

- To determine the primary stellar parameters: effective temperature, surface gravity, metallicity
- To derive up to 30 individual chemical element abundances per star from Li to Eu
- To measure radial velocities
- To classify targets of an "unusual" nature: e.g., binaries, stellar activity, chemical peculiarities

Achieving the above delivery goals for millions of stars in an unrestricted parameter space is a major challenge; doing so consistently and in a timely manner takes us into new territory for spectral analysis methods. Teams have been required to revisit their classical approach and enter into other disciplines of data analysis to develop machinery suitable for meeting these new challenges. In recent years, we have learned to bring together many different strands to make progress (Ho et al., 2017b). This has required major advances in a range of areas, including template matching (Jofré et al., 2010), automated machine learning (Ness et al., 2015), atmospheric modelling (Magic et al., 2013), spectral line formation (Amarsi et al., 2016a) and internal instrument calibrations (Bland-Hawthorn et al., 2017; Kos et al., 2018). We discuss some of these advances, to

the extent that they have benefited the GALAH data reduction and analysis, as part of this paper.

The GALAH survey joins a vibrant and exciting landscape of Galactic spectroscopic surveys that are highly complementary in scale and scope. The *Gaia*-ESO Survey on the VLT (Gilmore et al., 2012; Randich et al., 2013) contains a sample of about 100,000 stars over 14 – 19 in V band, most of which are thick disc and halo stars, as well as numerous open clusters. The observations used specific spectral windows with the GIRAFFE+FLAMES fibre spectrograph system, and the typical spectral resolving power is $R \approx 20,000$, somewhat lower than that of GALAH. However, a subsample of targets observed with the UVES spectrograph have high-resolution ($R \approx 47,000$) spectra. The infrared APOGEE survey (Abolfathi et al., 2018) mainly targets the low-latitude Galactic disc, probing through the optically thick dust regions with a sample of 150,000 red giants at a resolving power of $R \approx 22,500$. To expand their survey, the APOGEE team have recently begun the APOGEE-South survey, using the Dupont telescope at Las Campanas Observatory, in order to study a similar number of stars in the southern sky. While the overlap in targets between the three surveys is currently only a few hundred stars, the scientific complementarity is significant. Given the different magnitude ranges and regions of the Galaxy observed, both *Gaia*-ESO and APOGEE are highly complementary to the GALAH sample. Several even larger high-resolution spectroscopic surveys of the Milky Way are expected to commence over the next decade, including WEAVE (Dalton et al., 2014), 4MOST (de Jong et al., 2014), and SDSS-V (Kollmeier et al., 2017).

LAMOST is a lower spectral resolution ($R \sim 1800$) survey but has observed a far greater number of stars than other surveys, with over 1.5 million stellar spectra collected to date (Luo et al., 2015). The RAVE survey (Kunder et al., 2017) contains a similar number of stars as the current GALAH sample but at a lower resolving power of $R = 7,500$ and with the wavelength coverage limited to the infrared calcium triplet region. The RAVE sample, spanning magnitudes from 9 - 12 in the I band, was selected from numerous sources (Tycho-2, super-COSMOS, DENIS and 2MASS) and included a colour selection of $J - K > 0.5$ mag for stars with $|b| < 25°$ to preferentially select giants (see Wojno et al., 2017). The simple selection function of the GALAH sample, on the other hand, is dominated by local disc dwarfs, making it more sensitive to local substructure. As part of the second *Gaia* data release in April 2018, radial velocities for some seven million stars brighter than $G \approx 13$ have been measured based on $R = 11,500$ spectra around the Ca infrared triplet (845-872 nm) that also provide information on stellar parameters and some limited elemental abundances.

2.2.3 TARGET SELECTION

In order to carry out a large-scale survey with broad applications across astrophysics and Galactic archaeology, the GALAH survey uses a very simple observational selection function. This makes it relatively straightforward to transform between the observed data set and the underlying Galactic populations. It also makes a clear imprint on which types of stars across which regions of the Milky Way are sampled by GALAH because of their luminosities.

The GALAH input catalogue is constructed from the union of 2MASS (Skrutskie et al., 2006) and UCAC4 (Zacharias et al., 2013) catalogues. Only stars with appropriate 2MASS quality flags (Q="A", B="1", C="0", X="0", A="0", prox≥ 6″) and having no bright neighbours closer than $(130 - [10 \times V])$ arcseconds of the bright stars V magnitude were chosen. Because APASS was not complete in the Southern sky at the start of observations, we use a synthetic $V_{\rm JK}$ magnitude calculated from 2MASS photometry:

$$V_{\rm JK} = K + 2(J - K + 0.14) + 0.382e^{((J-K-0.2)/0.5)}. \quad (2.1)$$

Using PARSEC isochrones (Marigo et al., 2017) it was shown in Sharma et al. (2018) that this transformation is reasonably accurate across the parameter space where the majority of GALAH stars fall.

The GALAH observations are done in following three fixed magnitude ranges of V_{JK}.

- Normal mode $12 < V_{JK} < 14$: Most observations are done with this selection function.
- Bright mode $9 < V_{JK} < 12$: This is used during twilight or poor observing conditions.
- Faint mode $12 < V_{JK} < 14.3$: This is used when fields with normal or bright configuration are not available to be observed.

As a result of this simple selection function, all stars with $-80° \leq \delta \leq +10°$ and $| b | > 10°$ within these magnitude limits are potentially targets for our survey. We imposed an additional requirement, namely that we only sample fields with an on-sky density of stars of at least 400 per π square degrees, to match the number of fibres and field of view of the fibre positioner that feeds our spectrograph. The potential targets are then tiled into 6546 normal fields. The radius of each field varies inversely with the target density, to improve efficiency in dense regions. A normal field can be observed in either normal or bright mode but not faint mode. In bright configuration, the radius is set to 1 degree. In addition to normal fields, 285 faint fields were added to be observed exclusively in faint mode, and they do not overlap with the normal fields.

Figure 2.1 shows the distance distribution for dwarfs and giants observed between 16th January 2014 and 12th September 2017, dividing them simply at $\log g = 3.5$. Dwarfs are mainly confined to the solar neighborhood (84% are within 1 kpc), while giants extend much further (84% are within 4 kpc). These 342,682 stars were part of GALAH DR2 **Paper I** and provide a very detailed sample of the Milky Way in the solar neighbourhood. To visualise the extent of these stars in the Galaxy, we transform the coordinates and distances into (x,y,z) heliocentric Cartesian and (R,ϕ,z) Galacto-centric cylindrical coordinates. Figure 2.2 shows the density of stars across the (R,z) and (x,y) planes.

The observational selections (location of the telescope, avoiding the Galactic plane and high-latitude fields) can be seen in the spatial footprint of GALAH. We have very few stars with $x < 0$ and $y > 0$ because we primarily observe fields with $\delta < 0$ and $|b| < 60$, which excludes the $90 < l < 180$ region (Figure 2.3).

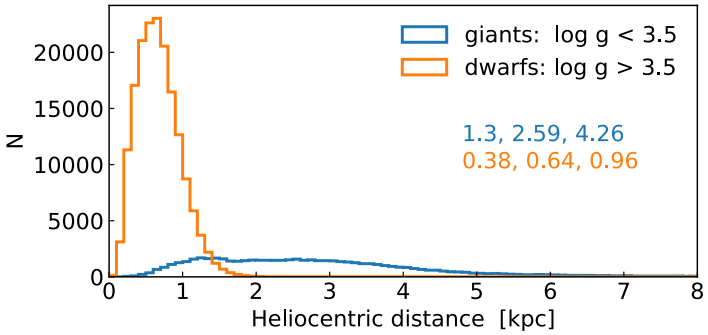

Figure 2.1: Distribution of distance for giants and dwarfs. The numbers denote the 16th, 50th and 84th percentile values. Stars shown are with distance error of less than 30% and `flag_cannon=0`. **Figure Credit:** Paper I.

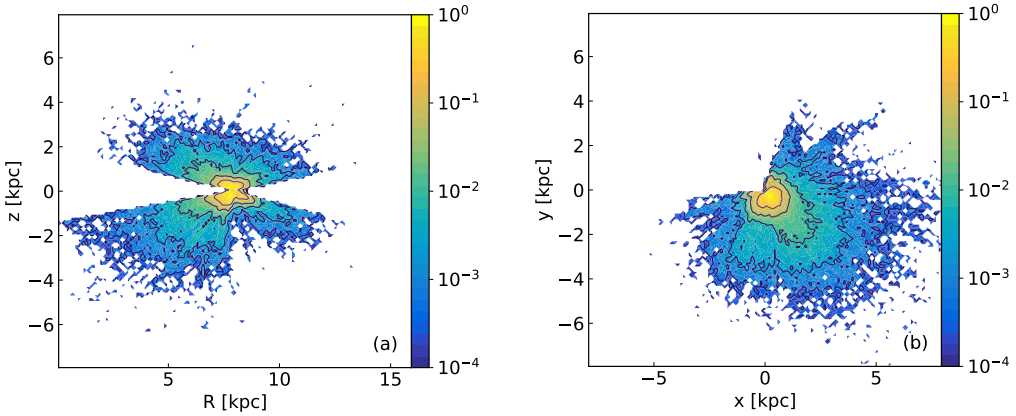

Figure 2.2: Distribution of stars in Galacto-centric (R, z) plane and heliocentric (x, y) plane (Galactic centre being at $(x, y) = (8, 0)$), colour coded by normalised stellar density. Stars shown are with distance error of less than 30% and `flag_cannon=0`. **Figure Credit:** Paper I.

2.2.4 OBSERVATIONS

Data for the GALAH survey are taken with the HERMES spectrograph on the 3.9-metre Anglo-Australian Telescope (AAT) at Siding Spring Observatory. HERMES is a fibre-fed high-resolution ($R = 28,000$) spectrograph optimised to do Galactic archaeology from a 4m-class telescope, with four discrete optical wavelength channels covering 4713–4903Å, 5648–5873Å, 6478–6737Å and 7585–7887Å (De Silva et al., 2015; Sheinis et al., 2015).

The 2dF top end for the AAT provides the fibre feed for HERMES (Lewis et al., 2002); its name derives from the two-degree diameter field of view. It has two metal field plates, each with 392 science fibres and 8 guide bundles. The fibres are affixed to magnetic "buttons" and placed on the field plate by a robotic fibre positioning system. While one field plate is being observed, the other is in position for setup by the positioning robot. The 2dF fibres are fed through the telescope structure to the HERMES enclosure

on the fourth floor of the AAT dome, where they are arranged into two pseudoslits, such that the set of fibres corresponding to the field plate that is currently being observed is fed into the spectrograph. Light from the fibres is collimated and then sent through a series of dichroic elements to separate the four wavelength channels. It is then dispersed using volume phase holographic diffraction gratings and imaged by four independently controlled cameras. Further details of instrument design, and its as-built performance, can be found in Barden et al. (2010), Brzeski et al. (2011), Heijmans et al. (2012), Farrell et al. (2014) and Sheinis et al. (2015).

The GALAH survey observations are carried out by team members, either at the AAT or from remote observing sites in Australia. The OBSMANAGER software developed by the team is used to select a field that will be near the meridian at the time of observation. This field is required to be at least 30 degrees from the Moon, to have a relatively small change in airmass over the exposure time, and to have no Solar System planets within it at the time of observation (as bright sources such as Jupiter have caused trouble with scattered light contaminating spectra in previous 2dF survey observations, though HERMES has been found to suffer much less from this than AAOmega; see Simpson et al., 2017). Fiducial targets, used for field acquisition and guiding, are chosen from the stars with $11 \leq V \leq 12$ in the input catalogue that are located in the field. For observations in bright mode fiducial are selected form stars with $12 \leq V \leq 13$. Once the observer chooses a field from the options provided by OBSMANAGER, it generates a list of targets in the correct input format for the CONFIGURE software (Miszalski et al., 2006), and it tracks which fields have been observed.

Figure 2.3 shows maps of GALAH DR2 stars (observed between 2014 January 16 and 2018 January 29) in equatorial and Galactic coordinates. The target selection can clearly be seen in the avoidance of the Galactic plane and of fields at high Galactic latitude where the target density is too low. Figure 2.4 shows the distribution of $V_{\rm JK}$ in DR2. The upper panel shows the overall distribution and subdivides the data into bright, regular and faint survey fields, and the lower panel is a cumulative histogram.

CONFIGURE uses a simulated annealing algorithm to identify a set of target allocations for the 2dF fibres that maximises the number of science targets observed and the number of fiducial targets used for field alignment and guiding. It then places a user-defined number of fibres on sky locations, follows user-defined target priorities and obeys restrictions on fibre placement (as an example, because of the size of the 2dF buttons, the minimum fibre spacing is 30 arcsec, although the fibres themselves have a field of view of only 2 arcsec). The output of CONFIGURE is then passed to the 2dF fibre positioning robot, which places the fibres serially onto the currently unused field plate, checking that each is within an acceptable tolerance of its intended position. Field setup typically takes 40 minutes for a full 400-target field, and essentially no survey observing time is lost waiting for reconfiguration.

As discussed in Martell et al. (2017), the exposure time is set to achieve a signal to noise ratio (SNR) of 100 per resolution element, at an apparent magnitude of 14 in the Johnson/Cousins filter closest to each bandpass. For regular survey fields, the standard procedure is to take three 1200-second exposures. If the seeing is between 2" and 2"5,

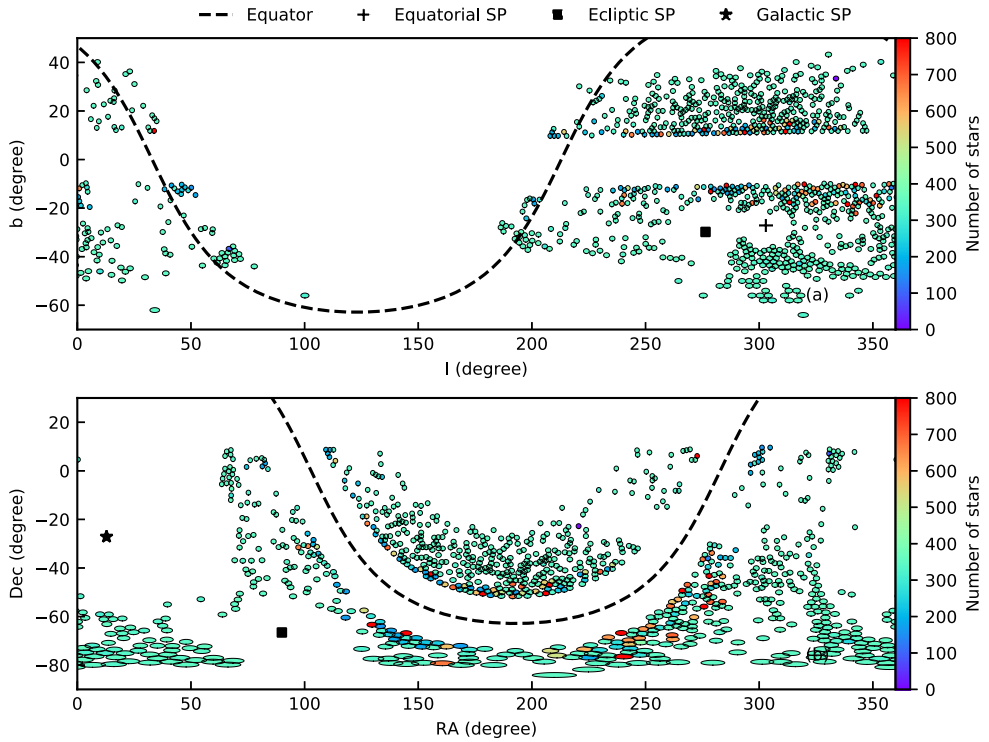

Figure 2.3: Distribution of observed GALAH fields in Galactic and Equatorial coordinates. The fields are color coded by the number of observed stars. The bold dashed line corresponds to equatorial (upper panel) and Galactic (lower panel) equators. The equatorial, the ecliptic, and the Galactic south poles are also marked as black symbols on the panels. **Figure Credit:** Paper I.

this is extended to four exposures, and to six exposures, if the seeing is between 2"5 and 3". For bright fields, three 360 s exposures are taken. Figure 2.5 shows cumulative distributions for SNR *per pixel* in each of the four HERMES channels. With about four pixels per resolution element, the SNR per resolution element is almost twice what is shown in Figure 2.5.

Fibre flat fields and ThXe arc exposures, both with exposure times of 180s, are taken along with each science field. Including the readout time of 71 s and a slew and acquisition time of 2–5 min per field, the time spent on overheads is roughly 20% of the time spent acquiring science data. The typical data rate in survey fields is 4.2 stars per on-sky minute. The GALAH survey has typically been awarded 35 nights per semester since 2014 February, secured across a number of competitive time-allocation rounds.

2.2.5 DATA REDUCTION

We use a reduction pipeline designed specifically for the GALAH survey, where steps are tailored to the observing strategy and scientific requirements of the survey. The reduction pipeline is described in detail in a separate paper (Kos et al., 2017) with only a short overview given here.

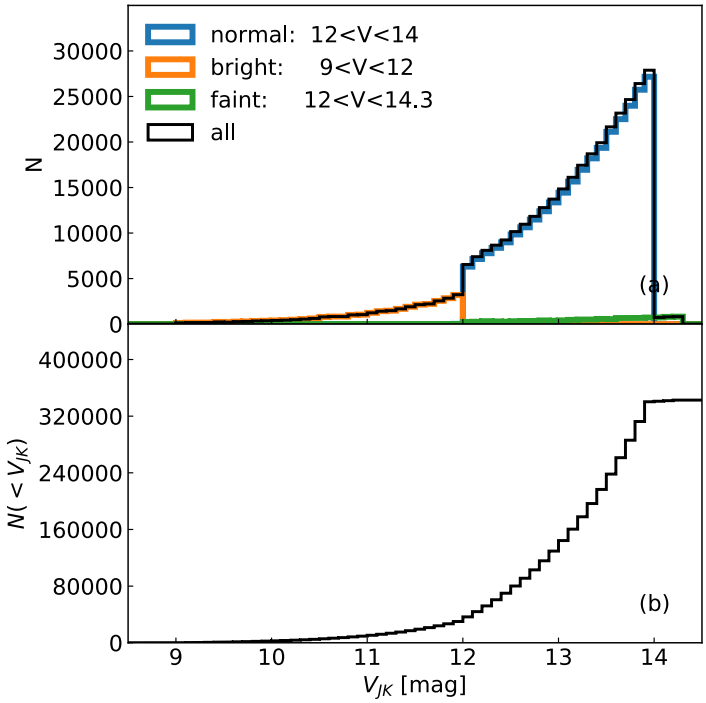

Figure 2.4: Distribution of V band magnitude of GALAH stars. The distributions for normal, bright and faint fields are shown separately. **Figure Credit:** Paper I.

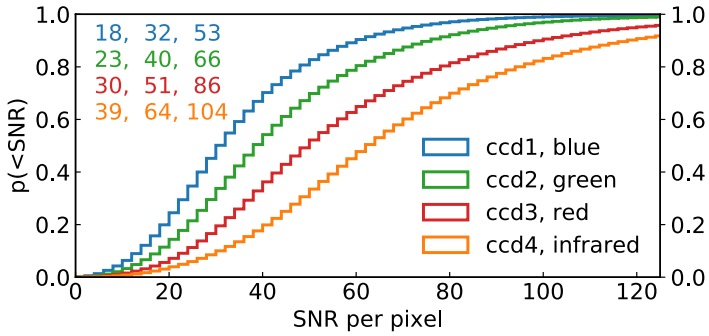

Figure 2.5: Distribution of SNR per pixel for the different HERMES wavelength bands. The numbers in the upper left corner denote the 16th, 50th and 84th percentile values. **Figure Credit:** Paper I.

Raw images are corrected for the bias level using a series of bias frames taken every night. One flat field exposure is taken for each science field, which is used to identify damaged columns and pixels, serves as a reference to find spectral traces on the science images, and supports the measurement of scattered light and fibre cross-talk.

After cosmetic corrections, the cosmic rays are removed utilizing a modified LaCosmic algorithm (Van Dokkum, 2001). Before the extraction of the spectra, a

geometric transformation is used to correct some basic optical aberrations. This reduces the variation of resolving power between different fibres and different wavelength regions.

To ensure the most accurate analysis of our data, we have refined the previously measured literature wavelengths for the ThXe arc lamp. The wavelength fitting algorithm has been improved since the publication of Kos et al. (2017), so it now learns the trends and instabilities in the wavelength calibration to predict a better solution when arc lamp spectra are hard to identify. We have to rely on weak lines in the ThXe arc lamp spectrum to calibrate the wavelengths. These are hard to measure in low throughput fibres, so the wavelength calibration for some fibres and some wavelength regions was suboptimal in previous reductions.

The sky spectrum is modelled from $\sim$ 25 dedicated sky fibres over the whole 2° focal plane. After the sky spectrum is subtracted, a telluric absorption spectrum is calculated using MOLECFIT software (Kausch et al., 2015; Smette, A. et al., 2015) and the science spectra are corrected.

The products of the reduction pipeline are unnormalized and normalized spectra, together with an uncertainty spectrum and a resolution map.

At the end of the reduction pipeline we calculate basic stellar parameters for all reduced objects. Radial velocities `rv_synt` and their errors `e_rv_synt` are computed by cross-correlating reduced spectra with 15 synthetic AMBRE spectra (De Laverny et al., 2012). Barycentric corrections are applied to the spectra (Kos et al., 2017). Barycentric radial velocities are measured independently in the blue, green and red channels, which are weighted to yield one radial velocity with its uncertainty. Such radial velocities are precise enough for most of the following analysis. First they are used for a continuum normalization calculated from regions minimally affected by spectral lines. Normalized spectra are then shifted to rest-frame wavelength and matched with 16783 synthetic AMBRE spectra to estimate initial values of effective temperature $T_{\rm eff}$, surface gravity $\log g$, and metallicity [M/H] for the subsequent detailed spectral analysis.

2.2.6 OVERVIEW OF DATA RELEASES

Since the commissioning of the HERMES spectrograph in 2013, the GALAH collaboration was awarded with more than 300 nights of observations. While observations are ongoing, the collaboration is releasing parts of the products to the public. Until now, four major releases (GALAH DR1, TESS-HERMES DR1, K2-HERMES DR1, and GALAH DR2) and one smaller release as part of the GALAH+TGAS analysis by **Paper II** were published. Because the important information for each release is presented in the accompanying release papers, only brief summaries will be given below to give an overview.

GALAH Data Release 1 The first GALAH DR was published in September 2016, just before the publication of *Gaia* DR1. It included the stellar parameters $T_{\rm eff}$, $\log g$, [Fe/H], $v_{\rm rad}$ as well as [α/Fe] for 10680 observations, of which 9860 were taken of stars contained in the Tycho-2 catalog (Høg et al., 2000) and hence expected to have parallax information from the TGAS as part of *Gaia* DR1.

TESS-HERMES DR1 The Transiting Exoplanet Survey Satellite (TESS) is a high-precision survey aiming to provide time-series photometry for millions of stars. With this photometric information it will be possible to detect planets, but also explore stellar rotation and asteroseismology, which can help to reach the highest precision and accuracy for stellar parameters like mass, radius and surface gravity possible to date. For their estimation however, additional information like effective temperatures are necessary, which can be delivered by spectroscopic surveys (see e.g. Pinsonneault et al., 2014). The TESS-HERMES survey is aiming to provide this information from spectra of the HERMES spectrograph for stars that will be observed by TESS. TESS DR1 (Sharma et al., 2018) provides stellar parameters $T_{\rm eff}$, $\log g$, [Fe/H], $v \sin i$, and $v_{\rm micro}$ for 16,000 dwarf and subgiant stars in TESS' southern continuous viewing zone.

K2-HERMES Data Release 1 In a similar fashion to TESS, the K2 mission, a successor of the Kepler mission with the same telescope, provides long and short cadence photometric information for several fields along the ecliptic plane. K2-HERMES DR1 (Wittenmyer et al., 2018) included 46 stars hosting 57 K2 candidate planets in K2 Campaigns 1–3.

The GALAH+TGAS analysis The analysis of the overlap of GALAH+TGAS (**Paper I**) is not a major survey release, but because of its nature as a pilot study to test the improvement of stellar parameters by including non-spectroscopic information, most notably *Gaia* parallaxes, it is important to mention. The spectrum synthesis analysis pipeline that was set up to analyse this overlap, was later applied to a large fraction of the training set for GALAH DR2.

GALAH Data Release 2 The second data release of the GALAH survey (**Paper I**) included the first individual element abundances. With up to 23 abundances for up to 342,682 it became the largest data set of high-precision chemical abundances to date.

GALAH Data Release 3 The third data release of GALAH (**Paper IV**)is not yet published, but will be the first data set that includes high-quality 6D information for most of its stars. This made it possible for the GALAH collaboration to include parallax information in the spectroscopic analysis of almost all stars and hence significantly improve the accuracy of the retrieved stellar parameters, as will be described in Chapter 2.4.

2.2.7 Analysis strategies used for the Data Releases

As outlined in Sec. 1.3.3.1, the analysis of large amounts of data is becoming an increasingly difficult task. Whereas smaller pilot studies, like the ones by Bensby et al. (2014) or **Paper II** can still be performed with larger computational costs per individual spectrum and still allow individual inspections of spectra and fitting results, the number of spectra for GALAH DR2 (342,682 spectra) is computationally expensive, especially if the analysis pipeline is still in development.

Because of the large volume of data, a new data analysis approach was used for most of the GALAH survey analysis so far, which has proven successful when dealing with very large datasets: train a data-driven approach on physics-driven input to connect data (spectra) with labels (in our case stellar parameters and element abundances) and then propagate this information onto the whole sample.

The applied analyses strategies for the different data releases of the GALAH collaboration are listed in Table 2.1 and include either the spectrum synthesis tool Spectroscopy Made Easy (Piskunov & Valenti, 2017) or a combination of the same with the data-driven tool *The Cannon*.

Table 2.1: Applied analyses strategies for the different data releases of the GALAH collaboration. SME stands for Spectroscopy Made Easy (Piskunov & Valenti, 2017), the tool used for a physics/model-driven analysis. *The Cannon* stands for the eponymous tool (Ness et al., 2015) used for a data-driven analysis.

Data release	Reference	Analysis strategy	Incl. *Gaia*?
GALAH DR1	Martell et al. (2017)	SME[1] + *The Cannon*[2]	None
TESS-HERMES	Sharma et al. (2018)	SME[1] + *The Cannon*[2]	None
K2-HERMES	Wittenmyer et al. (2018)	SME[1] + *The Cannon*[2]	None
GALAH+TGAS	**Paper II**	SME[3]	*Gaia* DR1
GALAH DR2	**Paper I**	SME[4] + *The Cannon*[2]	*Gaia* DR1
GALAH DR3	**Paper IV**	SME[5]	*Gaia* DR2

Notes: [1] See Sec. 2.3.1 for further details, but neglect the additional text on non-spectroscopic $\log g$ estimation, because $\log g$ was fitted like the other stellar parameters. [2] See Sec. 2.3.2 for further details. [3] The analysis is similar to the one in Sec. 2.3.1, but described in more detail in Sec. 3.3. [4] See Sec. 2.3.1 for further details. [5] The analysis is similar to the one described in Sec. 2.3.1, but described in more detail in Chapter 2.4.

2.3 SPECTROSCOPIC ANALYSES PRIOR TO *Gaia* DR2

As outlined in the last section, several spectroscopic analyses approaches can be chosen, which typically either involve the classical physics-driven spectral analysis or a combination of it with a data-driven tool.

For the latest and most advanced analysis run of the GALAH collaboration, GALAH DR2, a training set of 10605 stars was created and stellar labels estimated through detailed spectrum synthesis using the code Spectroscopy Made Easy (Section 2.3.1), investing much effort ensuring that the inferred stellar parameters and abundances are trustworthy (e.g. line selection, atomic/molecular data, blends, non-LTE effects). Subsequently, spectral models were created with *The Cannon* and used to propagate the information from the training set on to the whole survey (Section 2.3.2). This approach makes the implementation of a flagging algorithm vital, because *The Cannon* in its current form will always produce label estimates, which then have to be vetted as we describe in Section 2.3.3.

2.3.1 SPECTRUM SYNTHESIS ANALYSIS WITH SPECTROSCOPY MADE EASY

For the model-driven analysis, we use the spectral synthesis code SME (*Spectroscopy Made Easy*) v360 (Valenti & Piskunov, 1996; Piskunov & Valenti, 2017). SME performs

spectrum synthesis for 1D stellar atmosphere models, which in our case for DR2 consist of MARCS theoretical 1D hydrostatic models (Gustafsson et al., 2008); we use spherical symmetric stellar atmosphere models for $\log g \leq 3.5$ assuming $1 M_{\odot}$ and plane-parallel models otherwise. While the radiative transfer in SME is typically carried out under the assumption of LTE, it is possible to provide departure coefficients for level populations calculated elsewhere; we make use of this feature in the GALAH survey in order to derive accurate stellar parameters and elemental abundances as free of systematic errors as possible. For DR2 we incorporate non-LTE line formation for several key elements, including Li (Lind et al., 2009), O (Amarsi et al., 2016a), Na (Lind et al., 2011), Mg (Osorio et al., 2015), Al (Nordlander & Lind, 2017), Si (Amarsi & Asplund, 2017), and Fe (Amarsi et al., 2016b), mostly with additional dedicated calculations in addition to those previously published. In all cases the non-LTE computations have been performed using exactly the same grid of 1D MARCS model atmospheres. Future GALAH data releases will have additional elements treated in non-LTE.

In addition to providing a formal solution of the radiative transfer, SME attempts to find the optimal solution for various free parameters specified by the user; we use this feature to estimate the stellar parameters of the GALAH targets, allowing $T_{\rm eff}$, $\log g$, [Fe/H], [X/H], V_{broad} (spectral line broadening, consisting of the combined effects of macroturbulence and rotation), v_{rad} and continuum normalisation to vary during the optimisation process.

We have carefully selected the most reliable atomic lines within the HERMES wavelength regions to ensure accurate determination of the stellar parameter and abundances for the analysis of late-type stars. The line-list selection was originally done in conjunction with the corresponding compilation for the *Gaia*-ESO survey (Heiter et al., 2015b). Our guiding principle has been to include only spectral lines that both have reliable atomic data and be as little affected by blending lines as possible. Naturally this dramatically limits the number of spectral features to be used in late-type stellar spectra, since the majority of lines are either blended to various extent and/or lack good atomic data, especially transition probabilities. The selection of lines to employ was initially based on a detailed comparison of the predicted spectrum against observations for the Sun and Arcturus but also tested for other benchmark stars. Whenever possible, experimental oscillator strengths are used if trustworthy, but for some lines used as elemental abundance diagnostics we have had to resort to more or less uncertain theoretical transitional probabilities in the absence of better alternatives. Astrophysical calibration of f-values was not performed. In addition to the primary line list for abundance purposes we have included background blending lines, which have largely been taken from the *Gaia*-ESO linelist; in several cases we have updated the oscillator strengths ($\log gf$) empirically compared to those in the *Gaia*-ESO master linelist in order to provide better agreements between observed HERMES spectra and the predicted stellar spectrum for stars.

To determine stellar parameters, we make use of the $T_{\rm eff}$-sensitive Hα and Hβ lines (e.g. Amarsi et al., 2018) and neutral/ionized lines of Sc, Ti, and Fe; the latter elements provide constraints on the effective temperature and surface gravity $\log g$

through excitation and ionisation balance as well as metallicity. SME first synthesises the initial model based on radial velocities from the reduction process and a set of initial stellar parameters. If available and not flagged, stellar parameters from a prior version of *The Cannon* (version 1.3) are chosen. This version was also used for previous data releases of GALAH (Martell et al., 2017), TESS-HERMES (Sharma et al., 2018), and K2-HERMES (Wittenmyer et al., 2018). If these parameters are flagged or not available, the synthesis commences with the stellar parameter estimates from the reduction process. If these are also flagged, we start from an arbitrary set of stellar parameters ($T_{\rm eff}$ = 5000 K, $\log g$ = 3.5 dex, and [M/H] = −0.5 dex).

We then use two main iteration cycles in SME to optimise the parameters, unless we have to use the arbitrary set of stellar parameters, in which case the second iteration cycle is repeated. In the first cycle, each wavelength segment of typically 10 Å is normalized using a linear function, which is adequate for the short wavelength intervals used here. SME then computes synthetic spectra in 46 selected (masked) regions. The free parameters $T_{\rm eff}$, $\log g$, [M/H][2], ξ_t (micro turbulence), $v \sin i$ (rotational velocity)m and radial velocity ($v_{\rm rad}$) are simultaneously determined. SME uses the Levenberg-Marquardt algorithm to find parameters that correspond to the near-minimum χ^2.

The final parameters from the first cycle are used to synthesise the initial model in the second cycle and re-normalize each segment. SME goes through the same iteration process, optimising χ^2 until convergence is achieved (when χ^2 changes by less than 0.1%). The number of iterations necessary to reach convergence varies from star to star. Typically, more metal-rich and cooler stars take longer to converge, but normally still do so in less than 20 iterations. During the parameter determination, we implement non-LTE departure coefficients from Amarsi et al. (2016b) for Fe lines.

While the nominal resolving power of HERMES is $R \approx 28000$, it is known to vary from fibre to fibre, and as a function of wavelength (Kos et al., 2017). This issue is resolved by interpolating the observed spectrum with pre-computed resolution maps from Kos et al. (2017) to estimate a median resolution for each segment. The GALAH survey is currently implementing a photonic comb, which will map the aberrations and point-spread-function across the full CCD images (Bland-Hawthorn et al., 2017).

2.3.1.1 CONSTRAINTS ON SPECTRAL LINE BROADENING

The resolving power and SNR of GALAH spectra are not adequate to separate the projected rotational velocity ($v \sin i$) and macroturbulence ($v_{\rm mac}$) due to degeneracies in their line broadening. When both $v \sin i$ and $v_{\rm mac}$ are allowed as free parameters the results show greater scatter and poorer convergence performance. Therefore, we solve for $v \sin i$ and set all $v_{\rm mac}$ values to zero. This effectively incorporates $v_{\rm mac}$ into our $v \sin i$ estimates, hereafter used as $v_{\rm broad}$.

Similarly, setting micro-turbulence (ξ_t) as a free parameter causes additional scatter in the results. While micro-turbulence is updated in every iteration, it is dictated by the empirical formulae that have been calibrated for the LUMBA node of the *Gaia*-ESO

[2]SME returns the iron abundance of the of the best-fit model atmosphere and spectrum during the parameter determination stage, which is called metallicity, or [M/H].

survey (Smiljanic et al., 2014), which uses a similar SME-based analysis pipeline to ours. For cool main sequence stars ($T_{\rm eff} \leq 5500$K; $\log g \geq 4.2$):

$$\xi_t = 1.1 + 1.6 \times 10^{-4} \times (T_{\rm eff} - 5500), \tag{2.2}$$

For evolved and hotter stars ($T_{\rm eff} \geq 5500$K; $\log g \leq 4.2$):

$$\xi_t = 1.1 + 1.0 \times 10^{-4} \times (T_{\rm eff} - 5500) + 4 \times 10^{-7} \times (T_{\rm eff} - 5500)^2 \tag{2.3}$$

where ξ_t is given in km s^{-1} and $T_{\rm eff}$ in K.

Since macroturbulence (and microturbulence) is reflecting convective motions and oscillations in the stellar atmosphere (Asplund et al., 2000) those velocities are typically limited to < 10 km/s for late-type stars (Gray, 2008). For greater v_{broad}, the broadening is dominated by rotation, which is normally the case for $T_{\rm eff} \gtrsim 7000$ K.

2.3.1.2 CONSTRAINTS ON SURFACE GRAVITY

There are few unblended ionized lines of suitable strength in HERMES spectra, making a fully spectroscopic surface gravity determination a challenge; we note that the HERMES spectrograph and GALAH survey were designed with the expectation that parallaxes from *Gaia* would provide superior surface gravities in general. For dwarf stars cooler than about 4500 K the purely spectroscopic surface gravities are underestimated, causing an 'up-turn' in the lower stellar main sequence. This is a common shortcoming in stellar spectroscopic studies relying on excitation and ionisation balance in the framework of LTE spectral line formation in 1D stellar atmosphere models (e.g. Yong et al., 2004; Bensby et al., 2014; Aleo et al., 2017). The cause for this breakdown of 1D LTE ionisation balance has not yet been identified.

To help improve the accuracy of the $\log g$ determination, the GALAH survey observed fields that are in the HIPPARCOS (Perryman et al., 1997; van Leeuwen, 2007) and *Tycho-Gaia* Astrometric Solution (TGAS) catalogues and within the K2 footprint, to provide spectra with parallax and asteroseismic information (Perryman et al., 1997; Brown et al., 2016; Stello et al., 2017). These are then used to determine $\log g$ during the parameter optimisation process.

For stars with asteroseismic information, surface gravity is not strictly a free parameter, but is determined at each SME iteration with respect to solar values using the scaling relation (Kjeldsen & Bedding, 1995):

$$\nu_{\rm max} = \nu_{\rm max,\odot} \frac{g/g_\odot}{\sqrt{T_{\rm eff}/T_{\rm eff,\odot}}} \tag{2.4}$$

Here $\nu_{\rm max}$ is the measured frequency at maximum power.

For stars with reliable parallax information, the surface gravity is updated at each SME iteration using the fundamental relation (Nissen et al., 1997; Zhang & Zhao, 2005):

$$\log \frac{g}{g_\odot} = \log \frac{\mathcal{M}}{\mathcal{M}_\odot} - 4 \log \frac{T_{\rm eff}}{T_{\rm eff,\odot}} + 0.4\,(M_{\rm bol} - M_{\rm bol,\odot}) \tag{2.5}$$

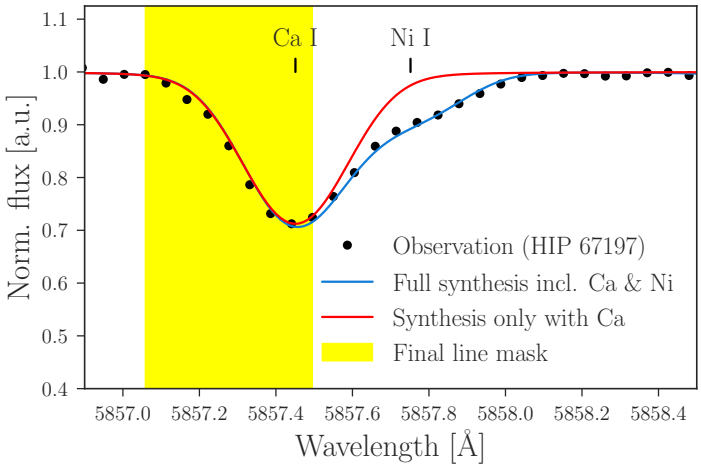

Figure 2.6: Example for the blending test as part of the abundance estimation for the Ca I at 5857 Å line in HIP 67197. The black dots show the observed spectrum with a Ca I line, partially blended with a Ni I line. Syntheses with all lines (blue) and only calcium (red) show that the red wing of the Ca I line for this particular star is strongly blended. Hence the line mask (yellow) is adjusted to only include this region for the calcium abundance determination. **Figure Credit:** **Paper I**.

where

$$M_{\rm bol} = K_S + BC_{K_S} - 5\log D_\varpi + 5. \tag{2.6}$$

Here the mass $\mathcal{M}$ of each star is estimated with the age estimation code ELLI (Lin et al., 2018) using 2MASS photometry and parallaxes from Hipparcos or *Gaia*. For the absolute bolometric magnitude $M_{\rm bol}$, bolometric corrections (BC) from Casagrande & VandenBerg (2014) are applied to the 2MASS K magnitude. For all stars from the HIPPARCOS catalogue, the distance D_ϖ is computed by the transformation $D = 1/\varpi$ with ϖ being the parallax. For all stars from the TGAS catalogue, Bayesian distances from Astraatmadja & Bailer-Jones (2016) are used. For more details on the use of astrometry for the GALAH+TGAS overlap, we refer the reader to **Paper II**.

2.3.1.3 ELEMENTAL ABUNDANCES

After the atmospheric parameters have been established, we apply corrections of the biases estimated in Section 2.3.3.3 (shift of +0.15 dex for purely spectroscopic $\log g$ and +0.1 dex for all metallicities) and then fix them for abundance determination. The lines of each element are synthesised, and line blending is modelled using the atomic and molecular information provided. The blended wavelength points are excluded from the line mask (see Figure 2.6).

The element lines used for this data release were initially selected from the lines identified by Hinkle et al. (2000) within spectra of the Sun and Arcturus, but carefully vetted in order to be strong enough across the parameter range, have line data based on laboratory measurements, and blend-free, if possible. Therefore, we only use a subset

(marked in black in the line region overview of Figure 2.7) of the lines from Hinkle et al. (2000), indicated as blue regions, to measure element abundances.

We define lines as detected, when the line is deeper than 3σ of the flux error within the line mask, and at least 5% below the continuum flux, otherwise the measurement is considered an upper limit. Additionally, we require the measurement error to be less than 0.3 dex, be based on at least 3 data points, and neglect the measurements if it is above an empirically calibrated SNR-dependent χ^2-limit.

Abundance ratios are given in bracket notation as [X/Fe]. To minimize systematic errors and to calibrate the solar zero point, we analysed HERMES twilight spectra with the same SME set-up as other spectra and compute solar-relative abundances,

$$[\mathrm{X/H}] = \mathrm{A(X)} - \mathrm{A(X)}_\odot \tag{2.7}$$

where $\mathrm{A(X)}_\odot$ is the measured abundance from our solar spectra. Elemental abundance ratios are then defined as

$$[\mathrm{X/Fe}] = [\mathrm{X/H}] - [\mathrm{Fe/H}]. \tag{2.8}$$

These may be converted back to absolute values ($\mathrm{A(X)}^{\mathrm{A+09}}$) on the absolute abundance scale of Asplund et al. (2009) by computing

$$\mathrm{A(X)}^{\mathrm{A+09}} = [\mathrm{X/Fe}] + [\mathrm{Fe/H}] + \mathrm{A(X)}_\odot^{\mathrm{A+09}}. \tag{2.9}$$

The values of the solar abundances $\mathrm{A(X)}_\odot$ measured with GALAH as well as the reference values from Grevesse et al. (2007) that are adopted in the MARCS atmosphere grids and the solar composition $\mathrm{A(X)}_\odot^{\mathrm{A+09}}$ from Asplund et al. (2009) are given in Table 2.2. We note that both reference compositions are very similar with the latter being more recent and commonly used.

We report the individual abundances of α-elements, but also include an error-weighted combination of unflagged abundances of the elements Mg, Si, Ca, and Ti reported as

$$[\alpha/\mathrm{Fe}] = \frac{\sum_\mathrm{X} \frac{[\mathrm{X/Fe}]}{(\mathrm{e\_[X/Fe]})^2}}{\sum_\mathrm{X} (\mathrm{e\_[X/Fe]})^{-2}}, \text{ where X = Mg, Si, Ca, Ti} \tag{2.10}$$

We recommend this definition, because the different elements are estimated with different precisions and a simple average would hence lead to a less precisely estimated [α/Fe]. We note, however, that because Ti is typically the most precisely measured element among these four α-elements, the combined [α/Fe] is mainly tracing Ti. [α/Fe] is reported also for stars where one or more of Mg, Si, Ca, and Ti is not available.

Although HERMES spectra in principle cover a large variety of element lines, their strength varies with the abundance of the element itself, but also the line properties and the stellar parameters. For this reason, we can not detect all elements equally well in all stars from the GALAH spectra. To visualise this, we show Kiel diagrams for the four elements Li, O, Al, and Eu in Figure 2.8, where we color each point by the depth of the strongest line of the respective element. For example, the majority of stars only show weak Li lines. However, both in warm dwarfs and several cool giants, it can be detected. For this element, we have added stars to the training set with detectable high Li projected

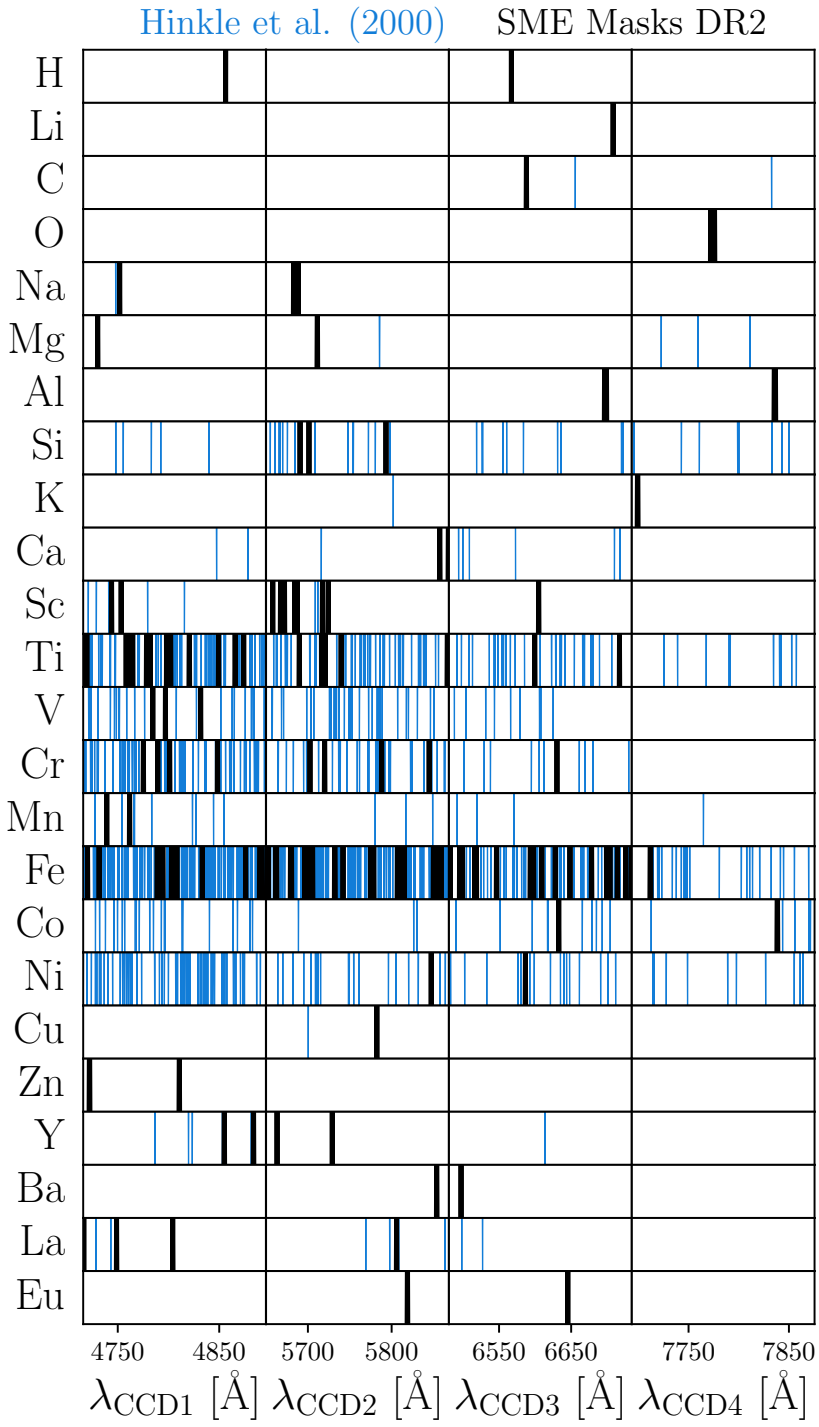

Figure 2.7: Visualisation of the element lines within the GALAH wavelength range. Blue regions indicate the lines identified by Hinkle et al. (2000) in the Sun and Arcturus, including weak and blended lines. The subset of these regions used for the SME and *The Cannon* analysis are indicated as black regions. **Figure Credit:** Paper I.

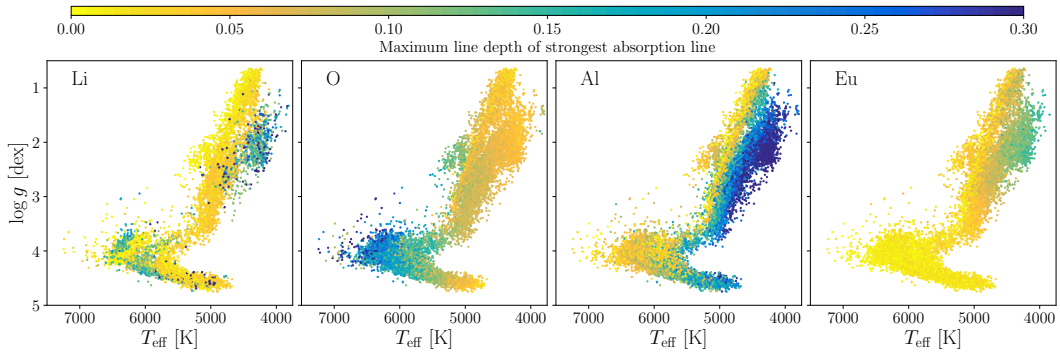

Figure 2.8: Visualisation of the parameter dependence of line strengths for the four elements Li, O, Al, and Eu. Shown are Kiel diagrams coloured by the maximum normalized absorption line depth within the used masks of the four elements, ranging from 0 to 0.3. For clarity, we truncated the plotted line strength at 0.3. These panels show that Li can not be measured in most stars (except hot dwarfs and especially Li-rich stars), while O has strong lines in hotter dwarfs and Al lines are very strong in cool, metal-rich giants. Eu is, similar to most neutron-capture elements within the GALAH range, almost exclusively detectable in giants. **Figure Credit:** Paper I.

Table 2.2: Comparison of solar abundances (A(X)) with respect to the standard composition of MARCS model atmospheres (Grevesse et al., 2007) and the solar photospheric abundances by Asplund et al. (2009).

X	$A(X)_\odot$	Grevesse et al. (2007)	Asplund et al. (2009)
Li	0.95 ± 1.00	1.05 ± 0.10	1.05 ± 0.10
C	8.50 ± 0.23	8.39 ± 0.05	8.43 ± 0.05
O	8.85 ± 0.04	8.66 ± 0.05	8.69 ± 0.05
Na	6.10 ± 0.04	6.17 ± 0.04	6.24 ± 0.04
Mg	7.54 ± 0.03	7.53 ± 0.09	7.60 ± 0.04
Al	6.45 ± 0.03	6.37 ± 0.06	6.45 ± 0.03
Si	7.45 ± 0.04	7.51 ± 0.04	7.51 ± 0.03
K	5.50 ± 0.05	5.08 ± 0.07	5.03 ± 0.09
Ca	6.36 ± 0.06	6.31 ± 0.04	6.34 ± 0.04
Sc	3.12 ± 0.04	3.17 ± 0.10	3.15 ± 0.04
Ti	4.89 ± 0.02	4.90 ± 0.06	4.95 ± 0.05
V	3.93 ± 0.55	4.00 ± 0.02	3.93 ± 0.08
Cr	5.62 ± 0.04	5.64 ± 0.10	5.64 ± 0.04
Mn	5.31 ± 0.03	5.39 ± 0.03	5.43 ± 0.04
Fe	7.40 ± 0.01	7.45 ± 0.05	7.50 ± 0.04
Co	4.91 ± 0.48	4.92 ± 0.08	4.99 ± 0.07
Ni	6.21 ± 0.04	6.23 ± 0.04	6.22 ± 0.04
Cu	4.03 ± 0.07	4.21 ± 0.04	4.19 ± 0.04
Zn	4.43 ± 0.04	4.60 ± 0.03	4.56 ± 0.05
Y	1.89 ± 0.09	2.21 ± 0.02	2.21 ± 0.05
Ba	2.18 ± 0.21	2.17 ± 0.07	2.18 ± 0.09
La	1.10 ± 0.11	1.13 ± 0.05	1.10 ± 0.04
Eu	0.58 ± 0.28	0.52 ± 0.06	0.52 ± 0.04

by the spectrum classification algorithm t-SNE (see Section 2.3.3.2), which show up as blue dots in the left panel of Figure 2.8. The O triplet shows strongest lines for hot dwarf and turn-off stars due to its high excitation potential, but is in general detectable across the whole parameter space. Al is usually detectable in cooler and metal-rich stars across the parameter space, but not always in warmer stars. Eu lines are in general not detectable for dwarfs with the GALAH setup, but are for giants. The training set therefore contains stellar parameters for all stars, but not all stars have abundance measurements for all elements.

2.3.2 DATA-DRIVEN PROPAGATION OF INFORMATION WITH *The Cannon*

We implement *The Cannon* as described in Ness et al. (2015), adopting a simple quadratic model with coefficients $\boldsymbol{\theta}_\lambda$, which describes the flux $f_{n,\lambda}$ of a given spectrum n with stellar labels $\boldsymbol{\ell}_n$:

$$f_{n,\lambda} = g\left(\boldsymbol{\ell}_n|\boldsymbol{\theta}_\lambda\right) + \text{noise} \tag{2.11}$$

We augment this procedure with a number of additional processing steps and derive many more labels than the original implementation. We interpolate all spectra of the survey on to a common wavelength grid of 14304 pixels and use the normalized spectra at rest from our reduction pipeline, see Section 2.2.5.

A limitation of the currently published versions of *The Cannon* is that all labels have to be known for each training set spectrum. For our reference objects, we have many stars that have a subset of the full number of the possible abundances measured. There are relatively fewer stars in the set of reference objects with all individual abundances measured. While efforts are being made to extend *The Cannon* in order to handle label errors or partially missing labels (Eilers et al., in preparation), we still have to rely on a different approach in this data release. We handle this issue of partial labels in the training set by creating an ensemble of models; one for each element [X/Fe]. We start with a training set for which all stellar parameters are known and train a model using these parameters only. We then use this model on the training set itself and re-derive the stellar parameter labels. We then exchange the labels of the initial training set with the re-derived labels. Then, for each element, X, we create a new training set by adding one more label, the element abundance [X/Fe], using only the subset of stars in the training set with this measured abundance. We therefore train a new model based on the six stellar parameter labels, plus one additional element label, and do this step for each element. In each case, for each model and each corresponding element, we restrict (mask) all coefficients with [X/Fe]-terms to be zero outside of pre-selected line regions of that element.

2.3.2.1 *The Cannon* MODEL FOR STELLAR PARAMETERS

Our training data are a high-fidelity set of stars with labels generated using SME, as described in Section 2.3.1. The final training set for stellar parameters of 10605 spectra consists of 21 *Gaia* benchmark stars, 12 stars overlapping with Bensby et al. (2014),

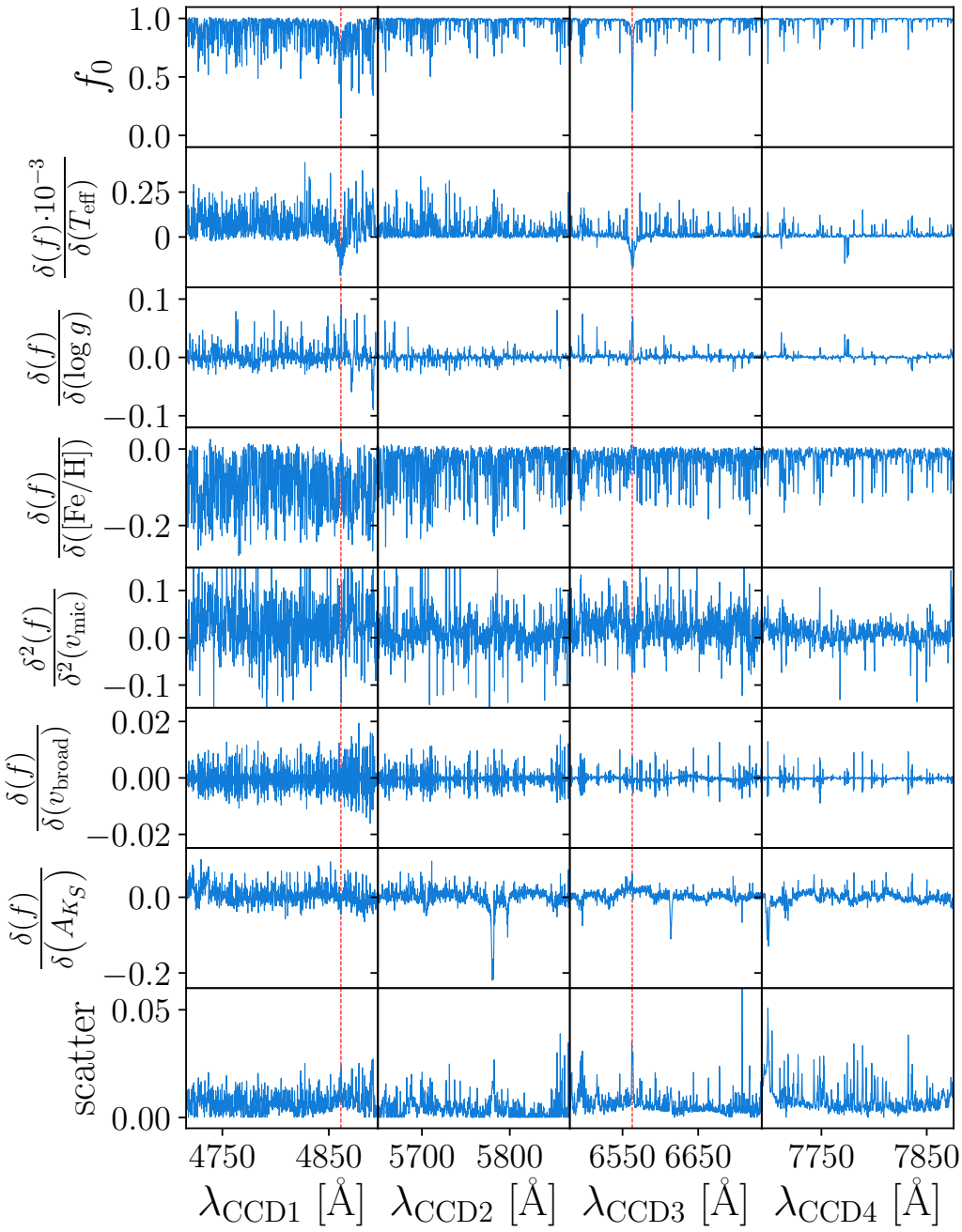

Figure 2.9: Linear coefficients of *The Cannon* model as a function of wavelength across the four HERMES wavelength regions. We show the spectrum f_0 with labels equivalent to the median of the training set and linear coefficients for five stellar labels. We also include the quadratic coefficient for microturbulence velocity, showing the same pattern as the molecular absorption bands and the scatter of the model. Red dashed lines indicate the Balmer lines. **Figure Credit:** Paper I.

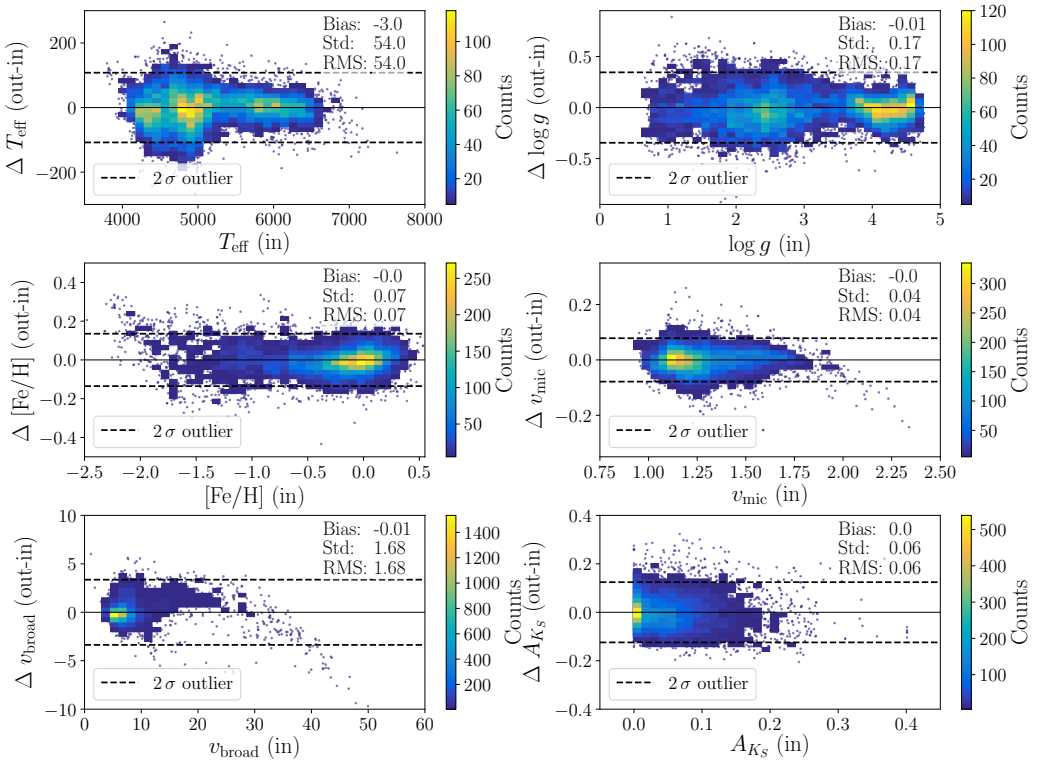

Figure 2.10: Comparison of training set labels from SME (input) and *The Cannon* interpolation (output) for the labels of the stellar parameter model, i.e. $T_{\rm eff}$, log g, [Fe/H], $v_{\rm mic}$, $v_{\rm broad}$, and A_{K_S}. **Figure Credit: Paper I.**

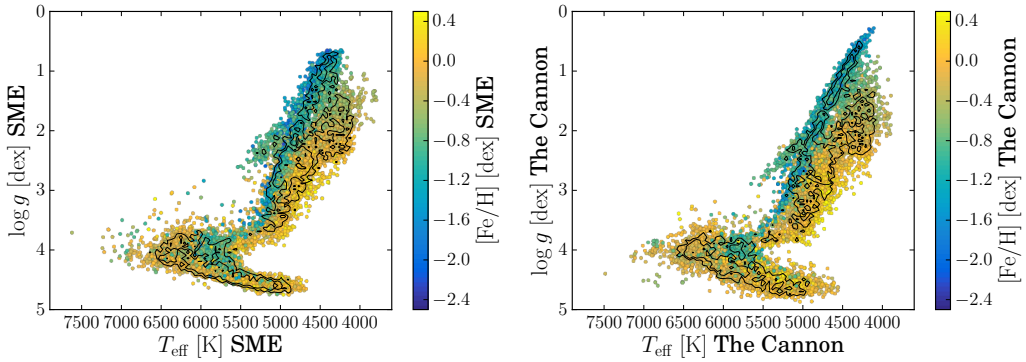

Figure 2.11: Kiel diagram for the GALAH DR2 training set as determined with SME (left; as input into *The Cannon*) and as reproduced by *The Cannon* (right). **Figure Credit: Paper I.**

77 stars with HIPPARCOS parallaxes, 3807 stars with TGAS parallaxes, 915 stars with asteroseismic information, 669 open or globular cluster stars as well as 1805 stars already included in previous training sets (Martell et al., 2017; Sharma et al., 2018; Wittenmyer et al., 2018). To ensure a sufficient coverage of parameter space for the training step, we expand the set with 1057 selected stars in the parameter range of [Fe/H] < -1.0, 1055 additional stars with $-1.0 <$ [Fe/H] < -0.5, 654 additional giants with $T_{\rm eff} < 5000$ K, $\log g < 2.0$ dex, and SNR > 125 in the green channel, 388 stars with projected high Li abundances based on the work by Traven et al. (2017), and 145 stars with SNR > 100 or SNR > 50 at $\log g < 2$ overlapping with APOGEE DR14. We stress that we excluded spectroscopic binaries from the training set, either based on previous automated stellar classifications, see Section 2.3.3.2 or via visual inspection of the training set spectra. The training set parameters span maximum ranges of $3800 \leq T_{\rm eff} \leq 7620$ K, $0.65 \leq \log g \leq 4.74$ dex, $-2.48 \leq$ [Fe/H] ≤ 0.53, $0.95 \leq v_{\rm mic} \leq 2.66\,{\rm km\,s^{-1}}$, and $1 \leq v_{\rm broad} \leq 106\,{\rm km\,s^{-1}}$.

We emphasise that we include more stars and labels than Ness et al. (2015) because our parameter space covers a much larger part of the HR-diagram than the RGB. The lines of the majority of the GALAH survey main sequence and turn-off stars, are in general significantly more broadened than in giants. Therefore, the model needs to be flexible enough to track these changes in the lines of the spectrum. We build our reference labels on similar parameters as the free parameters of the SME optimisation, i.e. $T_{\rm eff}$, $\log g$, [Fe/H], $v_{\rm mic}$, and v_{broad}.

Additionally, we found that it was important to include interstellar extinction $A_{\rm K}$, similarly to Ho et al. (2017b), as diffuse interstellar bands are present in the spectra. There is a degeneracy between abundance and extinction present if this label is not included. The values for $A_{\rm K}$ with a range of 0.0 to 0.4 mag are estimated from the RJCE method (Majewski et al., 2011). We note that Kos & Zwitter (2013) have shown that the ratio of the strength of diffuse interstellar bands to extinction is a function of the ultraviolet radiation field in the interstellar medium while Nataf et al. (2016) have demonstrated that this ratio also depends on the shape of interstellar extinction curve. In the future, we will calibrate these additional parameters to unprecedented precision with GALAH data.

For the stellar parameter estimation we use a quadratic model with six stellar labels, resulting in 22 coefficients for each of the 14304 pixels of *The Cannon* wavelength range, on to which we interpolate each spectrum. The linear coefficients of this model for the labels are shown in Figure 2.9 and indicate how the median flux f_0 of the training set (with median labels $T_{\rm eff} = 5114$ K, $\log g = 3.0$ dex, [Fe/H] $= -0.33$, $v_{\rm mic} = 1.28\,{\rm km\,s^{-1}}$, $v_{\rm broad} = 7.7\,{\rm km\,s^{-1}}$, and $A_{K_S} = 0.05$, respectively) changes with each of these labels. These linear coefficients are a good first diagnostic for the sensitivity of *The Cannon* regarding certain labels within the GALAH range, but the quadratic terms have to be taken into account as well for the full model spectrum. In Figure 2.12, we show two examples of GALAH observations and the model spectrum from *The Cannon*.

The panels in Figure 2.9 show that the effective temperature $T_{\rm eff}$ is strongly correlated with the strength of the two hydrogen Balmer lines (indicated by red dashed lines). We note also a strong connection between the O triplet in the IR arm and $T_{\rm eff}$. Many

ionized lines show positive correlations with the linear coefficient for $\log g$, while for example the Fe I lines around 4872 and 4891 Å show strong negative correlations, as expected due to their pressure broadened wings. The coefficient of [Fe/H] shows not only correlations with Fe, but is a tracer of metallicity itself and consequently responds to all lines since the abundances of all elements track each other to first-order; especially the blue channel is sensitive to the metallicity due to the preponderance of lines there. The linear coefficient for $v_{\rm mic}$ shows the strongest sensitivity in the blue channel. Because of the empirical, temperature-dependent relation used for this label with SME, $v_{\rm mic}$ is most sensitive to changes at the hot and cool end of the parameter space. To visualise this, we plot the quadratic coefficient of $v_{\rm mic}$, which shows the influence of molecular absorption bands in the spectrum for the coolest stars in the training set. The broadening label $v_{\rm broad}$ indicates positive correlations in the core of lines and negative ones in the wings, i.e., lines become broader with larger $v_{\rm broad}$ while maintaining the overall line strength. In a similar fashion to Ho et al. (2017b), our linear coefficient for A_{K_S} correlates strongly with the strength of the diffuse interstellar bands within the GALAH range (De Silva et al., 2015). We also show the scatter term of the model, which corresponds to regions not well described by the stellar labels, including telluric lines from imperfect corrections as well as the regions of the diffuse interstellar bands and the interstellar component of K I 7699. However, the scatter is in general very low (with a median around 0.01), suggesting that our model fits the data well.

We apply this best-fitting model to the training set spectra as a self-test and subsequently compare the stellar labels from SME with those estimated by *The Cannon* in Figure 2.10. *The Cannon* reproduces the labels of the training set with small biases and within a scatter of $\sigma(T_{\rm eff}) = 71\,{\rm K}$, $\sigma(\log g) = 0.25\,{\rm dex}$, $\sigma([{\rm Fe/H}]) = 0.1\,{\rm dex}$, $\sigma(v_{\rm mic}) = 0.06\ {\rm km\,s^{-1}}$, $\sigma(v_{\rm broad}) = 3.1\ {\rm km\,s^{-1}}$, and $\sigma(A_{K_S}) = 0.08\,{\rm mag}$. We note that although the Kiel diagrams of the input and output labels look very similar (see Figure 2.11), the scatter values are slightly larger than those of previous analyses (Martell et al., 2017; Sharma et al., 2018). While we have not yet found the reason for this, an explanation could be the expansion of the training set to cover a larger (and hence different) parameter space, including fast rotators ($v_{\rm broad} > 30\ {\rm km\,s^{-1}}$) and metal-poor stars, which stretches the flexibility of the quadratic model to its limits. Contrary to the previous models estimated with *The Cannon* for the GALAH survey, we do not fit [α/Fe] as part of the stellar parameters, as it would interfere with the subsequent estimation of individual α-element abundances, and because it did not significantly decrease the scatter of the label validation.

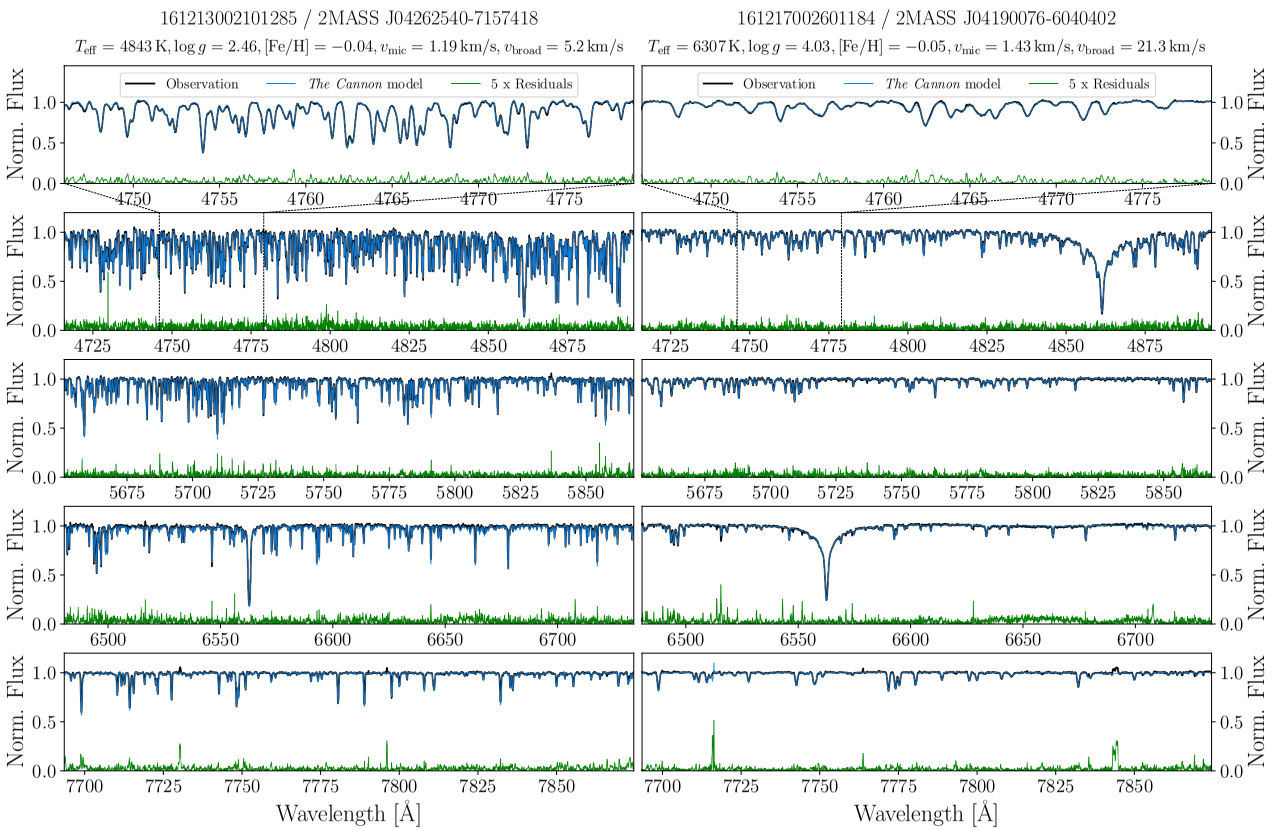

Figure 2.12: Spectra of the giant stars 2MASS J04262540-7157418 (left panels) and the dwarf star 2MASS J04190076-6040402 (right panels). Shown are the observed spectrum (black) as well as the model spectra from *The Cannon* (blue) and the magnified residuals (5 times larger in green) for different parts of the GALAH spectral range. The top panels show a magnification of a part of the blue arm (CCD 1), while the other panels show the spectral range of the four bands (CCD 1 to 4). *The Cannon* is only applied to the second half of the IR-arm. The agreement between the normalised observation and model are overall very good with mean residuals around 0.005. The largest residuals can typically be seen in regions with imperfect skyline and telluric line corrections in the observed spectrum. **Figure Credit:** Paper I.

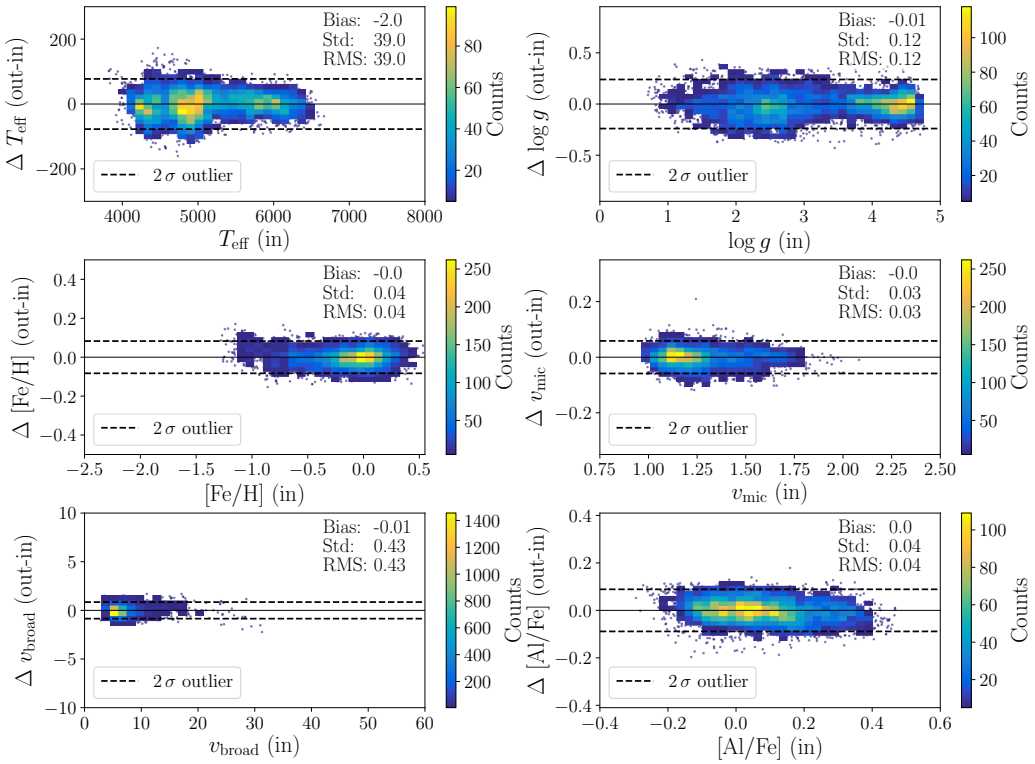

Figure 2.13: Self validation of *The Cannon* model for Al. **Figure Credit:** Paper I.

2.3.2.2 *The Cannon* MODELS FOR ELEMENT ABUNDANCES

We reiterate that we use an ensemble of models to infer our elements, based on the six stellar parameters plus one additional element, for all elements. For each training set for each model, we only include those stars in the individual models which have abundance detections for the respective element. Table 2.3 summarises the relative fractions of stars in the training set with each element measurement. For each model, we exchange the stellar parameters of SME with those from the self test, before using this model at test time to estimate the individual element abundance. This introduces a minor perturbation to the model (and the stellar labels are slightly different, within the error of the inference). We confirm that the perturbation is minor; the scatter term of the labels from the self test is significantly smaller than before the exchange of stellar parameter labels, see for example the self validation for Al in Figure 2.13.

We emphasise that we have chosen to restrict the abundance determination to use only lines of each element being inferred. We therefore restrict *The Cannon's* model to use only certain wavelength regions for each element inference (e.g. for [O/Fe] we use the pixels of the O I 7771-5 Å triplet). This masking is achieved by setting the element-dependent coefficients of the model to zero outside specified regions.

The masks we use for the individual elements are the same as for SME, see Section 2.3.1.3. This differs from the regularised approach of Casey et al. (2016), where

Table 2.3: Training set size for individual *The Cannon* abundance models, compared to the stellar parameter model with 10605 spectra.

Model	Nr. of spectra (%)	Model	Nr. of spectra (%)
Li	1652 (16%)	V	3495 (33%)
C	1204 (11%)	Cr	10015 (94%)
O	8538 (81%)	Mn	10204 (96%)
Na	10222 (96%)	Co	5574 (53%)
Mg	10470 (99%)	Ni	6388 (60%)
Al	8529 (80%)	Cu	9312 (88%)
Si	6422 (61%)	Zn	10012 (94%)
K	10237 (97%)	Y	9354 (88%)
Ca	9217 (87%)	Ba	10417 (98%)
Sc	10438 (98%)	La	5215 (49%)
Ti	10335 (97%)	Eu	4419 (42%)

the model decides which coefficients of the model to force to 0, but can still identify strongly correlated features. It may be legitimate to learn these correlations and take advantage of this information (e.g. Ting et al., 2018a). Based on previous analyses, which showed a strong correlation of [α/Fe] and telluric lines for the GALAH survey, we have chosen to use the most conservative approach for this analysis.

2.3.2.3 *The Cannon* ERRORS

The errors reported by *The Cannon* are based on the formal covariance errors, which are typically very small. Our total error estimate for each label is based on an additional SNR-dependent performance test of the training set for each label. This is estimated by comparing the difference of the SME input and *The Cannon* output as a function of the training set SNR and fitting an exponential function to the mean values within bins of SNR of 25, 50, 75, and 100. These errors are then summed in quadrature with *The Cannon* covariance errors. We note that this performance test only includes SNR > 25 (as a result of our requirement for the training set spectra to be of high-fidelity). At SNR < 25, the performance test is an extrapolation and tends to underestimate the errors when compared with the scatter between repeat observations, see Section 2.3.3.4.

2.3.3 DATA QUALITY ASSESSMENT

Spectroscopic analyses are typically validated in several ways.

Firstly, the quality of both spectra and the spectroscopic analysis are evaluated internally by employing quality flags.

Secondly, to validate the results by both SME and *The Cannon*, we use a variety of tests, including the comparisons with fundamental parameters of the *Gaia* benchmark stars, repeated observations, photometric temperatures, asteroseismic surface gravities, open and globular clusters, and other spectroscopic surveys.

Table 2.4: Biases and RMS of the self validation test.

ℓ	Bias	RMS	K_ℓ	Bias	RMS
$T_{\rm eff}$ [K]	3	54	[Ca/Fe]	0.00	0.05
$\log g$ [dex]	0.01	0.17	[Sc/Fe]	0.00	0.04
[Fe/H]	0.00	0.07	[Ti/Fe]	0.00	0.04
$v_{\rm mic}$ [km s^{-1}]	0.00	0.04	[V/Fe]	0.00	0.06
$v \sin i$ [km s^{-1}]	0.0	1.7	[Cr/Fe]	0.01	0.05
A_{K_S} [mag]	0.00	0.06	[Mn/Fe]	0.00	0.06
[Li/Fe]	0.00	0.08	[Co/Fe]	0.00	0.06
[C/Fe]	0.00	0.05	[Ni/Fe]	0.00	0.07
[O/Fe]	0.00	0.11	[Cu/Fe]	0.00	0.06
[Na/Fe]	0.00	0.05	[Zn/Fe]	0.00	0.08
[Mg/Fe]	0.00	0.08	[Y/Fe]	0.00	0.08
[Al/Fe]	0.00	0.04	[Ba/Fe]	0.00	0.10
[Si/Fe]	0.01	0.08	[La/Fe]	0.00	0.06
[K/Fe]	0.00	0.09	[Eu/Fe]	0.00	0.07

2.3.3.1 FLAGGING OF STELLAR PARAMETER AND ELEMENT ABUNDANCE ESTIMATES

For a given spectrum m_{DR2} of the GALAH Data Release 2 with labels $\ell_{m_{DR2}}$, we estimate the label distance to the labels ℓ_{n_TS} of the training set points n_{TS} similarly to Ho et al. (2017b, see their Equation 7):

$$D = \sum_{\ell} \sum_{n_{TS}} \frac{(\ell_{m_{DR2}} - \ell_{n_{TS}})^2}{K_\ell^2} \tag{2.12}$$

For the stellar parameters we use

$$\ell \in [T_{\rm eff}, \log g, [{\rm Fe/H}], v_{\rm broad}]$$

and for the abundance of element X we use

$$\ell \in [T_{\rm eff}, \log g, [{\rm Fe/H}], v_{\rm broad}, [{\rm X/Fe}]]$$

. The uncertainties K_ℓ used to estimate the label distances are based on the RMS of the self validation as listed in Table 2.4. Subsequently, we estimate the mean distance of the 10 smallest label-distances, i.e. closest training set points, and raise the `flag_cannon` bitmask by 1, if this distance is larger than 8 for the stellar parameters (a mean of 2σ for 4 stellar labels) or 10 for the individual abundances (a mean of 2σ for 5 stellar labels). We nethertheless also report the mean label distance to the 10 closest training set points as `sp_label_distance` to allow the exploration of this flag.

Analogous to the analysis with SME, see Section 2.3.1.3, we estimate if the measured line is a detection or only an upper limit and raise the bitmask by 2, if the line is $< 3\sigma$ of the flux error, but at least 5% below the continuum flux.

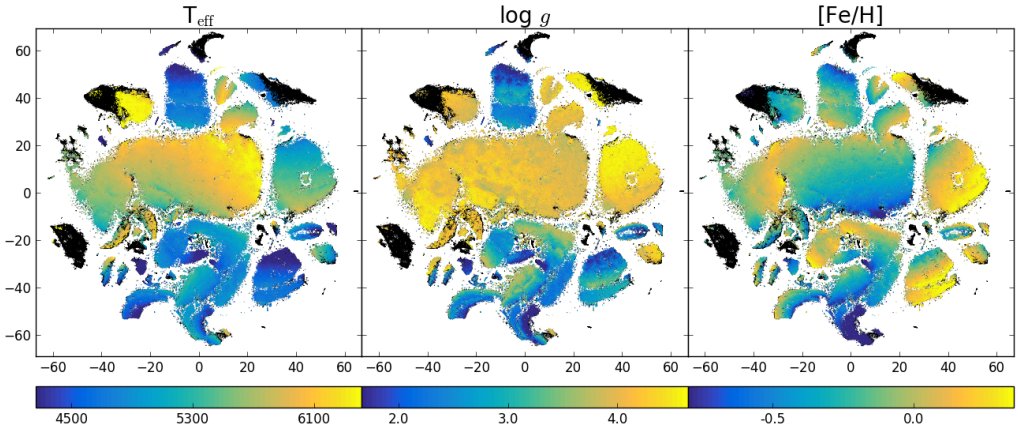

Figure 2.14: t-SNE projection map of 587 153 spectra. 413 920 of them have reliable stellar parameters derived by *The Cannon* pipeline, others are plotted as black points. The parameters are missing especially for hot and cool stars, but also for some binary stars and stars with emission lines, as seen by comparing this figure to Figure 2.15 where the classification categories are marked. The colour-scale is done with 2.5 % at both extremes of parameter values truncated for better contrast. **Figure Credit:** Paper I.

Additionally, we make use of the χ^2 fit statistic and raise the `flag_cannon` bitmask by 4, if the mean χ^2 per pixel (with an expectation of 1 for a perfect fit and perfectly known errors) is either below 0.5 or above 10, both indicating issues with the spectra or that *The Cannon* model can not describe the given spectrum.

2.3.3.2 AUTOMATED STELLAR CLASSIFICATION WITH T-SNE

Classification of data is one of the most important steps in any kind of automatic data reduction and analysis. This is especially true in the case where the sheer quantity of collected information prevents us from manually inspecting the data as it comes in, and also when it is not possible to determine all sorts of outliers and unexpected issues *a* priori. Because the GALAH sample of observed spectra fits this description, it was necessary to develop a semi-automatic classification procedure, which has been presented in Traven et al. (2017). Here we briefly outline the classification scheme of the spectra at rest wavelength and its recent improvements.

In order to facilitate the discovery and determination of diverse morphological groups of spectra, we make use of two mathematical techniques, an increasingly more popular dimensionality reduction method t-SNE (van der Maaten & Hinton, 2008), and the well-established clustering algorithm DBSCAN (Ester et al., 1996). These techniques enable us to condense the information contained in our entire dataset into a two-dimensional map (Figure 2.14), where the spectra are arranged in such a way, that similar ones are grouped together, while there is a clear separation between distinct groups. The strongest features in the data – indicating stellar physical parameters – clearly dictate its global structure, hence the map can be clearly divided between dwarfs and giants or hot and cool stars. Inside these larger groups there is rich local structure, usually driven by the chemical composition of stars or by any other slowly changing

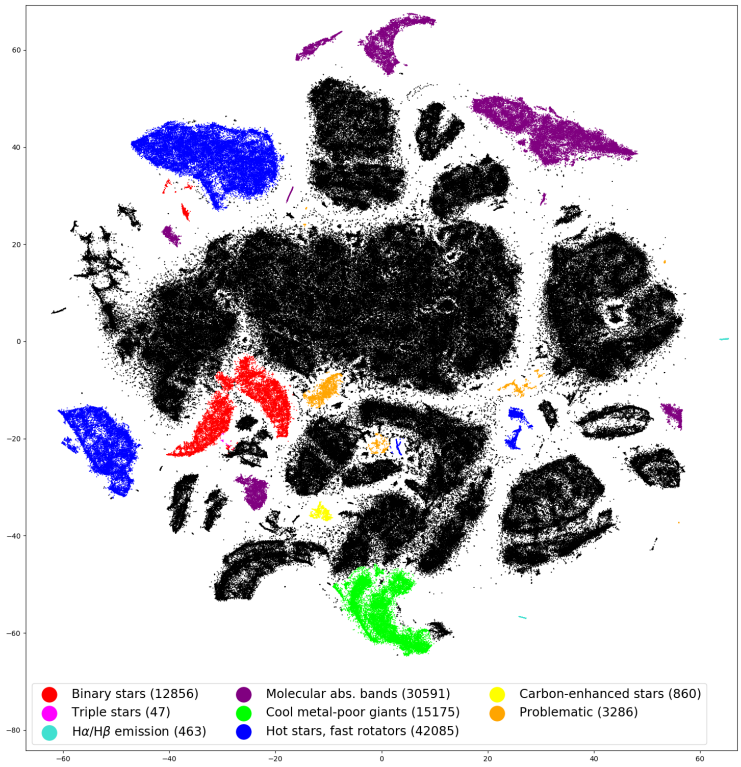

Figure 2.15: t-SNE projection map, same as Figure 2.14, except that the points (spectra) are color-coded by classification category. The majority of stars do not show peculiarities and are shown as black dots. The flagged triple stars are few and hardly seen next to the lower left group of binary stars, whereas the Hα/Hβ emission stars are on the far right and bottom right in the map. The count of spectra for each category is given in the legend. **Figure Credit:** Paper I.

spectral feature. In addition to the influence of stellar parameters, the shape of the projection is also driven by the presence of strong emission lines, or multiple lines from binary and higher order systems.

With the help of the above described map we are able to manually inspect the structure of our dataset and assign classification categories to groups of spectra of interest. To each group in the map, one assigns a category by either looking at the average spectrum of the subset of the group or by the help of previous classification and other existing information/labels. Therefore, with every subsequent classification of the growing dataset, it is easier to assign categories; however, new and unexpected features can add to the complexity of the map.

We no longer use the two-step procedure described in Traven et al. (2017) for producing a t-SNE map of peculiar spectra, since we have overcome the computational difficulties and can now produce the projection map using all available spectral information of the whole dataset in less than a day on a 24-core Xeon node. This became possible by using the parallel multicore t-SNE code (Ulyanov, 2016) and modifying it to remove the limit of overall information that we put into t-SNE. Additionally, we

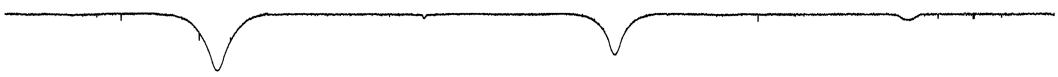

exclude the infrared band as it still suffers from the presence of strong spikes (see Traven et al. 2017), which are now understood and accounted for. The inclusion of this band would hamper our classification significantly compared to what could be gained from information contained therein.

Figure 2.15 presents classification results based on all spectra of this data release which passed the basic reduction as explained in Section 2.2.5. We flag all groups of spectra for which a sensible physical category can be determined, however our results are not exhaustive. The population of double-lined spectroscopic binary stars represents ~ 2.2 % of the whole dataset, down to a separation of $\sim 10\,\mathrm{km\,s^{-1}}$ in the case of most blended double lines. We see a morphological distinction between two larger groups of binaries, which is due to the stronger component being redshifted in one group and blueshifted in the other.

The flagged Hα/Hβ emission stars are very few in our dataset, which is partly because our observations are not focused on young open clusters, but also because a weak emission signature is sometimes not enough for those spectra to stand out in the map. Our observations and data reduction still introduce some issues that manifest in different features in the spectra and are flagged as problematic, however they are relatively few.

The classification presented in this section serves both as a source of intrinsically interesting objects which can be studied separately (Traven et al., in preparation), and also as a guide to the development and improvement of the reduction and analysis pipeline.

2.3.3.3 *Gaia* BENCHMARK STARS

We use *Gaia* benchmark stars (Jofré et al., 2014; Heiter et al., 2015a) as one way to validate the accuracy of our stellar parameters. Because of their independently estimated effective temperatures and surface gravities through interferometry and bolometric flux estimations, respectively, these parameters are less model-dependent than our spectroscopically derived ones. In Figure 2.16, we compare results with the SME analysis (only based on spectroscopy, as well as with astrometric information) and with the The Cannon-based parameters.

For the fundamental parameter T_{eff} we find no significant bias (see offset and dispersion in top panel of Figure 2.16). For the warmest *Gaia* benchmark stars, we see systematic trends of under-estimated temperatures for both SME analyses, which are propagated by *The Cannon*. For the luminous giants, we see a rather good agreement for SME within 200 K, while *The Cannon* overestimates the temperature of the most luminous giants by around 250 K. For these stars, *The Cannon* also overestimates the surface gravity significantly by around 1 dex, as the second panel of Figure 2.16 shows. While the agreement for surface gravity is good by construction when including parallax information in the SME analysis, there is an offset of 0.15 dex to both the *Gaia* benchmark stars and asteroseismically inferred $\log g$ when using a purely spectroscopic approach. As a result, we have opted to shift the spectroscopic SME results by this amount.

The iron abundances as well as the iron abundances of the best-fitting atmosphere (*sme.feh*) have both shown systematic biases of 0.1 dex. We have hence increased the iron abundance globally by 0.1 dex. and find good agreement along the metallicity range for

the SME results. *The Cannon*, however, shows biases of overestimated iron abundances for the most metal-poor stars (below [Fe/H] of −1) of around 0.7 dex, and 0.35 dex for the coolest giants.

The microturbulence velocity, $v_{\rm mic}$, agrees in general with those presented in (Heiter et al., 2015a; Jofré et al., 2014) except for luminous giants where our chosen relation differ by 0.5 to 0.7 km s^{-1}. We note that the microturbulence velocity is dependent on the adopted stellar parameters, model atmospheres and line selection among other things and it is thus not given that our values are inferior when the two sources differ. Similarly, our line broadening parameter v_{broad} is similar to the literature values when summing the published $v_{\rm mac}$ and $v \sin i$ in quadrature.

2.3.3.4 REPEAT OBSERVATIONS

About 50,000 spectra have independent repeated observations[3]. These repeats are useful for characterizing the uncertainty in the stellar parameters as well as the intrinsic variability of the stellar properties. The repeats span multiple programs with HERMES, including commissioning, and the pilot and main GALAH surveys, as well as the K2-HERMES, and TESS-HERMES surveys. About 50% of the repeats are due to bad observational conditions, which were repeated to boost the signal to noise ratio. These repeats were done using the same plate and fibre configuration as the original observation. The other 50% had different plate and fibre configuration. Of these, 25% are serendipitous observations of the GALAH pilot and commissioning programs, which did not have a well defined selection function and hence were not tracked when the main survey started its operation. To minimize the time spent on repeats, a significant number of the deliberate repeats were carried out for the bright fields, which require less than half of the exposure time.

In Figure 2.17 we make use of the repeats to estimate the uncertainty of the spectroscopic stellar parameters as a function of SNR. The uncertainty is estimated by computing, in each bin of SNR, the 16th and 84th percentile range of differences between repeats and dividing it by $2\sqrt{2}$. The uncertainty estimated from repeats (green and orange curves) is compared with the uncertainty estimated using The Cannon (blue curves) as described in Section 2.3.2. The repeats confirm the overall trend of uncertainties with SNR, namely a strong degradation for SNR < 20. Except for [α/Fe], [Ba/Fe] and $v \sin i$, the covariance based method in general overestimates the uncertainty compared to the repeat-based method. Below SNR= 15, for $\log g$, [Fe/H], v_{mic}, and $v \sin i$, *The Cannon* based method significantly underestimates the uncertainties as a result of the error-analysis described in Section 2.3.2.3.

The estimated repeat-based uncertainties for RV and v_{sini}, and to a lesser degree $\log g$, differ when based on observations using different fibres as opposed to using the same fibre. This is because of the systematic differences in wavelength calibration and point spread function of each fibre. The uncertainties for other parameters are not affected

[3]If stars were observed multiple times, we only report the highest SNR observation and remove duplicates in the final GALAH DR2 catalogue.

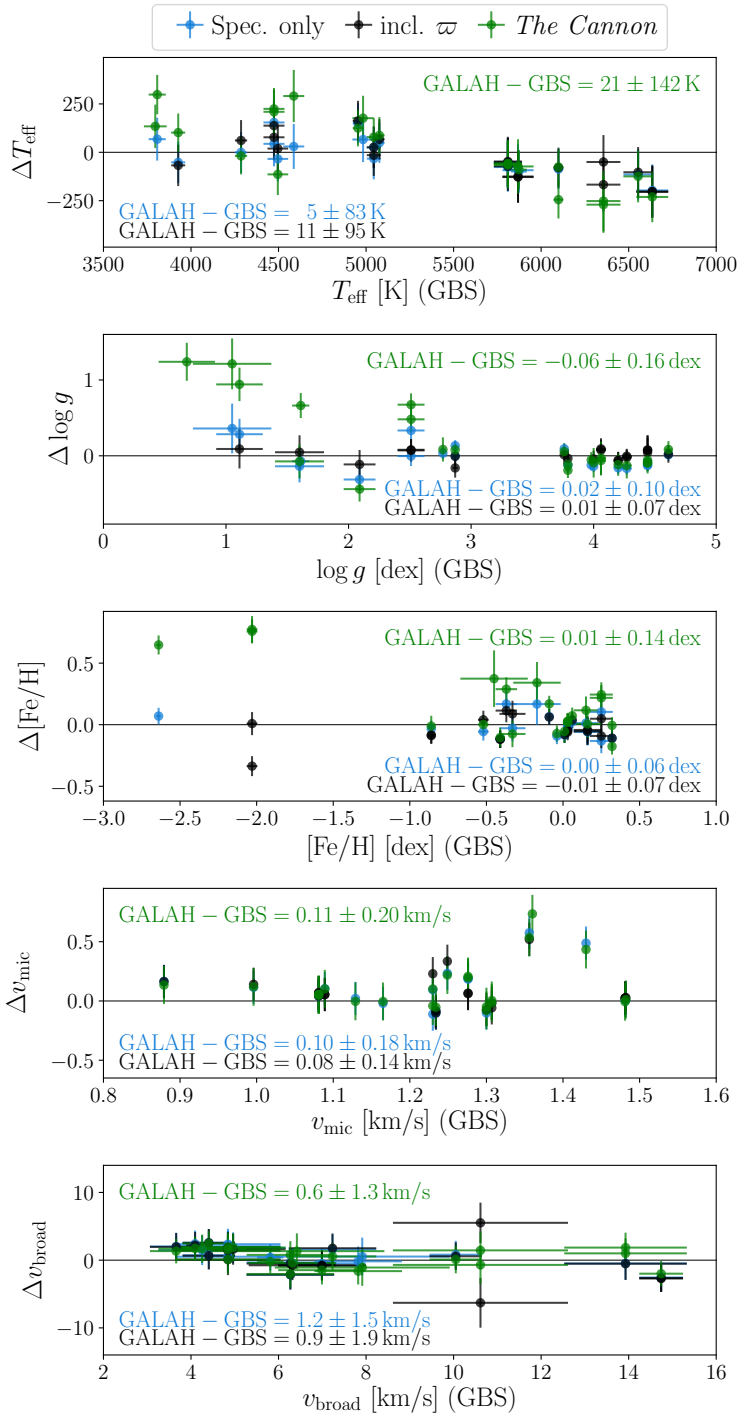

Figure 2.16: Comparison of GALAH stellar parameters with *Gaia* benchmark stars (GBS). Shown are differences for the training set (intended as GALAH-Gaia benchmark stars) only based on spectral information (blue), training set including astrometric information (black), and *The Cannon* output (green). **Figure Credit:** Paper I.

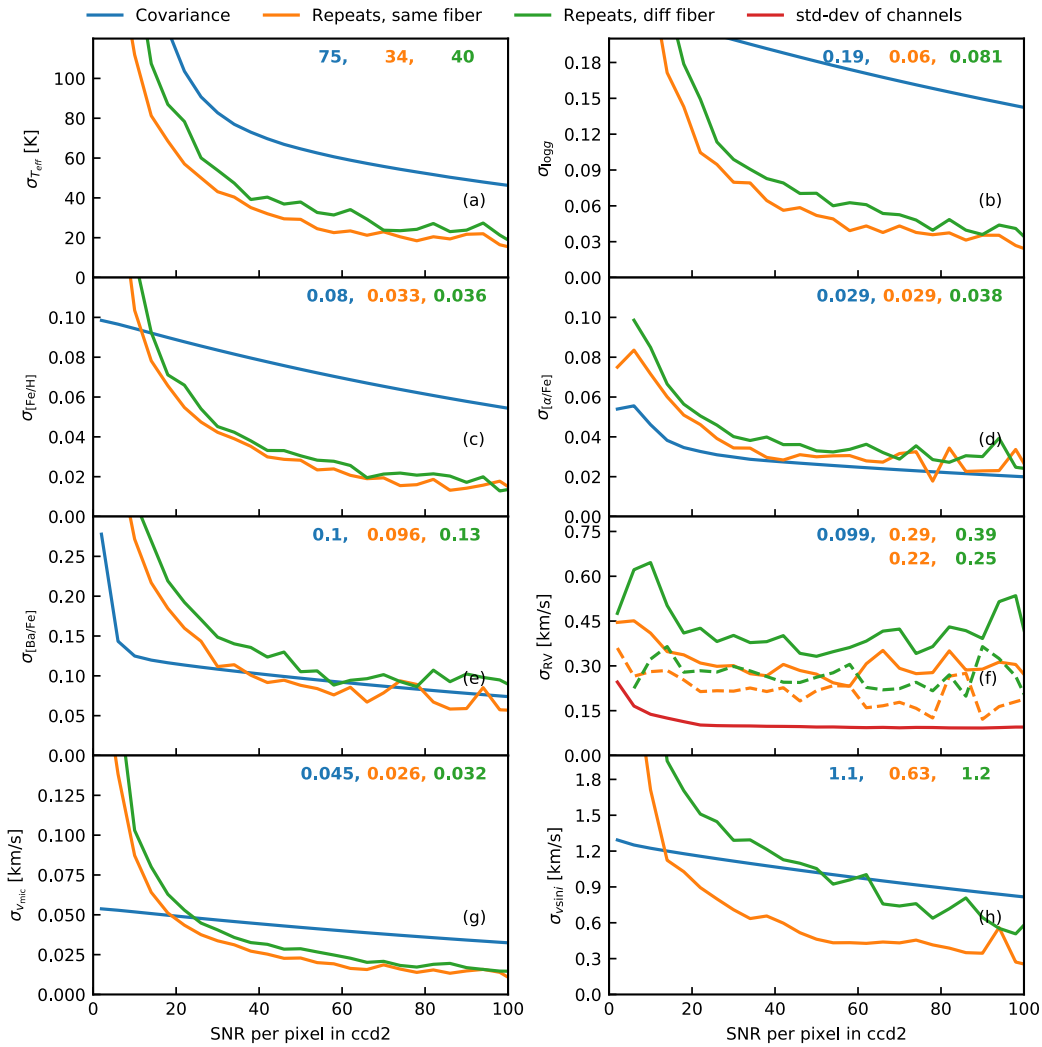

Figure 2.17: Uncertainty in spectroscopic stellar parameters, Ba abundance, and radial velocity as a function of SNR. The blue curve shows the uncertainty as predicted by *The Cannon* (based on covariance errors and the SNR-dependent RMS within the leave-out-test). The other two curves are for uncertainties estimated using repeat observations, where the repeated stars are on the same fibre (orange curve) and different fibres (green curve). The numbers given in each panel are the uncertainties estimated from *The Cannon* covariance and repeat observations for stars on the same and on different fibres at SNR=40, which is the median value of the SNR. For radial velocity, the solid lines are for `rv_synt` while the dashed lines are for `rv_obst`. **Figure Credit:** Paper I.

by this, because a small change in point spread function does not directly translate into a variation of those parameters.

2.3.3.5 INFRARED FLUX METHOD TEMPERATURES

We apply the infrared flux method (IRFM Casagrande et al., 2010, 2014) to over 280,000 GALAH stars having SkyMapper photometry (Wolf et al., 2018). Further details on the implementation of SkyMapper filters into the IRFM can be found in Casagrande et al. (in preparation). Apart from a few pointings along the plane, nearly all of the SkyMapper targets overlapping with GALAH targets have Galactic latitudes above |10°|, meaning that the most obscured and patchy regions of the Galactic plane are avoided. Yet, reddening can have a non-negligible contribution, which we account for with the same procedure used when implementing the IRFM for RAVE stars (Kunder et al., 2017).

Figure 2.18 shows the comparison between $T_{\rm eff}$ from the IRFM and GALAH, colour-coded by the adopted $E(B-V)$. For low reddening regions, the agreement is usually excellent across the entire stellar parameter range, although it deteriorates for regions of high extinction. Stars labelled as unreliable in GALAH (`flag_cannon` $\neq 0$) are plotted in grey. Effectively all of the stars above 7000 K are flagged in GALAH, because of the lack of stars in the training set in this regime, forcing the data-driven approach to extrapolate the determination of stellar parameters. The IRFM indicates that the GALAH pipeline underestimates effective temperatures in this regime, similar to what was seen from the *Gaia* benchmark star comparison, saturating at 8000 K which is the limit of the grid of model atmospheres used for the training set; we checked that this trend is not an artefact from stars affected by high values of extinction.

After removing flagged stars, the SkyMapper−GALAH mean (median) $\Delta T_{\rm eff}$ is 61 K (49 K) with a scatter of 183 K when stars are considered irrespectively of their reddening. The above numbers reduce to $\Delta T_{\rm eff}$ = 51 K (50 K) with a scatter of 132 K when restricting to $E(B-V) < 0.10$, and $\Delta T_{\rm eff}$ = 12 K (12 K) with a scatter of 123 K for $E(B-V) < 0.01$. Since we expect typical uncertainties of order 100 K for the IRFM in low extinction regions, the above scatters suggest that a slightly smaller uncertainty applies to the GALAH spectroscopic temperatures, in line with the conclusions discussed above.

2.3.3.6 ASTEROSEISMOLOGY

Although GALAH does not overlap with the *Kepler* field, there is a significant overlap with several observing campaigns of the K2 mission, in particular with the asteroseismic-based Galactic Archaeology Program (GAP) (Stello et al., 2015). The GAP has so far published seismic results for K2 Campaign 1 (C1) (Stello et al., 2017), and is in the process of releasing results for additional campaigns, including C4, C6, and C7 (Zinn et al., in preparation). Here, we use the results from the Bayesian Asteroseismology data Modeling Pipeline (Stello et al., 2017, see also Zinn et al., in preparation) of stars in C1, C4, C6, and C7 to verify $\log g$ from *The Cannon*.

In Figure 2.19 we show the comparison between the spectroscopic $\log g$ from GALAH and the seismic $\log g$ derived using Equation 2.4, with data from the K2-

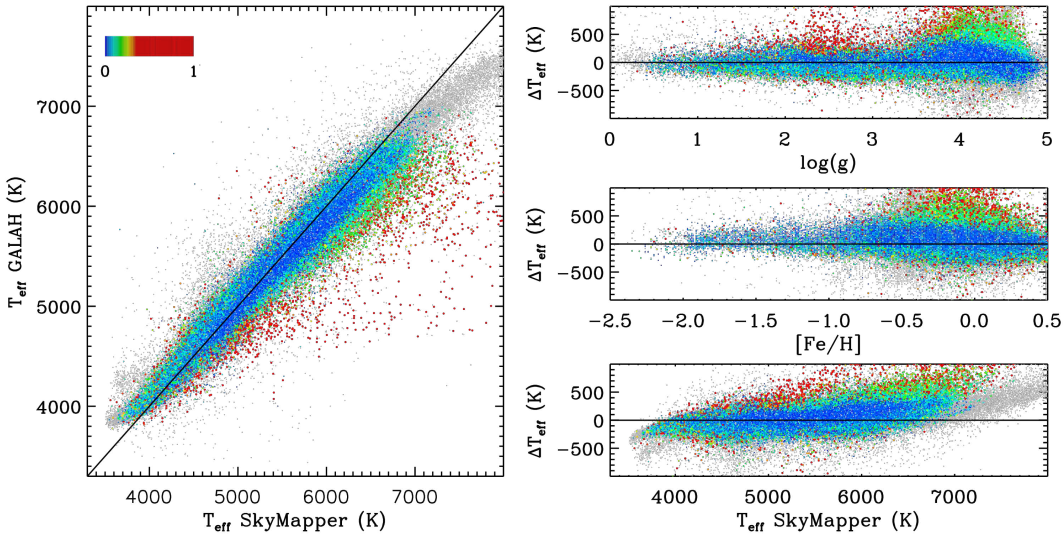

Figure 2.18: Comparison of GALAH effective temperatures $T_{\rm eff}$ with IRFM temperatures derived from SkyMapper photometry. Residuals (SkyMapper-GALAH) are shown as function of stellar parameters and colour coded by E(B-V) according to the scale on the top left. Grey points are stars flagged as unreliable in GALAH. **Figure Credit:** Paper I.

HERMES survey. The $\log g$ coverage of the seismic results is limited by the length ($\sim$ 80 days) and sampling ($\sim$ 30 min) of the K2 time series. To reach lower $\log g$ stars would require longer time series, while higher $\log g$ stars require faster sampling. The dispersion seen in Figure 2.19 is dominated by the uncertainty in the spectroscopic values, which is evident from the narrow seismic $\log g$ range around 2.4 for the red clump stars, as expected from stellar evolution theory, compared to the larger spread in spectroscopic $\log g$ values. Generally, we see a good agreement between the spectroscopic and seismic results, but with a slight bias for low luminosity red giant branch stars ($2.8 < \log g < 3.2$), where the spectroscopic values may be underestimated; see binned data in orange relative to the blue one-to-one line in Figure 2.19. This bias is also observed for each campaign separately. We also note that the dispersion (dashed orange curves) of about 0.3 dex, is larger than would be expected either from the spectroscopic $\log g$ uncertainty estimated by the GALAH pipeline or from the scatter between repeat observations, which in both cases is below 0.2 dex for the majority of stars (Figure 2.17). This may suggest that the asteroseismically inferred surface gravities also have unresolved issues. We note that stars with extreme differences between seismic and spectroscopic $\log g$ values can potentially be blends (in the K2 data) or misidentifications.

With the TESS launch scheduled for April 2018, there will be further opportunity in the near future to train and test the GALAH $\log g$ values using asteroseismology. In particular, stars in TESS's southern continuous viewing zone will be observed for up to one year, pushing the boundaries of the $\log g_{\rm seism}$ range GALAH can access.

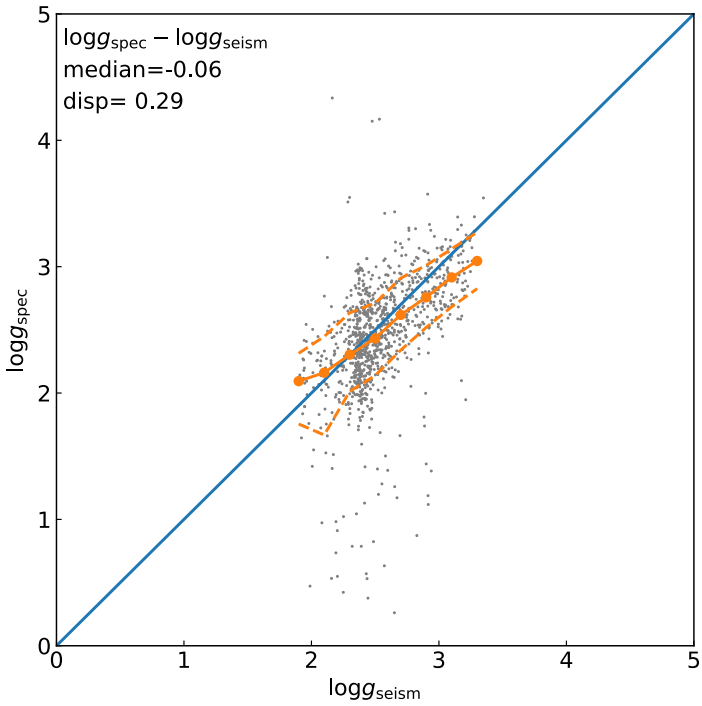

Figure 2.19: Comparison of GALAH surface gravity with asteroseismic surface gravity derived using data from the K2 mission (Campaign C1, C4, C6, and C7). Median and the confidence-interval-based dispersion of the difference between the two gravities are shown in the top left corner. The solid blue line shows the one-to-one relation. The solid orange line shows the 50th percentile, while the dotted lines show the 16th and 84th percentiles, derived in 0.2 dex wide bins in $\log g_{\rm seism}$. Stars shown are with `flag_cannon=0` and `snr_c2>30`. **Figure Credit:** Paper I.

2.3.3.7 GLOBULAR AND OPEN CLUSTERS

Stellar clusters provide an excellent sample of stars with which to validate the GALAH results. Many clusters have been extensively studied (e.g., see the review of globular cluster abundances by Bastian & Lardo, 2018), and they span a large range of metallicities, ages, and other parameters. GALAH has targeted several globular and open clusters for validation purposes during its pilot observing campaign, and several more fell within our survey fields and members were serendipitously observed. In this section we discuss clusters that were not only observed by the GALAH survey, but also by related surveys: TESS-HERMES (Sharma et al., 2018), K2-HERMES (Wittenmyer et al., 2018) and the HERMES Open Cluster Project (De Silva et al., in preparation). As such, some of the clusters and members discussed in this work are not available in GALAH DR2.

Cluster members were identified by cuts in radial velocity around the literature values (Kharchenko et al., 2013) and proper motions from UCAC5 (Zacharias et al., 2017). Only members within the cluster radius given in Kharchenko et al. (2013) were considered. We found reliable members of 7 globular and 11 open clusters. In Figure 2.20 we show the Kiel diagrams for the globular clusters and Figure 2.21 is the same

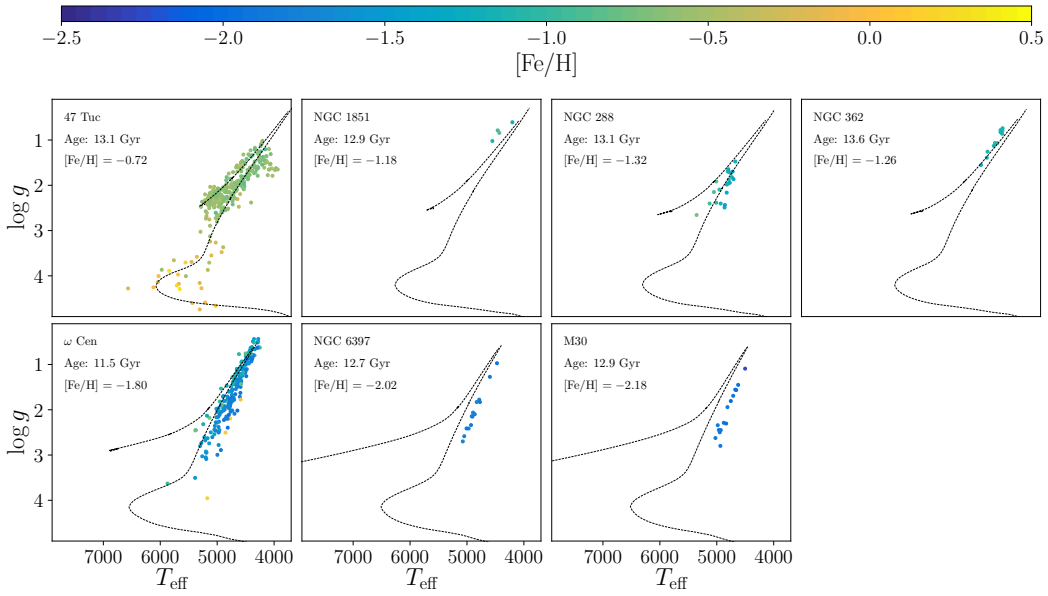

Figure 2.20: Kiel diagrams ($T_{\rm eff}$ [K] vs. $\log g$ [dex]) of globular cluster stars observed by GALAH. Cluster members were identified from our own radial velocity measurements, proper motions from UCAC5 (Zacharias et al., 2017), and parameters from Kharchenko et al. (2013). We stress that isochrones have not been fitted to the data. For each cluster, we plot PARSEC+COLIBRI isochrones (Marigo et al., 2017) with ages from Forbes & Bridges (2010) and metallicities from Harris (1996). **Figure Credit: Paper I.**

for the open clusters, overplotted with PARSEC+COLIBRI isochrones (Marigo et al., 2017). The isochrones have not been fitted to the data; rather, we are simply using the literature values for each cluster. For the globular clusters we use metallicities from Harris (1996) and ages from Forbes & Bridges (2010). For the open clusters we use the values in Kharchenko et al. (2013). We note that these references are compilations of literature data.

As would be expected for the magnitude range, the globular cluster members have been identified as giant stars. They are usually found on narrow sequences, though these are sometimes offset from the isochrone. Most of the open clusters are young and most of the observed targets are main sequence stars. For the youngest clusters (e.g., Blanco 1 and Pleiades) there is evidence for a temperature dependence of their metallicities due to fast rotation causing a degeneracy within the spectra and hence systematics in the stellar parameters. We stress that these also translate into abundance trends.

In agreement with many previous studies (e.g., Johnson & Pilachowski, 2010), we find that a large metallicity spread in ω Cen: $-2.0 <$ [Fe/H] < -0.5 (top panel of Figure 2.22) with four peaks in the metallicity distribution. We also confirm the distinctive distribution of s-process element abundance with metallicity, here demonstrated with [Ba/Fe] (bottom panel of Figure 2.22). [Ba/Fe] increases with metallicity until [Fe/H] ≈ -1.5 and appears to become roughly constant thereafter.

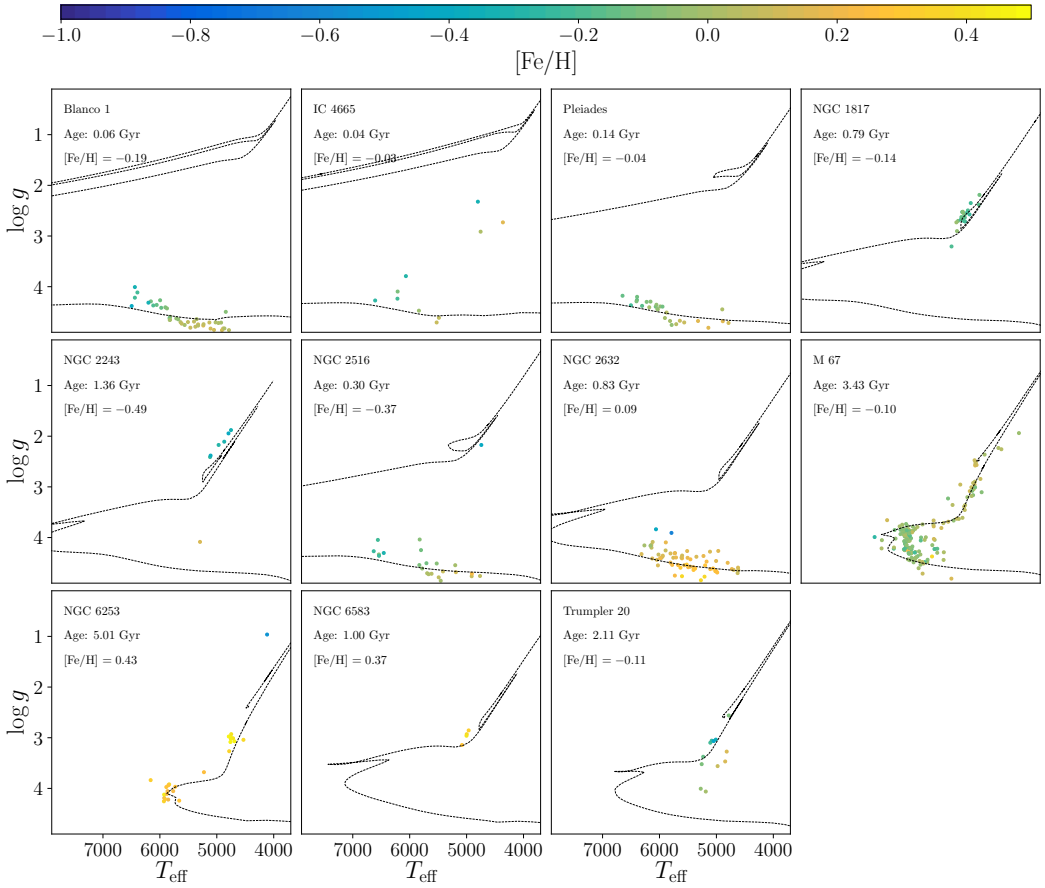

Figure 2.21: Kiel diagrams ($T_{\rm eff}$ [K] vs. $\log g$ [dex]) of open cluster stars observed by GALAH. Cluster members were identified from our own radial velocity measurements, proper motions from UCAC5 (Zacharias et al., 2017), and parameters from Kharchenko et al. (2013). We stress that isochrones have not been fitted to the data. For each cluster, we plot PARSEC+COLIBRI isochrones (Marigo et al., 2017) with ages from and metallicities from Kharchenko et al. (2013). **Figure Credit: Paper I.**

Open clusters are particularly valuable validation objects for our derived element abundances, because we expect stars from the same open cluster at the same evolutionary phase to show intrinsically very similar abundance patterns and they have metallicities similar to the majority of the GALAH main sample. As a result, these clusters are ideal benchmarks to validate abundance determinations.

For this data release, we are concentrating on the open cluster M67, for which we have observed turn-off, subgiant, red giant branch, and red clump stars with a mean iron abundance of [Fe/H] = -0.01 ± 0.08 and a radial velocity of $34.08 \pm 0.85\,\mathrm{km\,s^{-1}}$. We stress that the measured iron abundance is different from the value by Kharchenko et al. (2013) used in Figure 2.21. In addition to the Kiel diagram of the cluster members and histograms of both iron abundance and radial velocity, we show stellar parameters and element abundances as a function of effective temperature $T_{\rm eff}$ in Figure 2.23. We

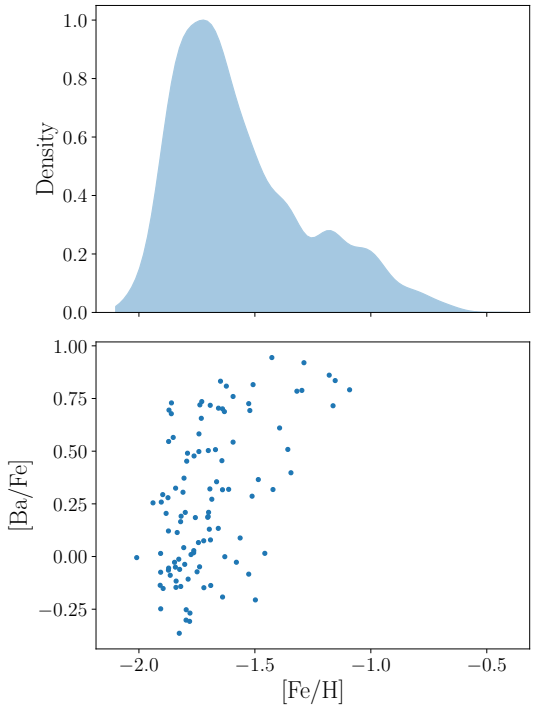

Figure 2.22: Top: Metallicity distribution of the members of ω Centauri observed. We find the main population at [Fe/H] ≈ -1.8, an intermediate metallicity population at about [Fe/H] ≈ -1.4, and a further population at [Fe/H] ≈ -1.2. There is a tail of stars that extends to [Fe/H] ≈ -0.5. Bottom: The distribution of [Fe/H] with [Ba/Fe] in ω Centauri. We find the expected rapid increase of s-process elemental abundances previously observed in ω Centauri. **Figure Credit:** Paper I.

note that the turn-off stars cover a larger range of broadening velocities, whereas the evolved stars are usually slow rotators. The larger broadening is coincident with lower iron abundance estimates of the pipeline and also manifested in the iron abundance distribution, showing an increase of iron abundance towards lower temperatures and lower broadening.

When we look at the difference between the abundances of dwarfs (defined as $T_{\rm eff} > 5500\,{\rm K}$ or $\log g > 4.0$) and giants ($T_{\rm eff} \leq 5500\,{\rm K}$ and $\log g \leq 4.0$) as part of the GALAH observations of M67, we see trends with effective temperature (above 1σ difference) for Al, K, Sc, and V in addition to Fe. We see no significant trends with $T_{\rm eff}$ (less than 1σ difference) for O, Ti, Ni, Zn. No trends (less than 0.5σ difference) can be seen for Na, Mg, Si, Ca, Cr, Mn, Cu, Y, Ba, La. For the elements Li, C, Co, and Eu we can not assess the trends due to the low number of stars in either category. Because of the possible intrinsic nature of these trends, we do not correct them but note that they increase the overall abundance scatter within the cluster (see Table 2.5). We stress that some of these trends expected and have been found in other studies. For O and Al similar trends have been found by Gao et al. (2018), when analysing higher resolution data with a very similar analysis. For K, an artificial trend with temperature is expected because of strong non-LTE effects. As outlined in Section 2.3.1.3, the lines of some

Table 2.5: Abundances of the open cluster M67. For this compilation, we define dwarfs as stars with $T_{\rm eff} > 5500$ K or $\log g > 4.0$, and giants as stars with $T_{\rm eff} \leq 5500$ K and $\log g \leq 4.0$.

Abundance	Nr. stars	Mean	Nr. dwarfs	Mean	Nr. Giants	Mean
[Fe/H]	156	−0.01 ± 0.08	107	−0.05 ± 0.07	49	0.06 ± 0.05
[Li/Fe]	4	0.92 ± 1.58	2	2.48 ± 0.10	2	−0.64 ± 0.29
[C/Fe]	49	0.05 ± 0.09	49	0.05 ± 0.09	0	–
[O/Fe]	131	−0.03 ± 0.15	84	0.02 ± 0.14	47	−0.13 ± 0.12
[Na/Fe]	134	0.09 ± 0.09	96	0.10 ± 0.09	38	0.06 ± 0.07
[Mg/Fe]	143	−0.00 ± 0.12	94	0.02 ± 0.12	49	−0.05 ± 0.11
[Al/Fe]	122	−0.05 ± 0.09	93	−0.08 ± 0.07	29	0.05 ± 0.05
[Si/Fe]	155	−0.04 ± 0.12	106	−0.06 ± 0.12	49	0.01 ± 0.09
[K/Fe]	113	0.25 ± 0.17	97	0.28 ± 0.15	16	0.01 ± 0.11
[Ca/Fe]	137	0.03 ± 0.12	96	0.03 ± 0.12	41	0.04 ± 0.12
[Sc/Fe]	153	0.09 ± 0.09	107	0.12 ± 0.08	46	0.01 ± 0.04
[Ti/Fe]	142	0.00 ± 0.06	106	−0.01 ± 0.05	36	0.05 ± 0.07
[V/Fe]	129	0.13 ± 0.14	101	0.07 ± 0.08	28	0.37 ± 0.07
[Cr/Fe]	144	0.02 ± 0.10	107	0.01 ± 0.11	37	0.06 ± 0.06
[Mn/Fe]	141	0.06 ± 0.09	95	0.05 ± 0.07	46	0.08 ± 0.11
[Co/Fe]	9	−0.04 ± 0.15	5	−0.04 ± 0.18	4	−0.03 ± 0.08
[Ni/Fe]	147	0.17 ± 0.17	106	0.13 ± 0.14	41	0.29 ± 0.17
[Cu/Fe]	121	−0.03 ± 0.08	94	−0.05 ± 0.09	27	0.01 ± 0.06
[Zn/Fe]	154	0.03 ± 0.14	105	0.06 ± 0.13	49	−0.04 ± 0.14
[Y/Fe]	156	0.17 ± 0.15	107	0.14 ± 0.15	49	0.22 ± 0.14
[Ba/Fe]	122	0.18 ± 0.21	102	0.19 ± 0.21	20	0.12 ± 0.20
[La/Fe]	31	0.06 ± 0.23	18	0.11 ± 0.24	13	−0.01 ± 0.20
[Eu/Fe]	5	−0.02 ± 0.19	1	0.19	4	−0.08 ± 0.18

elements are not strong enough in dwarf or giant spectra within the GALAH range to be detected precisely or at all. When assessing the scatter within dwarfs and giants of the cluster separately, we hence find a lower scatter for several elements, which are a more appropriate measure of our internal precision. These range from the highest precisions of 0.04 − 0.08 dex (Fe, Al, Sc, Ti, V, and Cu) over high precision of 0.08 − 0.12 dex (C, Na, Si, Cr, and Mn) and intermediate precision of 0.12 − 0.16 dex (O, Mg, K, Ca, Co, Ni, Zn, and Y) to low precision above 0.16 dex (Li, Ba, La, Eu) for the stars observed in M67.

2.3.3.8 COMPARISON WITH OTHER STUDIES AND SURVEYS

Because of the variety of high-resolution, high-quality, and large-scale spectroscopic studies and surveys to compare with, we have decided to only choose two homogeneously analysed samples for comparison in this study: Bensby et al. (2014) and its follow-up studies (Battistini & Bensby, 2015, 2016; Bensby & Lind, 2018) for dwarf stars and APOGEE DR14 (Abolfathi et al., 2018) for giants. While we only use those stars with `flag_cannon` = 0 and `flag_X_Fe` = 0 (see Figures 2.24-2.26), we append the same comparisons including extrapolated abundances (`flag_X_Fe` ≤ 1) in Section 2.3.3.9.

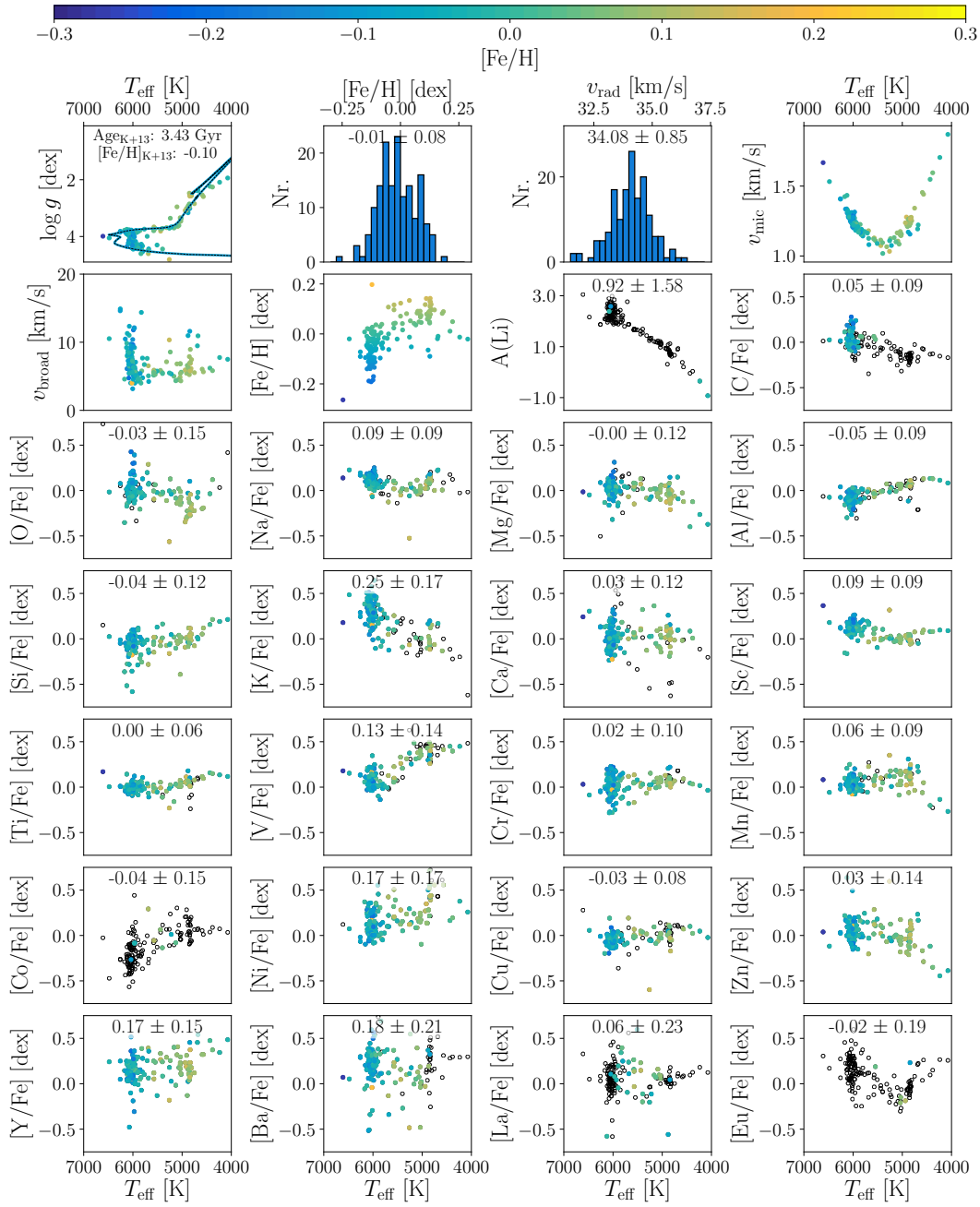

Figure 2.23: Overview of stellar parameters and element abundances for the open cluster M67. The top left panel shows the M67 Kiel diagram, followed horizontally by the metallicity and radial velocity distributions. The top right panel show the microturbulence velocity $v_{\rm mic}$ as a function of effective temperature $T_{\rm eff}$. The other panels show two more stellar parameters ($v_{\rm broad}$ and [Fe/H]) as well as element abundances. Colour indicates the iron abundances and black circles indicate flagged measurements. Text annotates mean values and dispersion, which can also be found in Table 2.5 together with individual lists for dwarfs and giants. **Figure Credit:** Paper I.

GALAH DR2 vs. 714 dwarf spectra from Bensby et al. (2014) In this section, we compare the general trends of the stars with similar parameters ($T_{\rm eff} > 5500$ K or $\log g > 3.3$) to the stars analysed by Bensby et al. (2014). Their first study included the elements O, Na, Mg, Al, Si, Ca, Ti, Cr, Ni, Zn, Y, and Ba. Battistini & Bensby (2015) added a similar, homogeneous follow-up analysis of Sc, V, Mn, and Co. The follow-up study of neutron-capture elements by Battistini & Bensby (2016) includes the elements La and Eu, while Bensby & Lind (2018) have published Li measurements for the 714 dwarfs. We here abbreviate these studies together as "Bensby studies". Similar to the study in **Paper II**, the majority of dwarfs in GALAH DR2 covers metallicity / iron abundance ranges of $-0.7 <$ [Fe/H] < 0.5. We hence refer the reader to the detailed discussion by **Paper II** and only briefly discuss the trends we see for each element represented in the Bensby studies. From Figures 2.24, 2.25, and 2.26 we see:

- For several element abundances (O, Si, Ca, Ti, Mn, and Zn), measured in the Bensby studies and our Data Release 2, we find a strong agreement of the trends, manifested in the overlap of the majority of our stars (with highest density in the yellow regions in these figures) with the high-quality data points of the Bensby studies.
- For Na, Al, Sc, Cr, Ni, Y, and Ba we see good agreement of the general trends, but minor shifts of the mean abundance around iron abundances of -0.2 dex, which might originate in zero-point offsets or target selection differences. For Y and Ba, the different mean abundances might be a manifestation of the different ages and hence different s-process enhancements.
- In GALAH we see a rather flat but not decreasing Mg abundance in the super-solar regime. Contrary to Bensby et al. (2014), this trend is also found by APOGEE (see neighboring panel in Figure 2.24).
- Because of the detection limits and flagging algorithm, we can not measure a large number of Li, C, Co, La, and Eu abundances.
- In the case of Li, we can usually only estimate the abundance for Li-rich stars. However, we have also been able to identify numerous metal-poor dwarfs following the Spite plateau (Spite & Spite, 1982) and giants with lower Li around the solar photospheric value, which show strong enough lines due to their cool atmospheres (**Paper I**). For Co and Eu, the metal-rich end of GALAH overlaps with stars of the Bensby studies. For La, however, we see a disagreement. Zero-point offsets of around 0.25 dex would however lead to an agreement for dwarfs (but La under-abundances in giants). Additionally, we can not estimate C abundances in almost any giants (due to the highly excited line we can use in the GALAH range).

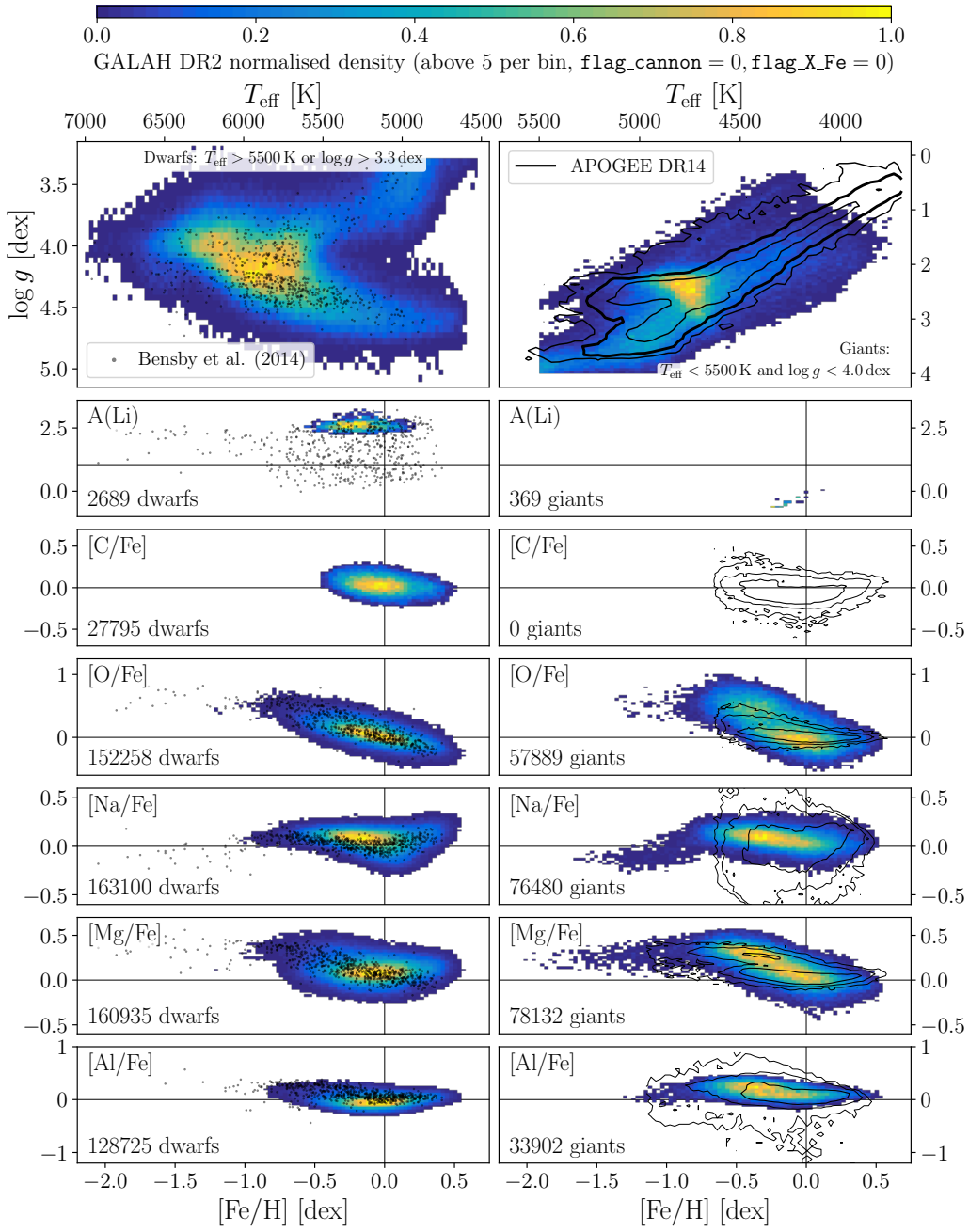

Figure 2.24: Comparison of the Kiel diagrams (top panel) and individual abundances (Li through Al) for the sample of 714 dwarfs (Bensby et al., 2014; Battistini & Bensby, 2015, 2016; Bensby & Lind, 2018) on the left hand side as well as APOGEE DR14 giants (Abolfathi et al., 2018) on the right hand side. GALAH DR2 data (with `flag_cannon` = 0 for stellar parameters and `flag_X_fe` = 0 for the respective element X) are plotted as colored density with a minimum of 5 stars per bin. The literature values for dwarfs are overplotted as black dots, while the APOGEE giants (with finite values, `ASPCAPFLAG` = 0, and `STARFLAG` = 0 for stellar parameters as well as `X_FE_FLAG` = 0 for the respective element X) are shown as contours. **Figure Credit:** Paper I.

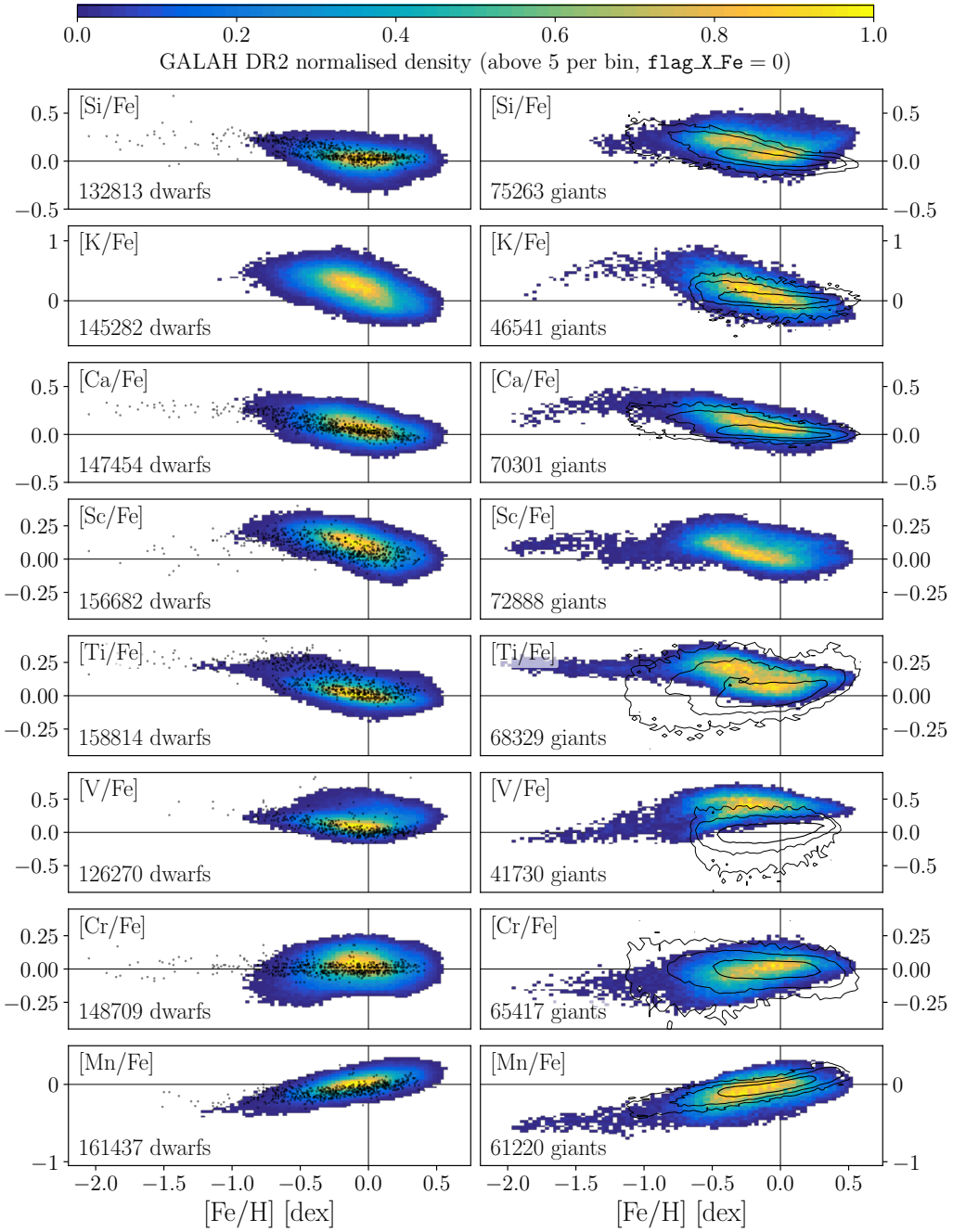

Figure 2.25: Continuation of Figure 2.24 for elements Si through Mn. **Figure Credit:** Paper I.

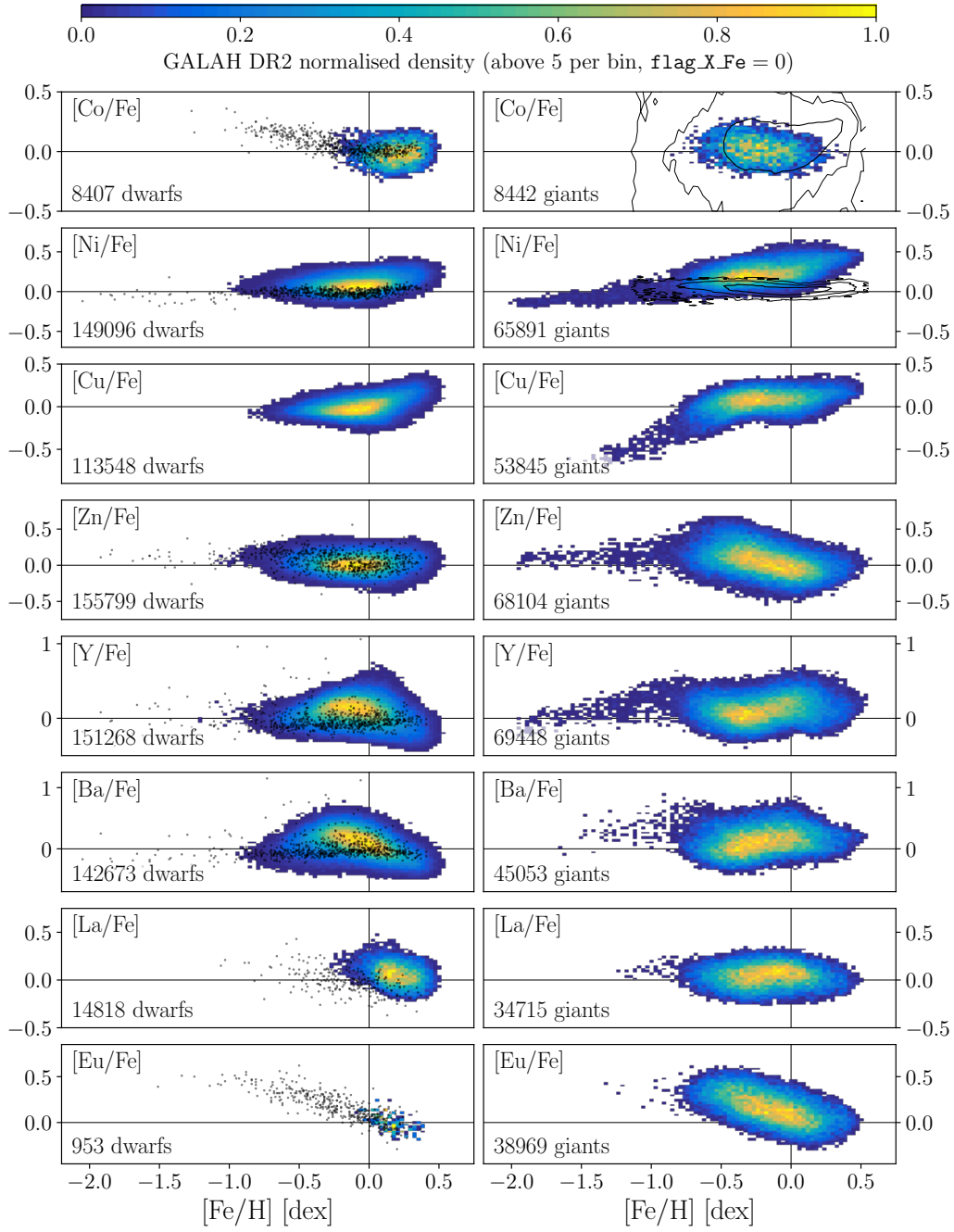

Figure 2.26: Continuation of Figures 2.24 and 2.25 for elements Co through Eu. **Figure Credit:** Paper I.

GALAH DR2 vs. APOGEE DR14 In the right hand panels of Figures 2.24 to 2.26, we compare GALAH DR2 giants with those of APOGEE. The GALAH DR2 giants and their abundances are based on the selection of stars with $T_{\rm eff} < 5500$ K and $\log g < 4$, covering the majority of stars from the calibrated APOGEE sample. While we can see a good agreement of the APOGEE-based contours along the red giant branch, we note that the red clump region of APOGEE is more elongated and GALAH DR2 shows a rather local overdensity. We note that stars identified as red clump stars have been shifted based on calibrations with asteroseismic values. For GALAH DR2, we include a large number of stars with asteroseismic surface gravities, but to span the parameter space in this region, we have to also include stars without this precise gravity information. We also want to stress, that the parameter space for which the GALAH pipeline is optimised, does not include the very luminous giants and therefore we can not reliably provide stellar parameters for stars below 4000 K.

- When comparing our results with APOGEE DR14, we see good agreement of the abundance trends for Mg, Al, and Mn.
- The [O/Fe] vs. [Fe/H] trends exhibit a steeper slope for giants in GALAH than for dwarfs or for giant stars in APOGEE DR14. These differences might result from the use of different lines and assumptions. While GALAH uses atomic O lines and takes non-LTE into account, APOGEE uses molecular OH bands assuming LTE to estimate [O/Fe]. Additionally, the disagreement could be caused by 3D effects (Amarsi et al., 2016a). We note that the missing flattening of [O/Fe] for the metal-rich regime measured by GALAH is however consistent with other studies and a reason to not treat oxygen as a regular α-element.
- Na agrees for the highest density of stars, but in the GALAH giant abundances, the upturn of [Na/Fe] in the metal-rich regime is not seen, contrary to the results in dwarfs and APOGEE.
- For Si in giants, we note a disagreement at the metal-rich regime ([Fe/H] > 0) where we measure an increase of [Si/Fe] contrary to measurements for dwarfs and APOGEE DR14. We note however a significant bimodality in [Si/Fe] as one would expect from an overlap of thin and thick disc stars.
- K is affected by non-LTE effects in giants as well as by interstellar absorption, which makes the comparison with APOGEE more difficult.
- For [Ca/Fe] there is a zero point difference but otherwise a good agreement for this element.
- We note strong disagreement for Ti, where GALAH follows the expected α-element behaviour but APOGEE does not; for further discussions see e.g. Albareti et al. (2017) and Hawkins et al. (2016).
- For V we see a significant disagreement with both the dwarf abundances and APOGEE DR14. We report this element anyway, because of the useful abundances in dwarfs, but advise not to use of [V/Fe] in giants.

- For Cr, we see a good agreement, but the Cr abundance of APOGEE DR14 giants follows Fe even closer than for GALAH DR2 stars.
- Even though we have not been able to measure many Co abundances due to weak and blended lines, the number densities of the two surveys seem to be consistent.
- Our Ni trend for giants with [Fe/H] > -0.5 is higher than the one seen APOGEE DR14, where Ni tracks Fe closely, as expected from other studies (e.g. Bensby et al., 2014; Hawkins et al., 2016). We note that our dwarf-based [Ni/Fe] results are significantly better.
- In addition, in this data release we include some elements not covered by APOGEE DR14, including Li, Sc, Cu, Zn, Y, Ba, La, and Eu. In general the GALAH results for giants and dwarfs are in reasonably good agreement but with giants we can trace those abundance trends to lower metallicities.

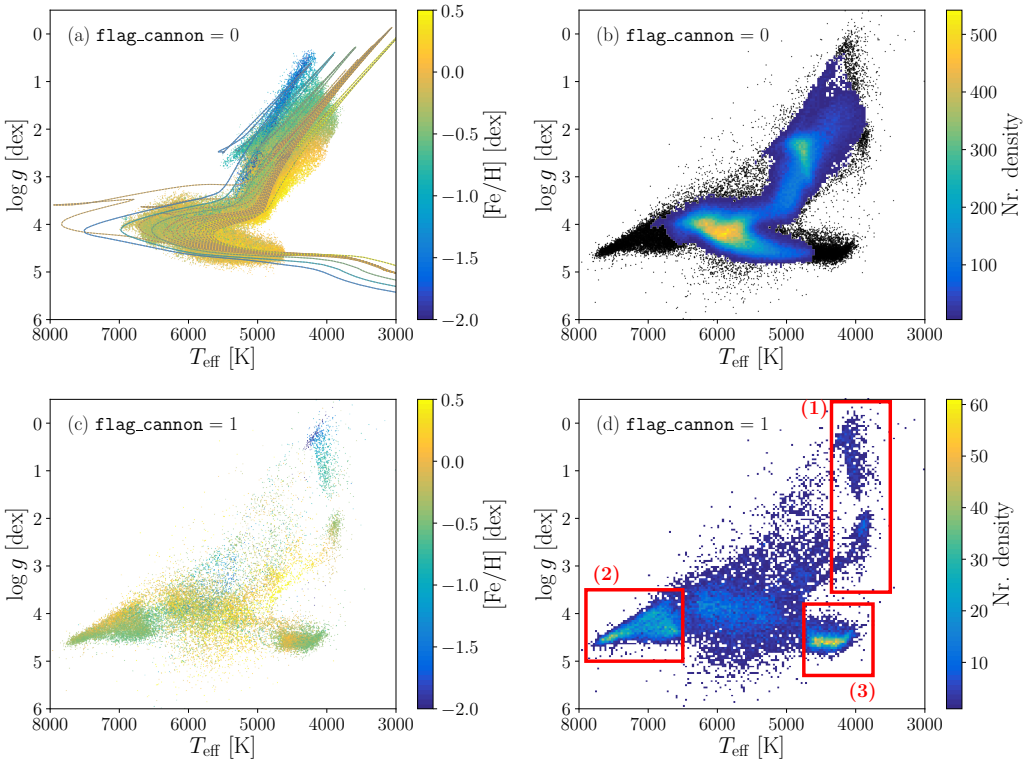

Figure 2.27: Kiel diagrams of the GALAH data release 2. (a) stars with `flag_cannon` = 0 colored by their iron abundance, (b) stars with `flag_cannon` = 0 as density plot with stars with `flag_cannon` = 1 as black dots in the background for perspective, (c) stars with `flag_cannon` = 1 colored by their iron abundance, (d) stars with `flag_cannon` = 1 as density plot. **Figure Credit:** Paper I.

2.3.3.9 SYSTEMATIC TRENDS IN THE PARAMETER SPACE

The GALAH survey data covers a large range of stars with different stellar parameters and includes spectra with peculiarities. Although the majority of stars can be described with one set of stellar labels (see the unflagged stars of this data release shown in Figure 2.27), we face many challenges in the analysis, which can compromise these labels. The identification of the influence of shortcomings of our analysis is complex and an ongoing process. We want to stress that our pipeline is only tailored for non-peculiar spectra of single stars of spectral type F, G and K, which constitute the vast majority of the survey targets. We are also mindful that a quadratic model might not describe all spectra perfectly within the parameter space and imperfect training labels can introduce systematic trends in the final results. We hence identify and point out several systematic trends in the parameter space of this data release, which may contribute to these shortcomings of the analysis:

- Red clump stars: According to stellar evolution models, red clump stars should be concentrated at a certain locus in the Kiel diagram due to their similar stellar parameters. For solar metallicity, these stars are expected around $4600 < T_{\rm eff} < 4850\,\mathrm{K}$ and $\log g \approx 2.5\,\mathrm{dex}$ with extensions towards $T_{\rm eff} = 4950\,\mathrm{K}$ and $\log g \leq 2.9\,\mathrm{dex}$ (Bovy et al., 2014). While there is an over-density in the expected locus, with the DR2 stellar parameters the shape of the red clump is not entirely as expected, but extending to too high surface gravities (Figure 2.27b). Although we note that this density structure might partially originate from stars at the red giant branch bump, the reason for this behaviour is not yet known. We have tested this behaviour using only asteroseismically-based estimates of the surface gravities for the training set around this region but have not achieved a significant improvement in the appearance of the red clump.
- Cool giants: In the optical regime, strong molecular absorption lines dominate the HERMES spectra for $T_{\rm eff} \lesssim 4500\,\mathrm{K}$. The resulting blending of our diagnostic lines (H, Sc, Ti, and Fe) introduces degeneracies and systematic trends like the overestimation of surface gravities with coincident underestimation of metallicity. Without external information to break those degeneracies, we are currently unable to estimate reliable stellar parameters for the most luminous cool giants in our sample and had to exclude this region from the training set. *The Cannon* is therefore extrapolating the labels of these stars, covering the cool end of the red giant branch (group (1) in Figure 2.27d).
- Hot stars: Stars hotter than cool F types are typically dominated by extended Balmer lines and exhibit only a few, weak metal lines within the HERMES wavelength range. The spectra of these stars hence include less and degenerate information on all stellar parameters. Until now, we have neither been able to analyse these stars with our pipeline, nor include these stars in the training set. Although *The Cannon* model can extrapolate the stellar parameters of these stars, their parameters show systematic trends (group (2) in Figure 2.27d). The surface gravities of these stars are overestimated and stars with effective temperatures $> 7000\,\mathrm{K}$ are typically

underestimated, as the comparison with Gaia benchmark stars (Section 2.3.3.3) and IRFM (Section 2.3.3.5) have shown. It is also noted that the high rotational velocities of these hotter stars make the analysis more difficult both for the SME and *The Cannon* steps.

- Cool dwarfs: Similar to cool giants, molecular absorption lines dominate the spectra of cool dwarfs. Because of the low amount of non-peculiar cool dwarfs overlapping with TGAS, we have not been able to include enough cool dwarfs in the training set to ensure a good coverage of these stars and are hence flagging them (group (3) in Figure 2.27d). We note however, that the significant upturn for cool dwarfs in the previous data releases (Martell et al., 2017; Sharma et al., 2018) has been largely removed by the use of astrometric information to break degeneracies with surface gravity.
- Some over-densities in abundance space: We have tried to implement a flagging algorithm to identify unreliable data but we can not exclude that some reliable stars are flagged and vice-versa. We recommend that only unflagged stars and abundances should be used as far as possible. This would for example avoid the problematic groups in Figure 2.27, or under-abundant [Si/Fe] or [Ti/Fe] that otherwise would lead to erroneous abundances. In some cases however it has not been possible to flag the results even if the abundances are expected to be questionable. We caution that the K I 7699 Å line can be affected by interstellar medium absorption, which has not been taken into account; this is expected to be of particular concern at low metallicity when the stellar line is weak and for low-latitude fields where the reddening is high. We also stress that the V lines employed in GALAH are especially vulnerable to blending, which is likely causing the inferred V abundances in giant stars in particular to be susceptible to systematic errors (Figure 2.26). As always when not accounting for departures from LTE, systematic errors may be present; in DR2 we have made an effort to include non-LTE calculations for key elements such as Li, O, Na, Mg, Al, Si, and Fe, but several other elements remain to be studied in detail.

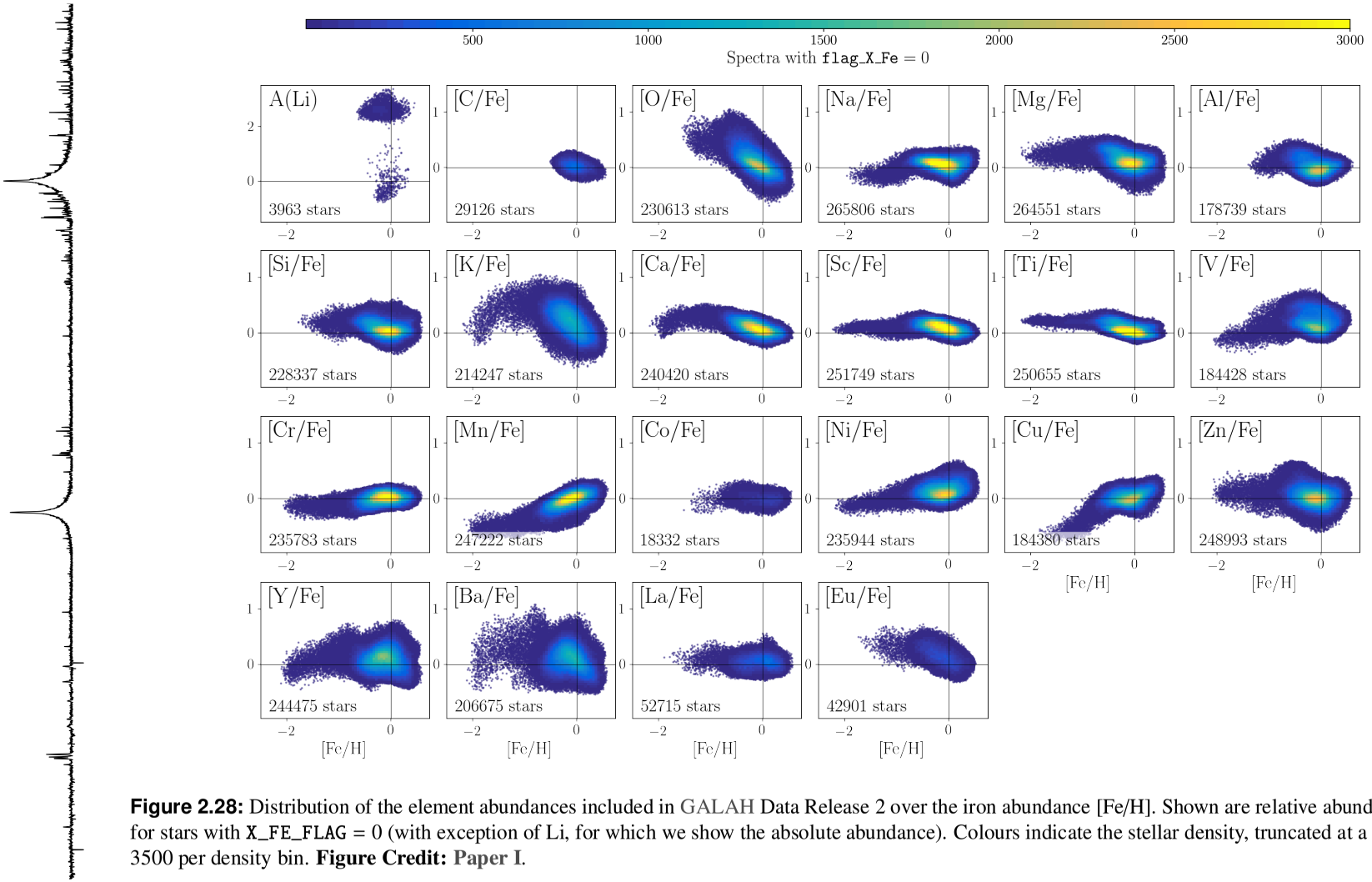

Figure 2.28: Distribution of the element abundances included in GALAH Data Release 2 over the iron abundance [Fe/H]. Shown are relative abundances [X/Fe] for stars with `X_FE_FLAG` = 0 (with exception of Li, for which we show the absolute abundance). Colours indicate the stellar density, truncated at a maximum of 3500 per density bin. **Figure Credit:** Paper I.

2.4 SPECTROSCOPIC ANALYSES AFTER *Gaia* DR2

Until 25 April 2018, the analyses described in Sec. 2.3 were the most advanced ones for individual spectra of the GALAH survey - they included the use of data-driven approaches to improve both speed and precision, but were performed almost entirely without non-spectroscopic information for individual spectra. The publication of *Gaia* DR2 on the aforementioned day provided 5-parameter astrometry for 1.3 billion stars and can be understood as a game changer for stellar analysis; in particular, the large number of stars with high-precision parallaxes.

Parallaxes are now available for almost all stars observed by GALAH and a vast majority of them are very precise, see Fig 2.29. Overall, currently 728651 spectra have matched parallax measurements, 85 % (619333) even with parallax uncertainty < 10 %. When dividing the sample into giants (TEFF < 5500 K and M_{K_S} < 2 mag), 93 % (454406/488192) of the observed dwarf spectra have parallax uncertainties below 10 % and 69 % (164927/240459) of the observed giant spectra have parallax uncertainties below 10 %. The use of inferred distance estimates by Bailer-Jones et al. (2018) delivers even more reliable distance estimates, which is most important for the largest parallax uncertainties (see right panel of Fig. 2.29).

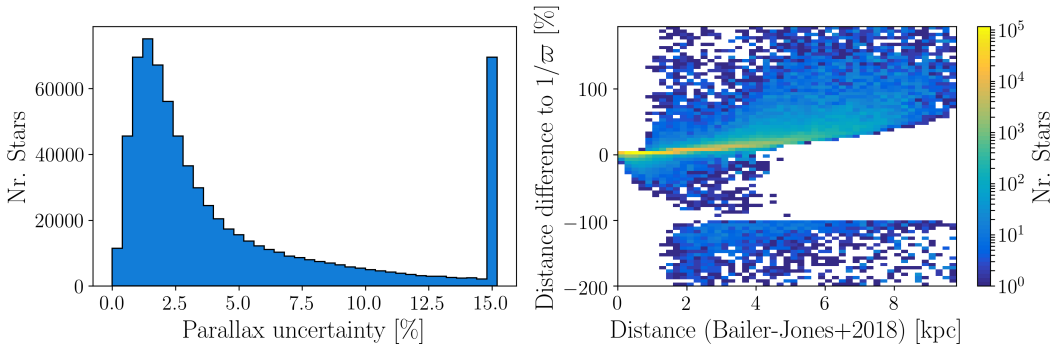

Figure 2.29: Overview of parallaxes/distances of the stars observed by GALAH until January 2019. **Figure Credit:** **Paper IV**.

Additionally, the progress in the analyses of observations of the K2 campaigns is providing more and more asteroseismic information. The overlap between GALAH targets and K2 targets from campaign C1-C8 and C10-C13 has increased the number of stars with measured asteroseismic $\nu_{\max}$ values to almost 15,000 and covers almost the entire giant branch, that is 1.5 < log g < 3.5, with its various evolutionary stages.

While the use of such external data has been implemented in the spectrum synthesis pipeline of the GALAH collaboration, the implementation for the data-driven pipeline is yet to be done and it was hence decided produce the stellar labels for the next data release with the spectrum synthesis pipeline as a first step. The collaboration will also test data-driven algorithms like *The Cannon* to improve the precision of the estimated parameters and abundances even further. The achieved improvements and implementations of the spectrum synthesis pipeline for the stellar parameters are described in Sec. 2.4.1 and

Sec. 2.4.2, respectively, and the quality of the final stellar parameters is assessed in Sec. 2.4.3

At the same time, several other improvements have been made to the abundance analysis, which includes now a line-by-line analysis, as laid out in Sec. 2.4.4 and an assessment of the abundance quality in Sec. 2.4.5.

In addition to stellar parameters and abundances, two value-added-catalogs of stellar ages and dynamical information will be provided with the next data release and both catalogs are described in Sec. 2.4.6.

2.4.1 THE 'FREE', 'BOLOMETRIC', AND 'ASTEROSEISMIC' PIPELINE

With the available non-spectroscopic information, three different pipeline setups can be used. The first pipeline setup is not using any non-spectroscopic information and we refer to it as the 'free' pipeline. The second one uses astrometric and photometric information and is referred to 'bolometric' pipeline. The last setup is using asteroseismic information and referred to as 'asteroseismic' pipeline. The main difference between those pipelines is the way in which $\log g$ is estimated:

$$\begin{aligned} \text{'Free' pipeline:} \quad & \log g = f(\text{spectrum}) \\ \text{'Bolometric' pipeline:} \quad & \log g = f(T_{\rm eff}, M, L_{\rm bol}) \\ \text{'Asteroseismic' pipeline:} \quad & \log g = f(T_{\rm eff}, \nu_{\rm max}) \end{aligned}$$

The latter pipeline is expected to deliver the highest fidelity estimates for $\log g$, because the asteroseismic information delivers both accurate and precise constraints in the framework of the scaling relations from Eq. 2.4 (see e.g. Kjeldsen & Bedding, 1995). Contrary to the estimation via bolometric measurements, these relations do also not rely on stellar masses, iron abundances, or reddening. Furthermore the dependence on $T_{\rm eff}$ is lower for the asteroseismic scaling relations than for the 'bolometric' pipeline. We hence treat it as reference value when subsequently testing the differences between the pipelines.

We have selected a set of 3175 spectra, for which both astrometric and asteroseismic information is available from *Gaia* DR2 and four K2 campaigns (C1, C4, C6, and C7, see e.g. Stello et al., 2017, and priv. communication), but included all information, regardless of quality (e.g. low S/N, wrong $\nu_{\rm max}$ values, and problematic reductions) and employed all three aforementioned pipeline setups to estimate stellar parameters. Because of the cadences and observation periods of the K2 campaigns, the sample is expected to contain almost exclusively giant stars with $1.5 < \log g < 3.0$.

The results are shown in 2.30, where the upper panels show the density distribution in the $T_{\rm eff}$ vs. $\log g$ plane and the lower panels show the mean [Fe/H] for selected parameters bins. The parameters in the left panels are the results of the 'free' pipeline, the middle ones from the 'bolometric' pipeline, and the right ones from the 'asteroseismic' pipeline. From the top panels it can be concluded, that the 'bolometric' performs significantly better than the 'free' pipeline and only performs slightly worse than the 'asteroseismic' pipeline. This is most evident for the RC stars, which smear out when only spectroscopic information is used. The mean [Fe/H] also shows a trend towards

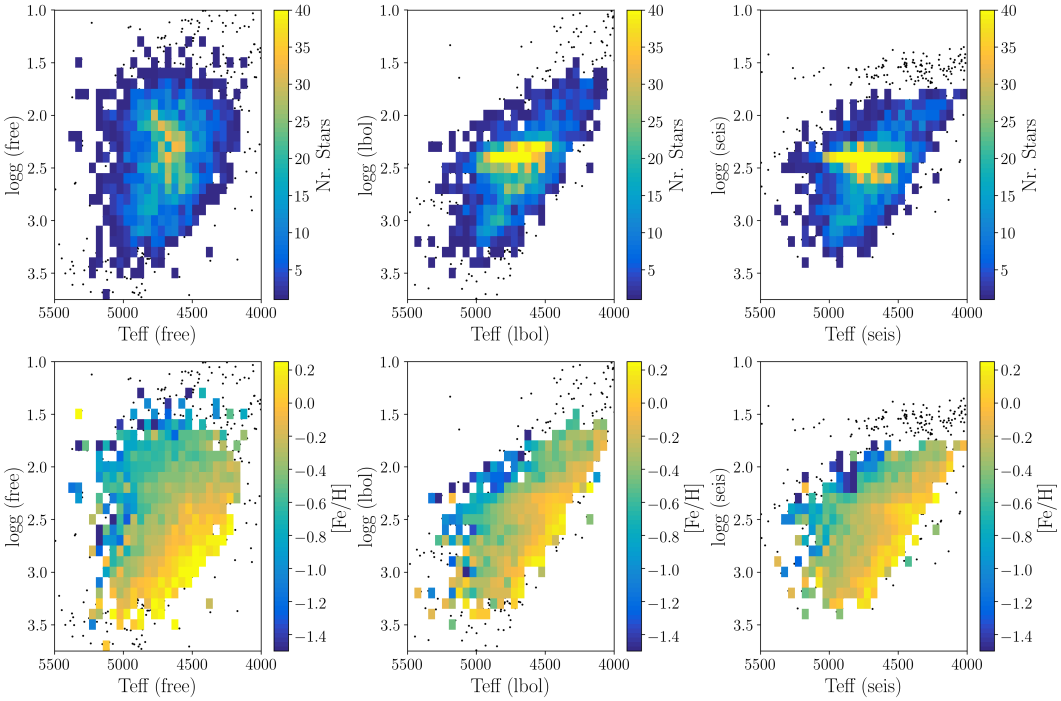

Figure 2.30: $T_{\rm eff}$ vs. $\log g$ diagrams showing the performances of the three GALAH synthesis pipelines, that is 'free' (left panels, abbreviated with 'seis'), 'bolometric' (middle panels, abbreviated with 'lbol'), and 'asteroseismic' (right panels). The upper panels show the density distributions, whereas the lower panels depict the mean iron abundances [Fe/H] for chosen bins. **Figure Credit:** Paper IV.

both under- and overestimated values (see bottom left and right panels). When looking at the differences between the estimated surface gravities of the 'free' and 'asteroseismic' pipelines, as shown in the left panel of Fig. 2.31, it becomes evident that surface gravity of RGB stars is in general more scattered but shows no significant bias. The RC stars (around $\log g \sim 2.4$), however, suffer from a significant systematic bias and are hence driving a general bias of $\Delta \log g = -0.10 \pm 0.28$ with respect to the 'asteroseismic' results.

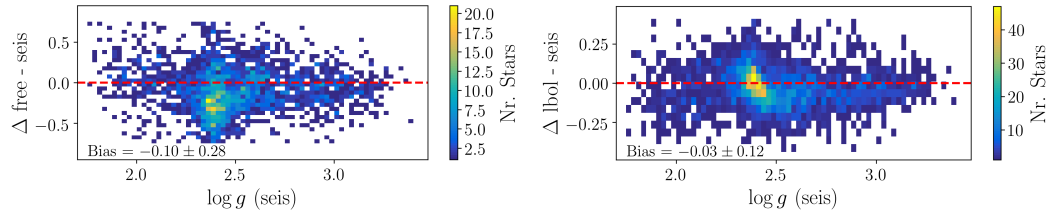

Figure 2.31: Difference of $\log g$ for the 3175 analysed stars with asteroseismic information, that is 'free' - 'asteroseismic' in the left panel and 'bolometric' - 'asteroseismic' in the right panel. **Figure Credit:** Paper IV.

The comparison of $\log g$ between 'bolometric' and 'asteroseismic' pipelines, see right panel of Fig. 2.31 shows that there is no bias for the RGB stars. For RC stars the

'bolometric' pipeline tends to over- or under-estimate $\log g$ towards the hot and cool ends of the RC, respectively. This trends is, however, limited to less than 0.15 dex and we hence conclude that the 'bolometric' pipeline is delivering surface gravities in good agreement with the 'asteroseismic' pipeline, that is a difference of $\Delta \log g = -0.03 \pm 0.12$ with a standard error of 0.002 throughout the range of $1.5 < \log g < 3.5$. Given the 3175 measurements, this bias is significant but small. Similarly small biases are found for the other two stellar parameters, that is $\Delta T_{\rm eff} = -21 \pm 39$ K and Δ[Fe/H] $= -0.03 \pm 0.05$. This agreement suggests that the 'bolometric' pipeline is not only delivering accurate parameters for the dwarfs, as shown in **Paper I** and **Paper II**, but also the giants and hence applicable for the vast majority of stars observed by the GALAH survey. Although the 'asteroseismic' pipeline is the most accurate one, its use is limited to the significantly smaller fraction of stars with measured asteroseismic information. In any case, the 'free' pipeline should only be used if both the 'asteroseismic' and 'bolometric' pipeline are either not applicable or their information is expected to be biased. This is for example expected in the case of the observation of an unresolved photometric binary star with significantly overestimated bolometric luminosity and thus underestimated surface gravity. However, the binarity may of course affect the purely spectroscopic analysis as well.

2.4.2 SPECTROSCOPIC ANALYSIS APPLIED FOR GALAH DR3

We have implemented the same analysis procedure as for the spectrum synthesis analysis of GALAH DR2 (see Sec. 2.3.1), but adjusted the pipeline for the stellar parameter estimation in the following ways:

- We only employ the 'bolometric' pipeline, which estimates the surface gravity consistently as a function of spectroscopic $T_{\rm eff}$, isochrone estimated mass, and bolometric luminosity derived from the 2MASS K_s-band, following Eq. 2.5.
- We are now using SME version 536, which includes a χ^2 optimisation with a double-sided partial derivative estimation as outlined by Piskunov & Valenti (2017).
- We have slightly adjusted the continuum selection and normalisation schemes, by lowering the number of data points to be used as continuum points and made the outlier identification of spikes more robust.
- We employ the same mass and age estimation code as in **Paper I**, that is a maximum likelihood estimation in the Bayesian framework of the ELLI code (Lin et al., 2018). Contrary to **Paper I** (using Dartmouth isochrones without core helium burning stages) and the code version from Lin et al. (2018) (using MIST isochrones without α-enhancement), we use PARSEC isochrones (Bressan et al., 2012), which includes both core helium burning stages and a metallicity estimate inferred from iron- and α-abundances. For this study, we use a grid of PARSEC-v1.2S isochrones (Bressan et al., 2012; Tang et al., 2014; Chen et al., 2014, 2015), downloaded with the default values from CMD 3.0 (`http://stev.oapd.inaf.it/cmd`) for ages $\tau = 0.5(..0.5..)13.5$ Gyr and [Fe/H] $= -2.4(..0.1..)0.6$, which was converted to

[M/H] with the enhancement formula from Salaris & Cassisi (2005) and standard α-enhancement ([α/Fe] = 0 for [Fe/H] $\geq$ 0, [α/Fe] = 0.4 for [Fe/H] ≤ -1, and a steady linear relation between both iron abundances). We calculate ages and masses as the weighted averages of ages and masses of each isochrone in the set, with the weights being the likelihood (assuming no covariance between the parameters, see Eq. 2 in Lin et al. (2018)).

- We are using departure coefficient grids for the non-LTE abundance estimation for H (Amarsi et al., 2018). Furthermore, Amarsi et al. (in prep.) have recalculated the departure coefficient grids that were already employed for GALAH DR2 (Li, O, Na, Mg, Al, Si, and Fe) and have expanded the grids for more elements. For GALAH DR3 we are thus testing the use of 1D non-LTE grids for H, Li, C, N, O, Na, Mg, Al, Si, K, Ca, Mn, Fe, Co, and Ba.

An overview of the (reliable) stellar content of GALAH DR3 is shown in Fig. 2.32, where the left panel shows the density distribution of the spectra across the $T_{\rm eff}$ vs. $\log g$ plane and the right panel the mean iron abundance across the same parameter space for those stars with reliable parameters (`flag_sp` = 0). Stars with raised quality flags (`flag_sp` > 0) are neglected in the figure, but are discussed later subsequently, when the the quality assessment is discussed in Sec. 2.4.3.

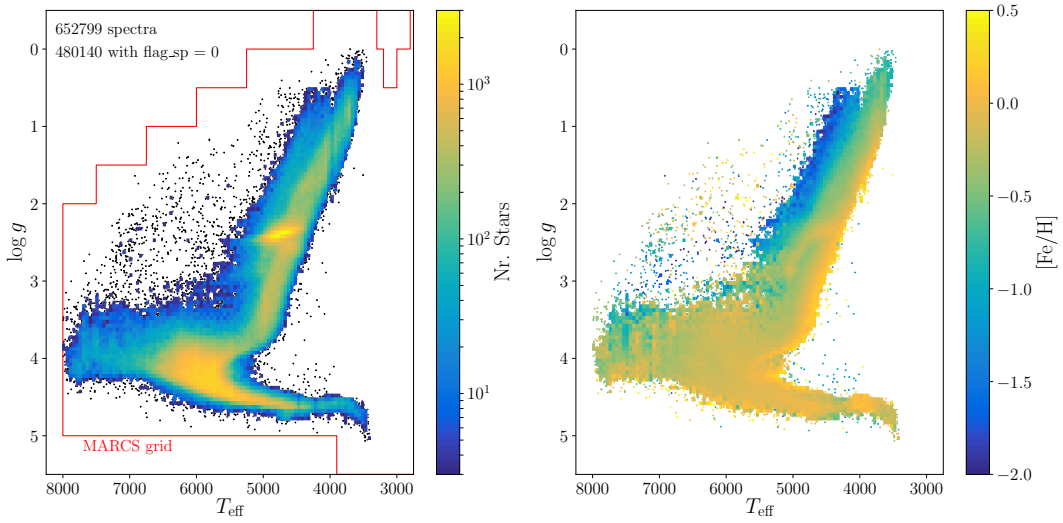

Figure 2.32: Kiel diagrams ($T_{\rm eff}$ vs. $\log g$) color coded by the density of stars per bin (left panel) and mean iron abundance [Fe/H] within a bin (right panel) for all stars of the GALAH data release 3 with exquisite `flag_sp` = 0. The total number of spectra and those below the quality threshold are annotated in the upper left corner of the left panel. In the same panel, red lines indicate the grid limit of the MARCS atmosphere grid, which marks the limits of the synthesis computations. **Figure Credit:** Paper IV.

The computations are limited by the available MARCS atmosphere grids (building a convex hull for the estimated parameters). Almost two-thirds of all stars are distributed in the MS and turn-off regime between 4500 and 6500 K. Roughly a third of the stars are situated along the RGB, with a significant overdensity around $\log g \sim 2.4$ dex, that is, the

RC. We stress that for the first time we can also identify an overdensity at $\log g \sim 2.6$ dex as part of the spectroscopic GALAH analyses. Such an overdensity was first identified observationally in CMD by King et al. (1985) and attributed to the RGB bump, but so far not seen in the spectroscopic $T_{\rm eff}$ vs. $\log g$ plane.

2.4.3 QUALITY ASSESSMENT OF STELLAR PARAMETERS

To assess the quality of the stellar parameters, we resort to the commonly used comparison samples for accuracy, that is the *Gaia* FGK benchmark stars (GBS) and the stars with asteroseismic information. For the precision assessment we use the internal uncertainty estimates and repeat observations of the same stars. We calculate the final stellar parameter errors for a given parameter X via

$$e^2_{\rm final}(X) = e^2_{\rm accuracy}(X) + e^2_{\rm fit}(X) + e^2_{\rm repeats}(X). \tag{2.13}$$

We note that $e^2_{\rm fit}(X)$ and $e^2_{\rm repeats}(X)$ are typically expected to be the same tracer of precision and hence only their maximum value should be used, that is

$$e^2_{\rm final}(X) = e^2_{\rm accuracy}(X) + \max\left(e^2_{\rm fit}(X) + e^2_{\rm repeats}(X)\right). \tag{2.14}$$

We elaborate on the choice of error combination when we assess the precision of the stellar parameters.

To identify those stars and spectra with less or unreliable information, we have implemented a combination of the flagging algorithms already applied to GALAH DR2 (see **Paper I**) and new algorithms.

ACCURACY ASSESSMENT WITH THE *Gaia* FGK BENCHMARK STARS (GBS)

When comparing the estimated stellar parameters (blue error bars) for the observed GBS with those from Jofre et al. (2018), we do not find any significant biases regarding $T_{\rm eff}$ and $\log g$, but had to correct a bias of [Fe/H] = −0.10 (underestimated [Fe/H]), see Fig. 2.33. Underestimated temperatures for the hottest stars are still likely, but more testing is needed as the continuum normalisation has been improved and hydrogen has been implemented in non-LTE now. More importantly, the scatter with respect to the GBS values by Jofre et al. (2018) has decreased significantly for $\log g$ and noticeably for $T_{\rm eff}$ and [Fe/H] as can be seen in the diagram, where also results from a purely spectroscopic analysis are shown in black for the same stars.

In addition, we have been able to show that the pipeline can now also estimate stellar parameters of core-helium burning stars, including horizontal branch stars. Horizontal branch stars have not been included in the training set used for the analysis of GALAH DR2. We have noted however, that for very distant stars (e.g. the bright stars in the LMC), the inferred distances by Bailer-Jones et al. (2018) are too low and lead to an overestimated $\log g$.

ACCURACY ASSESSMENT WITH THE STARS WITH ASTEROSEISMIC INFORMATION

The biases between the 'asteroseismic' and 'bolometric' pipeline for the stellar parameters are minor as discussed in Sec. 2.4.1. However, we find systematic differences

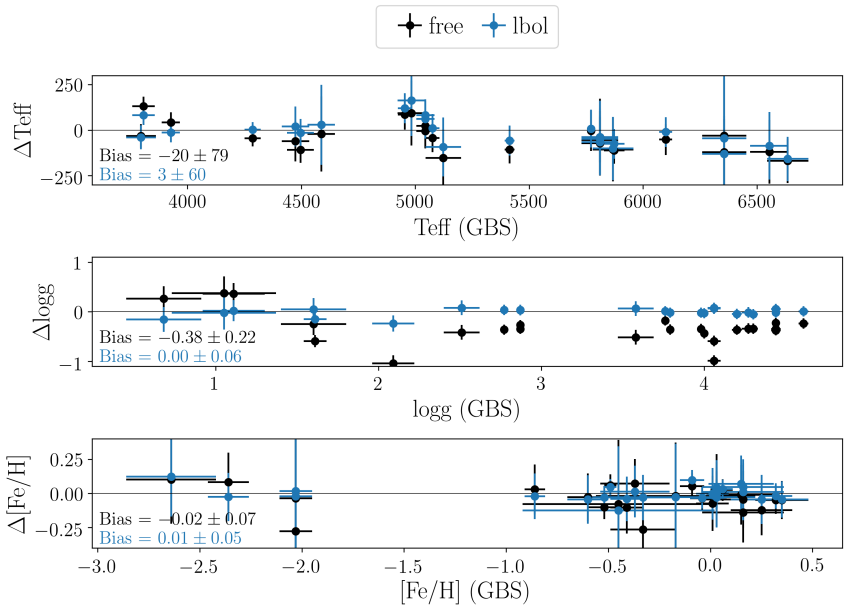

Figure 2.33: Performance of GALAH synthesis pipeline with the 'free' (black) and 'bolometric' (blue) pipeline. **Figure Credit:** Paper IV.

between photometric (isochrone) and asteroseismic masses of RC stars, in particular for the most metal-rich isochrones. The isochrone grid is very dense in this regime and and spectroscopic parameters of the RC stars overlap strongly with those of RGB stars. An et al. (2019), however, found similar differences and suggest that standard RC isochrone models need to be re-examined. Additionally, we suggest that the validity of the asteroseismic scaling relations (see e.g. Epstein et al., 2014; Huber et al., 2017; Viani et al., 2017; Pinsonneault et al., 2018) for the most metal-poor and metal-rich stars should be examined further.

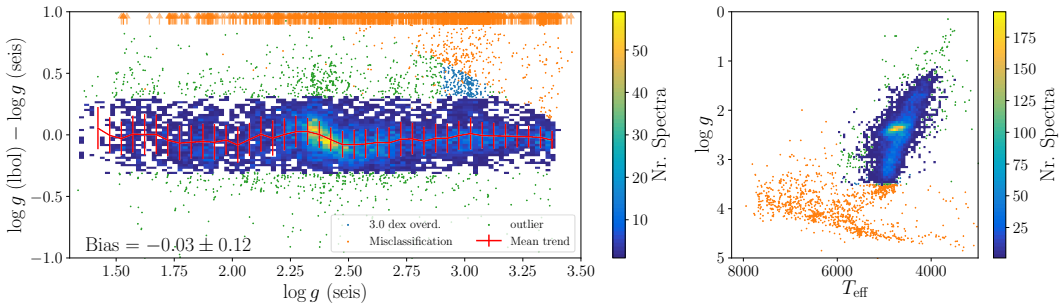

Figure 2.34: All stars with asteroseismic information from the K2 asteroseismic analyses (Sharma and Stello, priv. communication). The colorbar indicates spectra with good asteroseismic information. Misclassifications, that is clear dwarfs with underestimated $\nu_{\max}$ values are shown in orange, an overdensity with wrong $\nu_{\max}$ values at $\log g = 3$ is shown in blue and significant outliers are shown in green. **Figure Credit:** Paper IV.

In addition to the sample of 3175 spectra that we analysed with different pipelines, we have examined the accuracy of our surface gravities for an even larger sample of stars with asteroseismic information from the complete K2 analysis (Sharma and Stello, priv. communication). We compare the $\log g$ estimated from $T_{\rm eff}$ and $\nu_{\rm max}$ with the $\log g$ from the 'bolometric' pipeline in the left panel of Fig. 2.34. As stated in Sec. 2.4.1, the K2 data is expected to currently only allow reliable asteroseismic results for giants with $1.5 < \log g < 3.0$. The comparison of the 'asteroseismic' and 'bolometric' pipeline showed that the K2 pipelines also estimate wrong $\nu_{\rm max}$ value for 7.5% of the sample (orange misclassifications), that is $\nu_{\rm max}$ values that are too low for the actual log. We identify such wrong classifications in Fig. 2.34 in orange and blue. The latter color indicates an overdensity of wrong $\nu_{\rm max}$ values suggesting $\log g = 3.0$, although the actual $\log g \sim 3.5$ is beyond the expected detection limit. Orange colors indicate all other misclassified stars, that is mainly dwarfs with significantly underestimated $\nu_{\rm max}$ values. After cleaning the sample from these outliers, we estimate the systematic difference between the $\log g$ from the 'bolometric' pipeline and $\log g$ from $T_{\rm eff}$ and $\nu_{\rm max}$ (see color coded distribution in Fig. 2.34) and find the same small bias as for the 3175 spectra, that is -0.03 ± 0.12. The lower standard error of this measurements is 0.001 indicates that this bias is even more significant.

PRECISION ASSESSMENT WITH INTERNAL AND UNCERTAINTIES

To estimate the precision of stellar parameters, we use both internal SME covariance errors and repeated observations of the same star. We have estimated the standard deviations of repeated observations for the same fiber, different fibers, and irrespective of the fibre and plot their standard deviations as a function of S/N in CCD2 together with the median SME covariance errors in Fig. 2.35 for the fitted stellar parameters $T_{\rm eff}$, $\log g$, iron line abundance [Fe/H], the atmosphere iron abundance [Fe/H], rotational broadening $v_{\rm broad}$, and radial velocity $r_{\rm rad}$.

The trends of internal and repeat precision are expected to be similar, but we find that the uncertainties from the internal SME covariance uncertainties are typically significantly lower than those from repeat observations (with exception of $\log g$, which we discuss subsequently). As discussed when introducing the final error estimation with Eq. 2.13, the two precision estimates should be the same and a rescaling of the internal SME-based uncertainties would lead to a consistent precision measure. First estimates suggest that a rescaling with a factor of 2.5 yields an agreement of repeat observations and internal uncertainties for $T_{\rm eff}$. For the other parameters, however, also an the uncertainty floors of the two precision estimates are different and we thus need to still explore more complex scaling relations. For the purposes of the internal data release, we hence decide to calculate the precision as a combination of both estimates. This allows to combine the individual estimate of the fit quality (through the internal SME-based uncertainty) with the general precision expected for a given S/N, which would otherwise be underestimated when only using to the internal uncertainty. In order to allow the estimation of the repeat precision $e_{\rm repeats}$ for each spectrum, we fit an

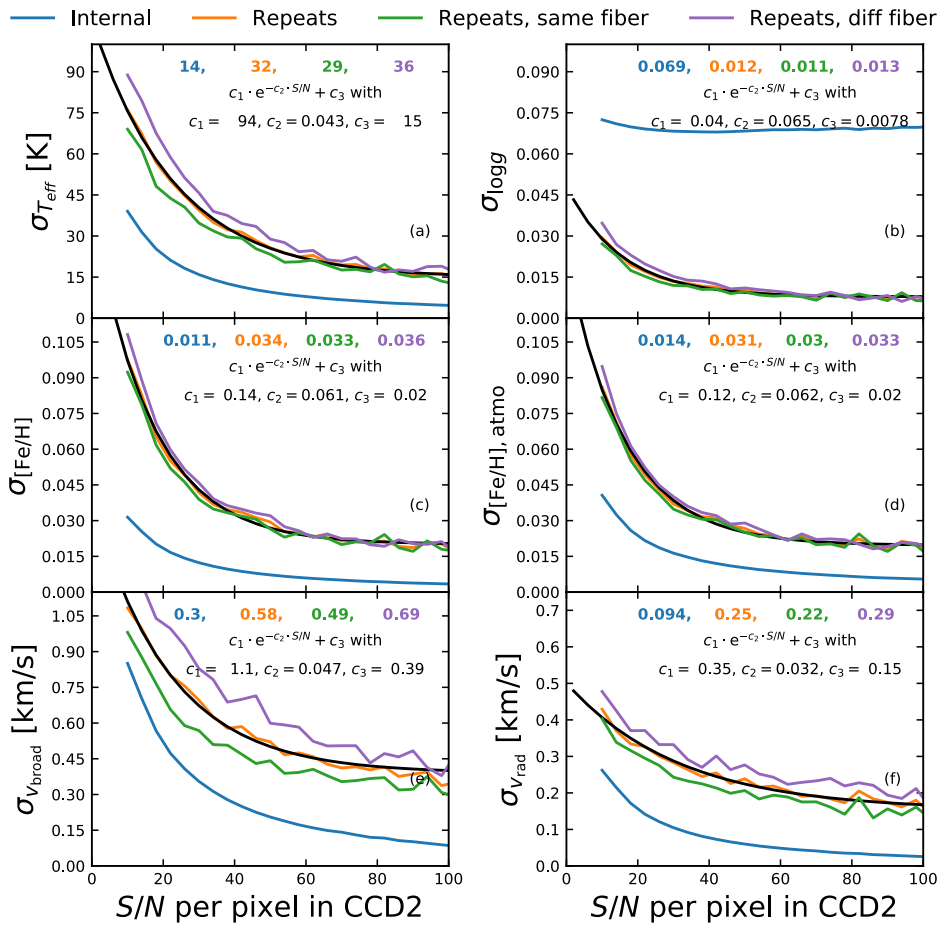

Figure 2.35: Precision estimates from internal SME covariance uncertainties (blue) as well as standard deviations from all (orange), same fibre (green), and different fibre (violet) repeat observations. The numbers in each panel indicate the uncertainties estimated for $S/N = 40$ per pixel, similar Fig. 15 from **Paper I**. **Figure Credit: Paper IV**.

exponentially decreasing function to the orange repeat uncertainty distribution (shown as black line in Fig. 2.35).

We stress that $\log g$ values are not optimised from the χ^2-determination of the spectra like the other parameters, but from Eq. 2.5. We thus sample the parameters used for Eq. 2.5 via MC sampling to estimate the 'internal' uncertainties for $\log g$. We note that in the current MC sampling, the parameters are sampled from fixed Gaussian distributions with $\sigma M = 0.1 \cdot M$ as well as $\sigma BC = 0.1$ mag. $T_{\rm eff}$, σD_{ϖ}, σK_s, and σA_{K_s} are sampled from their uncertainties. The internal standard deviation for $\log g$ is hence S/N independent.

The comparison of the GALAH DR3 precision estimates with those from GALAH DR2 (**Paper I**) shows that the precision (for the median $S/N \sim 40$ of all spectra) has marginally improved, for example from 34 K for $T_{\rm eff}$ of same fiber repeats to 27 K. We

note that for $\log g$ the repeat observation precision is significantly better by construction, that is it decreased from 0.060 for GALAH DR2 to 0.012 for GALAH DR3.

FLAGGING FOR QUALITY CONTROL

After all stellar parameters have been estimated, the results are vetted and flags raised for the individual criteria listed in Table 2.6. Fig. 2.36 shows all those spectra with raised flags. It can be seen that our flagging algorithm is rather conservative, because the plot resembles Fig. 2.32 quite well. The most used flags are 8 (7%), 1 (6%) and 4 (3%).

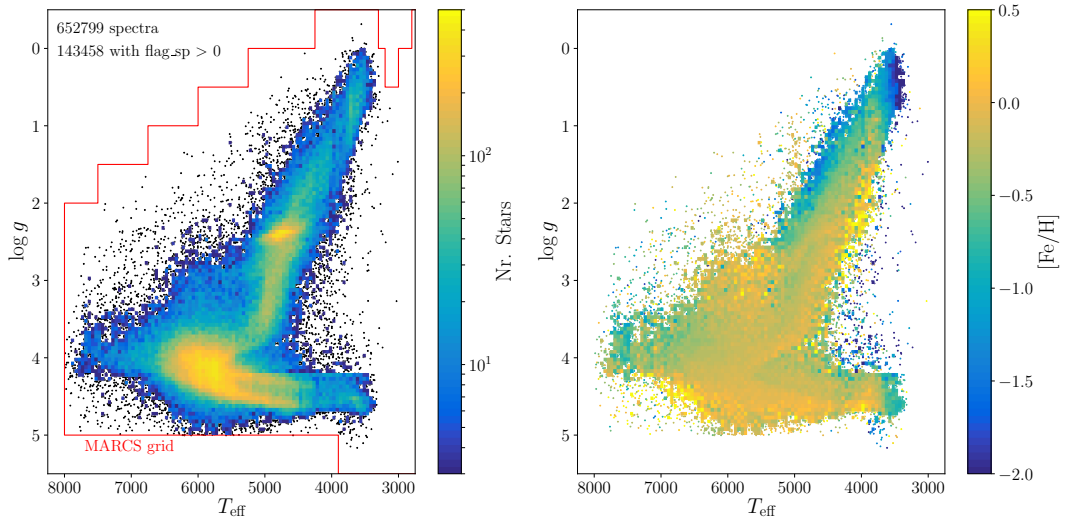

Figure 2.36: Kiel diagrams ($T_{\rm eff}$ vs. $\log g$) color coded by the density of stars per bin (left panel) and mean iron abundance [Fe/H] within a bin (right panel) for those 129369 spectra of the GALAH data release 3 at least have estimated stellar parameters, but have been flagged (`flag_sp` > 0), contrary to the unflagged spectra in Fig. 2.32. The total number of spectra and those below the quality threshold are annotated in the upper left corner of the left panels. In the same panels, red lines indicate the grid limit of the MARCS atmosphere grid, which marks the limits of the synthesis computations. **Figure Credit:** Paper IV.

We have identified astrometric binaries (`flag_sp` = 64) by selecting the oldest isochrones for the particular iron abundance of each star and selecting all stars with surface gravity lower by $\Delta \log g = 0.15$ and cooler by $\Delta T_{\rm eff} = 150\,\mathrm{K}$. This selection is most effective for the identification of binaries on the secondary MS (with slightly lower $\log g$). For stars with equal bolometric luminosity, for example a binary system with the same stellar parameters, the estimated $\log g$ can be smaller by up to ~ 0.3. This deviation can be approximated via Eq. 1.5 when assuming that the bolometric luminosity of the system is twice that of a single star and the mass is estimated to be that of a single star, so that $\Delta \log g \sim -\log L_{\rm bol,\,binary} + \log L_{\rm bol,\,single} = -\log\left(2 \cdot L_{\rm bol,\,single}\right) + \log L_{\rm bol,\,single} = -\log 2$. We have also identified unreliable parameter estimates for the coolest bright giants, for which unreasonably low iron abundances have been estimated (see tip of the RGB in right panel of Fig. 2.36).

Table 2.6: Flags used for GALAH DR3 to estimate the final bit-flag `flag_sp` via summation of the individual flags.

Flag	Description
1	*Gaia* RUWE > 1.4 (bad astrometric solution, see Lindegren, 2018)
2	Unreliable broadening
4	Low S/N (10 for CCD 2)
8	Reduction issues
	a) Wavelength solution (propagating of `red_flag`)
	b) t-SNE projected reduction issues: Negative/positive fluxes, spikes, etc.
16	t-SNE projected emission features
32	t-SNE projected binaries
64	Astrometric binarity flag
128	SNR-dependent high SME chi2 (bad fit)
256	Problems with Fe lines, where line flux is not between 0.03 and 1.00
512	SME did not finish
	a) No convergence == non-finite stellar parameters
	b) Gaussian RV fit failed
	c) Timeout on ISAAC
1024	MARCS grid limit reached or outside of reasonable parameter range

2.4.4 LINE-BY-LINE ABUNDANCE ANALYSES

Coincidentally with the significant improvements of stellar parameters, we have improved the determination of individual chemical abundances. Contrary to the previous GALAH analyses, we are now analysing element abundances as a simple error-weighted combination of all individual element line measurements. This approach has several advantages and we discuss several of them by looking at the combined and individual line abundances for Si in Fig. 2.37.

By using individual lines, we are less prone to unreliable line data, such as $\log gf$ values. Wrong oscillator strengths introduce a bias in the absolute abundance for each line. The Si lines at 5666 Å is for example less accurate than the rest of the lines, because the oscillator strength that was measured in the laboratory (Garz, 1973; O'brian & Lawler, 1991) is contaminated by a theoretically estimated lines by Kurucz (2007). When such a line would be used for a global synthetic fit of [Si/Fe], they would introduce both a bias in the final abundance and parameter- as well as S/N-depending systematic trends. When the Solar abundance for these lines are however estimated independently from the others, they can still be used for the combined [Si/Fe] abundance, after applying individual Sun-based corrections to the absolute abundances.

The use of individual lines also allows to identify less reliable lines in terms of blending, reduction problems, and saturation. The Si lines at 6722 and 7680 Å are two line that display a significant amount of outliers towards higher and lower abundances than the other lines. In a global fit for [Si/Fe], they would hence introduce a higher scatter for the abundance.

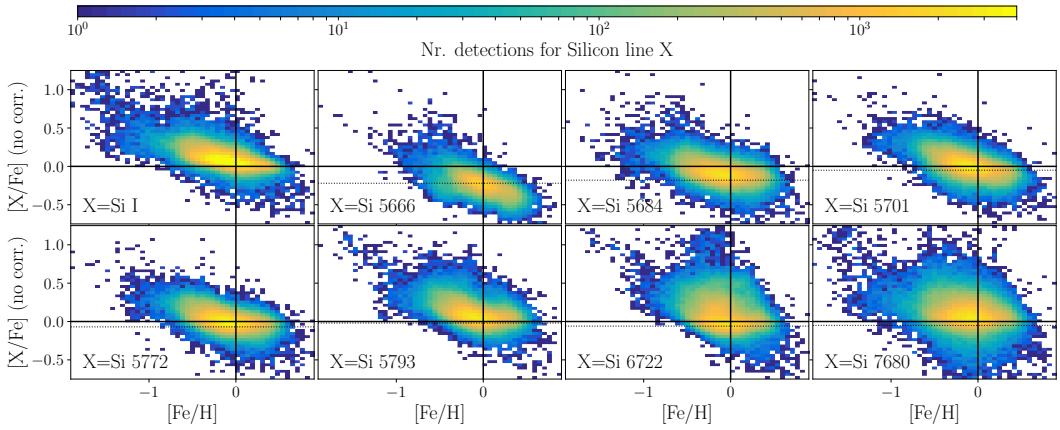

Figure 2.37: Abundance trends for the Si I. The top left panel shows the final combination of all Si I lines, whereas the other panels show the abundance trends for individual lines (indicated in the bottom left of each panel), when a global value $A(\mathrm{Si}) = 7.51$ is assumed for all lines. The black lines indicate the global solar value, whereas the black dotted lines indicate the individual solar value estimated from each line independently. **Figure Credit:** Paper IV.

2.4.5 QUALITY ASSESSMENT OF ELEMENT ABUNDANCES

For several lines of the GALAH wavelength range, we are facing a different issue, that is that we can not use a Solar or sky flat spectrum for the accuracy assessment of the abundance, because the line is too weak in these spectra. We are hence also using Arcturus as a different standard star with well studied absolute abundances to estimate the abundance accuracy (see Fig. 2.38). We see differences for several elements both with respect to the literature (e.g. K) and between dwarf and giants (e.g. V). More work is needed to scrutinise the line selection and abundance zeropoints. The line-by-line analysis of element abundances has also been shown to been important for several elements (e.g. Al, Ca, and Ba) and has to be done to improve the accuracy and precision of abundance measurements. Whenever possible, we use the estimate from the sky flat spectrum for the accuracy assessment, but resort to a manual assessment from Arcturus as well as literature samples.

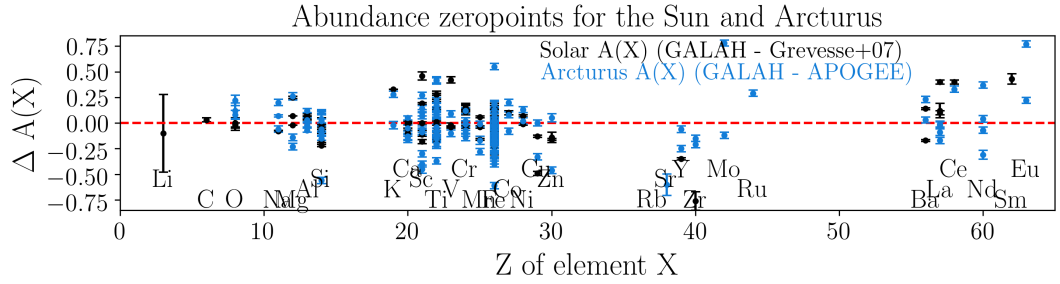

Figure 2.38: Abundance offsets between GALAH pipeline for a skyflat (150405000901378) and Arcturus (150210005801171). Reference values are taken from Grevesse et al. (2007) and the APOGEE collaboration (priv. communication). **Figure Credit:** Paper IV.

We assess the precision by comparing the internal SME covariance uncertainties with those from repeat observations of the same star in Fig. 2.39. Contrary to the stellar parameter estimation, we see that the covariance errors from the individual line measurements are in excellent agreement for almost all lines. The standard deviations of the measurements are also consistent irrespective of the fibre combination. In the chosen example of Si lines, only the Si line at 7680 Å shows a slightly lower trend than the repeat observations. When combining the individual Si abundances to the error-weighted mean [Si/Fe], we see the expected improvement of precision down to 0.041 dex at $S/N = 40$ per pixel. We note however that the finally estimated internal SME-based errors are lower than the those from the repeat observations. This seems to illustrate that the SME-internal method has problems to estimate realistic errors when many pixels are involved, likely reflecting on the many imperfections of the models. Contrary to the stellar parameter estimation, we only report the final abundance error from the internal covariance error.

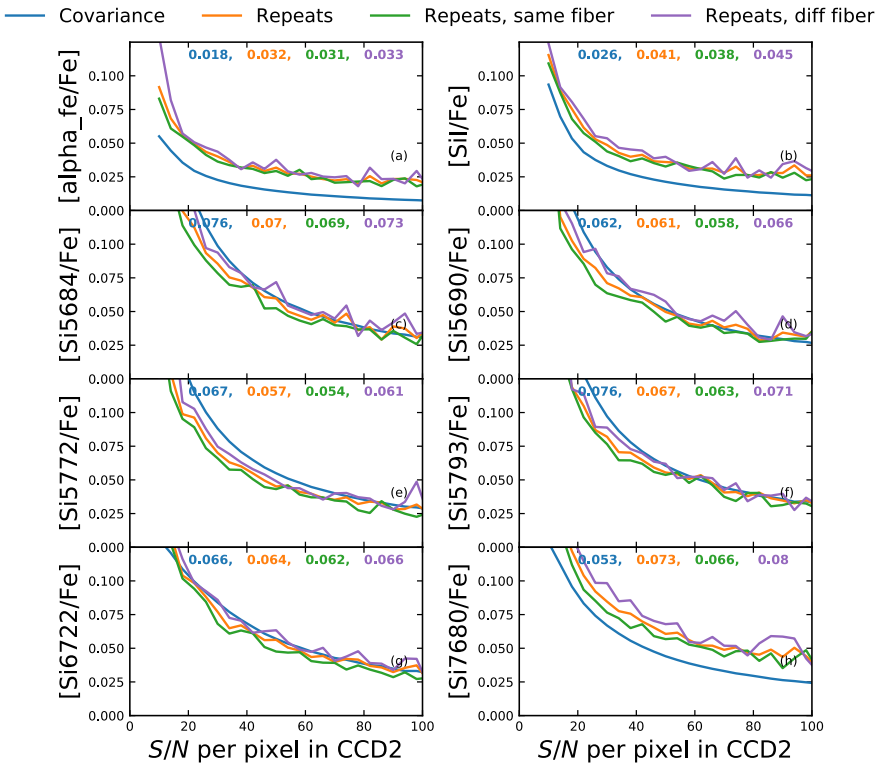

Figure 2.39: Precision estimates from internal SME covariance uncertainties (blue) as well as standard deviations from all (orange), same fibre (green), and different fibre (violet) repeat observations for the combined α-abundances (top left), the combined Si abundances (top right) as well as six individual Si lines. **Figure Credit:** Paper IV.

2.4.6 VALUE-ADDED-CATALOGS

The third Data Release of GALAH is accompanied by two value-added-catalogs and we explain them in this section. One value-added-catalog includes stellar ages and masses and another one kinematic as well as dynamic information for each star.

STELLAR MASSES AND AGES

As part of the stellar parameter estimation (see Secs. 2.3.1.2 and 2.4.2), both stellar masses and ages have been estimated and are added to the data release in a value-added-catalog. In Fig. 2.40, we compare the mass and age difference to the study by Sanders & Das (2018), who estimated both values based on GALAH DR2 as well as *Gaia* DR2 in a Bayesian framework. We only compare those 215493 stars with `flag_sp=0` from GALAH DR3 and `flag=0` as well as `log10_age>-1` (expected binaries) from Sanders & Das (2018) and find a good agreement between both analyses. For the masses we find an agreement in $\log_{10}(M)$ within 0.1 for 95% of the stars and even within 0.05 for 82% of the stars. The largest deviations are found both for massive stars (where GALAH masses are higher) and the metal-rich RC stars (where GALAH masses are lower). Regarding stellar ages we find a generally good agreement as well, with 73% of the ages agreeing within 30%. We note however, that especially for the young MS and secondary RC stars (on the GALAH scale), Sanders & Das (2018) tend to estimate even lower ages, whereas they estimate higher ages for cool MS and metal-rich RC stars than our algorithm. Both regimes are prone to systematic trends, because the isochrone grids are very dense, that is tracks for very different masses and metallicities are very close.

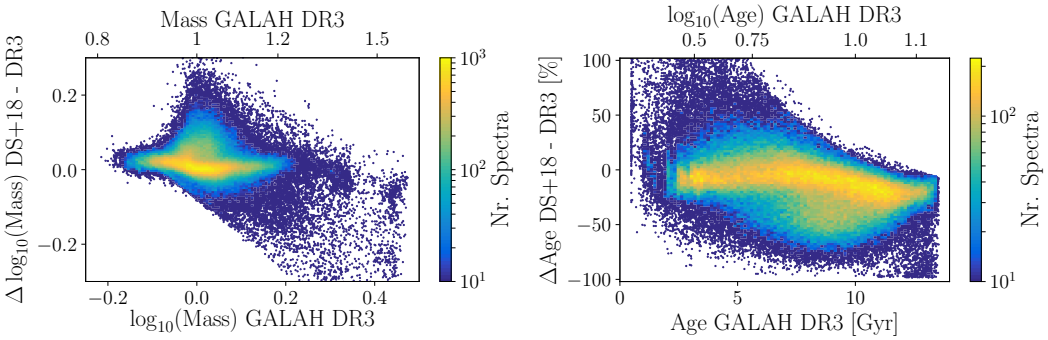

Figure 2.40: Comparison of mass (left) and age (right) estimates from GALAH DR3 and Sanders & Das (2018). **Figure Credit: Paper IV**.

We have further tested how well our algorithm can reproduce stellar ages from mock data, by selecting isochrone points of the 4 stellar ages (4.5, 8.0, 10.0, and 13.5 Gyr), 4 different iron abundances ([Fe/H] $\in [-2.0, -1.1, -.07, 0.0]$), and 5 evolutionary stages, that is MS ($T_{\rm eff} \sim 5250$ K), Turn-off (TO) (hottest around $\log g \sim 4.1$), RGB ($\log g \sim 3.25$), tip of the RGB ($\log g \sim 1.0$), and core helium burning RC (hottest for $2.0 < \log g < 3.0$). Each mock star is fed into the the mass and age estimation algorithm with generic uncertainties for the input parameters of $\Delta T_{\rm eff} = 100$ K, $\Delta \log g = 0.5$, Δ[Fe/H] = 0.2, and $\Delta L_{\rm bol} = 10\%$. We compare the retrieved age with the input age in

Fig. 2.41 and find that the age estimation tends to recover the stellar ages very well for TO stars as well as intermediate age stars around 8 – 10 Gyr. For younger stars, the code tends to overestimate the age by up to 75% for MS stars and those at the tip of the RGB. The age of the oldest is typically underestimated, but RC and RGB star ages are better recovered than those of the tip of the RGB and the MS. This means that the age of the oldest stars are typically underestimated and those of the youngest stars overestimated, resulting in an artificially tighter age distribution towards intermediate age stars. The code can, however, identify truly young stars and truly old stars.

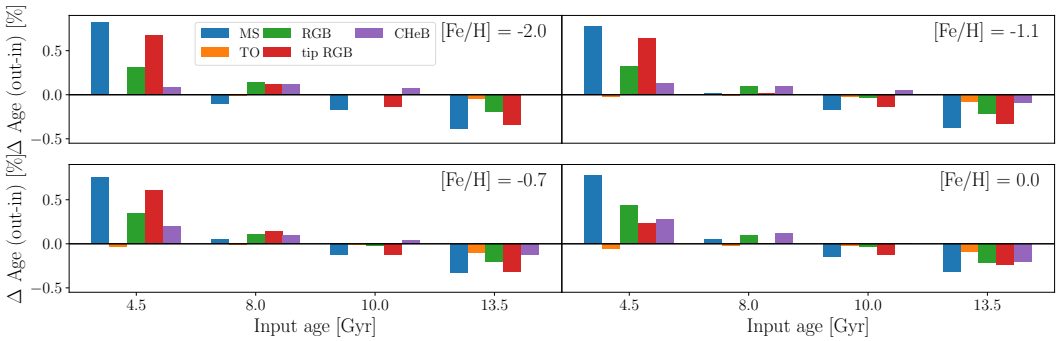

Figure 2.41: Relative deviation of estimated stellar age from stellar ages as chosen from isochrone points at different [Fe/H] $\in [-2.0, -1.1, -.07, 0.0]$ (as indicated in lower right of each panel), different stellar ages $\in [4.5, 8.0, 10.0, 13.5]$ Gyr (different bars with same colours as indicated by axis labels) and different evolutionary stages (different colours as indicated by plot legend in upper left panel). **Figure Credit: Paper IV**.

KINEMATIC AND DYNAMIC INFORMATION

The second value-added-catalog includes coordinates as well as kinematic and dynamic information for each star, following the procedure outlined in Sec. 1.3.4. We use the astrometric information from *Gaia* DR2 (Gaia Collaboration et al., 2018b), that is `ra`, `dec`, `parallax` (converted into distances by Bailer-Jones et al., 2018), `pmra`, and `pmdec` as well as the radial velocities from GALAH DR3 **Paper IV**, that is `rv_galah`.

We use GALPY (Bovy, 2015) to transform these 6D information into the same Galactocentric reference frames (both cartesian and cylindrical) as stated in Table 1.2, that is with a circular velocity of 229.0 km s^{-1} (Eilers et al., 2019). We place the Sun at $R_\odot = 8.178$ kpc (Abuter et al., 2019) and $z_\odot = 0.025$ kpc (Jurić et al., 2008) with a Solar motion relative to the LSR of $(U_\odot, V_\odot, W_\odot) = (11.1, 12.24, 7.25)$ km s^{-1} (Schönrich et al., 2010).

The distribution in Galactocentric cylindrical coordinates (R, z) is shown in panel a) and a top view (X, Y) in panel b) of Fig. 2.42. The vast majority of targets are distributed within less than 4 kpc from the Sun and covers a large fraction of the disk. The distribution shows an asymmetry along R as well as in the (X, Y) plane due fact that the observations are carried out from Australia. Because of the target selection of the GALAH main program ($|b| > 10$ deg), no stars are observed close to the Galactic

plane. We note, however, that GALAH DR3 includes also observations from TESS-HERMES, K2-HERMES, and several smaller projects that targeted the Galactic bulge and clusters. The distribution in the panel a) is hence also including observations with $|b| < 10\,\mathrm{deg}$ especially towards the Galactic center at $(R, z) = 0$. A combination of distance uncertainties and special targeting of clusters and K2/TESS fields is causing finger-of-god effects in both panels.

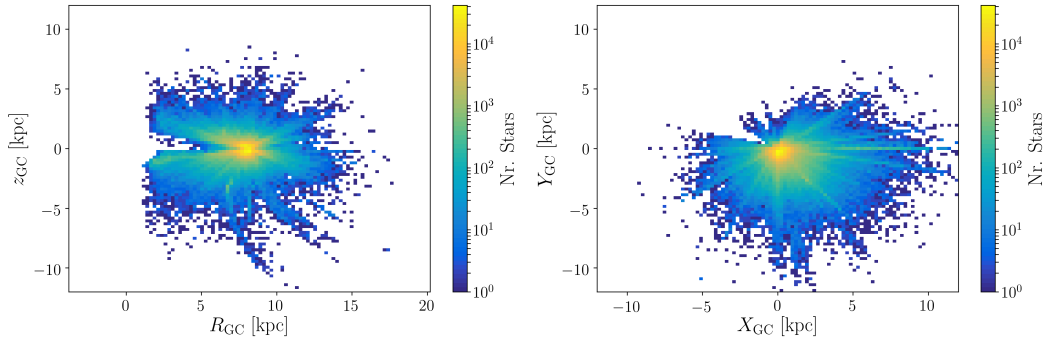

Figure 2.42: Overview of space information of GALAH DR3 with (R, z) in left panel and (X, Y) in right panel. **Figure Credit:** Paper IV.

The space velocities (U, V, W) in the Galactocentric cartesian coordinate frame are shown in a Toomre diagram (see Sec. 1.2.3) in panel a) of Fig. 2.43. Most of the stars observed as part of GALAH DR3 have disk-like kinematics similar to the LSR, but an extension of stars with lower rotational velocity than the disk ($V \ll 0\,\mathrm{km\,s^{-1}}$) are shown and indicate that also several stars with halo-like kinematic properties are part of GALAH DR3.

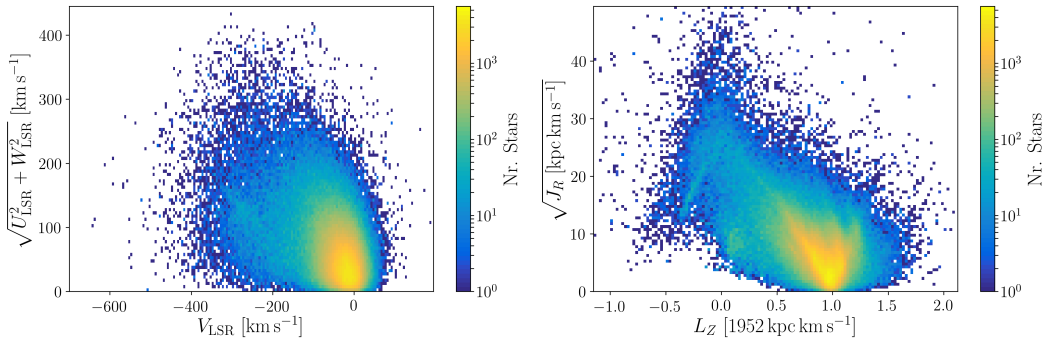

Figure 2.43: Overview of kinematic/dynamic information of GALAH DR3 with Toomre diagram (left) and Action diagram (right). **Figure Credit:** Paper IV.

We compute stellar dynamic properties, that is actions J_R, L_z, J_z, eccentricities e, and orbit boundary information such as z_{max}, R_{peri}, and R_{apo} with GALPY (Bovy, 2015) in the MWPOTENTIAL2014 and a Staeckel fudge with 0.45 as focal length of confocal coordinate system.

The distribution of stars in action space is shown in a view of vertical angular momentum (normalised to the Solar value) and radial action in panel b) of Fig. 2.43. Most of the stars in this diagram show a similar vertical angular momentum radial action as the Sun. Similar to the analyses by Trick et al. (2019), a rich substructure along J_R can be seen. Similar to the extensions seen in the left panel of that figure, an extension of stars with lower vertical angular momentum is visible. We also note an overdensity close to $(L_Z, J_R) = (0, 0)\,\mathrm{kpc\,km\,s^{-1}}$, that is an overdensity of stars with near-circular orbits close to the Galactic center and bulge. The overdensity of stars around $L_Z \sim 0\,\mathrm{kpc\,km\,s^{-1}}$ with higher radial actions is typical for stars of the Galactic halo and is assessed in Chapter 4.

For each of the computed phase space and dynamic properties, we report a variety of statistical values. In addition to the best-value, that is computed by using the best values as input, we also sample the distribution for each property within the uncertainties via Monte Carlo sampling with size 10000 and report the 5th, 50th, and 95th percentiles of these distributions. An example of the sampling of parameters for 100 randomly selected stars is shown in Fig. 2.44. We also provide the code to perform this sampling with different sampling choices. Whereas we currently sample the properties by assuming their input parameters are uncorrelated, we also provide the code to sample with the *Gaia* correlation matrices. The latter are currently not applying a distance prior and are thus problematic for large distances. However, we stress, that the vast majority of the stars from GALAH DR3 have very precise parallax measurements, for which the sampling choice is negligible (see Fig. 2.29).

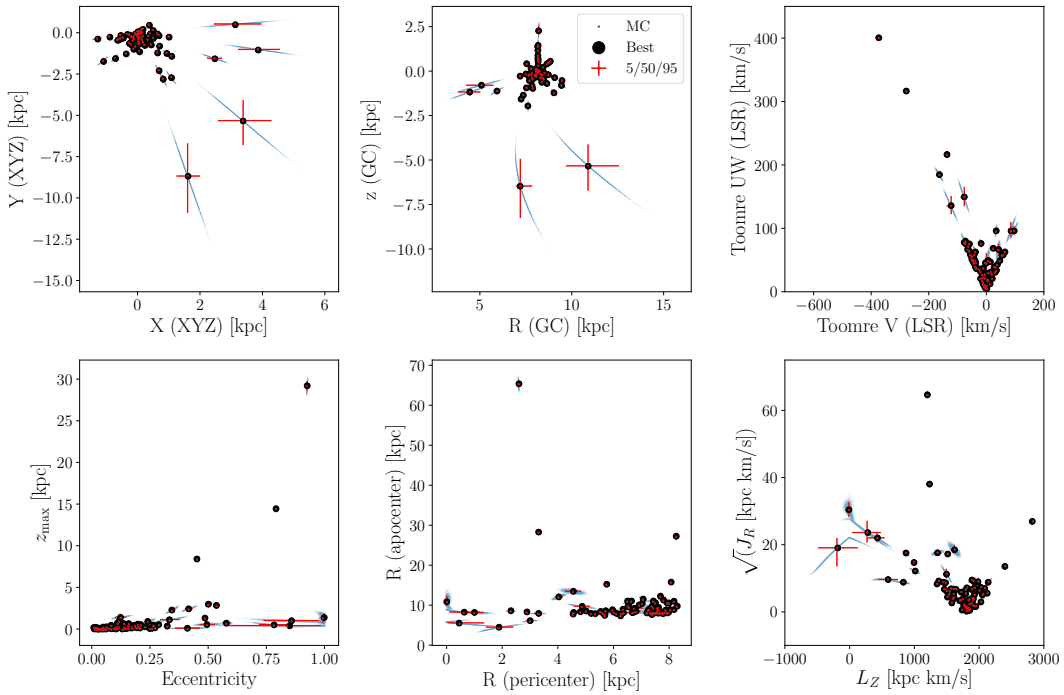

Figure 2.44: Overview of phase space and dynamic stellar properties for randomly chosen stars from GALAH DR3, including their sampling within the measurement uncertainties. The black points indicate the values calculated from the best 6D information. Blue points indicate 10000 samples from the 6D information per star within the uncertainties. Red error bars indicate the distribution between 50th percentile (middle of the cross) and the 5th and 95th percentile, respectively. **Figure Credit:** Paper IV.

Chapter 3

Chemodynamics of the stellar disk with GALAH and *Gaia*

3.1 Preface

In Chapter 1, I have motivated why chemodynamic studies are vital for unraveling the history of our MW. The necessary data for such studies was provided by the observations carried out by the GALAH survey (see Chapter 2) and the *Gaia* satellite. The sample used for this study was selected from the overlap of the first astrometric sample from *Gaia* DR1, the Tycho-*Gaia* Astrometric Solution, with the stars that have been observed by GALAH until September 2016, as is laid out in the description of the observations and the sample itself (see Sec. 3.2). The chemical and dynamical information was extracted as described in the aforementioned chapters, but tailored to the sample of dwarfs and described in more detail in Sec. 3.3. Due to the limited distance of the sample, it is almost exclusively consisting of disk stars. The aim of the work is to analyse the chemodynamic and temporal composition of the disk in Sec. 3.4. Focussing on the relation of stellar age, iron abundance, and α-enhancement, our main finding is that the two disk components (introduced in Sec. 1.2.1.1) can be separated significantly better with those quantities than with kinematic ones. We discuss this and other results in Sec. 3.5 and conclude the study in Sec. 3.6.

This chapter is based on the published and peer-reviewed paper by Buder et al. (2019) (**Paper II**) and my contributions to this chapter include:

- Selecting of stars based on the crossmatch between GALAH and the Tycho-*Gaia* Astrometric Solution (Michalik et al., 2015; Lindegren et al., 2016),
- Building a custom-made pipeline for derivation of stellar parameters and abundances based on the spectroscopic analysis tool SME and
- Applying the pipeline to derive this information, including several validation tests,
- Estimating dynamic information by transforming the 6D information from GALAH and *Gaia* into the appropriate coordinate frames and estimation of orbit parameters with GALPY (Bovy, 2015)

- Estimating stellar ages with a version of the ELLI code (Lin et al., 2018) adjusted by me for this data set
- Performing all analyses of the chemodynamic information in this section and writing the manuscript

The contribution of my co-authors have been the observation and reduction of the data as well as valuable comments regarding the figures or passages of the text or their contribution to the GALAH survey as builders.

3.2 OBSERVATIONS AND SAMPLE SELECTION

The GALAH survey collects data with HERMES, which can observe up to 360 science targets at the same time plus 40 fibres allocated for sky and guide stars (Sheinis et al., 2015; Heijmans et al., 2012; Brzeski et al., 2011; Barden et al., 2010). The selection of targets and observational setup are explained in detail by De Silva et al. (2015) and Martell et al. (2017). The observations used in this study were carried out between November 2013 and September 2016 with the lower of the two resolution modes ($\lambda/\Delta\lambda \sim 28000$) with higher throughput, covering the four arms of HERMES, that is, blue (4716 – 4896 Å including H_β), green (5650 – 5868 Å), red (6480 – 6734 Å including H_α), as well as the near infrared (7694 – 7876 Å, including the oxygen triplet).

The initial simple selection function of the GALAH survey was achieved with a random selection of stars within the limiting magnitudes $12 < V < 14$ derived from 2MASS photometry (De Silva et al., 2015). To ensure a large overlap with TGAS (Michalik et al., 2015), our team added special bright fields ($9 < V < 12$) including a large number of stars in the Tycho-2 catalogue (Høg et al., 2000) which were brighter than the nominal GALAH range (Martell et al., 2017). The exposure times were chosen to achieve a signal-to-noise ratio (S/N) of 100 per resolution element in the green channel / arm; 1 hour for main survey targets in optimal observing conditions, often longer in suboptimal observing conditions. The spectra are reduced with the GALAH pipeline (Kos et al., 2017), including initial estimates of $T_{\rm eff}$, $\log g$, [Fe/H], and radial velocities ($v_{\rm rad}$).

The GALAH+TGAS sample, observed until September 2016, consists of 23096 stars, covering mainly the spectral types F-K from pre-main sequence up to evolved asymptotic giant branch stars. For an overview of the sample, the spectroscopic parameters are depicted in Fig. 3.1, coloured by the parallax precision from TGAS. We note that the shown parameters are estimated as part of this study (see Sect. 3.3.1). The most precise parallaxes ($\sigma(\varpi)/\varpi \leq 0.05$) are available for main sequence stars cooler than 6000 K, decent parallaxes ($\sigma(\varpi)/\varpi \leq 0.3$) for most dwarfs and the lower luminosity end of the red giant branch. As expected by the magnitude constraints of TGAS as well as GALAH (De Silva et al., 2015), most of the overlap consists of dwarfs and turn-off stars (62 %) which also have smaller relative parallax uncertainties than the more distant giants, see Fig. 3.2. Cool evolved giants as well as hot turn-off stars have the least precise

parallaxes of the GALAH+TGAS overlap because of their larger distances and are hence not included in the online tables.

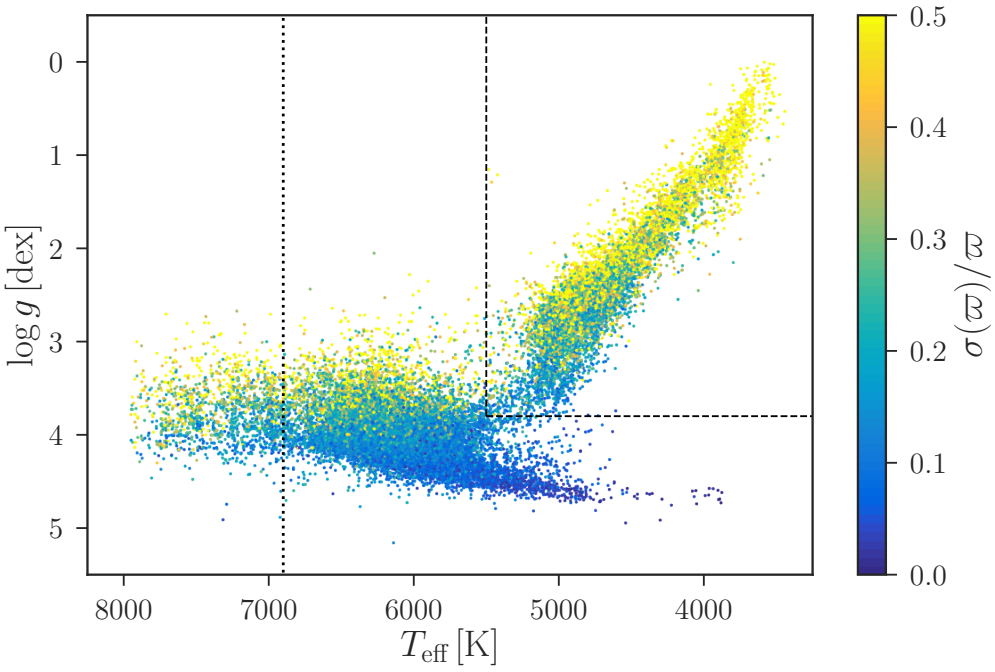

Figure 3.1: Kiel diagram with effective temperature $T_{\rm eff}$ and surface gravity $\log g$ for the complete GALAH+TGAS overlap. The spectroscopic parameters are results of the analysis in Sect. 3.3.1. Colour indicates the relative parallax error. Most precise parallaxes are measured for the cool main sequence stars and the parallax precision decreases both towards the turn-off sequence and even more drastically towards evolved giants, which are the most distant stars in the sample. Dotted and dashed black lines indicate the limits to neglect hot stars ($T_{\rm eff} > 6900$ K) and giants ($T_{\rm eff} < 5500$ K and $\log g < 3.8$ dex) for the subsequent analysis, respectively. See text for details on the exclusion of stars.

In this work, we limit the sample for the analyses to dwarfs and turn-off stars ($T_{\rm eff} \geq 5500$ K or $\log g \geq 3.8$ dex, see dashed line in Fig. 3.1) with relative parallax uncertainties smaller than 30 %. This allows the best estimation of ages from isochrones as well as reliable distance and kinematical information and avoids possible systematic differences in the analysis due to the different evolutionary stages of the stars. Evolutionary effects, such as atomic diffusion, have been studied both with observations of clusters (see for example studies of the open cluster M67 by Önehag et al. (2014); Bertelli Motta et al. (2017); Gao et al. (2018)) as well as a theoretical predictions (Dotter et al., 2017) and are beyond the scope of this paper.

In addition to removing 8740 giant stars and 7674 stars with parallax uncertainties above 30%, we exclude some stars after a visual inspection of the spectra and using our quality analysis (explained in Sect. 3.3.1). We construct a final sample with reliable stellar parameters and element abundances. We neglect 54 stars with emission lines, 926 stars with bad spectra or reductions, 448 double-lined spectroscopic binary stars,

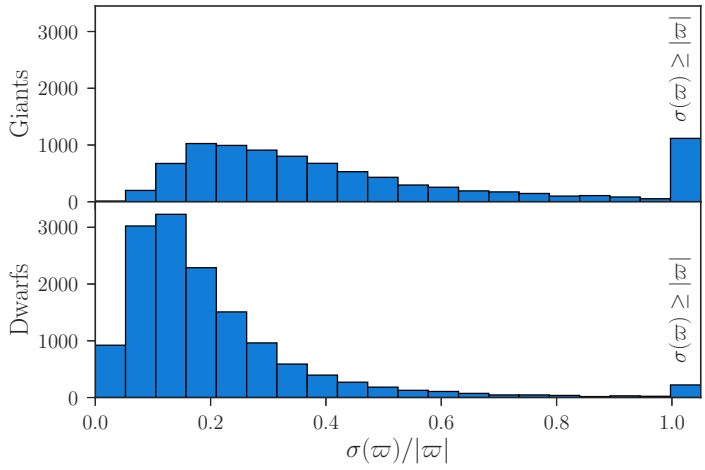

Figure 3.2: Histograms of relative parallax uncertainties for both giants (top panel with $T_{\rm eff} < 5500\,{\rm K}$ and $\log g < 3.8\,{\rm dex}$) and dwarfs (lower panel, including main-sequence and turn-off stars). The majority of the GALAH+TGAS overlap consists of dwarfs. Their mean parallax precision is in the order of 10%, while giants parallaxes are less precise with most uncertainties above 20%. The histograms are truncated at $\sigma(\varpi) = \varpi$ for readability. All stars with parallax uncertainties larger than the parallax itself are hence contained in the last bin.

338 photometric binaries (see Sect. 3.3.4), 3429 stars with broadening velocities above 30 km/s (mostly hot turn-off stars with unbroken degeneracies of broadening velocity and stellar parameters with the GALAH setup), 1390 stars with $T_{\rm eff} > 6900\,{\rm K}$ (for which we have not been able to measure element abundances) and 1048 stars with S/N below 25 in the green channel. We note that the different groups of excluded stars defined above are overlapping with each other.

For the final selected sample of 7066 stars, the majority of the individual S/N vary between 25 to 200, see Fig. 3.3. Most of the stars have a higher S/N than the targeted nominal survey value for the green channel. We note that the S/N of the blue arm is lower than in the others. For abundances measured within this arm, like Zn, we also estimate typically lower precision, see Sect. 3.4.2.6.

3.3 ANALYSIS

Our analysis combines the use of information derived from our GALAH spectra with additional photometric and astrometric measurements to achieve the best possible parameter estimation. We validate our analysis in a manner similar to other large-scale stellar surveys, such as APOGEE (Majewski et al., 2017; Abolfathi et al., 2018; García Pérez et al., 2016) or *Gaia*-ESO (Gilmore et al., 2012; Randich et al., 2013; Smiljanic et al., 2014; Pancino et al., 2017), using a set of well-studied stars, including the so called *Gaia* FGK benchmark stars (hereafter GBS, see Heiter et al., 2015a; Jofré et al., 2014). The stellar parameters $T_{\rm eff}$ and $\log g$ of the GBS have been derived from direct observables:

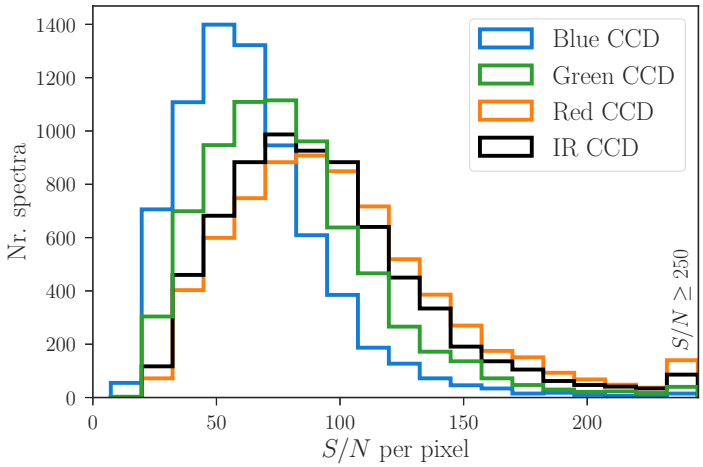

Figure 3.3: Distribution of S/N per pixel for the different HERMES wavelength bands (S/N per resolution element is about twice as high) for the final sample. The S/N for the green, red and IR channels are mainly in the range of 50 to 150, that is, above the nominal survey aim of S/N of 100 per resolution element in the green channel. The S/N in the blue channel is smaller, with typically 25 to 100. The mean values per band are 59/75/94/88. This indicates a smaller influence of the blue band in the parameter estimation with χ^2 minimisation explained in Sect. 3.3 and lower precision of element abundances measured within this channel.

angular diameters, bolometric fluxes, and parallaxes, and are thus less model-dependent. They therefore provide reference parameters that do not suffer from the same model dependence as isolated spectroscopy. Among others, Schönrich & Bergemann (2014) and Bensby et al. (2014) showed the strength of combining spectroscopy and external information. The latter applied this approach for a sample of 714 nearby dwarfs with high accuracy astrometric parallaxes (van Leeuwen, 2007) from the HIPPARCOS mission. We use their sample as a reference for this study, because the spectral analysis was performed in a similar way, including the anchoring of surface gravity to astrometric information. We stress that their study was performed with higher quality spectra (both regarding the spectral resolution and S/N) which allowed a higher precision on measurements to be achieved.

3.3.1 STELLAR PARAMETER DETERMINATION

By using the fundamental relation between surface gravity, stellar mass, effective temperature, and bolometric luminosity

$$\log g = \log g_{\odot} - \log \frac{L_{\rm bol}}{L_{\rm bol,\odot}} + 4 \log \frac{T_{\rm eff}}{T_{\rm eff,\odot}} + \log \frac{\mathcal{M}}{\mathcal{M}_{\odot}}, \tag{3.1}$$

the degeneracies with $\log g$ and other spectroscopically determined stellar parameters are effectively broken. The thereby improved values of $T_{\rm eff}$ and $\log g$ leads to improved estimates of metallicities. Using broad band photometry (apparent magnitudes K_S and inferred bolometric corrections BC_{K_S} as well as extinction A_{K_S}) in combination with

parallaxes ϖ or distances D_ϖ, it is possible to estimate the bolometric magnitudes ($M_{\rm bol}$) and luminosities ($L_{\rm bol}$) to high precision and accuracy (see e.g. Alonso et al., 1995; Nissen et al., 1997; Bensby et al., 2014):

$$-2.5 \cdot \log \frac{L_{\rm bol}}{L_{\rm bol,\odot}} = K_S + BC_{K_S} - 5 \cdot \log(D_\varpi) + 5 - A_{K_S} - M_{\rm Bol,\odot}. \quad (3.2)$$

The nominal values for the Sun (used in Eqs. 3.1 and 3.2) of $T_{\rm eff,\odot} = 5772\,{\rm K}$, $\log(g_\odot) = 4.438\,{\rm dex}$, and $M_{\rm Bol,\odot} = 4.74\,{\rm mag}$ are taken from Prša et al. (2016).

Any filter with available bolometric corrections can be used for the computation of $L_{\rm bol}$; the V band is commonly used for nearby stars. However, our GALAH data set also contains stars with substantial reddening and published catalogues of V band magnitudes, such as APASS (Henden et al., 2016), have multiple input sources, affecting the homogeneity of the data. We therefore decide in favour of using the K_S band as given by 2MASS (Cutri et al., 2003), available for all our targets. Bolometric corrections $BC = BC(T_{\rm eff}, \log g, [{\rm Fe/H}], E(B-V))$ are interpolated with the grids from Casagrande & VandenBerg (2014). Distances are taken from Astraatmadja & Bailer-Jones (2016), using a Milky Way model as Bayesian prior. For attenuation, we use the RJCE method $A_K = A_K(K_S, W2)$ by Majewski et al. (2011); Zasowski et al. (2013). If K_S or $W2$ could not be used, we use the approximation $A_K \sim 0.38E(B-V)$ estimated by Savage & Mathis (1979) with $E(B-V)$ from Schlegel et al. (1998). The reddening of our sample is on average $E(B-V) = 0.12 \pm 0.14\,{\rm mag}$. For the nearby dwarfs, however, A_K is very small and thus hard to estimate given the photometric uncertainties; hence it was set to 0 if the RJCE method yielded negative values.

With the exception of $\log g$, stellar parameters and abundances are estimated using the spectrum synthesis code SME (Valenti & Piskunov, 1996; Piskunov & Valenti, 2017), which uses a Marquardt-Levenberg χ^2-optimisation between the observed spectrum and synthetic spectra that are calculated on-the-fly. As part of the GALAH+TGAS pipeline, SME version 360 is used, with MARCS 1D model atmospheres (Gustafsson et al., 2008) and non-LTE-synthesis of iron from Lind et al. (2012). The chemical composition is assumed equal to the standard MARCS composition, including gradual α-enhancement toward lower metallicity[1]. The pipeline is operated in the following way:

1. Stellar parameters are initialised from the analysis run used by Martell et al. (2017) if available and unflagged, otherwise the output from the reduction pipeline (Kos et al., 2017) is used and if these are flagged, we adopt generic starting values $T_{\rm eff} = 5000\,{\rm K}$, $\log g = 3.0$, and $[{\rm Fe/H}] = -0.5$.
2. Predefined $3-9$ Å wide segments are normalised and unblended and well modelled Fe, Sc, and Ti lines within each segment are identified. Broader segments are used for the Balmer lines. The continuum shape is estimated by SME assuming a linear behaviour for each segment, and based on selected continuum points outside of the line masks.

[1] $$[\alpha/{\rm Fe}] = \begin{cases} 0.4 & \text{for } [{\rm Fe/H}] < -1.0 \\ 0.4 \cdot (-[{\rm Fe/H}]) & \text{for } [{\rm Fe/H}] \in [-1.0, 0.0] \\ 0.0 & \text{for } [{\rm Fe/H}] > 0.0 \end{cases}$$

3. Stellar parameters are iterated in two SME optimisation loops.
   a) SME parameters $T_{\rm eff}$, [Fe/H], $v \sin i \equiv v_{\rm broad}$, and $v_{\rm rad}$ are optimised by χ^2 minimisation using partial derivatives.
   b) Whenever $T_{\rm eff}$ or [Fe/H] change, $\log g$ and $v_{\rm mic}$ are updated before the calculation of new model spectra and their χ^2. We adjust $\log g$ according to Eq. 3.1 with isochrone-based masses $M = M(T_{\rm eff}, \log g, [{\rm Fe/H}], M_{K_S})$ estimated by the ELLI code, see Sect. 3.3.3. We adjust $v_{\rm mic}$ following empirical relations estimated for GALAH[2]
4. Each segment is re-normalised with a linear function while minimising the χ^2 distance for the chosen continuum points between observation and the synthetic spectrum created from the updated set of parameters (Piskunov & Valenti, 2017)
5. The stellar parameters are iteratively optimised until the relative χ^2-convergence criterium is reached.

During each optimisation iteration, a suite of synthetic spectra based on perturbed parameters and corresponding partial derivatives in χ^2-space are computed to facilitate convergence. The parameters of the synthesis with lowest χ^2 are then either used as final parameters or as starting point of a new optimisation loop. For each synthesis, SME updates the line and continuous opacities and solves the equations of state and radiative transfer based on interpolated stellar model atmospheres (Piskunov & Valenti, 2017). The optimisation has converged, when the fractional change in χ^2 is below 0.001. Non-converged optimisations after maximum 20 iteration are discarded. Figure 3.4 shows the final spectroscopic parameters $T_{\rm eff}$ vs. $\log g$ of the final sample, colour coded by the fitted metallicities, masses, and ages from the ELLI code, see Sect. 3.3.3.

We report the metallicity as [Fe/H] and base it on the iron scaling parameter of the best-fit model atmosphere (SME's internal parameter *feh*). It is mainly estimated from iron lines and hence traces to the true iron abundance, as our validation with [Fe/H] from the GBS shows.

3.3.2 VALIDATION STARS

To estimate the precision, we can rely on stars with multiple observations as part of the GALAH+TGAS sample: 334 stars have been observed twice and 44 stars have been observed three times. The individual differences of selected parameters are plotted in Fig. 3.5. Because we also use these multiple observations to assess the precision of the abundance estimates (see Sect. 3.3.5), we show the two element abundances Ti and Y as examples. We assume the uncertainties to be Gaussian and estimate the standard deviation of the multiple visits as a measure of precision. The resulting precisions based on the repeated observations are shown in Table 3.1.

[2] If $\log g \leq 4.2$ or $T_{\rm eff} \geq T_0$ with $T_0 = 5500$ K:
$v_{\rm mic} = 1.1 + 1.0 \cdot 10^{-4} \cdot (T_{\rm eff} - T_0) + 4 \cdot 10^{-7} \cdot (T_{\rm eff} - T_0)^2$, else:
$v_{\rm mic} = 1.1 + 1.6 \cdot 10^{-4} \cdot (T_{\rm eff} - T_0)$

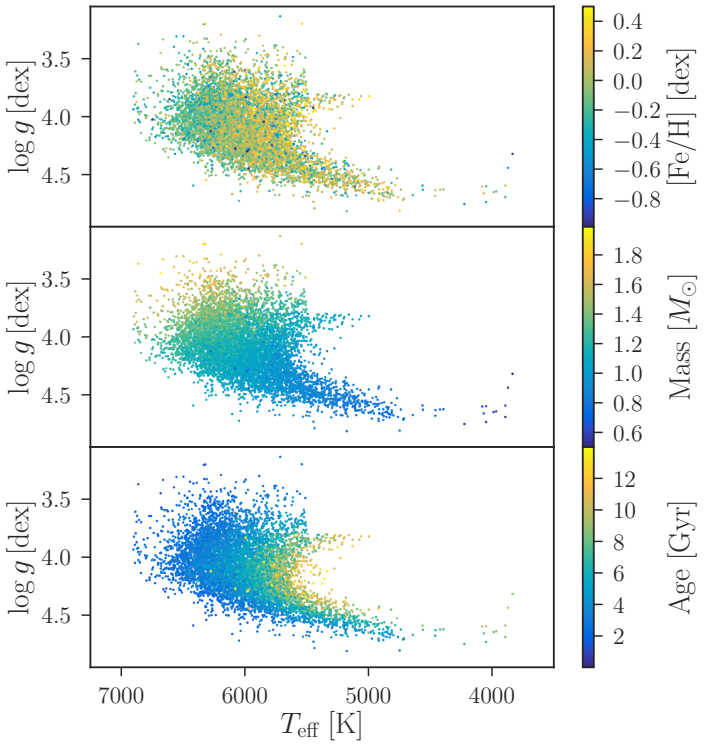

Figure 3.4: Kiel diagrams ($T_{\rm eff}$ and $\log g$) of the GALAH+TGAS dwarfs. Colour indicates the metallicity [Fe/H] in the top panel, mass in the middle panel, and age in the bottom panel. The sample is a subset of the clean GALAH+TGAS overlap, shown in Fig. 3.1 and excludes giants with $T_{\rm eff} \geq 5500$ K and $\log g \geq 3.8$ dex. Stellar masses increase from the cool main sequence ($\sim 0.8\,\mathcal{M}_\odot$) to the hottest turn-off stars ($\sim 2.0\,\mathcal{M}_\odot$). Stellar ages decrease towards higher surface gravities on the cool main sequence and towards higher effective temperatures in the turn-off region. In contrast to this rather smooth trend, few metal-poor stars stand out with smaller stellar masses and higher stellar ages also at effective temperatures around 6000 K.

To estimate the accuracy, we use the GBS. These are, however, typically much brighter and closer than the survey targets and brighter than the bright magnitude limit of *Gaia* DR1 TGAS. Hence HIPPARCOS parallaxes (van Leeuwen, 2007) are used additionally. New K_S magnitudes are computed for GBS with 2MASS K_S quality flag not equal to 'A', following the approach used by Heiter et al. (2015a)[3]. With this approach 22 GBS observations are analysed and compared to the estimates from the GALAH+TGAS pipeline, as depicted in Fig. 3.6. To have a statistically sufficient sample, we also include GBS giants in the analysis. We find a small bias of 51 ± 89 K in comparison to the systematic uncertainties present in both GBS and our parameters. We note, however, temperature-dependent biases of 110 ± 110 K for some stars around 5000 K. Towards higher temperatures, we also note an increasing disagreement, in-

[3]For GBS with bad qualities, we convert K_{BB} magnitudes from Gezari et al. (2000), using equation (A1) by Carpenter (2001).

Table 3.1: Precision and accuracy of the pipeline based on repeated observations and GBS respectively.

Parameter X	$e_{X,\mathrm{Repeats}}$	$e_{X,\mathrm{GBS}}$
T_{eff}	29 K	89 K
$\log g$	0.01 dex	0.05 dex
[Fe/H]	0.024 dex	0.07 dex
v_{broad}	0.51 km/s	2.0 km/s
v_{mic}	0.009 km/s	0.20 km/s
v_{rad}	0.43 km/s	
τ	0.13 Gyr	
$\mathcal{M}$	0.014 $\mathcal{M}_{\odot}$	
[Ti/Fe]	0.033 dex	
[Y/Fe]	0.081 dex	

dicating that the temperatures of hotter stars are underestimated by our spectroscopic pipeline (-150 ± 130 K at 6600 K), a result likely to be caused by the application of 1D LTE atmospheres for hot stars (see e.g. Amarsi et al., 2018), where Balmer lines are the strongest or only contributor for the parameter estimation. For surface gravity, $\log g$, and rotational/macroturbulence broadening, v_{broad}, we find excellent agreement of 0.00 ± 0.05 dex and 0.9 ± 2.0 km/s respectively. The latter is computed as quadratic sum of $v_{\sin i}$ and v_{mac} for the GBS. For the metallicity, [Fe/H], we found a significant bias with respect to the GBS. Similar to previous studies of HERMES spectra (Martell et al., 2017; Sharma et al., 2018) we therefore shift the metallicity by +0.1 dex for our sample. The shift is chosen so that the overlap with GBS has consistent [Fe/H] in the solar regime. Two outliers for v_{mic} can be seen to drive the bias of -0.14 ± 0.20 km/s, which we do not correct for, because the majority of the GBS sample agree well with our estimates and the two outliers are the most luminous giants, which are not representative of the final sample.

With these precision and accuracy estimates (the latter coming from the error-weighted standard deviation between GALAH and GBS estimates), we estimate the overall uncertainties of our parameters X (not mass and age, see Sect. 3.3.3) by summing them in quadrature to the formal covariance errors of SME ($e^2_{X,\mathrm{SME}}$):

$$e^2_{X,\mathrm{final}} = e^2_{X,\mathrm{SME}} + e^2_{X,\mathrm{Repeats}} + e^2_{X,\mathrm{GBS}}. \tag{3.3}$$

For element abundances, we estimate the overall uncertainties without the GBS term. In the case of $\log g$, we replace $e^2_{\log g,\mathrm{SME}}$ by the standard deviation of 10,000 Monte Carlo samples of Eq. 3.1. For this sampling, we use the uncertainties of $e_{T_{\mathrm{eff}},\mathrm{final}}$, the maximum likelihood masses as $\mathcal{M}$ with an error of 6% (based on mean mass uncertainties of an initial ELLI run), e_{K_S} from 2MASS with mean uncertainties of 0.02 mag, and propagate this information to adjust BC (with typical changes below 0.07). Because Astraatmadja & Bailer-Jones (2016) only state the three quantiles, we sample two Gaussians with standard deviations estimated from the 5th and 95th distance percentile respectively. Because there are no Bayesian distance estimates for HIPPARCOS, we choose

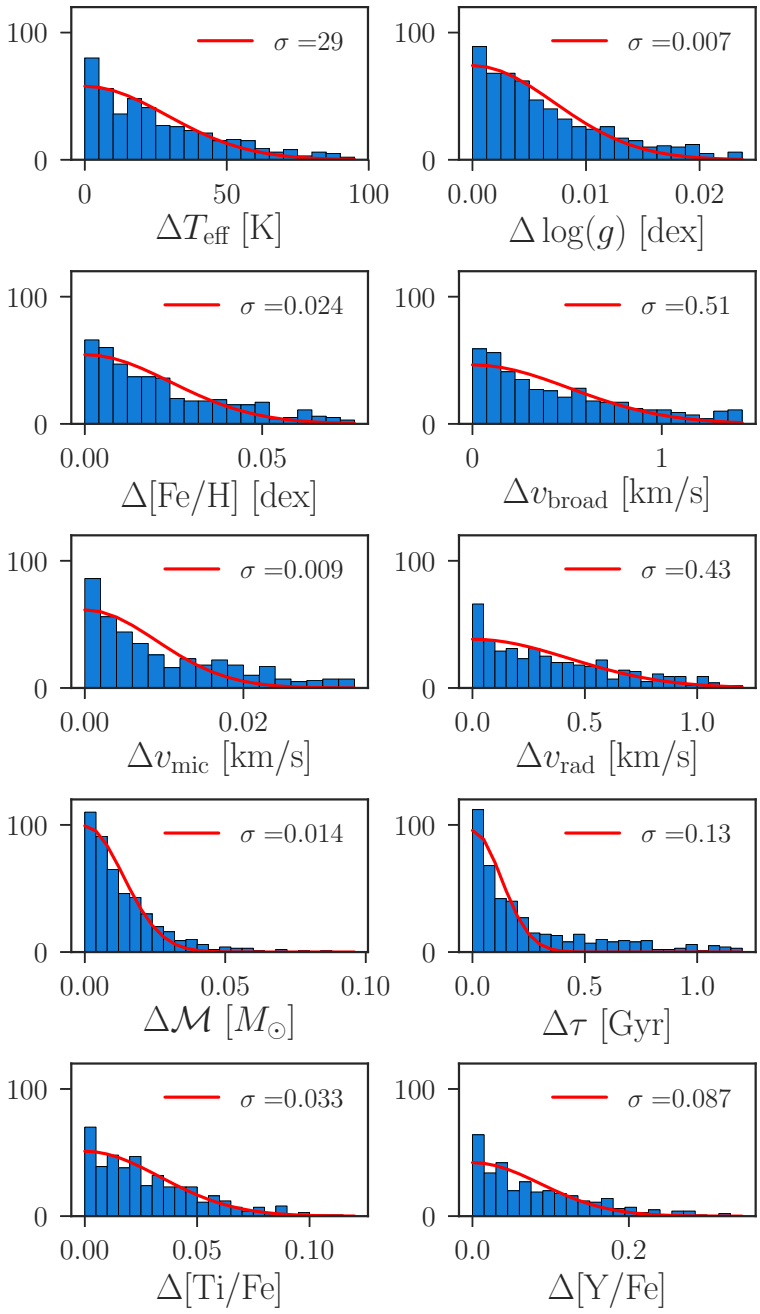

Figure 3.5: Histograms of parameter and abundance differences obtained from multiple observations of the same star. Shown are the absolute differences from two observations as well as from all three absolute difference combinations for three observations. A Gaussian distribution was fitted to the distributions (red curves). The obtained standard deviation is indicated in each panel.

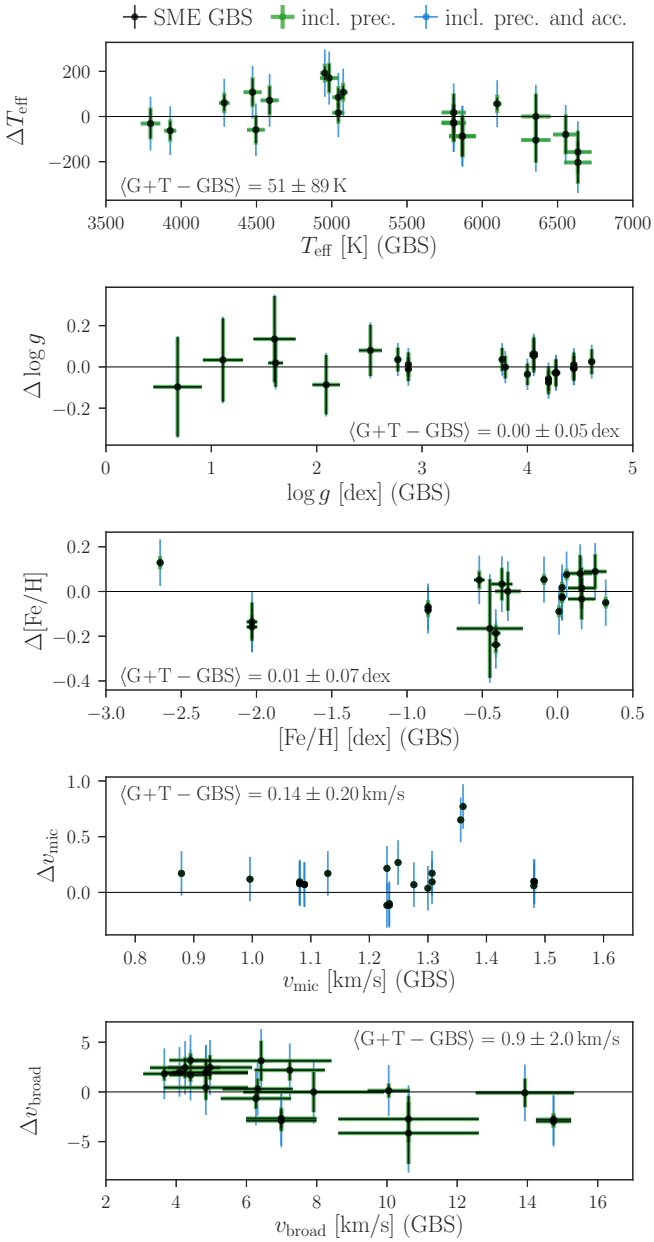

Figure 3.6: Comparison of the stellar parameters for GBS as estimated by this analysis and Heiter et al. (2015a); Jofré et al. (2014) (shown as ours theirs versus ours). The fundamental parameters $T_{\rm eff}$ and $\log g$ are shown in the two top panels, together with comparisons of metallicity with their recommended iron abundance [Fe/H], microturbulence velocity, and broadening velocity, a convolved parameter of macroturbulence and rotational velocity, in the three bottom panels. Black error bars are the combined uncertainties of GBS as well as the error output of our analysis pipeline (SME). Green error bars include precision uncertainties from repeated observations and blue error bars include both precision and accuracy estimates.

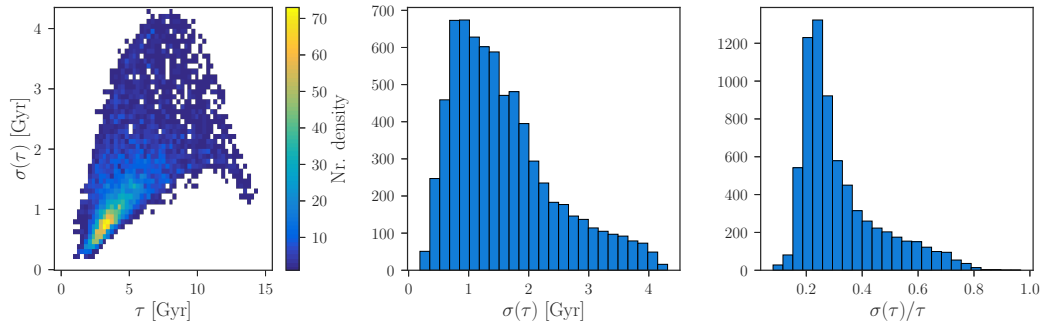

Figure 3.7: Distributions of stellar ages τ [Gyr] and their uncertainties. The left panel shows the distribution of uncertainties versus ages, the middle panel show the absolute age uncertainties and the right panel shows the relative age uncertainties. The majority of age estimates show uncertainties below 2 Gyr and relative uncertainties below 30%.

to sample parallaxes ϖ rather than distances D_{ϖ}. For e_{A_K} we use the quadratically propagated uncertainties from the RJCE method (with mean uncertainties of 0.03 mag) or assume 0.05 mag for estimates based on $E(B-V)$. We do not use Eq. 3.3 for age and mass, because they are estimated with the adjusted stellar parameters.

3.3.3 MASS AND AGE DETERMINATION

For the mass and age determination, we use the ELLI code (Lin et al., 2018), employing a Bayesian implementation of fitting Dartmouth isochrones based on $T_{\rm eff}$, $\log g$, [Fe/H], and absolute magnitude M_K. M_K is based on 2MASS K_S, the distance estimates from Astraatmadja & Bailer-Jones (2016) and accounts for extinction A_K (estimated as described in Sect. 3.3.1). The Dartmouth isochrones span ages from 0.25 to 15 Gyr and metallicities from −2.48 to +0.56 with α-enhancement analogous to the MARCS atmosphere models[1]. Starting with a maximum likelihood mass and age estimation, MCMC samplers as part of the EMCEE package (Foreman-Mackey et al., 2013) are used to estimate masses and ages. Stellar ages and their uncertainties are estimated by computing the mean value and standard deviation of the posterior distribution. The stellar ages estimated with the ELLI code have typical uncertainties of 1.6 Gyr (median of posterior standard deviations), which typically correspond to less than 30%, see Fig. 3.7. As pointed out for example by Feuillet et al. (2016), the posterior distribution does not necessary follow a Gaussian. Although this is the case for the large majority of our stars, we also provide the 5th, 16th, 50th, 84th, and 95th percentiles to the community for follow-up studies. Because the results of this study do not change significantly with quality cuts for stellar ages, we do not apply them.

3.3.4 BINARITY

The observational setup of the GALAH survey allocates one visit per observation (with exception of pilot and validation stars). Therefore, binaries or triples can usually not be identified via radial velocity changes.

Here, we use both the tSNE classifications by Traven et al. (2017), to identify obvious spectroscopic binaries, as well as visual inspection to identify double-line binaries which are less distinct from the tSNE classification. Within the sample, a binary fraction of 4% has been identified with high confidence from spectral peculiarities. Additionally, 338 probable photometric binaries on the main sequence are identified which show a significant deviation between spectroscopically determined $\log g$ or $L_{\rm bol}$ with respect to photometrically determined ones. For these, the suspected secondary contributes significantly to the luminosity of the system without obvious features within the GALAH spectra. These stars lie above the main sequence within a colour-(absolute) magnitude diagram. We have identified the stars with photometric quantities beyond what is expected for a single star on the main sequence (shown as black dots in Fig. 3.8) by using a Dartmouth isochrone with the highest age (15 Gyr) and metallicity (+0.56 dex). We note that some of these stars show colour excesses. While these might have been mis-identified as binaries, they are definitely peculiar objects (e.g. pre-main-sequence stars), for which the pipeline is not adjusted and have subsequently been neglected. We want to stress again, that identified binaries are excluded from the cleaned sample.

3.3.5 ABUNDANCE DETERMINATION

With the stellar parameters estimated in Section 3.3.1, elemental abundances are calculated in the following way:

1. Predefined segments of the spectrum are normalised and the element lines chosen with two criteria. First, the lines have to have a certain depth, that is, their absorption has to be significant. We use the internal SME parameter depth to assess this, see Piskunov & Valenti (2017).
2. The lines have to be unblended. This is tested by computing a synthetic spectrum of the segment with all lines and one only with the lines of the specific element. The χ^2 difference between the synthetic spectra for each point in the line mask has to be lower than 0.0005 or 0.01 (the latter for blended but indispensable lines), otherwise the specific point is neglected for the final abundance estimation.
3. The abundance for the measured element is optimised using up to 20 loops with the unblended line masks.

The selection of lines used for parameter and abundance analysis and their atomic data is a continuation of the work presented by Heiter et al. (2015b). The complete linelist is presented in **Paper I**.

Abundances are estimated assuming LTE, with the exception of Li, O, Al, and Fe, for which we use corrections by Lind et al. (2009), Amarsi et al. (2016a), Nordlander & Lind (2017), and Amarsi et al. (2016b), respectively, to estimate non-LTE abundances.

Solar abundances are estimated based on a twilight flat in order to estimate the difference to the solar composition by Grevesse et al. (2007, G07). This difference for each element X, that is, $A(X)_\odot - A(X)_\odot^{\rm G07}$, is then subtracted from the element abundance of the stars of the sample.

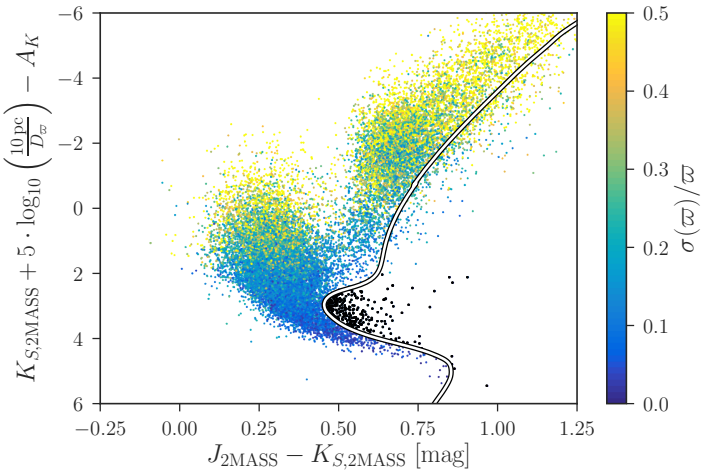

Figure 3.8: Colour magnitude diagram of the full GALAH+TGAS sample coloured by the parallax precision. The colour index is $J - K_S$ from 2MASS photometry and absolute magnitude for K_S, inferred from 2MASS as well as distances D_ϖ and extinction A_K. A Dartmouth isochrone with age (15 Gyr) and metallicity (+0.56) is shown as white curve. This is used to identify 338 dwarfs with photometry outside of the expected range (above the white curve) for cool single main sequence stars ($M_{K_S} > 2$ mag), here shown in black. The identified stars are all nearby and their reddening is negligible, especially in the infrared. We note that for some stars, possibly mis-identified as binaries, the photometry indicates colour excesses or a pre-main-sequence stage, which is still an important reason to eliminate them from the subsequent analysis, as the pipeline is not adjusted for these stars.

3.3.6 KINEMATIC PARAMETERS

For our target stars, the space velocities U, V, and W are calculated using the GALPY code by Bovy (2015), assuming $(U_\odot, V_\odot, W_\odot) = (9.58, 10.52, 7.01)$ km/s (Tian et al., 2015) relative to the local standard of rest.

We estimate kinematic probabilities of our sample stars to belong to the thin disc (D), thick disc (TD), and halo (H) following the approach by Bensby et al. (2014, see their Appendix A) with adjusted solar velocities.

To estimate the Galactocentric coordinates and velocities as well as the action-angle coordinates of the sample, we use GALPY. We choose the axisymmetric *MWPotential2014* potential with a focal length of $\delta = 0.45$ for the confocal coordinate system and the GALPY length and velocity units 8 kpc and 220 km/s respectively. We place the Sun at a Galactic radius of 8 kpc and 25 pc above the Galactic plane. To speed up computations, we use the ACTIONANGLESTAECKEL method. We estimate mean values and standard deviations of the action-angles per star from 1000 Monte Carlo samples of the 6D kinematical space randomly drawn within the uncertainties. We neglect the uncertainties of the 2D positions and estimate the standard deviation of the distances from the 5th and 95th percentiles given by Astraatmadja & Bailer-Jones (2016).

As shown in Fig. 3.9, the distance uncertainties are the dominant source of the action uncertainties. While for excellent parallaxes (left panel), the scatter in the action estimates is negligible, it becomes noticeable for parallaxes with uncertainties around

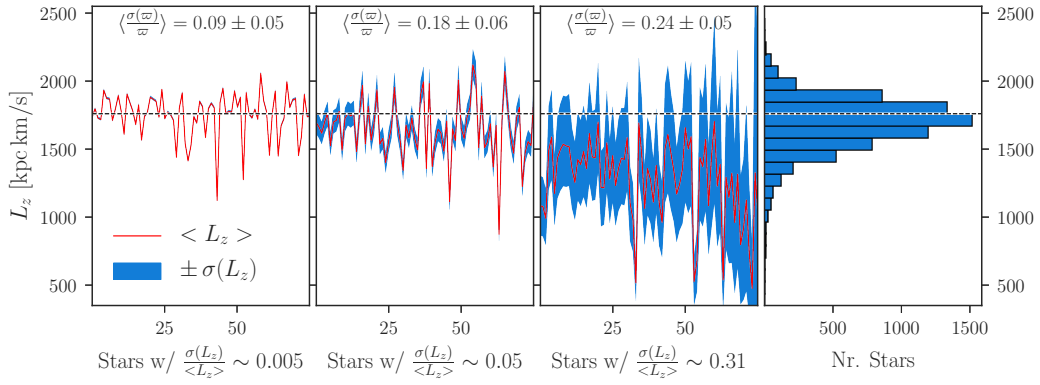

Figure 3.9: The left three panels show the distribution of angular momentum L_z, sorted by relative uncertainty and depict three close in views groups of with 75 stars with mean L_z uncertainties of first 0.5%, second 5%, and third 30% in order to demonstrate the precision reached for different parallax qualities. Red is mean L_z for each star and blue their 1σ area. A white dashed line indicated the Solar angular momentum. Average parallax precisions are indicated in the top of each panel. The best precision on parallaxes also lead to the most precise L_z. The values of the least precise momenta (third panel) are significantly lower than those of the Sun, even when taking the standard deviation of the angular momentum estimates into account. Due to the selection of stars and the density structure of the disc, these stars are statistically further away and are expected to be at larger Galactic heights and closer to the Galactic centre. We note that their angular momenta are also different from the majority of stars, which have a Sun-like angular momenta, as shown in the fourth panel. For a discussion of the angular momenta of the stars in the chemodynamical context see Sect. 3.5.

18%. For parallax uncertainties above 24%, the action uncertainties increase to as high as 31%. From the samples depicted in Fig. 3.9, one can see that these large uncertainties are particularly common for stars with low angular momentum. Because of the GALAH selection (observing in the Southern hemisphere and leaving out the Galactic plane) as well as the density structure of the disc with more stars towards the Galactic centre, we expect stars with larger distances (and hence larger distance uncertainties) to be situated at larger Galactic heights and smaller Galactic radii than the Sun. The right panels in Fig. 3.9 confirm this expectation. Stars with angular momenta comparable with the solar value have usually precisely estimated actions. The latter stars are also the majority of stars in the sample, as the histogram in the right panel shows.

3.4 CHEMICAL, DYNAMICAL, AND TEMPORAL INFORMATION OF THE STELLAR DISK

In Sect. 3.4.1, we describe the stellar age distribution, before presenting abundance and age trends in Sect. 3.4.3 and the kinematics of the sample in Sect. 3.4.4. We note that the vast majority of the dwarfs from the GALAH+TGAS sample are more metal-rich than −0.5 dex, as seen in the metallicity distribution function in Fig. 3.10. These stars have no intrinsic selection bias in metallicity or kinematics.

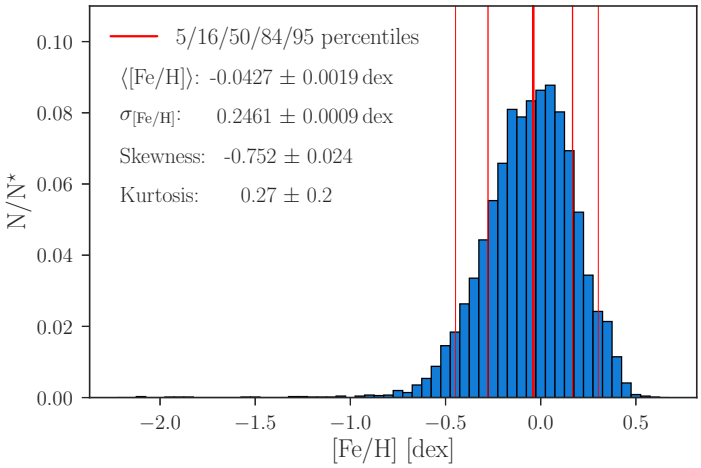

Figure 3.10: Metallicity distribution function of the GALAH+TGAS sample. The majority of the stars have solar-like metallicity, [Fe/H], within ±0.5. The distribution is skewed towards metal-poor stars between −2.0 dex and −0.5 dex. The 5, 16, 50, 84, and 95 percentiles are −0.45 dex, −0.28 dex, −0.04 dex, 0.17 dex, and 0.30 dex. respectively. Mean metallicity and standard deviation as well as skewness and kurtosis are indicated in the plot and discussed in the text. **Figure Credit:** Paper II.

From 10,000 Monte Carlo samples, we find the parameters of the metallicity distribution to be $\langle[\mathrm{Fe/H}]\rangle = -0.04$, $\sigma_{[\mathrm{Fe/H}]} = 0.26$, skewness $= -0.667 \pm 0.029$, kurtosis[4]$= -0.21 \pm 0.23$. The mean of our metallicity distribution is slightly lower but consistent within the uncertainties to the one estimated by Hayden et al. (2015) using APOGEE data for the same (solar) Galactic zone[5]. The APOGEE distribution also shows a narrower standard deviation (0.2 dex) around a mean value of +0.01 dex and is less skewed (-0.53 ± 0.04) but more extended towards the metal-rich and metal-poor tail of the distribution (with a kurtosis of 0.86 ± 0.26). The kurtosis, a measure for the sharpness of the peak, indicates that the APOGEE distribution has a sharper peak than the GALAH distribution. The skewness indicates that the GALAH sample contains in general also relatively more metal-poor stars compared to the APOGEE sample. This is possibly caused by the different selection functions of the two surveys. GALAH avoids the Galactic plane ($|b| \leq 10$ deg), whereas APOGEE targets the plane where we expect relatively more stars of the low-α-sequence that are more metal-rich than [Fe/H] = −0.7.

3.4.1 AGE DISTRIBUTION

The age distribution of the GALAH+TGAS sample is shown in Fig. 3.11. It peaks between 3 to 3.5 Gyr, which is at an older age than estimated by the studies of Casagrande et al. (2011) and Silva Aguirre et al. (2018) who both placed the peak at approximately 2 Gyr. While this might be partially explained by a combination of both selection

[4]Here we follow Hayden et al. (2015) and define kurtosis as the fourth standardised moment-3.
[5]We refer to the Solar Galactic zone ($7 < R < 9$ kpc and $|z| < 0.5$ kpc), which contains 99.5% of the GALAH+TGAS sample.

function, and target selection effects, we note that the exclusion of hot stars with effective temperatures above 6900 K in our sample, see Sect. 3.2, affects primarily stars with ages below the peak of the histogram. However, these hot stars have an average maximum likelihood age of 1.5 ± 0.8 Gyr and the location of the age peak does not change when including them.

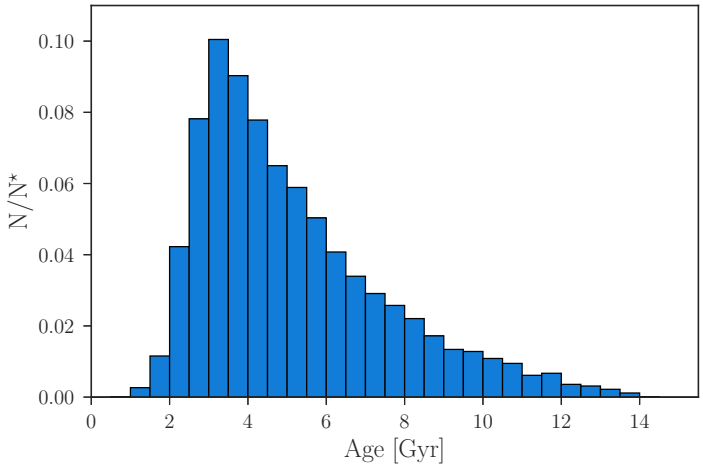

Figure 3.11: Distribution of stellar ages. The distribution peaks around 3 Gyr and decreases towards higher ages. We stress that the exclusion of stars with effective temperatures above 6900 K leads to fewer stars in the clean sample, with ages below 2 Gyr. The peak of the distribution is however not affected by this selection. **Figure Credit:** Paper II.

3.4.2 ABUNDANCE TRENDS

In total, the GALAH survey wavelength range includes detectable atomic absorption lines of up to 30 elements of FKG stars. A subset of 20 of these can be measured in the dwarf and turn-off star spectra, which we examine in this work: Li, C, O, α-process elements (Mg, Si, Ca, and Ti), light odd-Z elements (Na, Al, K), iron-peak elements (Sc, V, Cr, Mn, Co, Ni, Cu, and Zn), and s-process neutron capture elements (Y and Ba). We list the mean precision (estimated from repeated observations), accuracy (inferred from the uncertainties of the oscillator strengths), measured fraction of the clean sample in percent, and numbers of measured lines in Table 3.2.

In Figures 3.12 and 3.13, we show our measured element abundances as a function of metallicity. We present the density distribution for these in Fig. 3.12, coloured by stellar counts per bin. In Fig. 3.13, we plot the same distribution, but colour each bin by the median age of its stars. When available, we include results from previous studies (Bensby et al., 2014; Battistini & Bensby, 2015; Nissen et al., 2014; Zhao et al., 2016; Delgado Mena et al., 2017). These studies use spectra of higher quality (higher resolution and S/N), but are much smaller in sample size. Similar to the GALAH survey, these literature studies include dwarfs of both the low- and high-α sequences of the disc and span a large metallicity range ($-2.8 <$ [Fe/H] < 0.4). We note that the selection function

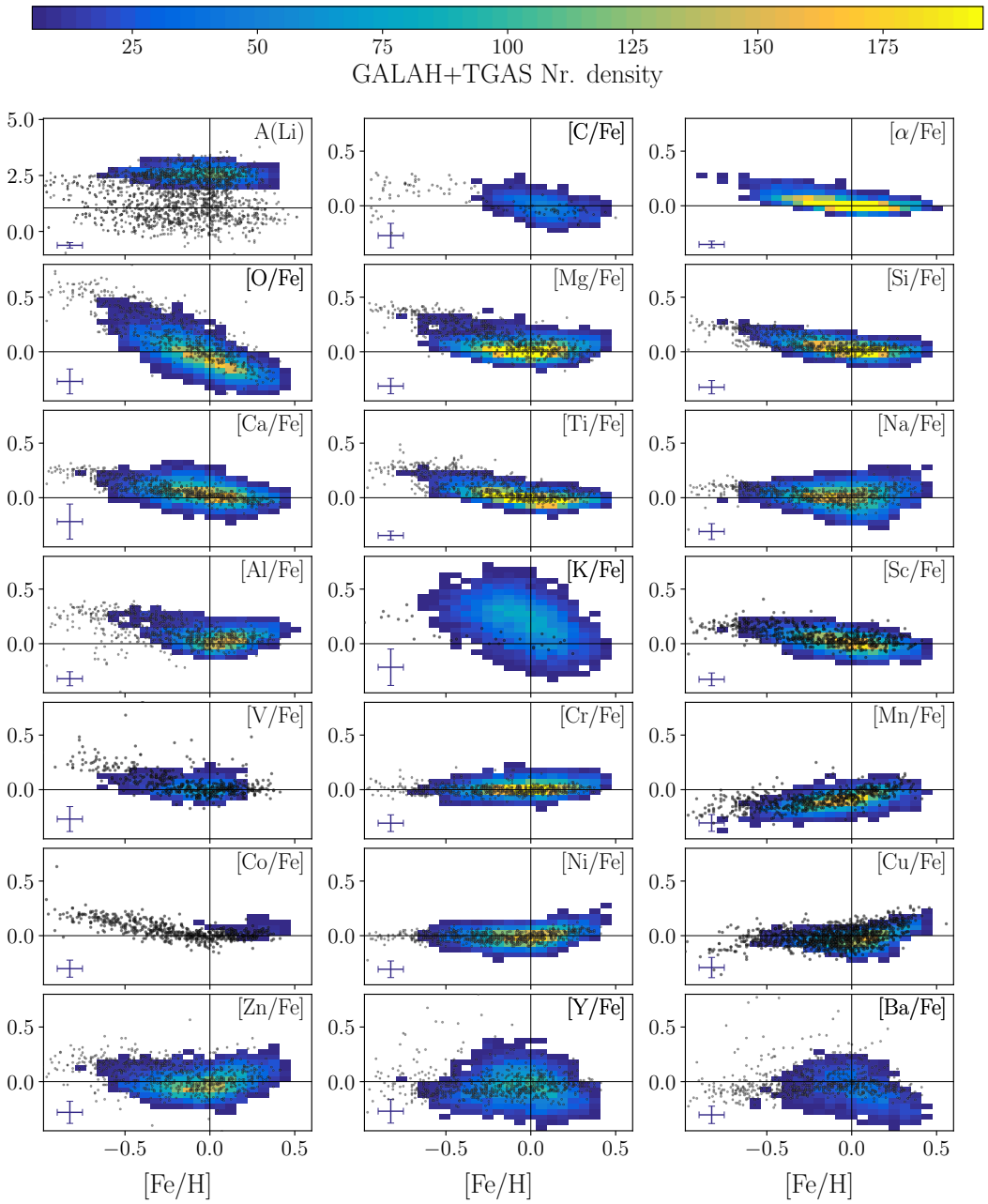

Figure 3.12: Distribution of elemental abundances of the measured elements as a function of metallicity, coloured by density (with a minimum of five stars per bin). All elements are shown relative to the iron abundance, except for Li (shown as absolute abundance). The elements are indicated in the upper right corner of each panel. Measurements from the literature are overlaid as grey dots, that is, results by Bensby et al. (2014) for O, Na, Mg, Al, Si, Ca, Ti, Cr, Ni, Zn, Y, and Ba, Battistini & Bensby (2015) for Sc, V, Mn, Nissen et al. (2014) for C, Zhao et al. (2016) for K, and Delgado Mena et al. (2017) for Cu. For details regarding the individual elements, see respective paragraphs in Sect. 3.4.2. **Figure Credit: Paper II.**

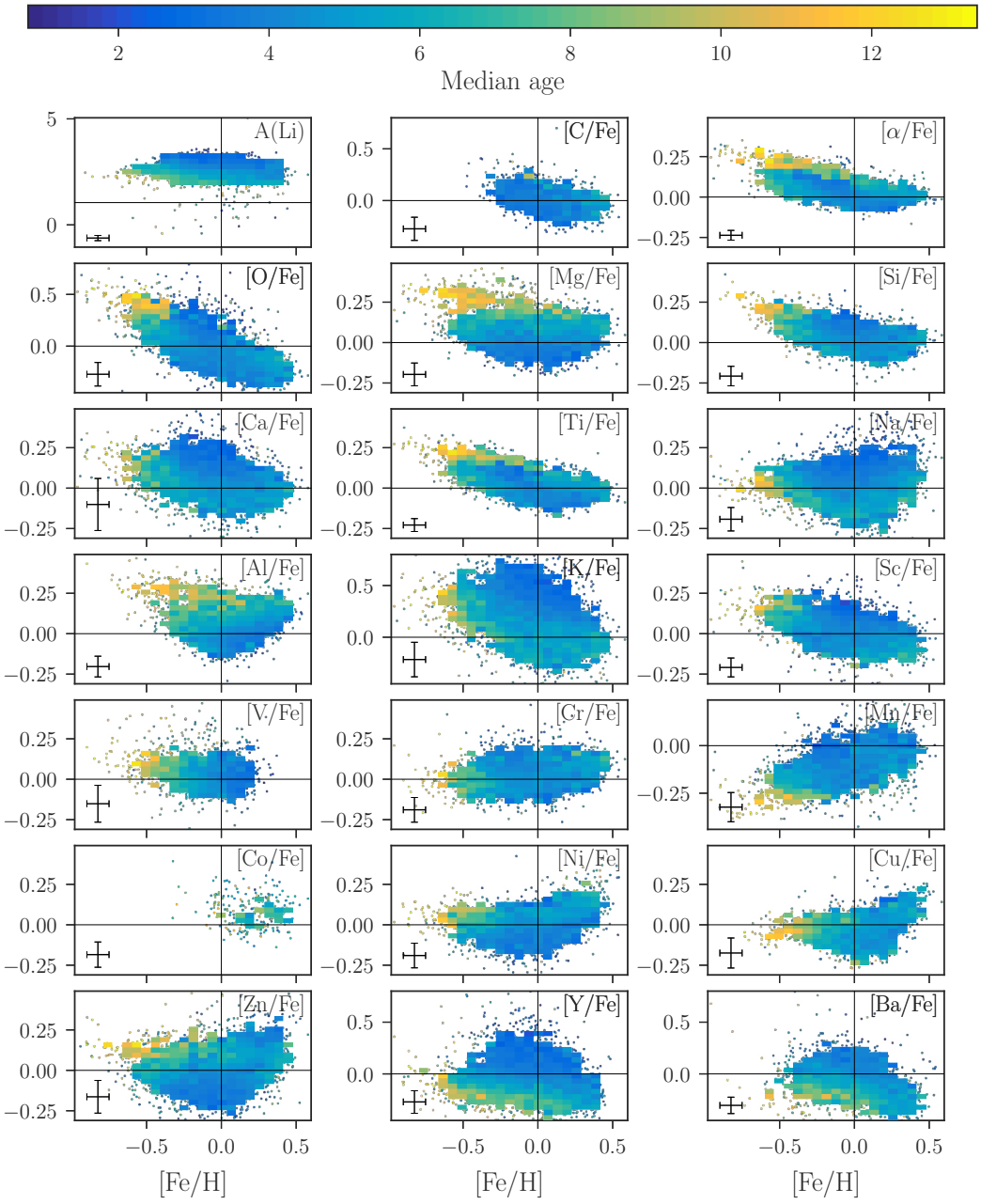

Figure 3.13: Distribution of elemental abundances of the measured elements as a function of metallicity, coloured by median age per bin (with a minimum of 5 stars per bin). Contrary to Fig. 3.12, individual stars outside the bins are shown as small dots and are also coloured by age. No literature samples are overlaid. All elements are shown relative to the iron abundance, except for Li (shown as absolute abundance). For details regarding the individual elements, see respective paragraphs in Sect. 3.4.2. **Figure Credit: Paper II**.

Table 3.2: Elements by atomic numbers and their precision and accuracy as well as number of measured lines

Z	Elem. X	Precision	Accuracy	Measured	Lines
	α	0.03		99%	
3	Li	0.12	0.01	42%	1
6	C	0.11	0.05	26%	1
8	O	0.12	0.01	97%	3
11	Na	0.08	0.01	94%	4
12	Mg	0.07	0.05	99%	3
13	Al	0.06	0.08	56%	4
14	Si	0.06	0.03	83%	4
19	K	0.17	0.01	95%	1
20	Ca	0.17	0.02	95%	2
21	Sc	0.06	0.05	77%	10
22	Ti	0.04	0.05	24%	20
23	V	0.12	0.05	25%	17
24	Cr	0.08	0.15	81%	9
25	Mn	0.08	0.02	69%	4
27	Co	0.09	0.09	4%	3
28	Ni	0.08	0.07	74%	7
29	Cu	0.10	0.08	52%	1
30	Zn	0.11	0.05	81%	2
39	Y	0.12	0.05	82%	4
56	Ba	0.08	0.05	34%	2

for these studies is different to that of GALAH and they contain much higher relative numbers of metal-poor stars.

For a quantitative discussion of age trends we refer the reader to other studies, for example for [Y/Mg] (Nissen, 2015; Spina et al., 2016), [C/N] (Masseron & Gilmore, 2015; Martig et al., 2016; Ness et al., 2016) or the study of 17 abundance-age trends for APOGEE by Feuillet et al. (2018).

3.4.2.1 LITHIUM

Li is measured using 1D non-LTE corrections by Lind et al. (2009). In our sample, we can only detect Li in stars with a relatively large absolute Li abundance, of A(Li) > 2.0. In the metal-poor regime, the warm stars are situated on the Spite plateau (Spite & Spite, 1982), around A(Li) = 2.3, as expected. Towards higher metallicities, A(Li) is mostly measured between 2.0 and 3.3. The latter value is close to the meteoritic A(Li) of 3.26 ± 0.05 (Asplund et al., 2009). Li is expected to be a good tracer of the evolution of the star, because the initial composition is depleted by the proton bombardment processes at temperatures higher than $2.5 \cdot 10^6$ K (Pinsonneault, 1997). From the respective panel in Fig. 3.16, we see a strong correlation of higher Li for higher effective temperatures. The

lines of Li in colder and evolved stars are below the 3σ detection limit. The strong anti-correlation between Li and effective temperature (or mass) is well known and previously depicted for thin/thick disc stars for example by Ramírez et al. (2012). This is due to the larger surface convective envelopes of cooler stars, extending to hotter layers in the stellar interior. When we look at the trend with ages, we find that among the stars with significant Li detections (all above the solar value of A(Li) = 1.05 dex), we see a tendency of lower Li with increasing age for a given metallicity, as expected (see e.g. the work for solar twins by Carlos et al. (2016) and references therein). The upper envelope for stars at $-0.5 <$ [Fe/H] < 0.5 goes significantly above the Spite plateau due to interstellar and stellar production (see e.g. Prantzos et al., 2017) and even reaches the meteoritic values estimated by Asplund et al. (2009). While we see indications that Li is a good tracer of age for the younger dwarfs in our sample, we do not draw any conclusions because of the uncertain temperature-age causality as well as the influence of the metallicity, detection limits, and other potentially important factors such as rotational velocity.

3.4.2.2 CARBON

In the spectra, only atomic C lines with high excitation energies could be identified, which are strongest in hot and metal-rich stars. Due to the high excitation energy of the C lines, in our sample only hot stars with metallicities above -0.3 dex have detectable line strengths. Starting from enhanced abundances at metallicities of -0.75 dex, we see a decreasing trend towards solar metallicities, which flattens at super-solar metallicities. Our results are consistent with the study of Nissen et al. (2014) who demonstrated a linear C-enhancement trend from [Fe/H] = 0 to -0.75 dex. Although it shows a behaviour like an α element, it is expected to follow the iron abundance more closely than these elements and the origin of C is still debated (see Nissen et al., 2014, and references therein). When we look at the trend with ages, we find no significant correlation between C and stellar age for our sample of dwarfs and turn-off stars. Several recent studies, for example Masseron & Gilmore (2015), have discovered significant age-trends for evolved stars, which is an observational manifestation of mass-dependent mixing during the dredge-up phase of the stellar evolution.(e.g. Feuillet et al., 2018). Since our study is limited to dwarf stars, we do not detect such correlations. Further, because of the detection limit, we can not draw conclusions regarding the stars with [Fe/H] < 0.

3.4.2.3 OXYGEN

For O, we apply 1D non-LTE corrections based on the model atom and non-LTE radiative transfer code described in Amarsi et al. (2015, 2016a), but using 1D MARCS model atmospheres. These corrections are vital for the O abundances estimated from the O triplet (O I 7772 Å, O I 7774 Å, and O I 7775 Å), as shown in Fig. 3.14. The corrections are significant for hotter stars and those at the turn-off region. While the global trend of [O/Fe] with metallicity is similar for LTE and non-LTE measurements, the attributed corrections can be as large as -0.5 dex for the hottest stars of the sample, hence shifting them down to a similar level as cooler main-sequence stars. We want to stress, that

non-LTE corrections for O play a particularly important role when it comes to magnitude limited selections of stars, especially for dwarfs, as more distant and luminous stars tend to be more evolved and in the turn-off region, hence being more affected by departures from LTE.

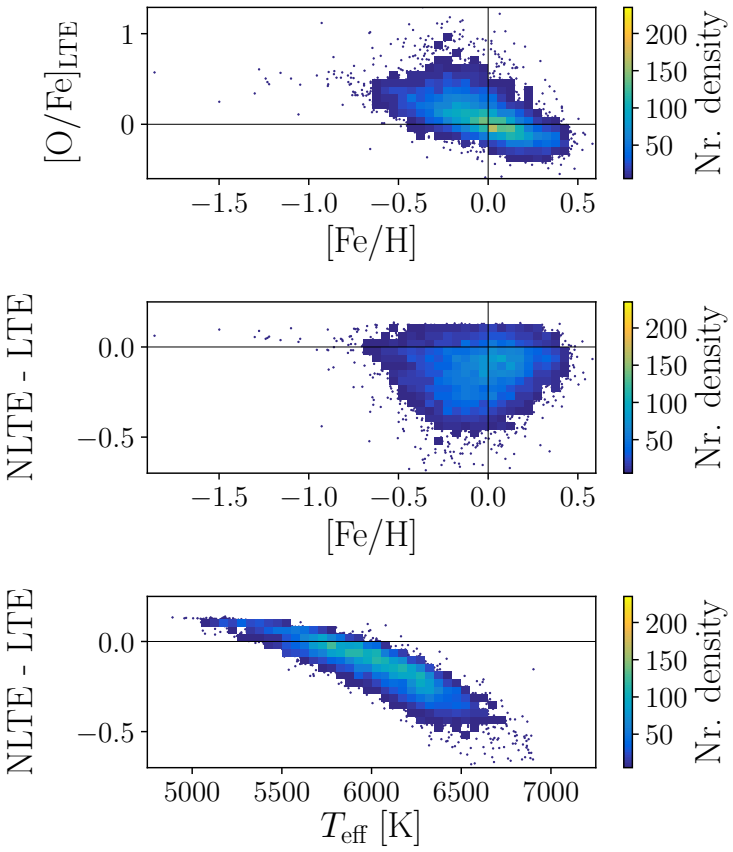

Figure 3.14: Visualisation of the change of O abundance with respect to the assumption of LTE. Top panel shows [O/Fe] assuming LTE, while middle and bottom panel show difference with respect to non-LTE abundances as a function of metallicity (middle) and effective temperature (bottom). Stars are shown as blue dots or in bins (containing a minimum of 5 stars). The plots indicate that the O abundance of hot stars need to be significantly corrected downwards by up to 0.7 dex, when estimated under the LTE assumption with [O/Fe] up to 1.0. **Figure Credit:** Paper II.

When comparing with the study by Bensby et al. (2014), who also analysed the O triplet, we see a strong agreement, that is, a steep and quite tight linear decrease of [O/Fe] around 0.5 dex for metal-poor stars to around −0.25 dex for the most metal-rich stars. The different behaviour of O with respect to the combined α-enhancement is an important nuance. Numerous simulations (e.g. Minchev et al., 2013) use O as main or sole tracer of α-enhancement. Accurate estimates of O in stars are vital for scaling measurements of nebulae and galaxies in general, because it is the most abundant element after hydrogen and helium. We note that for hot and young stars we measure large abundances of O also in non-LTE. For these stars, the stellar parameters are hard to estimate and their non-LTE

corrections are hence also less certain, because they are strongly changing with stellar parameters. We can not exclude atmospheric 3D effects for these stars. Although these effects are not expected to be as large as the LTE to non-LTE correction, they are still non-negligible as demonstrated by Amarsi et al. (2016a, see their Fig. 9). We note that hot and young stars scatter the age trend at intermediate metallicities, hence blurring the age trend in this regime.

3.4.2.4 α ELEMENTS

Because of the significantly different behaviour of O with respect to the other α-process elements Mg, Si, Ca, and Ti, in the GALAH range, as well as the strong non-LTE corrections (and possibly 3D corrections) needed for O, we have decided to not define O as an α-process element for this study.

Magnesium agrees with the combined α-enhancement trend, but with a larger spread and scatter at all metallicities. In agreement with Adibekyan et al. (2012), we find a flatter trend ([Mg/Fe] between 0.0 and 0.1 dex) at the metal-poor end of the low Mg regime than Bensby et al. (2014) (up to 0.2 dex). At the metal-rich end of the distribution, we find a larger relative fraction of Mg-enhanced stars than Bensby et al. (2014). Adibekyan et al. (2012) also found stars with these abundances, which they assigned to the high-αmetal-rich population. We note that Fuhrmann (2011) did not find these stars in his volume-complete study based on Mg. Mg shows a strong proportionality with age and on average, the trend seems to be metallicity- and temperature-independent.

Silicon measurements in GALAH spectra follow the expected α-enhancement trends. In agreement with the studies by Adibekyan et al. (2012) and Bensby et al. (2014), Si is in general closer to the solar value, that is, also less enhanced in the metal-poor regime than Mg and O.

Calcium is measured with lower precision and although a tight trend of Ca abundances is expected for this α element, the abundances derived from GALAH spectra are very scattered, but agree in general with Bensby et al. (2014) and Adibekyan et al. (2012).

Titanium agrees well with previous studies by Adibekyan et al. (2012) and Bensby et al. (2014). Ti can be very well measured in optical dwarf spectra, because numerous clean Ti lines are available with good line data. Hence Ti is one of the most precise elements for studies in the optical. Ti is however not well reproduced by chemical evolution models (Kobayashi & Nakasato, 2011; Kobayashi et al., 2011).

3.4.2.5 LIGHT ODD-Z ELEMENTS

Sodium shows a large abundance spread (0.15 dex) compared to the median measurement uncertainties, centred around the solar value for solar metallicities and trends towards more enhancement both towards the sub- and super-solar regime, with different steepness. In both metal-poor and metal-rich stars [Na/Fe] is elevated by up to 0.15 dex with respect to solar. The correlations with stellar parameter, see Fig. 3.16, indicate that the scatter is caused by non-LTE effects (Lind et al., 2011). The substantial star-to-star scatter persists in the super-solar metallicity regime. The estimated trends agree well the previous

LTE studies by Adibekyan et al. (2012) and Bensby et al. (2014). We note that the abundance trend of this element is very similar to those of Ni and Cu, although with a larger spread. The age-correlation indicates a slight Na-enhancement for the younger stars and Na-depletion for the intermediately old stars around solar metallicities, hence the opposite behaviour to that shown by α elements. The oldest stars of the sample tend to show solar [Na/Fe] at low metallicities, in agreement with Ni and Cu. We note that the similar behaviour of Na and Ni was already found for solar twins by Nissen (2015), who identified a very tight correlation of [Na/Fe] and [Ni/Fe] of their sample (see their Fig. 12). They also found that neither element correlates tightly with stellar age.

Aluminium is measured using 1D non-LTE corrections by Nordlander & Lind (2017)[6]. [Al/Fe] shows a significant spread of 0.25 around solar abundance ratios at solar metallicities and increasing abundances towards both the metal-rich and metal-poor regimes. The oldest and most metal-poor stars show Al enhancement up to 0.3 dex, but old stars with solar metallicity are still Al enhanced, while younger stars are closer to solar [Al/Fe] at sub- and solar metallicities, in agreement with Bensby et al. (2014) and Adibekyan et al. (2012). Contrary to Bensby et al. (2014), but in agreement with Adibekyan et al. (2012), the super-solar metallicity stars show an increasing trend similar to the odd-Z element Na. Our Al measurement behave in general very similar to the Mg measurements, including in the metal-rich regime, where a gradual increase with age and with [Al/Fe] can be noticed.

Potassium shows, similar to O abundance estimates in LTE, an increasing trend of [K/Fe] with effective temperature, most prominent for turn-off stars, see Fig. 3.16, indicating a large influence of non-LTE for the measured atomic resonance line K I 7699 Å. These effects are estimated to be of the order of −0.4 to −0.7 dex (Ivanova & Shimanskiĭ, 2000). This line suffers from an interstellar contribution, which increases the line depth as a function of a reddening-dependent component, which has not been corrected for. It is therefore expected that the LTE trend differs from the non-LTE study by Zhao et al. (2016). K behaves similar to O both when assuming LTE and non-LTE, which indicates that K behaves like an α element. Due to the observational difficulties and strong expected non-LTE effects, we do not draw strong conclusions for this element from our results.

3.4.2.6 IRON-PEAK ELEMENTS

Scandium shows a similar behaviour as the α elements Si and Ti, that is, a flat trend for super-solar metallicities and an increase of Sc abundances towards metal-poor stars, in agreement with Battistini & Bensby (2015). Adibekyan et al. (2012) found Sc trends similar to Al, with a significant increase of Al towards super-solar metallicities. All three studies have at least three Sc lines in common, hence it is unlikely that the difference originate in the chosen lines themselves. It is worth mentioning that Adibekyan et al. (2012), using the linelist by Neves et al. (2009), did not include hyper-fine structure splitting, contrary to this study. The difference in abundance measurements with or without the use of hyper-fine structure splitting is of a very complex nature, but has

[6]Using the grid available at `https://www.mso.anu.edu.au/~thomasn/NLTE/`.

been shown to play an equally important role for abundance estimations as blending, microturbulence velocities, line choices, line centres, and oscillator strengths (Jofré et al., 2017).

Vanadium stays flat over most of the metallicity range, but shows a slight increase towards lower metallicities. A large number of lines are however too blended or weak to be used for the V abundance estimation in the metal-rich and poor regime. The estimated trend is consistent with those estimated by Adibekyan et al. (2012) and Bensby et al. (2014). Where we can detect V, [V/Fe] seems to be rather independent of stellar age, that is, young and old stars span a range in [V/Fe] around ±0.15.

Chromium traces Fe along most of the metallicity range and our trends agree in general with Bensby et al. (2014) given our lower precision. In the metal-rich regime, super-solar [Cr/Fe] seems to be favoured. We note that Adibekyan et al. (2012) estimated a very slight anti-correlation of Cr with metallicity (around 0.03 dex [Cr/Fe] within 1 dex metallicity), which our measurements do not suggest.

Manganese measurements agree with the decreasing trend of Mn with metallicity found by Battistini & Bensby (2015) and Adibekyan et al. (2012) under the assumption of LTE. Battistini & Bensby (2015) also discuss the significant influence on this trend when considering non-LTE. We only use LTE in our study, but include non-LTE in future GALAH analysis

Cobalt was only detected for a very small number of stars with strong lines (4%), typically metal-rich stars in the sample. We therefore make no conclusions for Co.

Nickel traces Fe for [Fe/H] < 0 and increases towards super-solar metallicities, in agreement with Adibekyan et al. (2012) and Bensby et al. (2014).

Copper was not detected in the metal-poor regime; we observe solar [Cu/Fe] with a small spread at [Fe/H] < 0, an increasing spread of [Cu/Fe] towards solar [Fe/H], and increasing Cu abundance with metallicity in the super-solar regime. This trend agrees with previous studies by Delgado Mena et al. (2017), which was performed on a significantly smaller sample.

Zinc measurements in our sample follow the same trend as Ni and Cu, that is, showing a rather flat behaviour at low metallicities and stronger increase at super-solar metallicities. Zn is however more scattered than Ni and Cu, although the mean uncertainties are comparable. Zn is not created in SN Type Ia according both to theoretical yields (Iwamoto et al., 1999; Kobayashi et al., 2006) and observations (Nissen & Schuster, 2011; Mikolaitis et al., 2017; Skúladóttir et al., 2017). The yields of Zn are very metallicity-dependent (Kobayashi et al., 2006). We therefore do not expect Zn to behave exactly like α-elements. In our sample, stars with high [Zn/Fe] also show high [α/Fe] at and below solar metallicities. At super-solar metallicities, where the high- and low-α sequence can not be distinguished, our measurements suggest a linear increase of Zn with a large spread or scatter, as also found by Bensby et al. (2014). Strong blending (especially towards cooler temperatures) decreases the precision of our measurements, but we note that Bensby et al. (2014); Delgado Mena et al. (2017) also estimated a significant spread of Zn with their high-resolution and high S/N data.

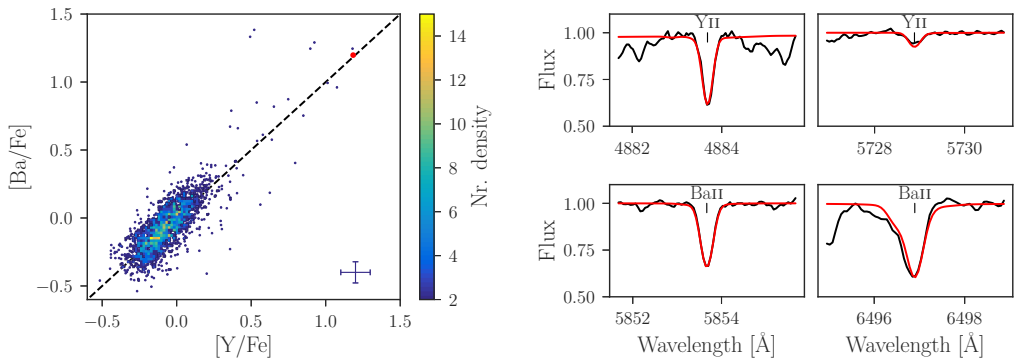

Figure 3.15: The left panel shows the distribution of Ba and Y abundances when measured for both elements. The elements behave close to a 1:1 correlation indicated by a dashed black line in the background. For higher abundances however, Ba is slightly more abundant than Y. Right panels show the observation (black) and synthesis (red) of Ba and Y lines of the s-process enhanced 2MASS J20120895-4129341 (indicated by a red dot in the left panel). **Figure Credit:** Paper II.

3.4.2.7 THE NEUTRON-CAPTURE ELEMENTS

Several neutron-capture elements have lines that are detectable in GALAH spectra only for giant stars. For this sample of dwarfs and subgiants, the line strength is too small to be significant at the survey, S/N. However, Y and Ba have strong singly ionised lines readily detectable also in the majority of our unevolved stars. We therefore only report the abundance of the s-process neutron capture elements Y and Ba relative to iron.

Yttrium shows a lens-like shape, with a lower almost flat lower limit at about −0.4 dex and a convex upper limit between metallicities of −0.7 and 0.4 dex with most abundances below +0.4 dex. While Bensby et al. (2014) also found some Y-enhanced stars, the vast majority of their stars showed roughly solar Y abundances relative to iron. High abundance measurements in stars could be a result of non-LTE effects. However, our sample shows such elevated Y values across a wide range of temperatures and surface gravities, see Fig. 3.17. We can not confirm a behaviour similar to O or K, for which LTE-based abundances are strongly overestimated in some stars. Additionally, a strong correlation between [Y/Fe] and age was found for solar twins by Nissen (2015) and Spina et al. (2016), which are insensitive to differential non-LTE effects because of the similar stellar parameters among solar twins. We find old stars of our sample to show depleted Y, while young stars are Y-enhanced. From both theory (Travaglio et al., 2004) and cluster observations (D'Orazi et al., 2009; Maiorca et al., 2011), this can be explained with the increasing contribution of s-process material from low-mass asymptotic giant branch stars to the Y and Ba abundances over time.

Barium was measured less frequently than Y, especially for metal-poor stars, but the overall lens-shaped trend of Ba with metallicity is similar and consistent with Bensby et al. (2014), who showed that a large fraction of their sample with $T_{\rm eff} > 6100$ K are Ba-enhanced (see their Fig. 16). We note that similar to Delgado Mena et al. (2017), the most metal-rich stars show lower [Ba/Fe] than [Y/Fe] by around 0.1 dex. Investigating

the flagged stars, this trend seems to be caused by detection limits for Ba. When we look at the trend with ages, we find these hotter stars are however also younger and their Ba abundance correlates, similar to Y, with the stellar age, as shown by Nissen (2015) and Spina et al. (2016).

When comparing [Y/Fe] and [Ba/Fe] in Fig. 3.15, we find a reassuringly strong correlation of both, with a slightly steeper slope of Ba abundance compared to Y. In the right panels of Fig. 3.15, we depict the s-process enhanced star 2MASS J20120895-4129341, indicated by a red dot in the left panel, with strong Y and Ba lines.

3.4.2.8 CORRELATIONS WITH STELLAR PARAMETERS

Correlations of abundances with effective temperature, surface gravity, and microturbulence velocity are shown in Figs. 3.16 and 3.17. If the actual element abundances do not change with evolutionary stage, we expect flat trends for all these parameters. An element, for which our measurements are systematically off, is K, which suffers from strong non-LTE effect especially for the turn-off stars. We note however, that some elements are subject to changes in the evolutionary stage (e.g. Li, which shows a steep trend with $T_{\rm eff}$).

3.4.3 AGE-[α/FE]-[FE/H] DISTRIBUTIONS

We detect abundances for up to 20 elements, as presented in Sect. 3.4.2. For this study, we focus on the αw-elements and iron as well as their correlations with stellar age. The combination of these three parameters is shown in Fig. 3.18.

The abundance patterns of α-elements in the Galactic discs are expected to follow roughly a similar pattern according to the stellar enrichment history by supernovae type Ia and II (see e.g. Gilmore et al., 1989). While both types of supernovae produce a variety of elements, there is a significant difference in the yields of iron and α-elements and the time in the Galactic evolution, when they each contribute to the chemical enrichment. Early in the chemical evolution of the Galaxy, SN Type II dominate the production of metals and large quantities of α-elements are then produced (e.g. Nomoto et al., 2013). The timescales for SN Ia are larger than those of SN Type II, with estimated intermediate delay times of around 0.42 to 2.4 Gyr (Maoz et al., 2012). After this delay time, SN Ia fed material into their environment - but with a larger yield ratio of iron to α-chain elements, therefore decreasing the abundance ratio [α/Fe] while increasing [Fe/H] (e.g. Matteucci & Francois, 1989; Seitenzahl et al., 2013).

The combined α-element abundance is estimated for 99% of our stars. For each of these stars, at least one α-process element is detected and all significant measurements are combined with their respective uncertainties as weight. Mg, Si, and Ti are the most precisely measured elements and have the highest weight. Hence, we note that the [α/Fe]-ratio, as defined here, is in practice very similar to the previously used error-weighted combination of Mg, Si, and Ti for GALAH DR1 (Martell et al., 2017) and for the study by Duong et al. (2018). We see overall good agreement in the [α/Fe] pattern with the stars in the solar vicinity analysed by the APOGEE survey (Hayden et al., 2015), that is, predominantly solar ratios for -0.7 and $+0.5$ dex and fewer stars

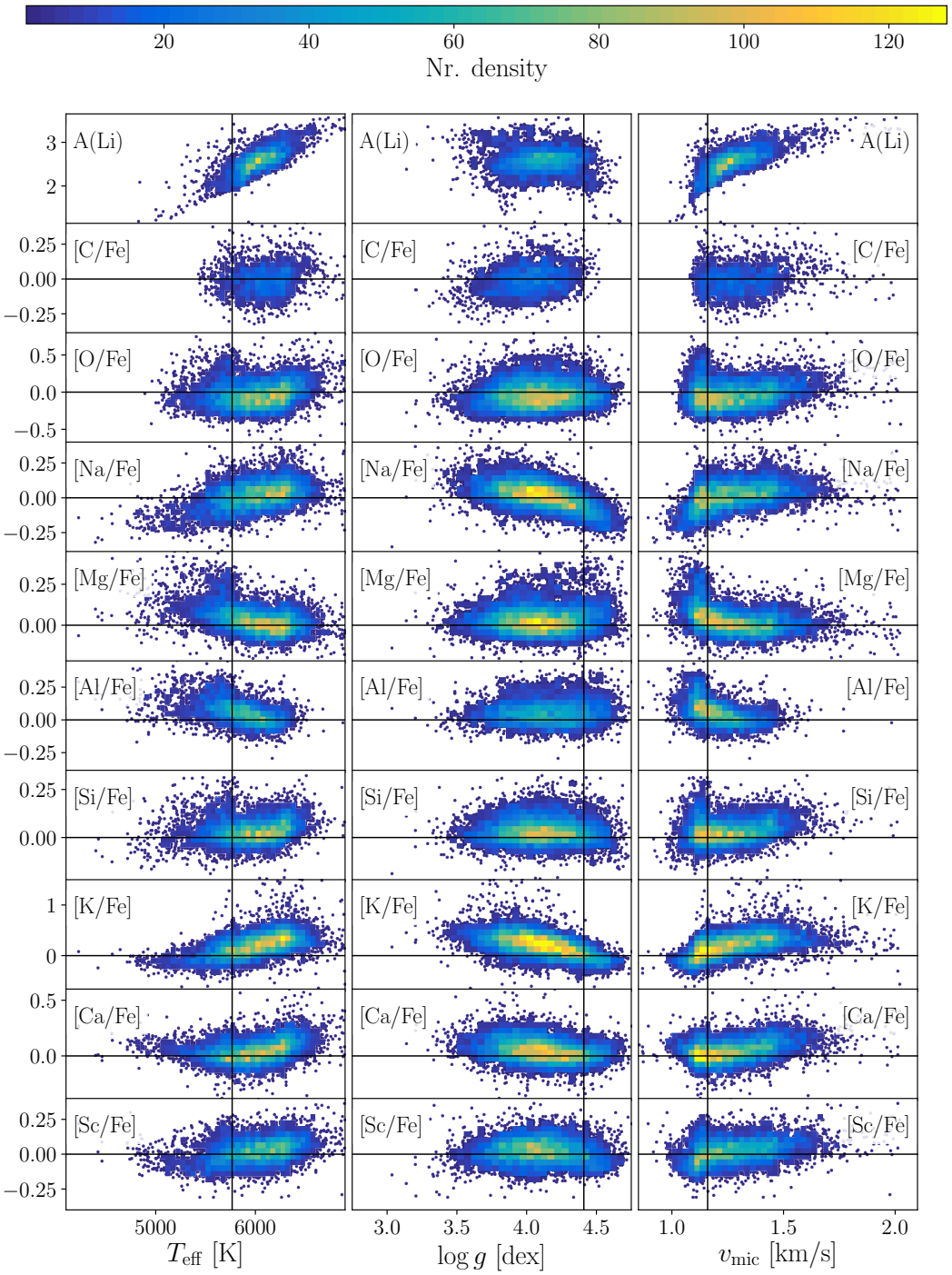

Figure 3.16: Element abundances ordered by atomic number for the clean sample of dwarf, turn-off and subgiant stars (elements X indicated in top right corner of each panel) as a function of $T_{\rm eff}$ (left panels), log g (middle panels), and $v_{\rm mic}$ (right panels). All elements are shown relative to the iron abundance, except for Li (shown as absolute abundance). Colour indicates the density of stars with a minimum of 5 star per bin. Individual stars outside the bins are shown as small dots. See individual paragraphs in Sect. 3.4.2 for further descriptions. **Figure Credit:** Paper II.

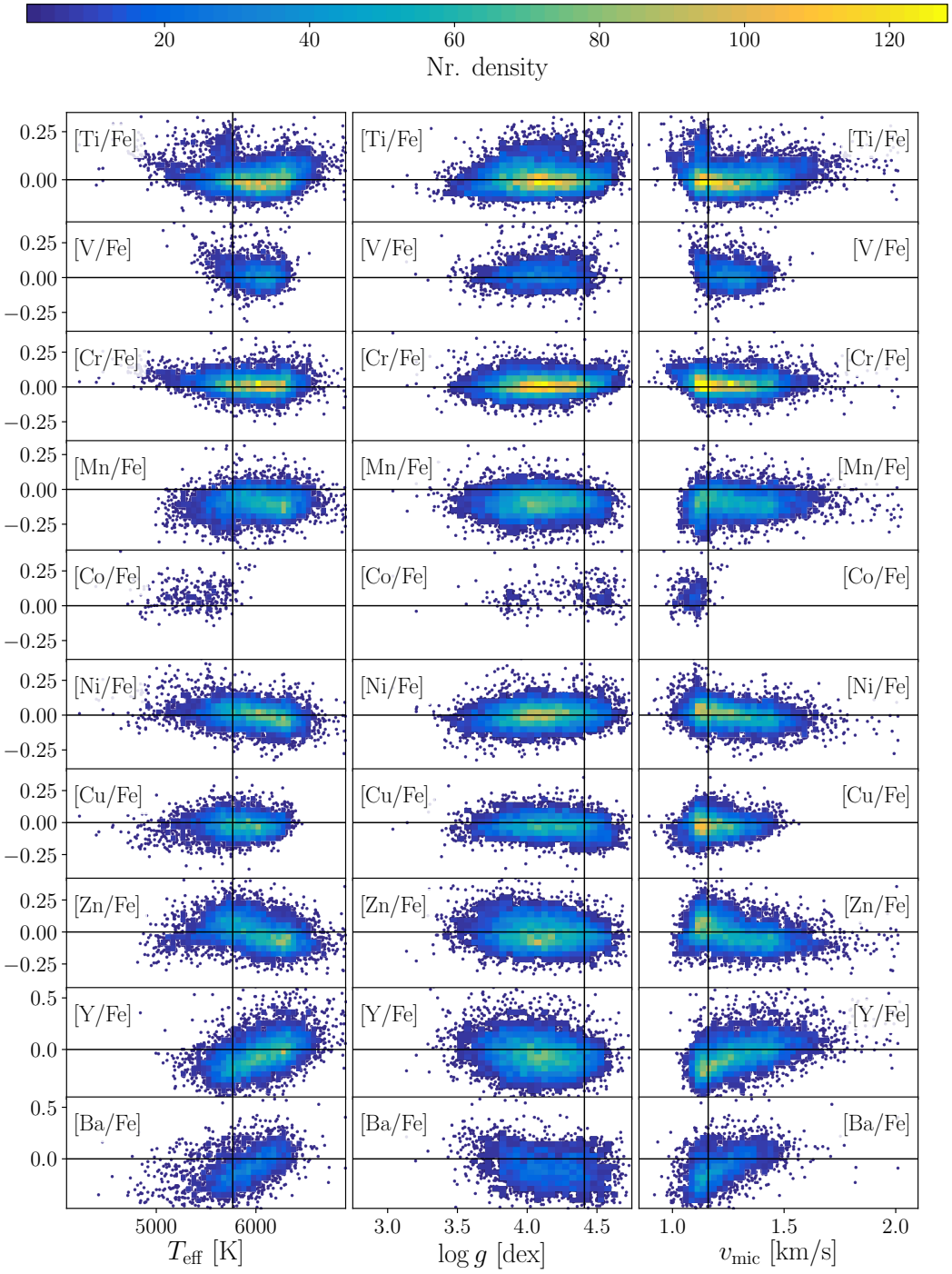

Figure 3.17: Continuation of Fig. 3.16. **Figure Credit:** Paper II.

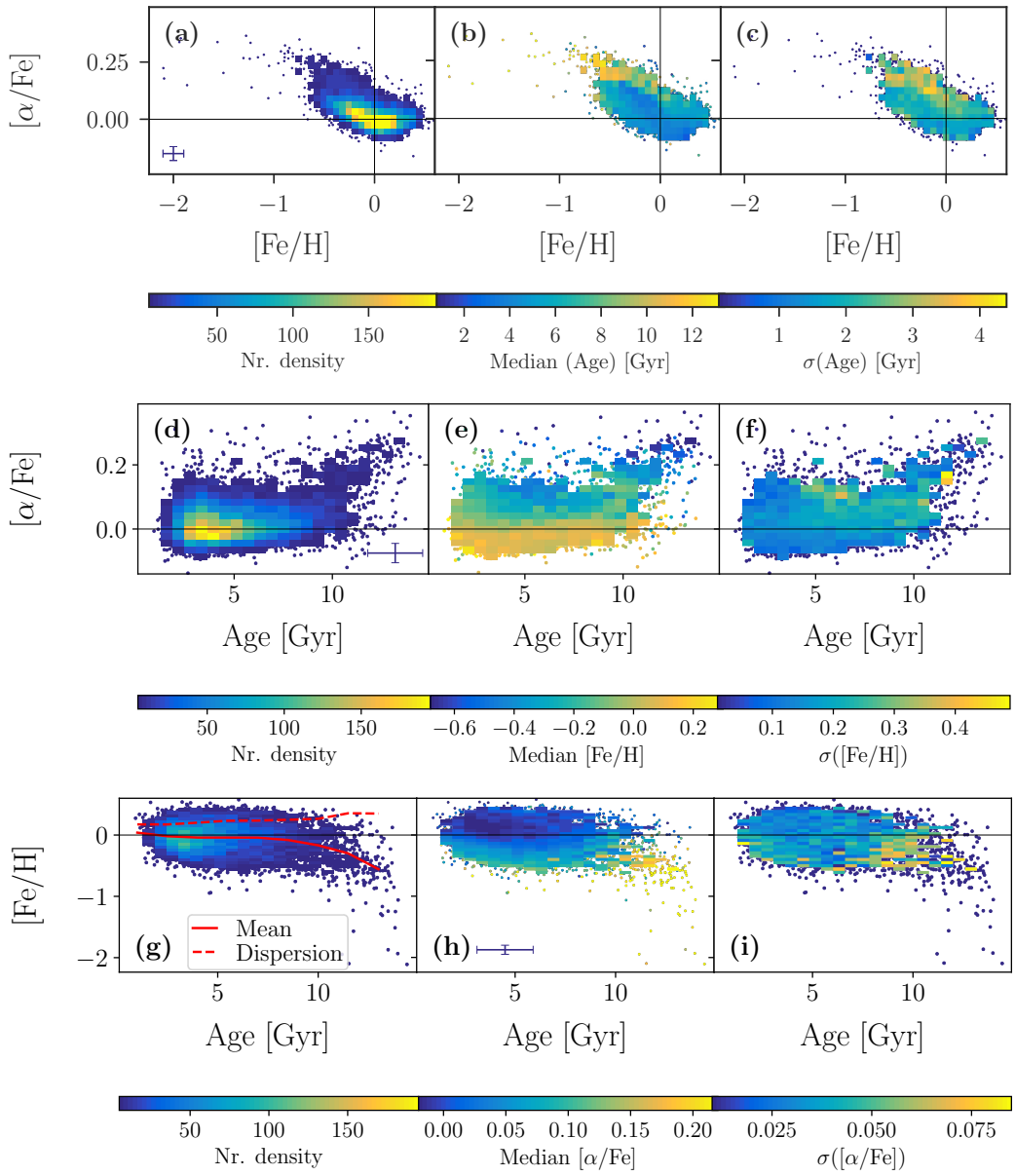

Figure 3.18: Diagrams of the age-[Fe/H]-[α/Fe] distribution in three rotating visualisations (top to bottom). (a) to (c) show [α/Fe] both as a function of [Fe/H]. (d) to (f) and (g) to (i) show [α/Fe] and [Fe/H] as a function of age, respectively. We show the density distributions in the left panels (a), (d), and (g). The same distributions are shown with bins coloured by the median age, [Fe/H], and [α/Fe] in the middle panels (b), (e), and (h), respectively. The right panels show the same distributions coloured by the standard deviation of age, [Fe/H], and [α/Fe] in the middle panels (c), (f), and (i), respectively. Dots are used for individual stars in sparse regimes instead of density bins. In (g), we also show the mean metallicity (red line) and dispersion (red dashed line) as a function stellar age. The mean is decreasing with age from 0.04 to −0.56 dex, while the dispersion is increasing with stellar age from 0.17 to 0.35 dex. See text in Sec. 3.4.3 for detailed discussion. **Figure Credit:** Paper II.

with increasing α-enhancement towards lower metallicity. We discuss this bimodality further in Sect. 3.4.3 by inspecting the quantitative distribution of [α/Fe] in several metallicity bins, see Fig. 3.19. We stress that there is no unambiguous or universal definition of α-enhancement, but studies estimate and define this parameter differently, which complicates comparison. Hereinafter we use an average, weighted with the inverse of the errors, of the four α-process elements (Mg, Si, Ca, and Ti) when we refer to [α/Fe] and α-enhancement. We note that because our definition of α-enhancement is driven by Ti as the most precisely determined element, our values are comparable with the study by Bensby et al. (2014) based on Ti. Fuhrmann (2011) use only Mg as tracer of the α-process ratio. All different definitions hence induce possible systematic trends.

The [α/Fe]-[Fe/H] distribution is shown in Fig. 3.18 (a) to (c).

The pattern of our study agrees very strongly with the results found by Ness et al. (2016) for APOGEE (see their Fig. 8) and Ho et al. (2017b) for LAMOST (see their Fig. 5), all three showing high age for the high-α sequence and younger ages for stars on the low-α sequence. We note that stars with larger ages usually have larger absolute age uncertainties. In contrast to the expected rather monotonic trend between α-enhancement and stellar age (especially at constant metallicity), we note that around $-0.4 <$ [Fe/H] < 0, young and fast rotating stars are dominating the interim-[α/Fe] regime. For hotter stars with $v \sin i > 15$ km/s, the estimated iron abundances A(Fe) are typically lower than the one of slow rotators. While this could be a trend introduced by the analysis approach that depends on sufficiently deep metal lines, another possibility is an actual correlation between [Fe/H] and rotation. An analysis of this correlation is complex and beyond the scope of this paper. When we neglect such stars (10% of the sample), the trend of stellar age and [α/Fe] is monotonic.

For the high-α metal-rich regime, a mix of different ages is noticeable, with an age spread up to 4 Gyr. We take a closer look at this region in Sect. 3.5.

To assess how distinct the two α-enhancement sequences are at different metallicities, we plot the histograms for five 0.15 dex-wide metallicity bins in Fig. 3.19. By eye, two clear peaks can only be identified for the three lower metallicities with decreasing separation. However, the fit of two Gaussians recovers the two peaks for all five distributions. For the most metal-poor bin, the α-enhanced stars are more numerous with an enhancement of 0.25 ± 0.03 dex, compared to the low-α stars at 0.13 ± 0.06 dex. We note that even the low-α stars are slightly enhanced at these metallicities. At higher metallicities, the mean enhancement of the low-α sequence decreases gradually to become solar at solar metallicity.

The enhancement of the high-α sequence decreases more steeply down to 0.04 ± 0.05 dex at solar metallicity. The peaks of the two (forced) sequences are thus consistent within one sigma (indistinguishable) at solar metallicity. We stress that in our fit we forced two Gaussian distributions and the actual distribution looks like a positively skewed Gaussian distribution. This means that an assignment to the high- or low-α sequence based on a given [α/Fe] threshold (for example Adibekyan et al., 2012) is significantly less accurate or meaningful than in the metal-poor regime (see also Duong et al., 2018).

The widths of the Gaussian fits to the high and low-α sequence are of order 0.02 – 0.08 dex for [α/Fe] and similar to our measurement uncertainties and we note that the separation between the two sequences in the metal-poor regime is larger than this.

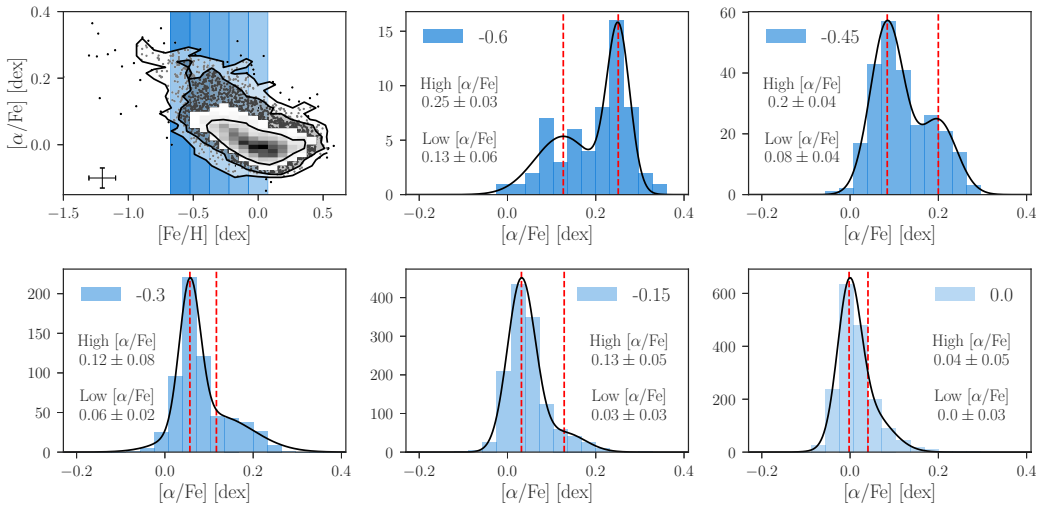

Figure 3.19: α-enhancement [α/Fe] over metallicity [Fe/H] for all metallicities (upper left panel). The blue bars indicate the metallicity bins, which are used to select stars to estimate the α-enhancement distribution in corresponding blue at different metallicities in the other panels, with mean [Fe/H] indicated in the upper left or right corner. Two Gaussian distributions are fitted to the data with mean values indicated by the red lines and their distribution in black. Mean and standard deviation of the two Gaussians are annotated in each panel. See Sect. 3.4.3 for detailed discussion. **Figure Credit:** Paper II.

The [α/Fe]-age distribution is shown in Fig. 3.18 (d) to (f). The main findings from these panels are:

The mean α-enhancement stays rather constant at [α/Fe] $\sim$ 0.05 up until 8 Gyr and then increases with stellar age. A comparison of our relation with the one found for the stars analysed by Bensby et al. (2014), see left panel of Fig. 3.20, shows that the observed relations agree within their measurement uncertainties.

We find 6% of the stars below 8 Gyr with [α/Fe] $>$ 0.125. The corresponding fraction for stars older than 11 Gyr is 60%. This indicates a small jump around 8 to 10 Gyr (from mean [α/Fe] $\sim$ 0.05 to 0.09) between high and low-α enhancement, as also found by Haywood et al. (2013). At around 8 to 12 Gyr, we note a large range of metallicity in these coeval stars.

We find 67 stars among the young ones (that is, 4978 stars with $<$ 6 Gyr), that are significantly α-enhanced ([α/Fe] $>$ 0.13) with normal rotational velocities (and another 59 with $v \sin i >$ 15 km/s). With $\sim$ 0.9% of our sample ($\sim$ 1.8% when including the fast rotators), their ratio is in agreement with the sample analysed by Martig et al. (2015), who found 14 out of 1639 stars to be α-rich and similar to most of the ratios of other samples listed by Chiappini et al. (2015). Looking only at the young stars ($<$ 6 Gyr) our ratio of 1.4 – 2.5% is however smaller than the one found by Martig et al. (2015) of 5.8%, pointing towards a different age distribution of the two different samples (containing

either only giants or main sequences/turn-off stars). The 59 (47%) of the young α-rich stars in our sample with increased broadening are all hotter than 6000 K. We want to stress that for such stars the broadening in addition to the decreasing line strengths due to the atmosphere structure make the parameter estimation more uncertain than for the rest of our sample.

Among the old stars (> 11 Gyr), we find that a significant fraction of the sample (30%), are low-α stars ([α/Fe] < 0.125), in contradiction to Haywood et al. (2013). These stars are primarily cool main sequence or subgiant stars with metallicities above −0.5 dex, which causes their ages to have larger error bars. Silva Aguirre et al. (2018) also found such stars among APOGEE giants from the Kepler sample of stars, using asteroseismology to determine precise ages (see their Fig. 10).

Haywood et al. (2013) claim a rather tight correlation between age and α-enhancement for the old high-α stars. However, Silva Aguirre et al. (2018) do not see evidence for such a tight relation. Our sample implies a tight trend, but is limited by the small number of these stars and we can not draw strong conclusions regarding the dispersion of chemistry and age.

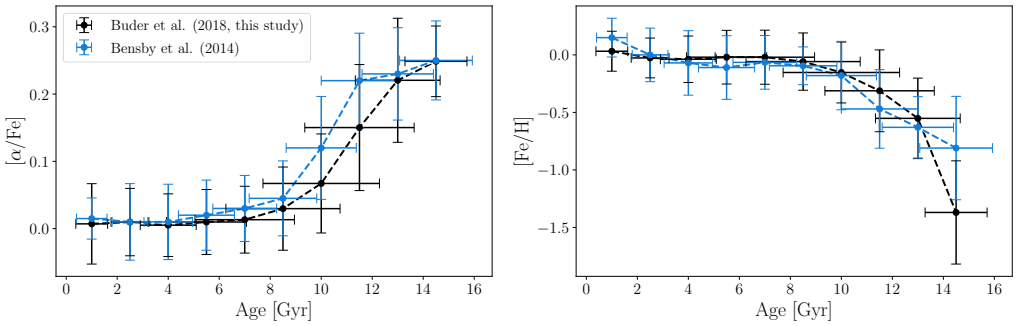

Figure 3.20: Comparison of the relations of stellar age and mean metallicity [Fe/H] (left) as well as mean [α/Fe] (right) for the stars of this study (black) and the stars from Bensby et al. (2014, blue), showing that the two relations agree between the studies within their uncertainties. The data points are calculated in 1.5 Gyr steps from 1 to 14.5 Gyr) and the errors are the means of the age uncertainties as well as the standard deviations for the mean [Fe/H] and [α/Fe], respectively. **Figure Credit: Paper II**.

The [Fe/H]-age distribution is depicted in Fig. 3.18 (g) to (i) and shows:

With increasing stellar age, the mean metallicity, indicated with a red line in panel (g), decreases steadily and non-linear from 0.04 at 1 Gyr to −0.56 at 13 Gyr respectively, but also with increasing dispersion. The recent study by Feuillet et al. (2018) finds that in their sample both the lowest [Fe/H] and highest [Fe/H] stars are older than the solar abundance stars and the iron abundance is hence less useful than [α/Fe] to predict age.

The [Fe/H] dispersion increases with stellar age from 0.17 at 2 Gyr to 0.23 at 5 Gyr, then only marginally to 0.25 at 9.5 Gyr and finally 0.35 at 13 Gyr, as the red dashed line shows in Fig. 3.18 (g). The trend has been calculated in bins of 1.5 Gyr, similar to the median age uncertainties, and each containing at least 50 stars.

Between ages of 0 and 8 Gyr, we see a rather flat mean metallicity with a spread of 0.5 dex around solar metallicity. In this age range, stars with lower metallicities (< -0.25) show an increase of α-enhancement of up to around 0.1 dex.

Above ages of 8 Gyr, metal-poor stars with [Fe/H] < -0.25 exhibit a decreasing trend of metallicity with increasing stellar age. We can not confirm the tight age-metallicity distribution for the oldest stars due to the small sample of these stars, although we note indications of a tight overdensity. Few old stars around solar metallicity stand out, as also found in previous studies by Casagrande et al. (2011, (see their Fig. 16)). These stars cause an increased dispersion, which is in agreement with the continuously increasing dispersion also seen at lower ages (see Fig. 3.18 (g)). Similar results are found by Haywood (2008b, see their Fig. 1), who interpreted this trend as an observational signature of radial migration. We follow this up, when including kinematics, in the following section.

We find that the old stars of the sample are more α-enhanced. The oldest stars (above 11 Gyr) are most metal-poor and α-enhanced (around 0.25 dex at metallicity [Fe/H]~ -0.5), while slightly younger stars (still above 8 Gyr) are less α-enhanced and more metal-rich (around 0.15 dex at solar metallicity). Most of the stars of the sample exhibit slightly increased or solar [α/Fe] and are on average younger than 6 to 8 Gyr, but the sample also contains a minority of old stars (around 8 Gyr) with low metallicity (around -0.6 dex) and only slight α-enhancement. We assess and discuss these results in more detail in Sect. 3.5.

3.4.4 KINEMATICS

To get an overview of the kinematical content of the GALAH+TGAS overlap, we first examine the 3D velocities. We then use these velocities to assign membership probabilities to different Galactic components.

From the Toomre diagram in Fig. 3.21, we can deduce that most stars belong to the disc, because their total velocities are lower than 180 km/s, which is typically adopted as a good limit of halo kinematics (Venn et al., 2004; Nissen & Schuster, 2010). This was expected from the target selection (De Silva et al., 2015). Most of the sample shows an azimuthal relative velocity close to the local standard of rest, that is, $|V| < 50$ km/s and also U and W are close to the local standard of rest, indicating a solar-like motion in the thin disc. However, there are stars that also show large deviations from the thin disc kinematics, with total velocities larger than 100 km/s relative to the local standard of rest. In previous studies, such stars have been identified as thick disc stars, based on a hard limit of 70 km/s (Fuhrmann, 2004).

Adopting hard limits to separate populations is however not appropriate when it comes to kinematics, as both thin and thick disc populations show significant dispersions in their characteristic space velocities (Nordström et al., 2004). Several more sophisticated approaches have been implemented (see e.g. Reddy et al., 2006; Ruchti et al., 2011; Bensby et al., 2014). To begin with, we follow the approach by Bensby et al. (2014) to estimate the probability of each star to belong to one of the Milky Way components thin disc (D), thick disc (TD) or halo (H) by their kinematical information including the

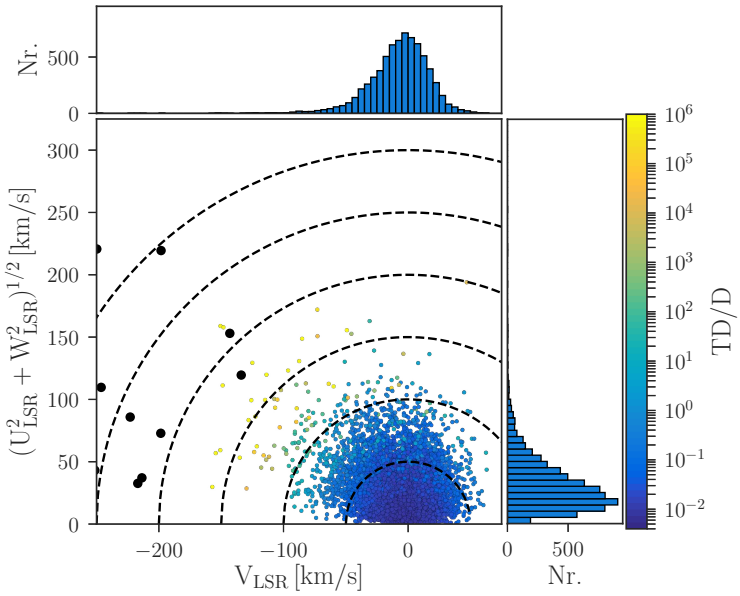

Figure 3.21: Toomre diagram of the sample from the perspective of the local standard of rest (LSR). Colour indicates the kinematic probability ratio of thick-to-thin disc membership, estimated in Sect. 3.3.6. For 12 stars (marked as enlarged black dots), the kinematic membership probabilities point to neither thick or thin disc membership, but actually the halo. Dashed circles indicate total velocities in steps of 50 km/s. The majority of the stars shares similar velocities to the local standard of rest and their kinematic membership ratio TD/D points towards the thin disc. Fewer stars are seen with total velocities above 100 km/s and they typically show lower space velocities V. These stars have a significantly higher TD/D ratio, characterising them as thick disc stars. **Figure Credit:** Paper II.

population velocity dispersions. The probability is influenced by the velocity distribution (assumed to be Gaussian), rotation velocities, as well as the expected ratio of stars among the components (Bensby et al., 2003). Similar to Bensby et al. (2014) we subsequently use the ratios of the membership probabilities.

For each component, it is possible to separate the sample into most likely thick disc stars ($TD/D > 10$) and most likely thin disc stars ($TD/D < 0.1$), as shown in Fig. 3.22. The 12 stars, that fit the kinematics of the halo best, are marked as big black circles and contribute 0.16 % to the sample. Almost all of these stars show a total space velocity of more than 180 km/s and would also be identified as halo stars with the simplified velocity criteria.

Most of the GALAH+TGAS dwarfs are most likely to be affiliated with the thin disc, while only a small fraction belongs to either thick disc or halo. For a very large fraction of the stars however, the probability ratio is indecisive.

While the analysis of kinematics with the classical Toomre diagram is a powerful tool for a small volume, the approximations (assuming similar positions and velocities) are less appropriate for larger volumes. We therefore include another way to interpret the kinematical information by calculating action-angle coordinates and characterise orbits with integrals of motion as proposed by McMillan & Binney (2008).

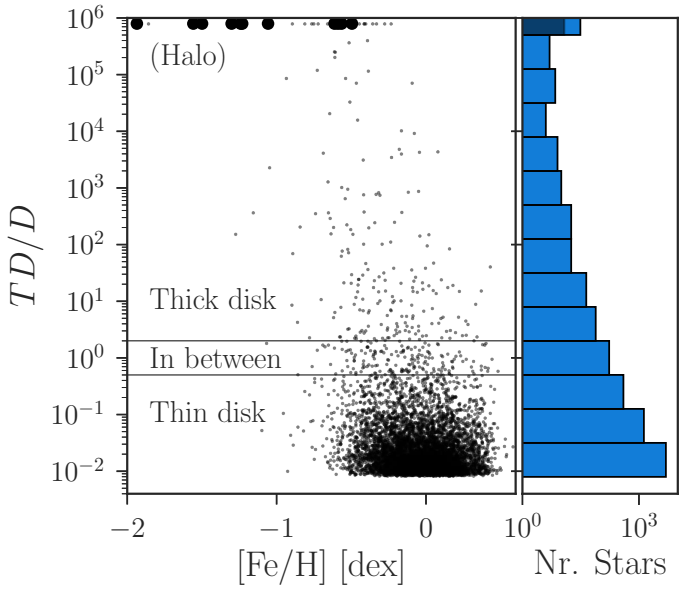

Figure 3.22: Ratio of kinematic membership probabilities of thick to thin disc TD/D of the sample, estimated in Sect. 3.3.6 following the approach by Bensby et al. (2014) and comparable with their Fig. 1. Most stars are assigned to the thin disc with this criterion. 12 stars, marked as enlarged black dots, are likely to be halo stars, based on their membership ratios with respect to the halo, D_H and TD_H respectively. **Figure Credit:** **Paper II**.

Contrary to U, V, and W, the three orbit labels, the actions J_R, $J_\Phi = L_z$, and J_z, allow us to quantify and compare orbits of stars independent of their position relative to the Sun or the local standard of rest. The distribution of the three actions is shown in Fig. 3.23 and shows that most of the stars have similar orbits to the Sun, meaning low eccentricities and radial actions J_R, low vertical oscillations and vertical actions J_z, and azimuthal actions similar to the one of the Sun (with $L_{Z,\odot} = R_\odot \cdot v_{\Phi,\odot} = 8\,\mathrm{kpc} \cdot 220\,\mathrm{km/s} = 1760\,\mathrm{kpc\,km/s}$). However there are several stars with $J_R > 75\,\mathrm{kpc\,km/s}$ on more eccentric orbits, which manifests in mean stellar radii either significantly closer to ($L_z \ll L_{z,\odot}$) or further away from ($L_z \gg L_{z,\odot}$) the Galactic center. We follow this up in Sect. 3.5, when analysing angular momenta of the individual stars with different ages and chemistry, see Fig. 3.24.

3.5 DISCUSSION OF CHEMODYNAMICS OF THE GALACTIC DISC

‘ The previous discussion highlighted that we report a significant change of chemistry around the stellar age of 8 to 10 Gyr. Haywood et al. (2013) and Bensby et al. (2014) used this to establish population assignments based on ages alone or ages and chemistry combined. Haywood et al. (2013) made a seemingly more arbitrary cut in the [α/Fe]-age.

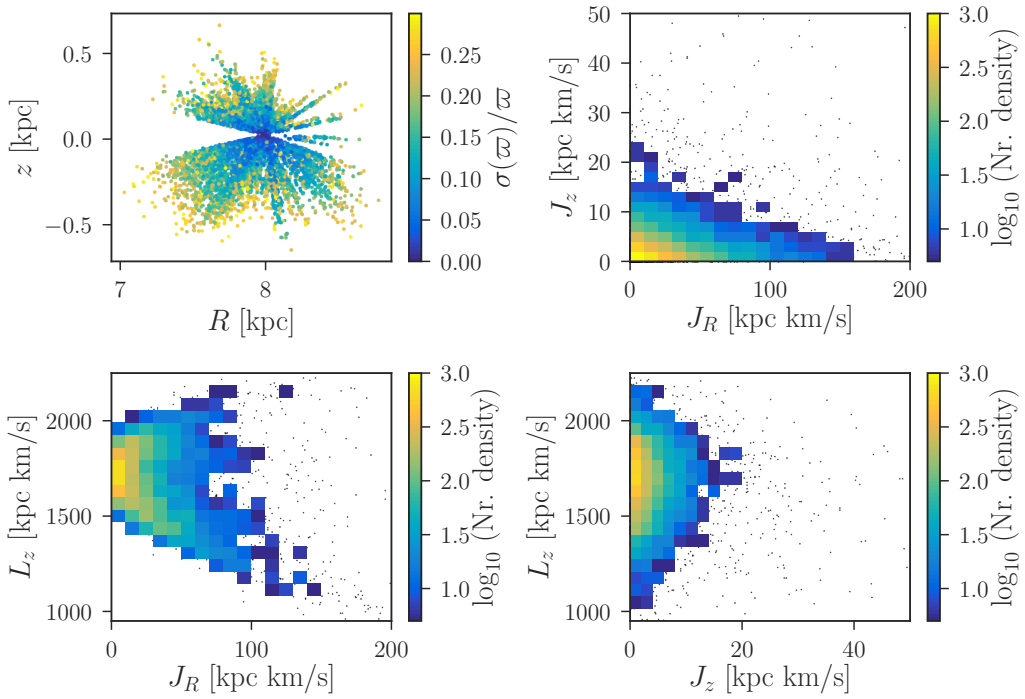

Figure 3.23: Distribution of the sample stars in the R-z plane (top left) as well as the three actions J_R-J_z (top right), J_R-$J_\phi = L_z$ (bottom left), and J_z-L_z (bottom right). With exception of the top left panel (coloured by parallax precision), colour indicates the number of stars per bin in each panel, with a lower limit of five stars per bin. Individual stars outside the bins are shown as black dots. The top left panel shows that increasing distance from the Sun, the parallax precision decreases. It also shows that with the exception of two special pointings, the Galactic plane ($|b| < 10$ deg) is neglected by GALAH. The individual action angle plots show that most of the stars move on circular orbits with solar Galactocentric orbit and angular momentum. The top right corner shows decreasing density with a diagonal pattern up to a line which intercepts with J_R at 150 kpc km/s and J_z at 20 kpc km/s and with only few stars with larger actions. The J_R-L_z shows trends of a minority of stars to be on eccentric orbits which have their apocentre in the solar neighbourhood (sub-solar L_z and increased J_R) or eccentric orbits with pericentres in the solar vicinity (super-solar L_z and increased J_R). While stars do not show increased vertical actions in the J_z-L_z plane (bottom right), an increase vertical actions can be seen for stars with solar angular momentum. **Figure Credit:** Paper II.

By assessing the [α/Fe]-[Fe/H] relation at different stellar ages, we take a closer look at the transition phase in Fig. 3.24. This slicing into mono-age populations has already been performed on output from numerical simulations (see e.g. Bird et al., 2013; Martig et al., 2014). However it has, to our knowledge, not yet been applied to observational data, especially chemical composition, beyond the analysis of the age-metallicity structure (see e.g. Mackereth et al., 2017).

In Fig. 3.24, we plot age bins; we can therefore focus on specific ages rather than age sequences. For each of the 1 Gyr bins, we show the [α/Fe]-[Fe/H] plane and colour the stars by their angular momentum, which is a function of Galactic radii. Our main findings are:

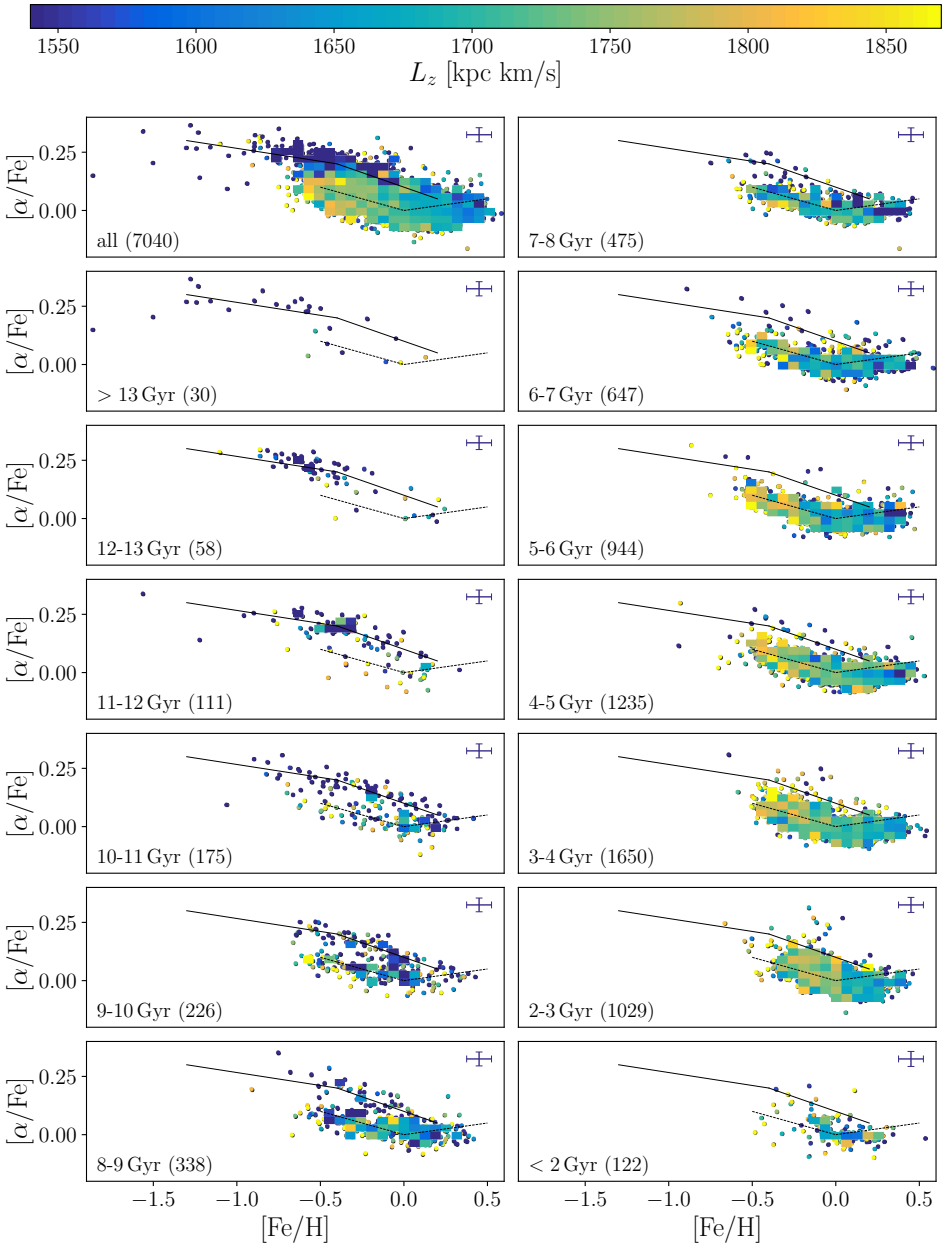

Figure 3.24: α-enhancement, [α/Fe] with [Fe/H] in different age bins. The top left panel shows the distribution of all stars and mean angular momenta L_z are shown in bins with more than five stars. The other panels show the stars bins of stellar age, ranging from above 13 Gyr (second left panel) to below 2 Gyr (bottom right panel). Colour indicates the angular momentum of each star, estimated in Sect. 3.3.6. The text in each panel indicates the age and respective number of stars. Fiducial lines indicate the low-α and high-α sequences to guide the eye. This plot shows, that stars with high-α enhancement have generally lower angular momentum, while stars in the low-α sequence, have mostly solar momentum. We note however that the metal-rich low-α stars have in general lower angular momenta than metal-poor stars with comparable α-enhancement. For a detailed discussion of the panels see Sect. 3.5. **Figure Credit: Paper II**.

The oldest stars (> 13 Gyr) are mostly α-enhanced and metal-poor and have not been significantly enriched by SN Ia because they were born before the delay time of SN Ia was reached. Their spread in metallicities can be explained by different SN II masses and and frequencies, as well as gas mixing efficiencies, in the progenitor clouds. Their angular momentum shows that stars older than 13 Gyr are usually located closer to the Galactic centre with mean $L_z = 1060 \pm 600$ km/s, which corresponds to an average Galactocentric distance of 4.8 ± 2.7 kpc.

We note however, four stars with roughly solar metallicities older than 13 Gyr, which could be unidentified binaries because of their proximity to the main sequence binary sequence. Such stars have also been found by Casagrande et al. (2011, see their Fig. 16), Bensby et al. (2014, see their Fig. 21), and Silva Aguirre et al. (2018, see their Fig. 10). Their angular momenta and actions point towards solar-like orbits for half of them or eccentric orbits with significantly lower angular momenta than the Sun for the other half. The presence of these stars could be explained via chemical evolution, radial migration, but also influence of the bar. The recent study by Spitoni et al. (2018) showed, that a revision of the 'two-infall' model can explain the presence of old stars with $-0.5 <$ [Fe/H] < 0.25 and [α/Fe] < 0.05. Such stars have however also been found in the inner disc (Hayden et al., 2015) and even the bulge (see e.g. Bensby et al., 2017). The latter found even a high fraction of one-third of low-α stars among the old stars. However the models by Spitoni et al. (2018) are not able to fully recover for example the age distribution and additional dynamic process are needed to explain the observed data. If we assume radial migration of such stars, we expect also them to arrive in our solar neighbourhood. Models for radial migration (see e.g. Frankel et al., 2018) however usually aim to model the secular evolution of stars and hence currently focus on stars younger than 8 Gyr. We do however not see a reason why the oldest stars, which clearly exist in the inner Galaxy (Hayden et al., 2015; Bensby et al., 2017) should not have migrated in a similar manor as the younger stars within the lookback time of the migration models. Further analyses beyond the scope of this paper will hopefully help to pin down the more likely reason for the presence of the old stars with solar [Fe/H] and [α/Fe]. Another explanation that can be tested with more extended data sets is the radial migration due to the influence of the Milky Way bar (see e.g. Grenon, 1999; Minchev & Famaey, 2010).

Stars between 12 and 13 Gyr exhibit more iron than the oldest stars although at similar [α/Fe]. In the metal-poor regime ([Fe/H] < 0), the high-α stars have lower angular momentum than the Sun ($\langle L_z \rangle = 1267 \pm 389$ kpc km/s with mean L_z uncertainties of 63 kpc km/s), while more metal-rich stars ([Fe/H] > 0) have angular momenta ($\langle L_z \rangle = 1513 \pm 262$ kpc km/s with mean L_z uncertainties of 46 kpc km/s closer to the solar one ($L_{z,\odot} = 1760$ kpc km/s).

Below 12 Gyr, all stars except three outliers have metallicities above -1.0 dex. Between 12 and 9 Gyr, the stars on the high-α sequence become gradually less α enhanced and show increasing metallicities, hence indicating a continuous evolution of high-alpha stars along this sequence. This is consistent with the increasing enrichment of the ISM by SN Ia with a delay time distribution (see e.g. Maoz et al., 2012), producing significantly

more iron than SN II. Their angular momenta are on average still significantly lower than the solar one. This indicates a continuous evolution of high-α stars along this sequence. We want to stress that these stars are still slightly α-enhanced, even at solar metallicities. Below 9 Gyr, only a few stars are on the high-α sequence and almost none below 7 Gyr.

Similar to previous studies (Lee et al., 2011; Haywood et al., 2013) we find a gradual increase of angular momentum and rotational velocity with metallicity among the *alpha*-enhanced metal-poor stars, which are is also correlated with age above 10 Gyr. For stars below 10 Gyr (but even more pronounced for stars below 8 Gyr), the angular momentum decreases with metallicity, as shown in Fig. 3.25.

Around 10 Gyr and at younger times, stars at the metal-poor end of the low-α sequence appear. This finding is consistent with previous results by Haywood et al. (2013, see their Fig. 8). The angular momenta of many of them indicate an origin at larger Galactic radii, that is, they are only visitors to the solar neighbourhood, in agreement with findings by Haywood (2008b) and Bovy et al. (2012b).

Between 3 and 9 Gyr, the full range of metallicities from −0.7 up to 0.5 at the low-α sequence is covered. The stars at the low-α metal-poor end show on average significantly larger angular momenta than the Sun, an opposite trend with respect to the high-α stars. The angular momenta of metal-rich stars (1640 ± 180 kpc km/s) are on average lower than the solar one.

At younger times than 3 Gyr, the spread in metallicities decreases and stars younger than 2 Gyr only cover metallicities between −0.3 and 0.3. We note that our cut for hot stars, see Sect. 3.2) has cut out most of the stars with ages below 2 Gyr, see Sect. 3.4.1. Casagrande et al. (2011) have found, however, that nearby stars younger than 1 Gyr also only cover the range of $-0.3 < [\mathrm{Fe/H}] < 0.2$ (see their Fig. 16).

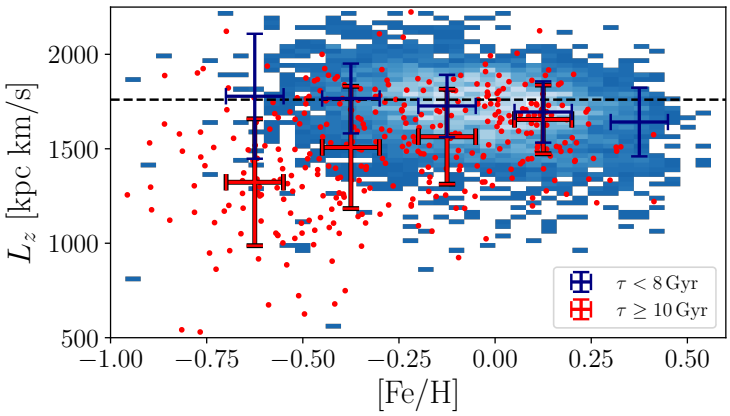

Figure 3.25: Angular momentum L_z as a function of metallicity [Fe/H]. Stars with ages below 8 Gyr are shown in a blue density plot and those with ages above 10 Gyr as red dots. For both sets, mean angular momenta have been calculated in 0.25 dex steps in [Fe/H] for bins with more than 50 entries and are shown with mean [Fe/H] error and a combination of L_Z uncertainty and standard deviation of the mean L_z as error bars. The solar angular momentum is indicated with a dashed line. **Figure Credit:** Paper II.

Similar conclusions of a gradual chemical enrichment of the high-α sequence with time can be drawn from the data by Hayden et al. (2017, see their Fig. 3), as well as from the analysis of Auriga simulations (Grand et al., 2018).

Finally, we revisit the α-enhancement of the sample, but dissect the sample by the kinematic probability of belonging to the thick or thin disc. These probabilities are estimated in Sect. 3.3.6 and we use them to recreate Fig. 19 from Bensby et al. (2014) with the GALAH+TGAS sample. From this dissection in Fig. 3.26 we conclude:

Stars that are kinematically more than ten times more likely to be part of the thick disc population (top panel), are mostly on the high-α sequence. We note that in contrast to Bensby et al. (2014), these stars are not all metal-poor, but also cover the high-α metal-rich regime. These stars are however almost exclusively older than 8 Gyr. The sample from Bensby et al. (2014) is expected to cover relatively more metal-poor stars, because they selected their sample specifically with the aim to trace the metal-poor limit of the thin disc, the metal-rich limit of the thick disc, the metal-poor limit of the thick disc.

Stars that are $2-10$ times as likely to belong to the thick disc ($2 < TD/D < 10$) and those with inconclusive kinematics ($0.5 < TD/D < 2$) cover both the high- and low-α metal-rich regime as well as a larger range of ages.

At the lowest probabilities of belonging to the thick disc ($TD/D < 0.5$), the stars are on average young (5.0 ± 2.2 Gyr) and cover the low-α sequence. However, there are still noticeable amounts of stars in the high-α metal-rich regime ([Fe/H] > -0.1 and above the dashed line, including stars older than 8 Gyr. This implies that there is no distinct kinematical separation of populations in the metal-rich regime and a significant overlap in kinematic properties is present.

3.6 CONCLUSIONS

The combination of spectroscopic data from the high-resolution GALAH survey and the astrometric data from the Tycho-*Gaia* Astrometric Solution (TGAS) spans a high-dimensional space of chemodynamical information. In this study, we have analysed 7066 dwarf and turn-off stars of this overlap. Our main results are summarised as follows:

3.6.1 ABUNDANCE AND AGE TRENDS

1. We show that our parameter and abundance estimates measured with the GALAH pipeline are accurate and precise.

2. Our selected stars are all within the solar vicinity and consist mostly of young stars with metallicities from -0.7 dex up to $+0.5$ dex as shown by the age and metallicity distributions.

3. We report stellar parameters (including iron in non-LTE), 18 element abundances in LTE, an error-weighted α-process element abundance in LTE, and Li as well as O abundances in non-LTE. We show that non-LTE corrections for the O triplet

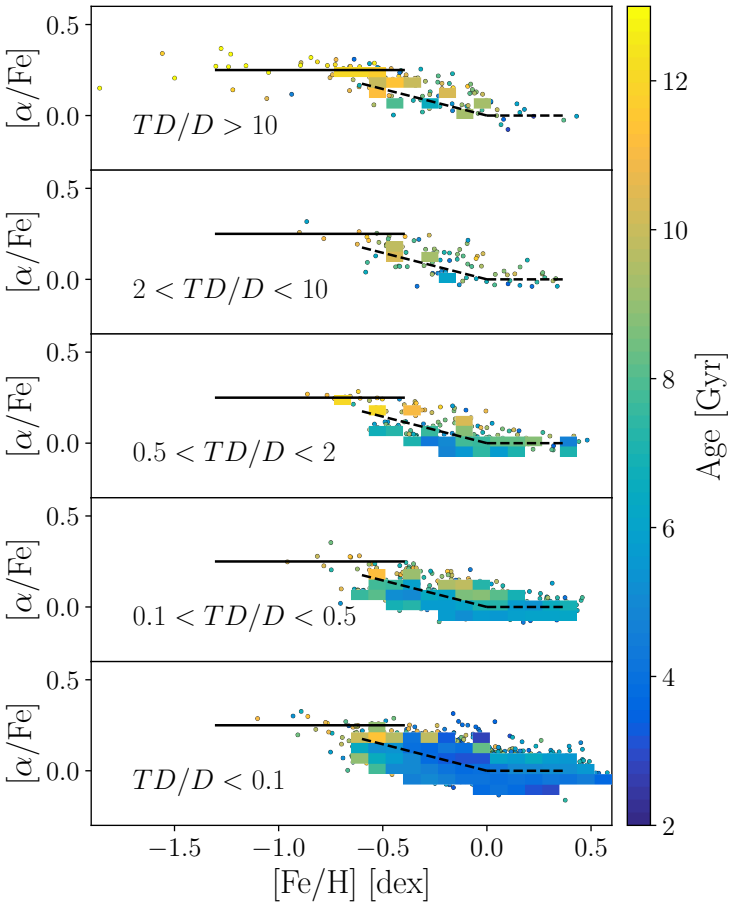

Figure 3.26: [α/Fe] as a function of [Fe/H] selected based on the kinematic probabilities of belonging to the thin or thick disc TD/D from kinematics. Colour indicates the estimated age. Analogous to Fig. 19 of Bensby et al. (2014), the abundance plateau of the thick disc and the decrease for thin disc have been plotted in black to guide the eye. While stars with highly thick-disc like kinematics (two upper panels) follow the high-α sequence, numerous stars with thin-disc like kinematics are also seen in the high-α metal-rich regime. However, most stars with thin disc like kinematics (TD_D < 0.5 two lower panels) follow the low-α sequence. See Sect. 3.5 for further discussion. **Figure Credit:** Paper II.

are a vital requirement for accurate abundance estimation of stars in different evolutionary stages.

4. We show in Fig. 3.12, that the abundance trends estimated for the GALAH+TGAS sample agree well with previous studies with higher spectral quality. Due to the larger number statistics and the selection of our stars, we are able to assess abundance trends of the low-α sequence in more detail than previous studies.

5. Among the studied elements, we find the expected similarities of abundance trends among the α-elements Mg, Si, Ca, and Ti. O, however, shows a significantly steeper decrease with metallicity and no flattening at super-solar metallicities and was hence not treated as an α-element. The odd-Z elements Na and Al show

similar increasing abundances towards the super-solar metallicities. We note that these trends also agree with those observed for the iron-peak elements Ni, Cu, and Zn.

6. We find significant trends of abundances with stellar age for α- and s-process elements, see Fig. 3.13, similar to previous studies of solar twins (Nissen, 2015; Spina et al., 2016) and dwarfs in general (Bensby et al., 2014).

3.6.2 THE AGE-[α/FE]-[FE/H] RELATIONSHIP

1. We recover the same pattern of the [α/Fe]-[Fe/H] in combination with age as previous studies (e.g. Ness et al., 2016; Ho et al., 2017b), namely that the high-α sequence is mainly consisting of old stars, while the low-α sequence covers ages usually below 8 Gyr. We note however, that at the the low-α metal-rich and low-α metal-poor regime, we also find stars with ages between 8 to 10 Gyr.
2. When using age and chemistry together, the high-α metal-rich stars can be well explained to be part of a population formed from the same material as the canonical (lower metallicity) thick disc, although significantly enriched by both SN II and Ia. This is in contradiction to the claim by Adibekyan et al. (2012), but backed up by stellar kinematics. The angular momenta of the high-α metal-poor and high-α metal-rich stars are both significantly and consistently lower than the solar value. We conclude that these stars belong to the high-α sequence rather than representing a distinct population.
3. At solar and super-solar metallicity, both old and young stars as well as slightly α-enhanced and solar [α/Fe] stars are observed. We have shown in Fig. 3.19, that in this regime, the two distinct α-sequences (as seen for [Fe/H] < 0) become indistinguishable in [α/Fe] vs. [Fe/H]. We conclude, similarly to Haywood et al. (2013), that stellar age is a better identifier and discriminator of formation origin than metallicity, especially at high metallicity. Stellar age, when available, is more fundamental than an arbitrary cut in [α/Fe] for the purpose of understanding Milky Way populations.
4. The decreasing spread of metallicities for stars younger than 4 Gyr is strong support for radial migration. Radial migration predicts that stars will change their orbits after they have been born. The panel of Fig. 3.24 with stars below 2 Gyr shows a narrower range in metallicity compared to the panel for stars with ages of $3 - 4$ Gyr. With increasing age, stars are observed at lower and higher metallicity ranges. Yet, there are no stars with metallicities at -0.5 and 0.5 dex for the youngest ages, although the GALAH selection is not biased against these stars. At increasingly younger ages we preferentially see stars formed in the solar neighbourhood, whereas older stars did not have time to migrate to this location. Therefore, we only see stars formed in the solar neighbourhood. This observational support for radial migration in the thin disc has also been found in other studies (Haywood, 2008a; Feuillet et al., 2016, see e.g.) and tested by comparison with models including radial migration by Feuillet et al. (2018). We stress however, that

we excluded stars with $T_{\rm eff} > 6900$ K from this study, which are mostly younger than 3 Gyr. While we advice caution that our result might be biased, Casagrande et al. (2011) have found a similar spread of [Fe/H] for stars below 1 Gyr in their analysis.

3.6.3 CHEMODYNAMICS OF THE DISC IN THE SOLAR VICINITY

1. Our sample includes a small fraction of stars of the distinctly old (> 10 Gyr) and α-enhanced ($[\alpha/\mathrm{Fe}] > 0.3$) thick disc. These stars are also kinematically consistent with the chemically defined thick disc.
2. Stellar age does not change after the birth of a star. However, kinematic properties of stars from different populations overlap and might also change. Thus, age should be a more reliable definition of a population.
3. Independent of the population assignment of the high-α-metal-rich stars (see Sect. 3.6.2), their kinematics (e.g. their lower angular momentum compared to the Sun) indicates, that they have migrated towards us via blurring, meaning they are on eccentric orbits with mean radii closer to the Galactic center.
4. Around ages of 8 to 10, Gyr, stars at the metal-poor end of the low-α disc are identified. When including kinematical information, we find a large number of these stars to be from outside the solar neighbourhood (on eccentric orbits with mean radii further out). At the metal-rich end of our sample, the kinematical information points to a significant number of stars from the inner radii on eccentric orbits. This result is in agreement with the seminal paper by Edvardsson et al. (1993, see their Fig. 22) and confirms blurring as reason for a broad age-metallicity relation at different radii.

3.6.4 FUTURE INVESTIGATIONS

The follow-up of our study with more detailed studies focusing of certain aspects of the high-dimensional chemodynamical space is promising. Anders et al. (2018) have shown that the chemical space can be dissected by using t-distributed stochastic neighbour embedding. For the high-α metal-rich regime they find that these stars are different from the classical thick disc. They find however, that the stars in this regime are spread within the t-SNE distribution, indicating an evolution within this regime (see their Fig. 1). The application of their approach onto our data is promising but beyond the scope of this paper.

In this study, we have shown that non-LTE corrections play a crucial role for several elements. We suggest a detailed further investigation of 3D and non-LTE effects for other elements. We are working on extending the non-LTE implementation and apply them to seven elements in GALAH DR2 **Paper I**.

A quantitative study of the correlation of element abundances and stellar ages for the stars of our sample could explore the influence of other parameters on the [Y/Mg]-age correlation beyond the solar twins (Nissen, 2015; Spina et al., 2016), to test the hypothesis

by Feltzing et al. (2017), that the [Y/Mg]-age relation is unique to solar analogues. Such analyses can be performed on all different elements, especially when using the second public Data Release from the GALAH survey **Paper I** and the second *Gaia* Data Release. With this large set of abundances, ages, and kinematics, it will also be possible to identify clumps in chemodynamical space or stellar streams (see e.g. Quillen et al., 2018). A central point of Galactic archaeology in the future will also be the improvement of stellar age estimation.

CHAPTER 4

CHEMODYNAMICS OF THE STELLAR HALO WITH GALAH AND *Gaia*

4.1 PREFACE

In Chapter 1, we have shown why chemodynamic studies are vital for unraveling the history of our MW. In this chapter, we are describing the analyses and interpretation of the preliminary data of GALAH DR3 with the aim to dissect and understand the MW stellar halo and its overlap with the stellar disk. The observation and spectral analysis of GALAH DR3 as well as the estimation of dynamical information and stellar ages is explained in Chapter 2 and we will only describe more detailed selection criteria in this chapter. Because the spectroscopic analysis of GALAH DR3 is still ongoing when this Thesis is handed in, the available chemical information for the full sample of the latest analysis run is limited to iron and the α-process elements. However, a pilot analysis run for all 30 elements was performed for all stars with total velocities above 180 km/s, which are kinematically attributed to the halo (as introduced in Sec. 1.2.3). Thus, the research presented in this chapter is divided into two main topics representing the full sample and the high-velocity sample, respectively.

In Sec. 4.3, we address the question how distinct the canonical stellar halo is from the high-α disk. To explore this, we study the transition between disk and halo by using the full sample of stars from GALAH DR3 and the combined information of stellar ages, stellar dynamics as well as the chemical dimensions of iron and α-element abundances. In Sec. 4.4, we use a combination of kinematic and chemical properties that showed non-smooth transitions to decompose the full sample with Gaussian Mixture Models (GMMs) with identify the major constituents of the MW and thereby shed light on its formation history. We refer to the detected components as 'hyper-components' to highlight their possibly non-Gaussian nature (as superpositions of several Gaussian components) and that they represent over-densities in a multi-dimensional space. We expect for example the low-α sequence, which shows a non-Gaussian shape in the [Fe/H] vs. [α/Fe] plane to be such a hyper-component built up from at least two individual components (see Fig. 1.7).

Sec. 4.5 addresses the second aspect of the halo research and tries to characterise the stellar halo in more detail - especially regarding chemistry, by using the kinematically selected halo stars. We investigate if our data confirms the identified bimodality of low- and high-α halo stars (Nissen & Schuster, 2010) with our significantly larger data set. We analyse if we can assign stars in our sample to the recently dynamically discovered accreted structure of the 'Sausage' (Belokurov et al., 2018; Helmi et al., 2018) with the aim to further characterise its chemical and age pattern.

In Sec. 4.6, we discuss our findings. We assess which combinations of stellar properties show smooth transitions or distinct differences between the disk and halo. We discuss the number of hyper-components that we find with a Gaussian Mixture Model decomposition and try to link them back to the canonical components of the MW. We also link them to those components that were found via the chemical decomposition of kinematically selected stars of our sample with the aim to assess if the low-α population found by Nissen & Schuster (2010) is actually the same as the accreted structure found by Belokurov et al. (2018) and Helmi et al. (2018). Furthermore, we will discuss the contentious ages of halo stars, for which either exclusively old ages (see e.g. Gallart et al., 2019) or an age gradient above 8 Gyr (see e.g. Das et al., 2019) are reported.

This chapter will be the basis for **Paper III** to be submitted as Buder et al. (in prep. a) and I have performed all analyses presented in this chapter myself. I want to stress however, that the data used in this chapter was provided as part of the combined effort of the data analysis group of the GALAH survey, as outlined in Chapter 2. Additionally I want to acknowledge the contribution of my co-authors to this chapter by the observation and reduction of the data as well as valuable comments regarding the figures or their contribution to the GALAH survey as builders.

4.2 OBSERVATIONS AND DATA

We use data from the internal data release 3 (iDR3) of the GALAH survey collaboration. This data set will be used for the public data release 3 (DR3) with only minor changes and the detailed analysis will be explained in **Paper IV**, but is in principal similar to the first analysis step of Data Release 2 (see **Paper I**), where the spectrum synthesis code Spectroscopy Made Easy (Piskunov & Valenti, 2017) is used to estimate stellar parameters and element abundances. GALAH DR3 will make extensive use of the *Gaia* information by constraining $\log g$ from spectroscopic $T_{\rm eff}$, isochrone interpolated masses, and bolometric luminosities inferred from the 2MASS (Skrutskie et al., 2006) K_S photometry. We want to stress that the element abundances are estimated with a line-by-line approach and 1D non-LTE calculations are used for the elements H, Li, O, Na, Mg, Al, Si, and Fe. For the final DR3, the list will be extended by K, Ca, Mn, Co, and Ba. For a detailed overview of the GALAH survey we refer the reader to Chapter 2 and the paper by De Silva et al. (2015). The dynamical data and stellar ages used for this study are obtained from the Value-Added-Catalogues accompanying GALAH DR3 (see Sec. 2.4.6), which will also be described in the data release paper (**Paper IV**).

To avoid selection biases from different target selections, we restrict our sample to those stars selected and observed in a similar manner as the GALAH main program. This includes the GALAH main program itself, with its bright and normal fields ($0 \leq$ FIELD_ID ≤ 6545) as well as faint fields ($6831 \leq$ FIELD_ID ≤ 7116), but also those stars observed as part of the K2-HERMES ($6546 \leq$ FIELD_ID < 6830) and TESS-HERMES ($7117 \leq$ FIELD_ID < 7365) programs with a sufficient height with respect to the Galactic plane ($|b| > 10$ deg). Our selection explicitly neglects the observing programmes of open and globular clusters as well as stars towards the Galactic bulge (compare panel a) of Fig. 4.1 with panel a) of Fig. 2.42). To avoid contamination from extra-Galactic stars, such as the stars of the Small or Large Magellanic Clouds, we further limit the distance of the stellar sample to less than 8 kpc, the same distance cut as chosen by Ivezić et al. (2008).

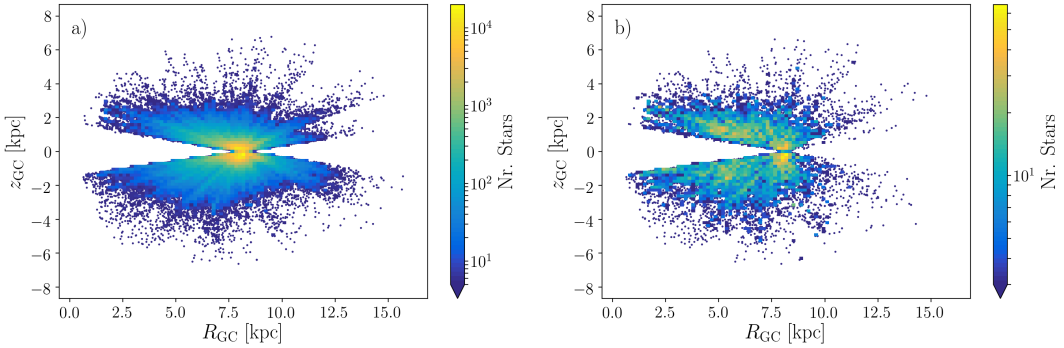

Figure 4.1: Density distribution of the 'full' (panel a) and 'high velocity' (panel b) samples in Galactocentric cylindrical coordinates (R, z). **Figure Credit:** Paper III.

To limit the data to reliable information, we apply several quality cuts, which are listed in Tab. 4.1. We restrict the sample to stars with unsuspicious information as estimated via the RUWE value (see Lindegren, 2018), but do not apply a cut on parallax precision. To ensure a minimum of spectral quality we enforce a minimum S/N of 5 in the green CCD 2. We only use stars with [Fe/H] > -2.5 to ensure that the abundance information is complete and we do not include the extremely metal-poor regime, in which stellar abundances are sensitive to the stochasticity of SN events in the early universe (e.g. Reggiani et al., 2017). The sample of stars that fulfil these criteria is hereafter called "full' sample', but is only containing iron and α-element abundances, which represent the chemical information available at the time when this Thesis is handed in.

When we refer to the 'high velocity' sample, we have employed an additional cut in total velocity, that is $v_{\rm tot} > 180$ km/s, where

$$v_{\rm tot} = \sqrt{v_{\rm rad}^2 + 4.7623 \cdot D_{\varpi} \left((\mu_{\alpha}^{\star})^2 + \mu_{\delta}^2 \right)}, \tag{4.1}$$

with parameters taken from *Gaia* DR2 (Lindegren et al., 2018), except for radial velocities $v_{\rm rad}$ (taken from GALAH iDR3) and distance D_{ϖ} in kpc (taken from Bailer-Jones et al. (2018)). The 'high velocity' sample contains all measurements of all (up to 30) elements

which are detectable within the GALAH range. For this study, we only use element abundances without flags.

Table 4.1: Selection criteria for the sub samples of GALAH DR3 considered in this study.

Category	Selection criteria	Nr. Spectra
'Full' sample	$0 \leq$ FIELD_ID < 6546 & $\lvert b \rvert > 10$ deg FLAG_SP < 7, RUWE < 1.4 (see Lindegren, 2018), Distance $r_{\rm est} < 8$ kpc, SNR_C2 > 5, and [Fe/H] > -2.5	437459
'High velocity' sample	'Full sample' criteria and $v_{\rm tot} > 180$ km/s	17756

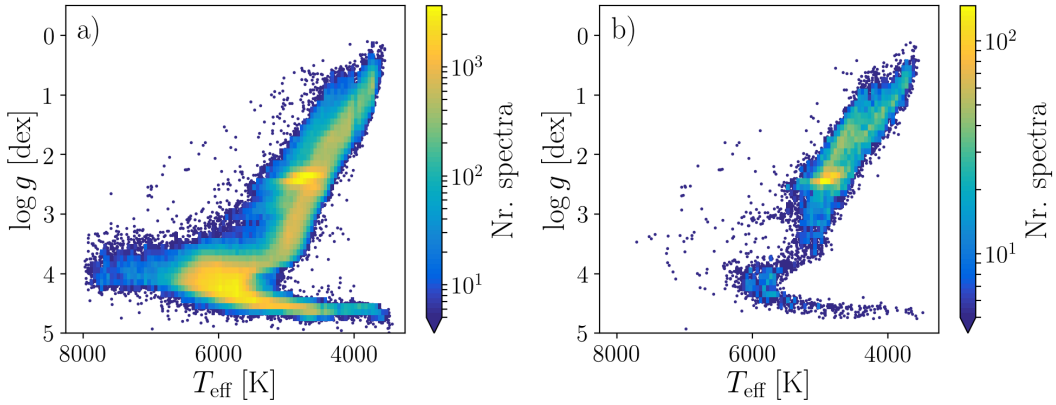

Figure 4.2: Density distribution of the 'full' (panel a) and 'high velocity' (panel b) samples in Kiel diagrams ($T_{\rm eff}$ vs. $\log g$). **Figure Credit:** Paper III.

An overview of the distribution of the spectroscopic parameters $T_{\rm eff}$ and $\log g$ for stars of both the 'full' and 'high velocity' sample is depicted in panel a) and panel b) of Fig. 4.2, respectively. The distribution of the 'full' sample in panel a) is very similar to the one presented in Fig. 2.32, because the quality cuts are only slightly different (see Table 4.1). The stars of the 'high velocity' sample are more confined in their stellar parameters and include mainly giants, but also includes a smaller fraction of several hundreds of stars in earlier evolutionary stages. It can be appreciated from panel b) that the high-velocity stars represent two distinct populations in the Kiel diagram, which we follow up in Sec. 4.5.

4.3 THE TRANSITION BETWEEN STELLAR DISK AND HALO

Several studies (see e.g. Morrison et al., 1990) have tried to find answers to the question, where the MW disk stops and the halo begins. As outlined in the introduction (see

Sec. 1.2.3), several rather distinct properties of the halo have already been explored, such as on average significantly larger total velocities with respect to the LSR. Nissen & Schuster (2010) have identified two distinct sequences among such high velocity stars in α-enhancement, that is a low-α and a high-α one, which however overlap in their metal-poor tails. These and other previously studied properties overlap, however, strongly with the disk and make discrete cuts to divide stars into halo and disk stars, imprecise.

In our study, we aim to assess how smooth the transition between the disk and the halo is with the aim to find either coherences in their properties and thus likely also their formation or to find properties with more distinct differences and only negligible contamination than for example the space velocities. Additionally, we aim to further characterise the stellar components and substructures.

For our analyses, we can use a significantly larger sample than most previous studies. In Sec. 4.3.1, we will thus assess our sample with the same tools as previous studies, that is combinations of vertical height, space velocities/actions, [Fe/H], and [α/Fe].

Contrary to most other studies, we also have estimated stellar ages for our sample. This allows us to assess the age distribution of the stellar halo and its connection with the disk, which is still contentious, in Sec.4.3.2. Although most studies agree that stars of the halo are almost exclusively older than 8 Gyr, Hawkins et al. (2014) find significant differences in the age-metallicity-relations of the low- and high-α halo, whereas Gallart et al. (2019) claim that the stars of the halo (both low- and high-α) are equally old and significantly older than the bulk of the disk stars.

4.3.1 THE TRANSITION BETWEEN STELLAR DISK AND HALO IN COMMONLY ANALYSED PROPERTIES

In Sec. 1.2.3, we have introduced commonly analysed parameters and diagrams by previous studies. Because the sample of stars that we can analyse is significantly larger or the selection significantly different from most of the literature samples, we first use the same diagnostic tools to examine our sample before we will expand our analyses in Sec. 4.3.2.

Vertical height Ivezić et al. (2008) identified distinct overdensities when looking at the distribution of iron abundance as a function of absolute vertical distance from the Galactic plane $|z|$. Ivezić et al. (2008) found a smooth metallicity distribution between [Fe/H] ~ -0.6 at 500 pc and [Fe/H] ~ -0.8 beyond several kiloparsecs, which they attributed to the disk. We plot our own visualisation of this distribution in panel a) of Fig. 4.3.

Our data shows a similar distribution, but extends also closer to the Galactic plane and shows a break around 1 kpc. Below this height, the low-α disk population with smaller scale-height and on average higher iron abundances is dominating. Above 3 kpc, Ivezić et al. (2008) found a change of the pattern with a different overdensity becoming dominant, that is with [Fe/H] ~ -1.4. We also find a change in morphology, with a more

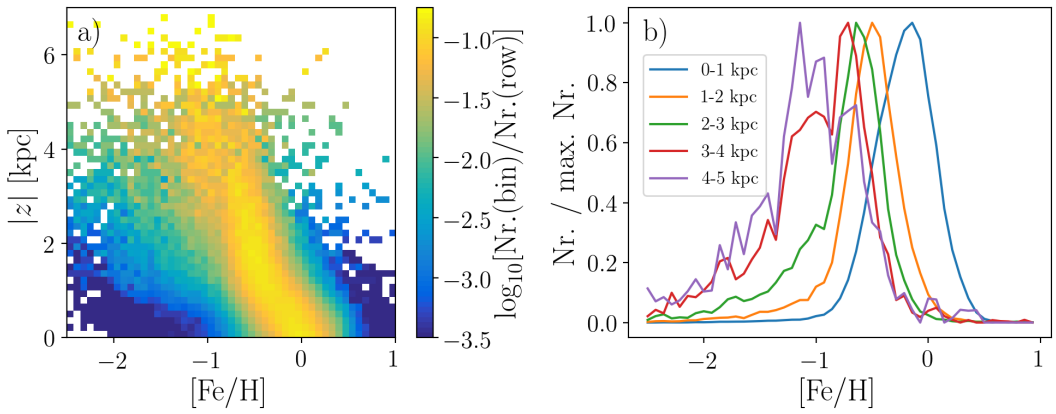

Figure 4.3: Distributions of iron abundance and absolute vertical distance $|z|$ from the Galactic plane of the 'full' sample. Panel a) shows a density distribution normalised to the sum of stars per absolute vertical distance bin in order to visualise the iron abundance distribution for each absolute vertical distance. Panel b) shows the normalised iron abundance distributions for absolute vertical distance bins of 1 kpc. **Figure Credit: Paper III**.

metal-poor below [Fe/H] < -1 starting to become more numerous. Contrary to their sample, our sample does not show a clear gap in the density around [Fe/H] ~ -1 at 3 kpc by eye. When we further bin the data in vertical density, we see two resolved overdensities above $|z| > 3$ kpc, more metal-poor and metal-rich than [Fe/H]=-1, respectively (see the apparently double-peaked red and purple histograms in panel b) of Fig. 4.3). Similar to Ivezić et al. (2008) we find that the metal-poorer of the two components becomes more dominant above 4 kpc. Above 5 kpc our sample does not contain enough stars to attempt a characterisation of the contribution of each component as a function of absolute vertical distance.

Space velocities In the Toomre diagram in panel a) of Fig. 4.4, we see that the 'full' sample mainly consists of disk stars with total velocities below 180 km s^{-1}. A significant majority of them are on almost circular orbits coherent with the disk motion, that is they are close to the origin of coordinates in this diagram. The transition towards stars on hotter orbits, those with larger differences with respect to the LSR, is smooth and confirms that the combination of these kinematic parameters is not showing a distinct separation between the disk and halo in this visualisation.

Belokurov et al. (2018) analysed SDSS DR9 data (Ahn et al., 2012) with a similar selection of $|b| > 10$ deg as our sample. They found three different overdensities, which they fitted with ellipsoids in the Galactocentric space velocities.

The first ellipsoid is located at disk-like Galactocentric velocities. Following the work of Belokurov et al. (2018), we plot the Galactocentric radial and azimuthal velocities of our sample in panel b) of Fig. 4.4 and find that again most of the stars are distributed within an ellipse at disk-like velocities.

The second overdensity is located around $V_\phi \sim 0$ km s^{-1} and shows a significantly larger extension towards lower and higher V_R, which prompted Belokurov et al. (2018) to call this overdensity the 'Sausage'. Their analysis revealed that the second radial

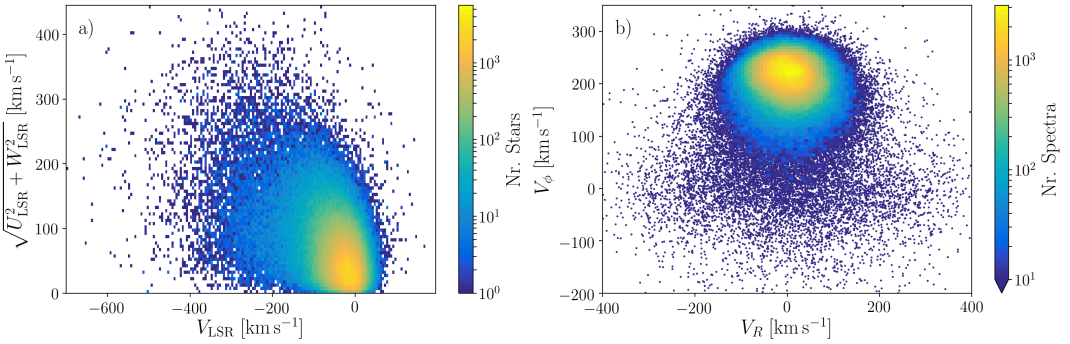

Figure 4.4: Density distribution of the kinematics with a Toomre diagram in panel a) and actions in panel b) of the 'full' sample. **Figure Credit:** Paper III.

overdensity is evenly distributed between $-1.7 <$ [Fe/H] < -1.0. In our sample, we notice the same overdensity extended towards higher and lower V_R around $V_\phi \sim 0\,\mathrm{km\,s^{-1}}$, which indicates that our sample also contains stars of the 'Sausage'.

The third overdensity, which is not possible to distinguish for our sample by eye from panel b) of Fig. 4.4, has only slightly positive mean azimuthal velocities between 20 and 60 km s^{-1}, but is not as extended in V_R as the second overdensity. Belokurov et al. (2018) find this overdensity mainly in the metal-poor regime.

Chemical composition ([Fe/H] vs. [α/Fe]) The chemical pattern of the 'full' sample in the [Fe/H] vs. [α/Fe] plane confirms that the majority of its stars belong to the stellar disk. 98% of the sample exhibits iron abundances above [Fe/H] ≥ -1. Only 22% of the latter stars are more α-enhanced than [α/Fe] ≤ 0.15.

In the introductory Sec. 1.2.3, we have presented the view that the chemical pattern of the canonical halo is expected to follow a plateau of high [α/Fe] ~ 0.35, similar to the high mean values of the high-alpha sequence of the disk, but distinguishable only below [Fe/H] < -1. Our sample, however, does not follow such a trend (see Fig. 4.5), but is void of [α/Fe] > 0.3 stars in this metallicity-regime.

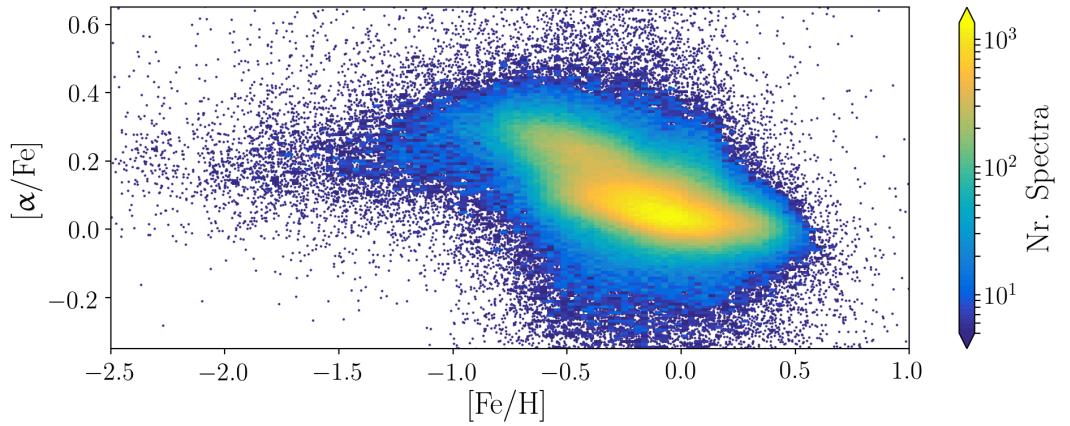

Figure 4.5: [Fe/H] vs. [α/Fe] for all stars of the 'full' sample. **Figure Credit:** Paper III.

One reason for this could be, that our sample does not include many stars of the canonical halo below [Fe/H] < -1. In the literature, both a plateau-like distribution with rather constant α-element abundances (see e.g. Schuster et al., 2006; Nissen & Schuster, 2010) as well as a significant drop of the stellar numbers below [Fe/H] < -0.9 and lower α-enhancements (see e.g. Holtzman et al., 2018; Hayes et al., 2018, for APOGEE DR13) can be found. The latter are consistent with our findings, but we note that such distributions could be resulting from selection effects. Another reason could be, that the stars of the canonical halo in our sample are present but actually are not as α-enhanced as expected, due for example to systematic errors present in either analysis, as we do see a continuous sequence of stars around [α/Fe] ~ 0.25 rather than 0.35 below [Fe/H] < -1. In order to assess the second reason, we need to disentangle the stars of the canonical halo from those of the accreted halo, whose stars are expected to be less α-enhanced than the high-α disk sequence, that is also in the regime around and below [α/Fe] ~ 0.25.

4.3.2 BEYOND CLASSICAL ANALYSIS WITH ACTIONS, ECCENTRICITY, AND STELLAR AGE

Azimuthal and radial actions L_Z and J_R The most commonly used combination of actions, L_Z and J_R, in panel b) of Fig. 4.6 shows a rather smooth transition between disk stars at $L_Z \sim L_{Z,\odot}$ and stars on retrograde orbits ($L_Z < 0\,\mathrm{kpc\,km\,s^{-1}}$). Similar to the distribution in space velocities (Fig. 4.4), we see that the majority of stars have similar dynamical properties as the Sun. We note though that in this visualisation of dynamic properties, more substructure can be seen, not only for the disk stars, but also those stars with lower angular momentum L_Z. Stars with $L_Z < 0.5 L_{Z,\odot}$ show a significantly higher radial action. We note that the sum of radial and azimuthal action for most of these stars is equal to or smaller than the Solar values, reaching maximum radial actions of $J_R \sim L_{Z,\odot}$ at $L_Z = 0\,\mathrm{kpc\,km\,s^{-1}}$. The region around $L_Z \sim 0\,\mathrm{kpc\,km\,s^{-1}}$ is where we would expect the stars of the elliptical overdensity, which we identified at $V_\phi \sim 0\,\mathrm{km\,s^{-1}}$. Contrary to the distribution in Galactocentric space velocities V_ϕ and V_R, the distribution in action space, however, looks more complex and we can not identify obvious overdensities and in particular none with an elliptical shape. From the inspection by eye, the V_R seems to be more promising than J_R for our aim to decompose our sample with Gaussian components.

L_Z and [Fe/H] The distribution of the iron abundance [Fe/H] as a function of L_Z (see panel a) of Fig. 4.6) shows a smooth extension of disk stars (at Solar L_Z and [Fe/H]) towards lower angular momenta with simultaneously decreasing iron abundances, which however stays above [Fe/H] > -0.8 down to $L_Z = 0.25\,L_{Z,\odot}$. This extension reaches all the way to $L_Z = 0\,\mathrm{kpc\,km\,s^{-1}}$, but not further towards even lower momenta. We indicate three regions in the panel to separate metal-poor from more metal-rich stars (indicated with a dashed red line at [Fe/H] $= -1$) as well as retro- from prograde stars (indicated with a red line at $L_Z = 0\,\mathrm{kpc\,km\,s^{-1}}$) and find that the ratio (I/II) of metal-rich to metal-poor stars on retrograde orbits is dropping from 52% for $-0.25\,L_{Z,\odot} < L_Z < 0\,L_{Z,\odot}$ to less than 9% below $L_Z < -0.4\,L_{Z,\odot}$.

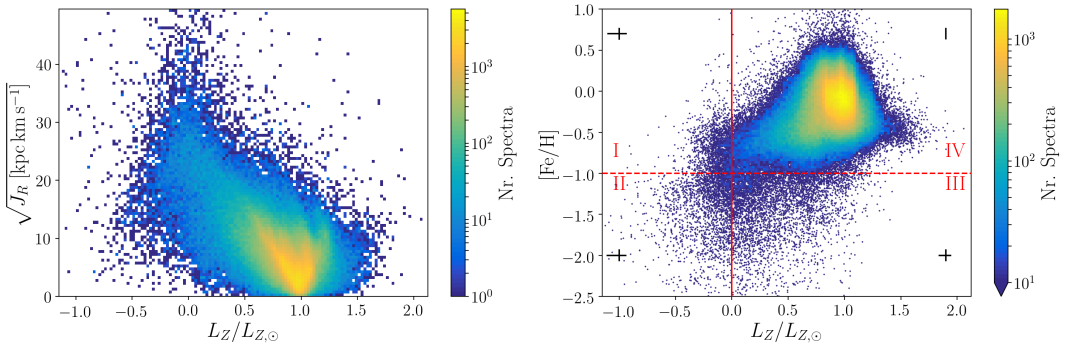

Figure 4.6: Density distribution of iron abundance [Fe/H] vs. angular momentum L_Z (panel a) and action in panel b) of the 'full' sample. **Figure Credit: Paper III.**

Eccentricity Schuster et al. (2012) found striking differences in the eccentricities of disk and halo stars and even showed that among kinematically selected halo stars, different α-enhancements correlated with different eccentricities, that is, the low-α halo stars showed high eccentricity above 0.8, whereas the high-α halo stars were distributed evenly between 0.5 and 1.0. With the larger sample of APOGEE stars, Mackereth et al. (2019b) studied the distribution of eccentricity and confirmed that stars with [Fe/H] < -0.7 and high eccentricities $e > 0.75$ are on average less α-enhanced. They further showed that the stars of this 'low-e' group occupy the same locus in V_R vs. V_ϕ as the 'Sausage' population identified by Belokurov et al. (2018).

We explore the average eccentricity of stars both in the [Fe/H] vs. [α/Fe] plane (panel a) of Fig. 4.7) and the V_R vs. V_ϕ plane (panel b) of Fig. 4.7). We see that most of the disk stars are typically on low-e orbits, with slightly higher eccentricities for the high-α disk stars (around 0.5) than those of the low-α disk (below 0.2). Stars with [Fe/H] < -1 exhibit significantly larger eccentricities above 0.5 and especially those with lower α-enhancement show eccentricities between 0.8 and 1.0, in agreement with the findings by Schuster et al. (2012) and Mackereth et al. (2019b). We furthermore see the same large eccentricities as Mackereth et al. (2019b) for stars with small $|V_\phi|$.

Stellar age Stellar ages are both valuable and hard to estimate. Although we have estimated stellar ages for the 'full' sample via isochrone fitting, we have shown in Sec. 2.4.6, that only TO stars deliver reliable age estimates across all ages. We have thus selected a subset of TO stars with expected reliable ages from the 'full' sample, which are distributed between $5000 < T_{\rm eff} < 7000$ K and above $\log g > 3.75 - 3 * (T_{\rm eff}/5000\,{\rm K} - 1)$.

For completeness, we show the distribution of stellar age as a function of L_Z for the 'full' sample in panel a) of Fig. 4.8 in addition to the same distribution for the TO stars of the sample in panel c). To illustrate the different selections of stars, we plot the distribution in the $T_{\rm eff}$ vs. $\log g$ plane for the 'full' sample in panel b) and for the TO stars of the 'full' sample in panel d). The TO stars contribute 58% to the 'full' sample.

Comparing panel a) and c) of Fig. 4.8 we see that the distribution of estimated stellar ages are quite different. We see that the stellar ages of giants were mainly distributed between 6 and 12 Gyr across all L_Z, an effect likely to be explained with the

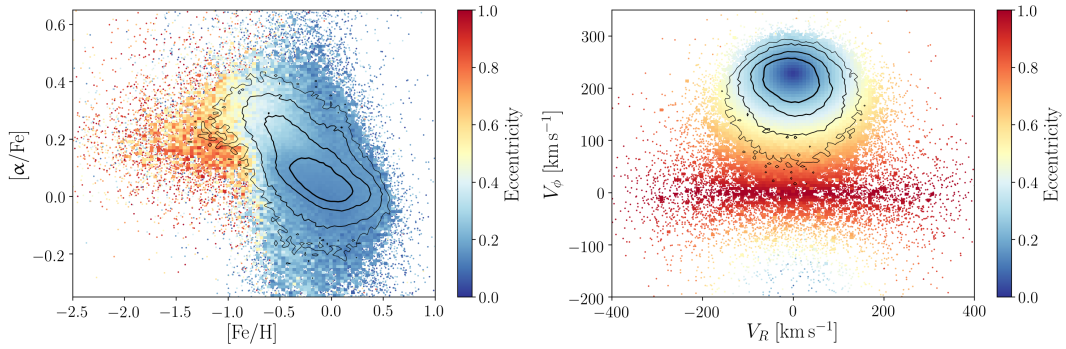

Figure 4.7: Distribution of eccentricity (color code) in the [Fe/H] vs. [α/Fe] plane (panel a) and Galactocentric space velocities V_ϕ vs. V_R (panel b). Black contours visualise the density contours of the sample. **Figure Credit:** Paper III.

tight isochrone distributions along the giant branch which leads to systematic biases of estimated ages towards intermediate values.

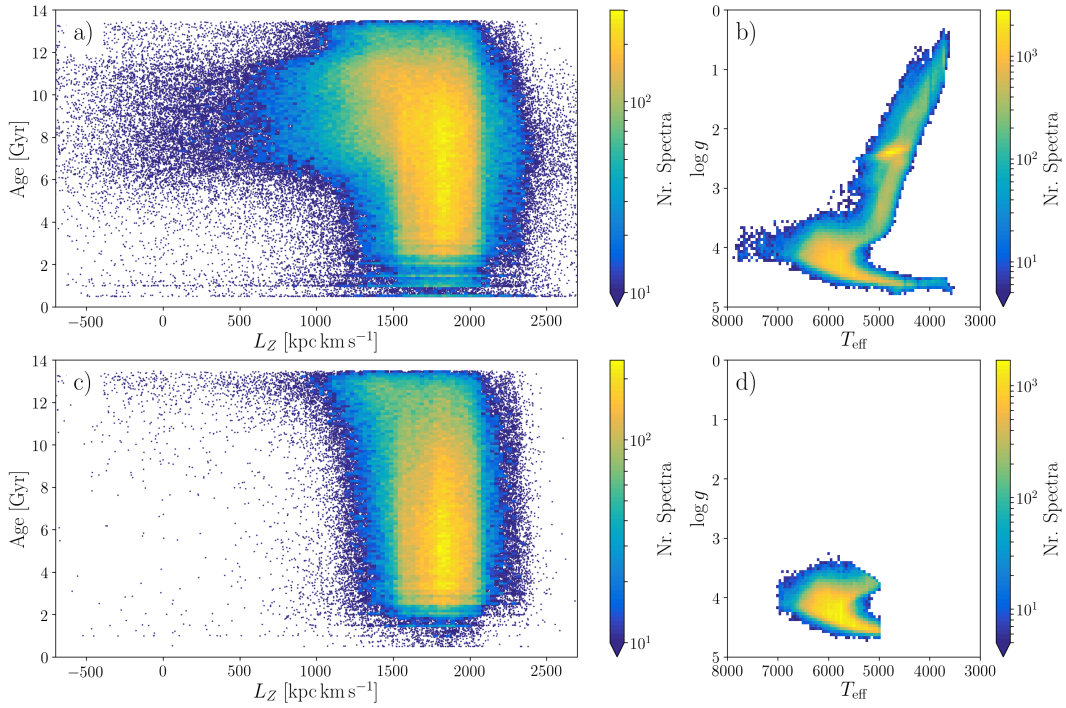

Figure 4.8: Distribution of L_Z vs. stellar age (left panels) and in the $T_{\rm eff}$ vs. log g plane for all stars of the 'full' sample in the top panels and only the turn-off stars in the bottom panels. **Figure Credit:** Paper III.

When we only look at TO stars, we see a significant change in the distribution of stars with $L_Z > 1000$ kpc km s^{-1} and those below this value. It is important to keep in mind, that TO stars are intrinsically less luminous than giants and thus probe a smaller volume than giants in a magnitude limited sample.

The stars on high angular momenta are distributed across all stellar ages, but their age distribution peaks around 3 to 7 Gyr. For older stars we see both a decrease in stellar numbers as well as a decrease of their mean L_Z. The median values of L_Z decrease steadily from 1802^{+174}_{-206} kpc km s^{-1} at 3 ± 1 Gyr to 1768^{+204}_{-254} kpc km s^{-1} at 10 ± 1 Gyr and even further to 1666^{+267}_{-322} kpc km s^{-1} at 12 ± 1 Gyr. Coincidentally, the dispersion is steadily increasing, as can be seen by the boundaries of the median values calculated from the 16th and 84th percentiles.

While for stars with $L_Z < 1000$ kpc km s^{-1}, ages up to 10 Gyr (457) seem to be exceptional, we see several of them (1713) above this age. Their relative shares of the TO stars are however very small with only 0.18% and 0.67%, respectively.

4.4 A CHEMODYNAMIC DECOMPOSITION OF THE 'FULL' SAMPLE

In the previous section, we have assessed, which combinations of stellar properties seem to be most promising when we want decompose the 'full' sample. Although we believe that stellar ages have possibly the strongest discriminative power, the current uncertainties for the giants as well as systematic trends are too high to currently use stellar ages when decomposing the 'full' sample and when restricting ourselves to turn-off stars, only very few can be used to assess the low L_Z regime, where the majority of halo stars is expected. We thus decide to not include stellar ages when decomposing the 'full' sample, but restrict ourselves to spatial, kinematic, dynamic, and chemical properties. Among these categories, we have identified the the Galactocentric space velocities V_R and V_ϕ, angular momentum L_Z, eccentricity e as well as [Fe/H] and [α/Fe] as most promising.

In this section, we are now aiming to use a combination of these parameters to decompose the 'full' sample via GMMs. Such models are trying to reconstruct the full parameter space with a mixture of multi-dimensional Gaussian components. For our models, we aim to limit the input to as many different parameters as possible. For our sample, the azimuthal velocity V_ϕ and the azimuthal action $J_\phi = L_Z$ are very similar and we thus decide in favour of the more sophisticated azimuthal action[1]. We further neglect eccentricity as input, as it we have seen a strong correlation of eccentricity with V_ϕ and V_R in the previous section and want to avoid degeneracies in the input. We note however, that Mackereth et al. (2019b) successfully implemented eccentricity in their Gaussian Mixture Model. They did however not use any additional dynamic information, contrary to our models.

[1]We want to stress that we ran the same setup of GMMs with V_ϕ instead of L_Z and found the same hyper-components with consistent distributions of stellar age and eccentricity as to those described subsequently.

4.4.1 DECOMPOSING THE 'FULL' SAMPLE VIA GAUSSIAN MIXTURE MODELS

We use the SCIKIT-LEARN (Pedregosa et al., 2011) mixture algorithm 'GaussianMixture' to decompose the four parameters L_Z, V_R, [Fe/H], and [α/Fe] of the 'full' sample. First, we assess the number of preferred components with a Bayesian Information Criterion (BIC) analysis by finding when adding another component to the mixture model does not significantly improve the fit further. We allow up to 40 components to be explored and find the best BIC value for 24 components. For each of the 24 components, we investigate the distribution in the input parameters and identify six hyper-components to which we have assigned the Gaussian components. The components are ordered somewhat arbitrarily starting from the low-α metal-rich disk to the intermediate and high-α disk, continuing with the two halo components and the outliers as last component:

1. Hyper-component 1 agrees with the low-α disk sequence, as can be seen in the [Fe/H] vs. [α/Fe] plane in panel b) of Fig. 4.9. Its kinematic properties are similar to the Sun for the majority of stars (see panel a) of Fig. 4.9). One of the components that we assigned to this hyper-component showed, however, significantly larger L_Z than the Sun, and its stars are located at the metal-poor end of the sequence in panel b) of Fig. 4.9. Although their kinematic parameters are thus significantly different from the majority of this hyper-component, similar results were found by previous studies, including the one presented in **Paper II** (see Sec. 3.5 and in particular Fig. 3.24) and attributed to low-α disk stars with guiding radii further out than the solar radius. Eight other components were combined with this high-L_Z one to assemble the hyper-component that we hereafter call 'low-α disk'.
2. Hyper-component 2 agrees is situated around solar [Fe/H], but with slightly enhanced [α/Fe] (see panel d) of Fig. 4.9). The low-α and high-α disk sequences are overlapping in this region and we are thus describing this component as intermediate disk. In **Paper II**, we have shown that the low-α and high-α sequences in this chemical regime also overlap kinematically and it is thus not possible to assign stars to the two populations with the four parameters used for the decomposition. This overlap is also confirmed with our dynamic information in panel c) of Fig. 4.9, showing that the angular momenta of this hyper-component are slightly smaller than those of hyper-component 1, but on average larger than those of hyper-component 3. This hyper-component is assembled from only one component, but some of the components of hyper-component 1 and 3 showed similar but less significant trends of intermediate dynamical or chemical distributions as this component. Hereafter we call this component 'intermediate disk'.
3. Hyper-component 3 agrees with the high-α disk sequence, as can be seen in the [Fe/H] vs. [α/Fe] plane in panel f) of Fig. 4.9. The velocity and momentum dispersions of this hyper-component are significantly larger than those of hyper-component 1 and show on average lower L_Z (see panel e) of Fig. 4.9). This hyper-component is assembled from seven components and hereafter we call this component 'high-α disk'.

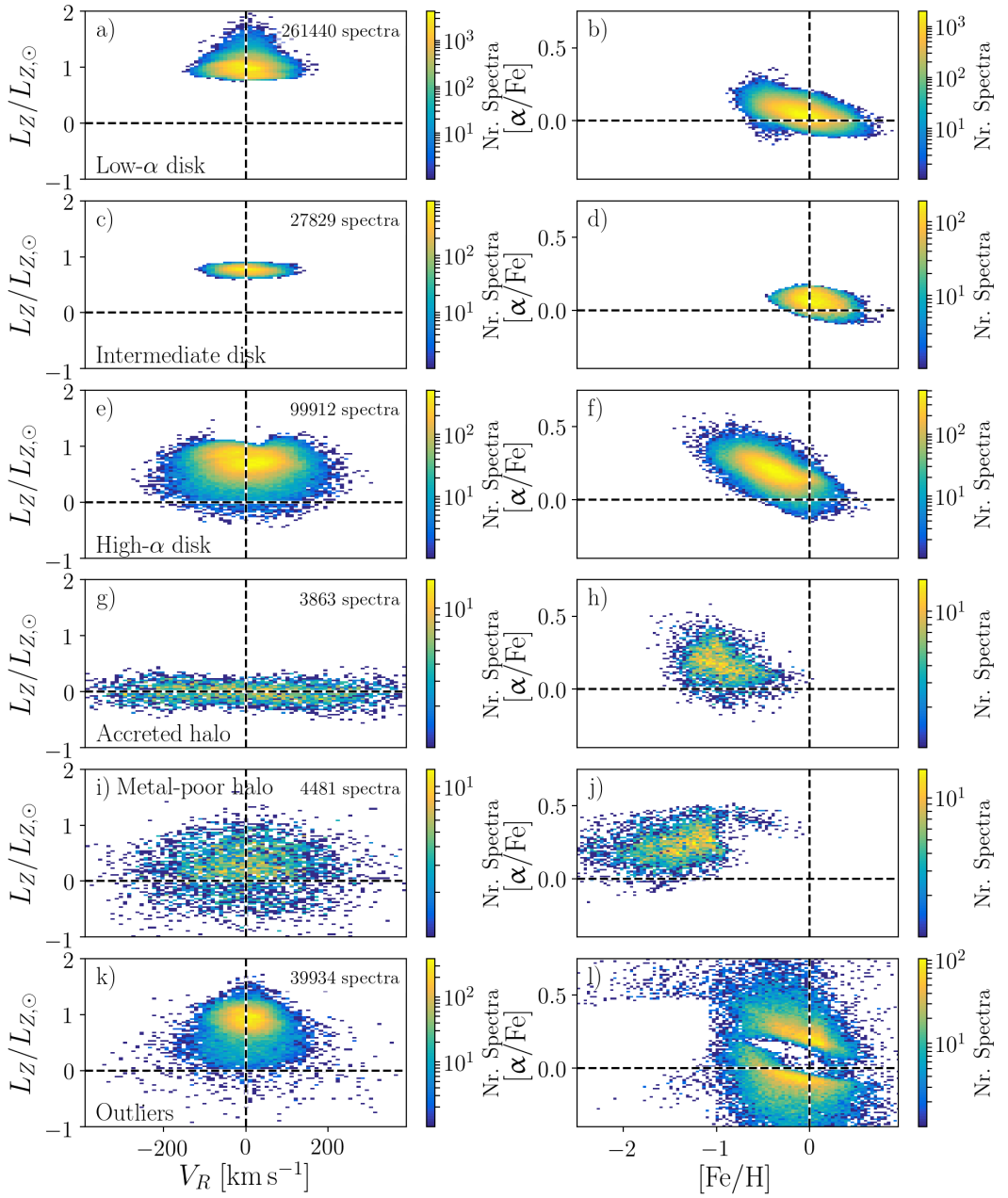

Figure 4.9: Distribution of V_R vs. L_Z (left panels) as well as chemical compositions ([Fe/H] vs. [α/Fe], right panels) for the six main groups (per row) of the 24 identified Gaussian components within the 'full' sample. Panels a) and b) show the 'low-α disk', panels c) and d) show the 'intermediate disk', panels e) and f) show the 'high-α disk', panels g) and h) show the 'accreted halo', panels i) and j) show the 'metal-poor halo', and panels k) and l) show outliers. **Figure Credit:** Paper III.

4. Hyper-component 4 is located around $L_Z = 0\,\mathrm{kpc\,km\,s^{-1}}$ and extends towards large absolute Galactocentric radial velocities (see panel g) of Fig. 4.9). This

hyper-component agrees well with the so-called 'Sausage' population identified by Belokurov et al. (2018). Chemically, this component is distributed around [Fe/H] ~ -1 with a slightly decreasing trend of [α/Fe] towards higher iron abundances (see panel h) of Fig. 4.9). This hyper-component is assembled from only one component and hereafter we call this component 'accreted halo'.

5. Hyper-component 5 covers the most metal-poor stars (see panel j) of Fig. 4.9) of the sample and its stars show the largest velocity dispersions (see panel i) of Fig. 4.9). This hyper-component is assembled from only one component and hereafter we call this component 'metal-poor halo'.
6. Hyper-component 6 contains those stars, which have significantly larger scatter towards higher and lower [α/Fe] (see panel l) of Fig. 4.9) than those of hyper-components 1, 2, and 3 but are distributed almost symmetrically above and below those. We thus assign this component as outliers in terms of their chemical properties and note that its size is about one tenth of that of the three disk-components combined. This hyper-component is assembled from five components and hereafter we call this component 'outlier'.

We list the distribution of the four input parameters for the six identified hyper-components in Table 4.2. The given values correspond to the 50th percentile and the lower and upper values correspond differences towards the differences between the 50th and 16th as well as 84th percentiles, respectively. We further list stellar ages and eccentricities in this table as well, which we analyse subsequently.

Table 4.2: Median values of selected parameters and their differences with respect to the 16th and 84th percentiles for the identified hyper-components.

Hyper-component	Age [Gyr]	Ecc. e	L_Z [kpc km s^{-1}]	V_R [km s^{-1}]	[Fe/H]	[α/Fe]
Low-α disk	$6.6^{+3.3}_{-2.7}$	$0.13^{+0.08}_{-0.06}$	1830^{+175}_{-189}	1^{+35}_{-37}	$-0.09^{+0.21}_{-0.21}$	$0.05^{+0.05}_{-0.05}$
Intermediate disk	$7.7^{+3.0}_{-3.5}$	$0.23^{+0.07}_{-0.08}$	1429^{+82}_{-99}	0^{+36}_{-34}	$0.05^{+0.19}_{-0.17}$	$0.06^{+0.05}_{-0.05}$
High-α disk	$11.2^{+1.6}_{-5.0}$	$0.28^{+0.15}_{-0.13}$	1333^{+326}_{-366}	4^{+61}_{-60}	$-0.39^{+0.23}_{-0.22}$	$0.19^{+0.08}_{-0.07}$
Accreted halo	$12.2^{+0.9}_{-3.9}$	$0.89^{+0.08}_{-0.19}$	-34^{+270}_{-282}	5^{+193}_{-197}	$-0.97^{+0.28}_{-0.23}$	$0.16^{+0.12}_{-0.10}$
Metal-poor halo	$12.7^{+0.5}_{-1.9}$	$0.62^{+0.25}_{-0.28}$	449^{+719}_{-840}	-3^{+122}_{-123}	$-1.40^{+0.31}_{-0.42}$	$0.23^{+0.11}_{-0.10}$
Outlier	$5.7^{+5.6}_{-3.0}$	$0.16^{+0.13}_{-0.08}$	1679^{+302}_{-400}	4^{+38}_{-39}	$-0.17^{+0.30}_{-0.36}$	$0.02^{+0.30}_{-0.20}$

4.4.2 IRON ABUNDANCES, STELLAR AGES AND ECCENTRICITIES OF THE IDENTIFIED HYPER-COMPONENTS

In the previous section, we have already described the distribution of stars for each identified hyper-components in the L_Z vs. V_R as well as [Fe/H] vs. [α/Fe] planes. In this section we focus on the distribution of iron abundances, stellar ages and eccentricities. We note again that the latter two were not included in the GMMs. The median values of

these parameters and their differences with respect to the 16th and 84th percentiles can be found in Table 4.2.

Panels h) and j) of Fig. 4.9 showed that the accreted and metal-poor halo component overlap in their iron abundances, but are quite different from the disk components. When we further investigate the distributions of iron abundances in panel a) Fig. 4.10, we see that the distributions of the halo components peak around the same iron abundance of [Fe/H] ~ -1.4. The distribution of the accreted component also extends towards higher values of -0.75, but is significantly different from those of the disk above [Fe/H] > -0.7. However, when we only look at the TO stars of the halo samples, the distribution looks slightly different. The peak of the accreted component is now at [Fe/H] ~ -1.0, whereas the distribution of the iron abundances of the metal-poor halo still peaks around -1.4. This indicates a strong metallicity gradient in this component with distance and that the TO sample is sampling on average closer distances.

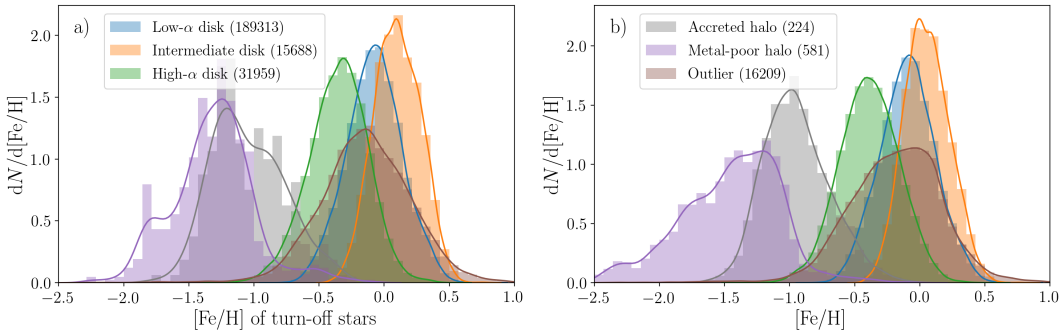

Figure 4.10: Distribution of iron abundances for all stars (panel a) and only turn-off stars (panel b) of the six hyper-components of the 'full' sample. **Figure Credit: Paper III.**

In panel a) of Fig. 4.11, we plot the stellar age distributions of turn-off stars for the six hyper-components. Similar to the findings of **Paper II**, we identify the vast majority (78%) of stars of the low-α disk at young ages with an almost plateau-like distribution between 3 and 10 Gyr and steep decrease below and above these ages, respectively.

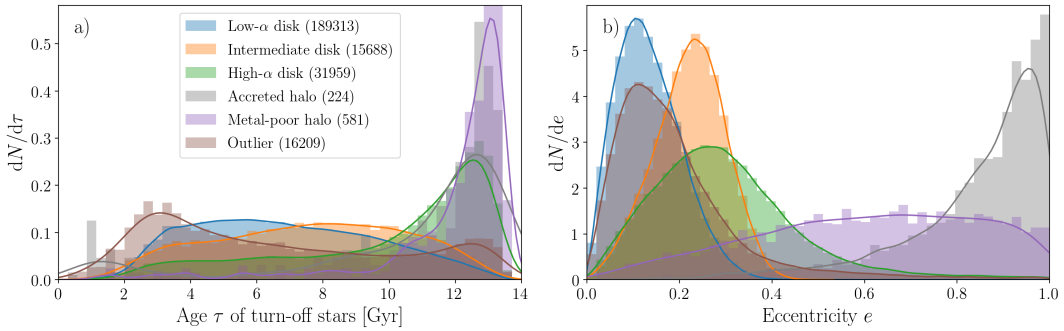

Figure 4.11: Distribution of stellar ages (panel a) and eccentricity (panel b) for the six main groups (per row) of the 24 identified Gaussian components within the 'full' sample. **Figure Credit: Paper III.**

Contrary to only 15% of stars of the low-α disk with ages above 10 Gyr, we find the majority of stars (63%) assigned to the high-α disk above this age, with a peak around 12.5 Gyr. The non-negligible amount of stars equally distributed at ages below 10 Gyr skews the age distribution and leads to a median age of $11.2^{+1.6}_{-5.0}$ Gyr. As shown in **Paper II**, dynamics and chemical composition alone were not sufficient to disentangle the overlap of old high-α and young low-α disk sequences. When inspecting the components that include the majority of young stars of the chemodynamically assigned high-α disk, we see that these are mainly distributed along the overlapping region of these two sequences. For one component, we have not been able to assign it to either disk population from chemodynamical aspects. Looking at the age distribution of this component (orange in panel a) of Fig. 4.11), we see that this component agrees with being the superposition of both disk populations, exhibiting all ages between 2 and 12 Gyr.

However, the focus of our attention lies on the components that were identified as the halo. For the accreted and metal-poor component, we find almost all stars to be older than 10 Gyr with 75% and 90%, respectively. We note that especially the metal-poor halo component shows a void of stars below 10 Gyr, whereas the accreted component still shows 10% of stars between 8 and 10 Gyr. The distributions of stellar age shows that the high-α disk ($11.2^{+1.6}_{-5.0}$ Gyr) is compatible with the accreted halo ($12.2^{+0.9}_{-3.9}$ Gyr) and the metal-poor halo ($12.7^{+0.5}_{-1.9}$ Gyr). The peaks of the halo components are however significantly narrower than those of the high-α disk. The similar ages and peaks of the iron abundances of the two populations suggest that they populate similar regions in the $T_{\rm eff}$ vs. $\log g$ plane. In Fig. 4.12, we show the distribution of stars in this plane for the accreted halo (panel a) as well as the metal-poor halo (panel b). Guided by an isochrone with 12 Gyr and [Fe/H] = −1.0, similar to the median values of the accreted halo, one can see that the sequences overlap for the turn-off stars and the subgiant branch stars. At the RGB, however, the isochrone does not match the metal-poor halo. This visualises that majority of the giants of the metal-poor halo are actually more metal-poor than [Fe/H] < −1.0, under the assumption that the turn-off stars ages of both populations are representative and their ages thus similar.

Contrary to the compatible age distributions of these three components, their eccentricities differ strongly (see panel b) of Fig. 4.11). Similar to Schuster et al. (2012) and Mackereth et al. (2019b) we find that the accreted halo component exhibits almost exclusively (92%) stars with eccentricities above $e > 0.6$, resulting in a mean value of $e = 0.9^{+0.1}_{-0.2}$. All disk components show almost exclusively eccentricities below this value, including the high-α disk with 95% of stars below $e \leq 0.6$. The eccentricities of disk stars show a clear difference between the low-α disk ($e = 0.1^{+0.1}_{-0.1}$) and the high-α disk ($0.3^{+0.2}_{-0.1}$) and as expected we see that the intermediate disk ($0.2^{+0.1}_{-0.1}$) shows eccentricities between the two disk populations.

Stars of the metal-poor halo are distributed across all eccentricities, but with a larger share of higher eccentricities ($e = 0.6^{+0.2}_{-0.3}$). If we consider only the metal-poor and accreted halo components as halo contributors, we find 3915 of these stars with

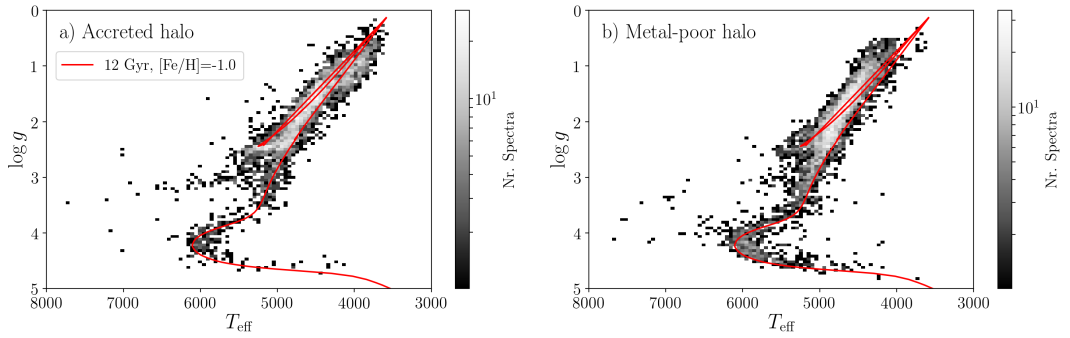

Figure 4.12: Density distribution of stars in the $T_{\rm eff}$ vs. log g plane for the accreted halo component (panel a) and for the metal-poor halo component (panel b)). The red line shows a Parsec isochrone (Bressan et al., 2012) with [Fe/H] = -1 and 12 Gyr (similar to the median iron abundance and age of the accreted component). **Figure Credit:** Paper III.

$e > 0.8$ and 4429 with $e < 0.8$, that is a lower ratio of 47% compared to the 68% found by Mackereth et al. (2019b).

For completeness we want to mention that the outliers from the chemodynamical analysis are distributed across all ages, but peak towards the lowest and highest ages. From a dynamical point of view, the outliers are mainly consistent with the disk and show a similar low eccentricity distribution as the disk. We caution that the unidentified nature of this hyper-component may bias the interpretations and average properties of the other components as described above.

4.5 CHEMICAL DECOMPOSITION OF THE KINEMATICALLY SELECTED HALO

For the 'full' sample, analysed in the previous section, only the iron and α-process abundances are yet available and we can thus not yet characterise the chemical composition of the identified hyper-components in detail. As mentioned in the introduction, all chemical abundances within the GALAH range are however available for the sample of stars with high velocities ($v_{\rm tot} > 180$ km/s). We thus analyse this 'high velocity' sample in this section from several points of view. First we assess if we can identify within our significantly larger sample the same bimodality in chemical information as Nissen & Schuster (2010), who also selected their sample from stars with $v_{\rm tot} > 180$ km/s. To identify these bimodalities and assign stars to different overdensities in chemical space, we again apply GMMs. We later characterise the identified overdensities and their distributions in chemical and dynamical space as well as stellar ages. In the discussion section we then aim to link the found distributions with the ones found in the previous section, when we analysed the 'full' sample.

We note that in the literature the characterisation of the MW halo has traditionally been approached in this manner, i.e. by identifying stars with halo-like kinematics and subsequently analysing their chemical properties (see Sec. 1.2.3).

4.5.1 THE CHEMICAL COMPOSITION OF THE KINEMATICALLY SELECTED HALO

The chemical patterns of the 17756 stars in the 'high velocity' sample is shown in Fig. 4.13. Note that the fraction of stars with abundance measurements is quite different for the 32 species, because of different detection limits for different species. Only for 10 species, more than 50% measurements of the spectra lead to significant detections. These include the four α-elements Mg (12883 detections), Si (12898), Ca (16722), and Ti (9987), but also other element groups like the odd-Z elements with Na (11210) and K (12689), the iron-peak group with Sc (11739), Ni (10903), and Cu (13735) as well as the s-process element Ba (10549). However, the coverage of detections across the iron abundance range differs significantly. The species that cover the majority of the metallicity range between -2.5 and 0 are Na, Mg, K, Ca, Sc, Mn, and Ba.

Looking at the iron abundances of the 'high velocity' sample we see that most of the stars are distributed between [Fe/H] ~ -2.5 and [Fe/H] ~ 0 with a significant overdensity around [Fe/H] ~ -0.6 and a less significant overdensity around [Fe/H] ~ -1.1 (see e.g. [Fe/H] vs. [Ba/Fe]). The sample analysed by Nissen & Schuster (2010) did, however, not show seem to show significant overdensities as a function of [Fe/H], but their sample only consisted of 94 stars compared to our up to 17756 stars and their rather complicated target selection did not allow an analysis of the metallicity distribution.

Our larger samples, however, is selected with a simpler magnitude limited selection and we thus aim to also assess the metallicity distribution of the two distinct halo populations found by Nissen & Schuster (2010), if we can identify those in the data. We thus plot the three different planes that Nissen & Schuster (2010) used to identify the chemically different populations, that is [Fe/H] vs. [Mg/Fe] in Fig. 4.14 and [Fe/H] vs. [α/Fe] in Fig. 4.15. On top of each of our density distributions (shown in greyscales), we plot the measurements of the three different populations from Nissen & Schuster (2010), that is stars of the low-α halo (red), the high-α halo (blue) and the thick disk (orange). We see that the same regions of the [Fe/H] vs. [Mg/Fe] plane as well as the [Fe/H] vs. [α/Fe] plane are populated, but we see distinct differences in the density pattern, that is our data clumps significantly more around [Fe/H] ~ -0.7 than the sample from Nissen & Schuster (2010). Furthermore our data does not show a significant gap between the low- and high-α halo populations (indicated by the red line in Fig. 4.14), which could be a result of our significantly lower spectral quality and thus abundance measurement precision.

When we look at the [Na/Fe] vs. [Ni/Fe] plane in Fig. 4.16, we see that the abundance trends again show a roughly similar pattern of correlated Na- and Ni-enhancement. However, our data, with Na computed in non-LTE, shows significantly lower [Ni/Fe] values for low values of [Na/Fe].

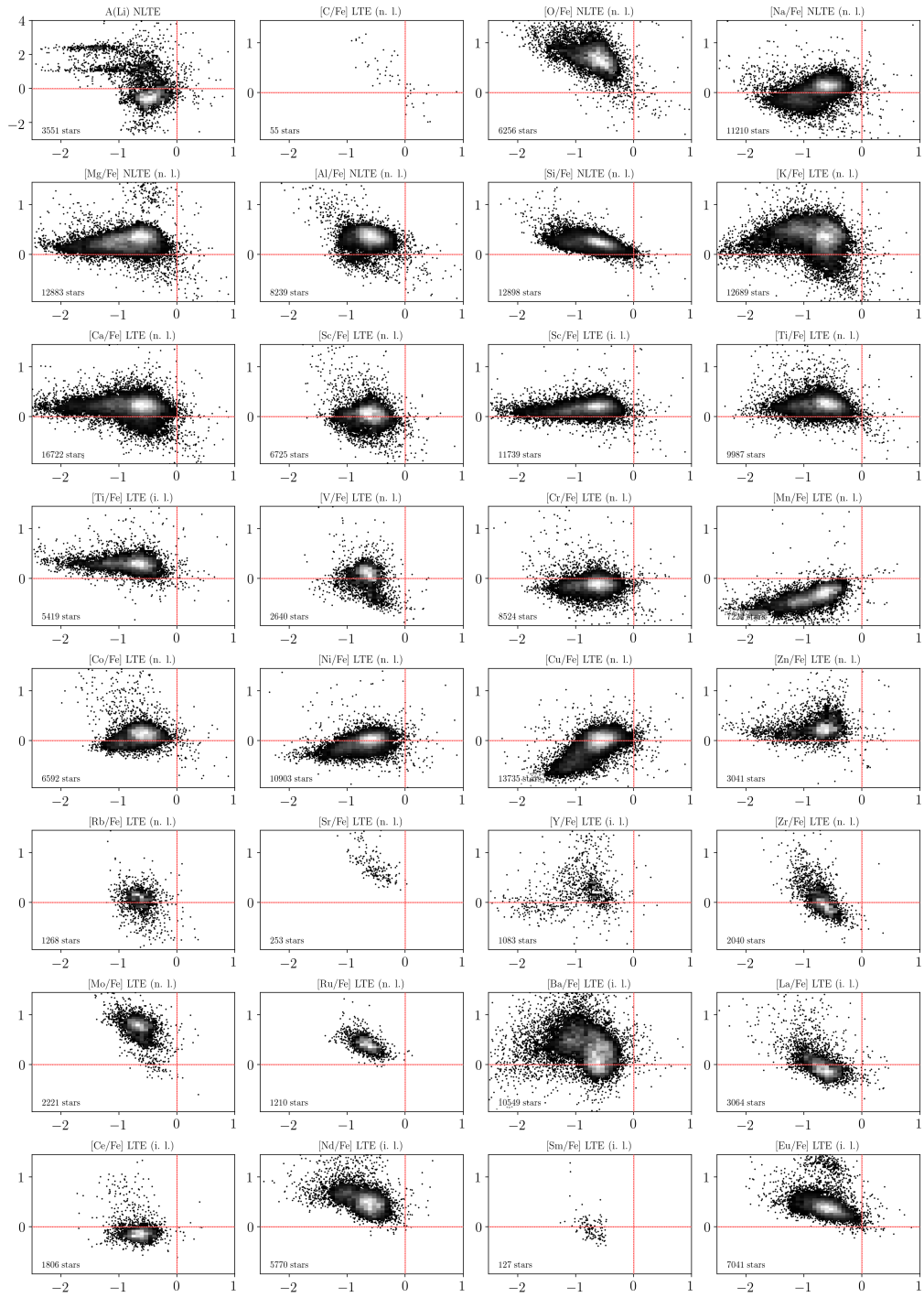

Figure 4.13: Distribution of element abundances as a function of iron abundance [Fe/H] for all stars with 'high velocity' sample in abundance (greyscale and black dots). Panel titles indicate the element, if LTE or non-LTE was used, and if neutral lines (n. l.) or ionised lines (i. l.) were measured. Red lines indicate solar abundances. **Figure Credit:** **Paper III**.

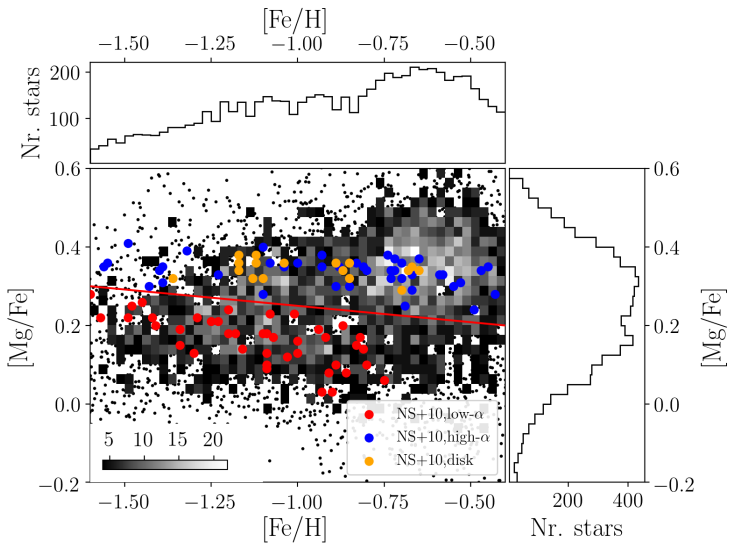

Figure 4.14: Comparison of [Fe/H] vs. [Mg/Fe] of our 'halo kinematic' sample (greyscale) with the three populations of the Nissen & Schuster (2010) sample. The latter are plotted as red (low-α halo), blue (high-α halo) and orange (thick disk) dots. **Paper III**.

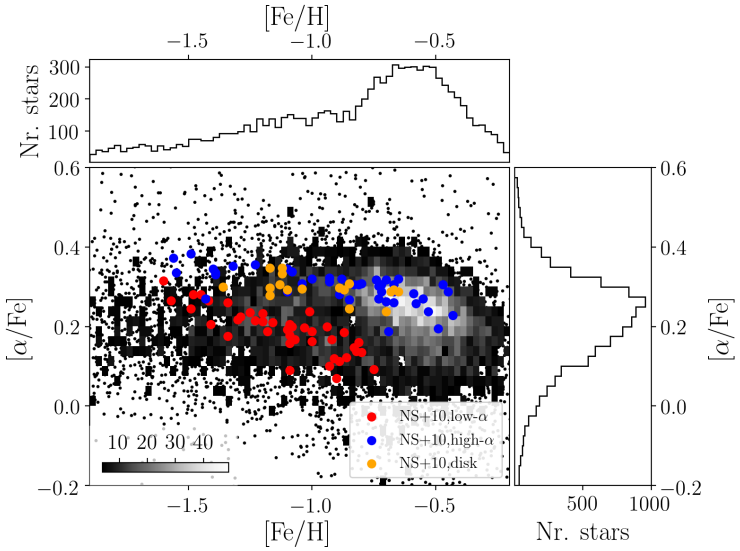

Figure 4.15: Comparison of [Fe/H] vs. [α/Fe] of our 'halo kinematic' sample (greyscale) with the three populations of the Nissen & Schuster (2010) sample. The latter are plotted as red (low-α halo), blue (high-α halo) and orange (thick disk) dots. **Figure Credit:** Paper III.

To avoid selection biases by dividing our sample into different populations via straight lines, we aim to divide our sample more in a more sophisticated manner by using combinations of distinct abundance trends, similar to the [Na/Fe] vs. [Ni/Fe] trends and employing GMMs to assign stars to populations.

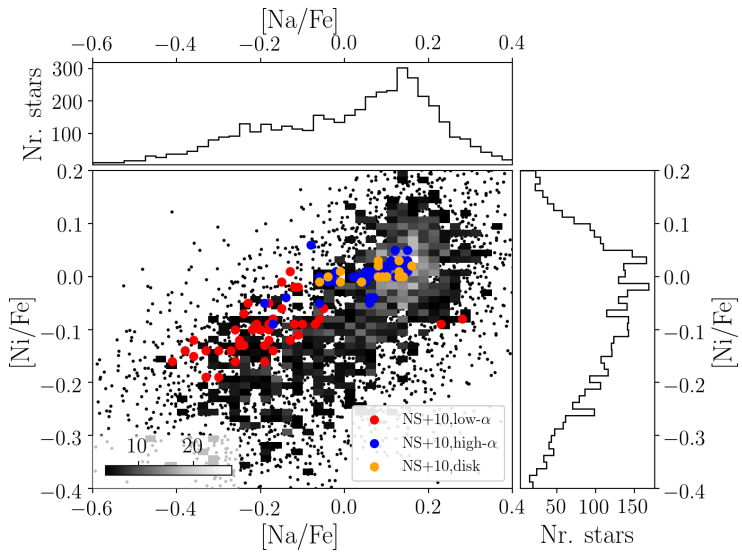

Figure 4.16: Comparison of [Na/Fe] vs. [Ni/Fe] of our 'halo kinematic' sample (greyscale) with the three populations of the Nissen & Schuster (2010) sample. The latter are plotted as red (low-α halo), blue (high-α halo) and orange (thick disk) dots. **Figure Credit:** **Paper III**.

4.5.2 DETECTING OVERDENSITIES IN CHEMICAL SPACE WITH GAUSSIAN MIXTURE MODELS

A good starting point for tracing distinct trends and populations in the abundances are abundance overdensities. When we trace back the aforementioned overdensities at [Fe/H] ~ -0.6 and [Fe/H] ~ -1.1 respectively, we can identify differences in the abundances between those two overdensities by eye for Na, Mg, Si, K, Mn, Ni, Cu, Ba, and Nd. These significant differences seem to only exist among some elements. In order to confirm that the abundances of other elements seem to be rather similar between those two overdensities and not effects of the detection limits, we aim to assign stars to them in one of the distinct abundance planes and tracing them back in the less distinct planes.

We have selected four the elements Na, Mg, Mn, and Fe, tracing different nucleosynthesis channels (see Sec. 1.2.4) with a large overlap and coverage of measured abundances as well as the most distinct separations (identified by eye) in abundance space as input. We stress however, that our sample does not cover most of the metal-poor stars below [Fe/H] < -1.5.

To identify chemical populations among the stars with high velocity, we have employed the SCIKIT-LEARN (Pedregosa et al., 2011) mixture algorithm 'GaussianMixture'. To test the number of components that are preferred to reproduce the input data, we use a Bayesian Information Criterion (BIC) analysis by exploring up to 20 components, but find the best BIC score for six components. To test the robustness of the mixture models, we repeat the mixture estimation ten times and always recover the same six Gaussian components that we show with black dots in the Fig. 4.17, where we plot the three abundance ratios [Na/Fe], [Mg/Fe], and [Mn/Fe] as a function of [Fe/H].

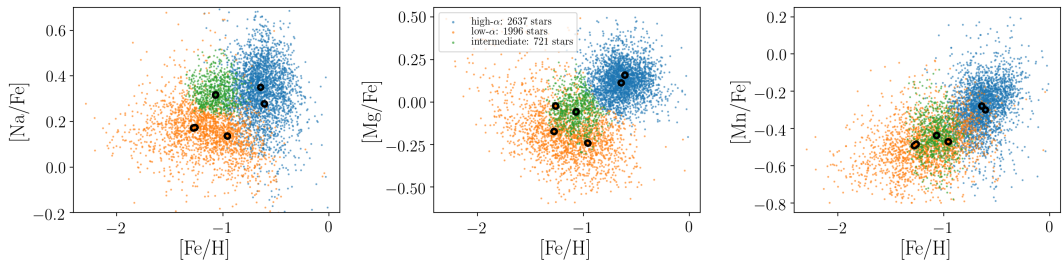

Figure 4.17: Distribution of element abundances [Na/Fe], [Mg/Fe], and [Mn/Fe] as a function of [Fe/H] for the 'high velocity' sample. Block points indicate the means of the six Gaussian components and are colored in the middle by the hyper-component they have been assigned to. The color of the individual measurements is then showing their assignment to the hyper-components indicated in the legend of the middle panel. **Figure Credit:** Paper III.

From these, we have identified three hyper-components, which show similar trends in all three projections. The first hyper-component is located at high [α/Fe] and high [Fe/H] comparable with the 'high-α' disk and is assembled from the two blue colored components. The second component is showing low abundances for all four elements and is assembled from three components, which follow the 'low-α' halo sequence found by Nissen & Schuster (2010). The sixth component is distinct from the aforementioned five components, because it is located between both in [Na/Fe] and [Mn/Fe], but shows high [Mg/Fe]. We thus assign it as a third 'intermediate' hyper-component with the aim to further assess if it can be affiliated with one of the two sequences as an extension in term of the chemical evolution of one of the two sequences.

We note that other studies have also applied a similar approach, with the same combination of element groups. For example Das et al. (2019) used also Mg, Mn, and Fe, but the odd-Z element Al instead of Na.

4.5.3 CHARACTERISATION OF THE IDENTIFIED GROUPS OF THE 'HIGH VELOCITY' SAMPLE

In this section, we briefly describe the three different identified hyper-components of the 'high velocity' sample. The distribution of the properties of these populations are listed in Table 4.3 with their median values and upper as well as lower values estimated from the 16th and 84th percentiles.

The high-α hyper-component This component shows strong enhancement in the α-elements, for example [Mg/Fe] = $0.34^{+0.11}_{-0.13}$, together with high values of odd-Z elements ([Na/Fe] = $0.12^{+0.10}_{-0.09}$ and [Al/Fe] = $0.32^{+0.11}_{-0.12}$). Most iron-peak elements like Cr, Ni, and Cu trace the iron abundance, but Mn ([Mn/Fe] = $-0.28^{+0.11}_{-0.12}$) and Zn ([Zn/Fe] = $0.25^{+0.26}_{-0.15}$) show significantly lower and higher values, respectively. The iron abundance, shown in panel a) of Fig. 4.19 is distributed narrowly around [Fe/H] = $-0.64^{+0.18}_{-0.15}$.

From a dynamical point of view it is consistent with an extension of the high-α disk in all parameters shown in Fig. 4.20. This can be well seen in panel a), where the most

Table 4.3: Comparison of different parameters estimated from the 16th, 50th, and 84th percentiles for the identified components of the kinematically selected halo.

Parameter	high-α		intermediate		low-α	
	Nr.	Value	Nr.	Value	Nr.	Value
[Fe/H][1]	2637	$-0.64^{+0.18}_{-0.15}$	721	$-1.07^{+0.12}_{-0.14}$	1996	$-1.15^{+0.29}_{-0.30}$
[α/Fe][1]	2637	$0.26^{+0.06}_{-0.08}$	721	$0.30^{+0.06}_{-0.06}$	1996	$0.17^{+0.08}_{-0.09}$
[O/Fe][2]	1882	$0.64^{+0.19}_{-0.17}$	284	$0.84^{+0.25}_{-0.16}$	634	$0.73^{+0.27}_{-0.22}$
[Na/Fe][2]	2637	$0.12^{+0.10}_{-0.09}$	721	$-0.05^{+0.09}_{-0.09}$	1996	$-0.19^{+0.15}_{-0.13}$
[Mg/Fe][2]	2637	$0.34^{+0.11}_{-0.13}$	721	$0.33^{+0.07}_{-0.05}$	1996	$0.16^{+0.08}_{-0.10}$
[Al/Fe][2]	2320	$0.32^{+0.11}_{-0.12}$	375	$0.29^{+0.17}_{-0.15}$	444	$-0.02^{+0.41}_{-0.13}$
[Si/Fe][2]	2503	$0.23^{+0.08}_{-0.09}$	639	$0.30^{+0.12}_{-0.09}$	1395	$0.21^{+0.13}_{-0.10}$
[K/Fe][2]	2592	$0.42^{+0.20}_{-0.17}$	711	$0.49^{+0.16}_{-0.18}$	1952	$0.43^{+0.17}_{-0.23}$
[Ca/Fe][2]	2564	$0.25^{+0.11}_{-0.12}$	676	$0.29^{+0.10}_{-0.12}$	1846	$0.20^{+0.11}_{-0.12}$
[Sc/Fe][2]	1553	$0.11^{+0.15}_{-0.13}$	277	$0.05^{+0.13}_{-0.12}$	524	$-0.07^{+0.19}_{-0.18}$
[Sc/Fe][3]	2587	$0.20^{+0.08}_{-0.09}$	685	$0.13^{+0.08}_{-0.07}$	1909	$0.09^{+0.09}_{-0.08}$
[Ti/Fe][2]	2358	$0.25^{+0.10}_{-0.11}$	610	$0.23^{+0.10}_{-0.09}$	1533	$0.15^{+0.12}_{-0.14}$
[Ti/Fe][3]	1396	$0.28^{+0.13}_{-0.12}$	398	$0.30^{+0.09}_{-0.10}$	1178	$0.29^{+0.11}_{-0.10}$
[Cr/Fe][2]	2213	$-0.08^{+0.12}_{-0.09}$	519	$-0.13^{+0.12}_{-0.11}$	1158	$-0.18^{+0.12}_{-0.13}$
[Mn/Fe][2]	2637	$-0.28^{+0.11}_{-0.12}$	721	$-0.44^{+0.10}_{-0.09}$	1996	$-0.49^{+0.13}_{-0.12}$
[Ni/Fe][2]	2015	$-0.02^{+0.09}_{-0.11}$	524	$-0.12^{+0.10}_{-0.11}$	1180	$-0.20^{+0.11}_{-0.11}$
[Cu/Fe][2]	2426	$-0.05^{+0.12}_{-0.15}$	591	$-0.32^{+0.14}_{-0.12}$	1229	$-0.52^{+0.14}_{-0.12}$
[Zn/Fe][2]	1339	$0.25^{+0.26}_{-0.15}$	205	$0.23^{+0.19}_{-0.14}$	575	$0.15^{+0.19}_{-0.13}$
[Ba/Fe][3]	2295	$0.26^{+0.31}_{-0.30}$	634	$0.50^{+0.30}_{-0.24}$	1721	$0.49^{+0.31}_{-0.25}$
[Nd/Fe][3]	1606	$0.52^{+0.15}_{-0.13}$	417	$0.65^{+0.16}_{-0.14}$	1075	$0.69^{+0.18}_{-0.16}$
$U(LSR)$ [km s^{-1}]		-83^{+172}_{-100}		-37^{+130}_{-117}		-24^{+203}_{-166}
$V(LSR)$ [km s^{-1}]		-175^{+73}_{-72}		-219^{+80}_{-97}		-237^{+81}_{-102}
$W(LSR)$ [km s^{-1}]		-17^{+76}_{-76}		-19^{+95}_{-94}		-8^{+101}_{-101}
V_R [km s^{-1}]		58^{+84}_{-157}		23^{+111}_{-124}		20^{+169}_{-221}
V_ϕ [km s^{-1}]		75^{+93}_{-76}		25^{+92}_{-96}		0^{+67}_{-64}
V_z [km s^{-1}]		-9^{+76}_{-76}		-12^{+95}_{-95}		-0^{+101}_{-101}
J_R [kpc km s^{-1}]		383^{+204}_{-194}		344^{+266}_{-216}		578^{+513}_{-366}
L_Z [kpc km s^{-1}]		482^{+687}_{-492}		132^{+560}_{-500}		2^{+404}_{-401}
J_Z [kpc km s^{-1}]		20^{+87}_{-19}		28^{+132}_{-25}		37^{+193}_{-34}
Ecc.		$0.70^{+0.21}_{-0.22}$		$0.75^{+0.18}_{-0.26}$		$0.87^{+0.09}_{-0.24}$
$R_{\rm apo}$ [kpc]		$8.46^{+2.56}_{-2.47}$		$7.24^{+2.85}_{-2.97}$		$9.47^{+6.47}_{-3.90}$
$R_{\rm peri}$ [kpc]		$1.32^{+2.16}_{-0.93}$		$0.92^{+1.51}_{-0.69}$		$0.65^{+1.21}_{-0.47}$
$z_{\rm max}$ [kpc]		$0.93^{+1.94}_{-0.72}$		$0.98^{+2.47}_{-0.74}$		$1.55^{+4.30}_{-1.24}$
$\|z\|$ [kpc]		$1.14^{+0.95}_{-0.73}$		$1.63^{+1.25}_{-0.87}$		$1.80^{+1.41}_{-0.88}$
Age [Gyr]	2637	$8.8^{+2.7}_{-2.4}$	721	$8.1^{+2.8}_{-1.7}$	1996	$8.1^{+2.6}_{-1.9}$
Age [Gyr] TO	517	$12.3^{+0.7}_{-2.7}$	49	$12.7^{+0.4}_{-1.5}$	87	$12.3^{+0.6}_{-3.6}$

Notes: (1) Estimated from neutral and ionised lines. (2) Estimated from neutral lines. (3) Estimated from ionised lines.

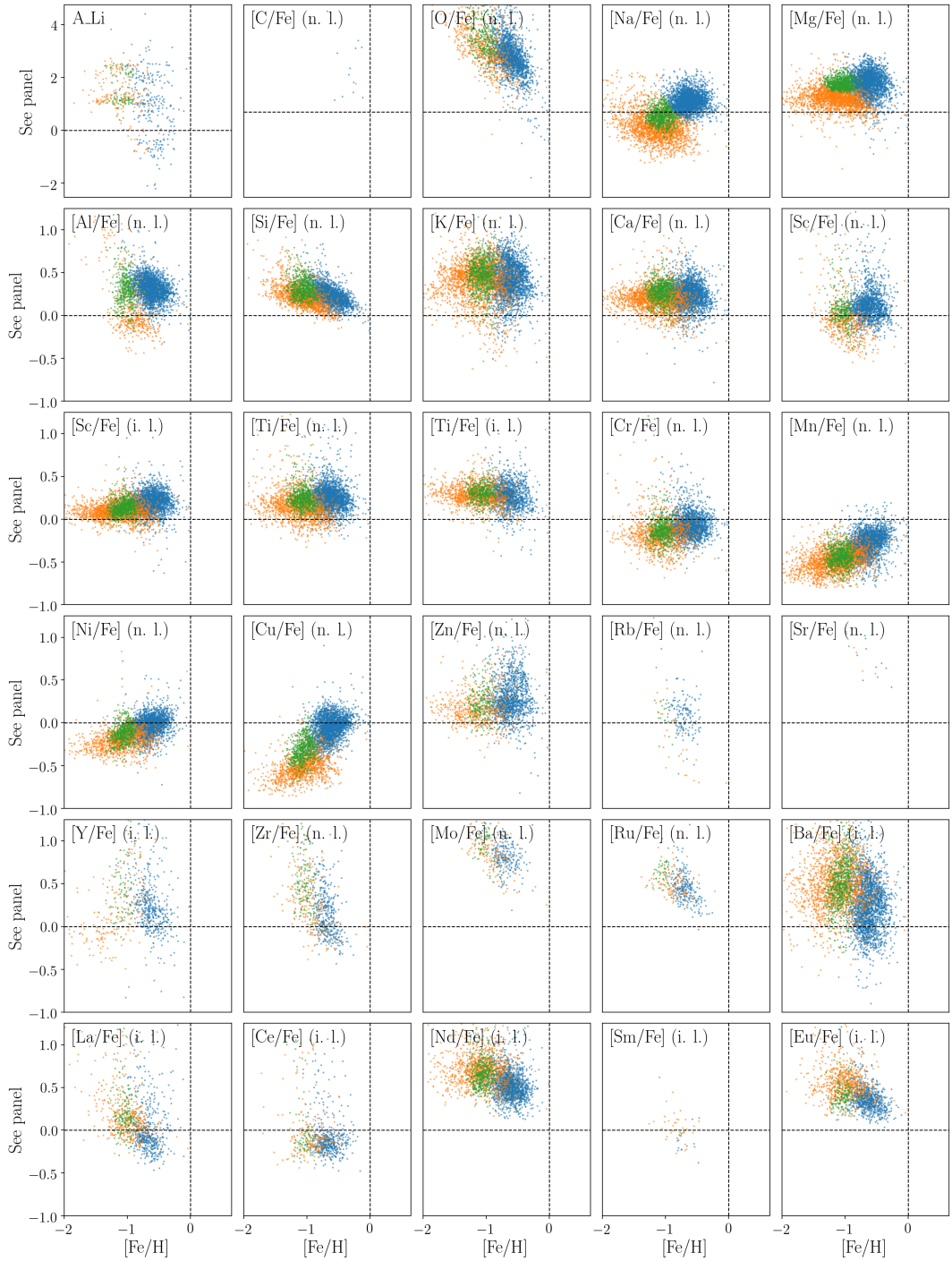

Figure 4.18: Abundance overview for the same stars and color coding as in Fig. 4.17, that is blue (high α disk), green (intermediate component) and orange (low-α halo). Panel annotations indicate the element and if neutral lines (n. l.) or ionised lines (i. l.) were measured. Red lines indicate solar abundances. **Figure Credit:** Paper III.

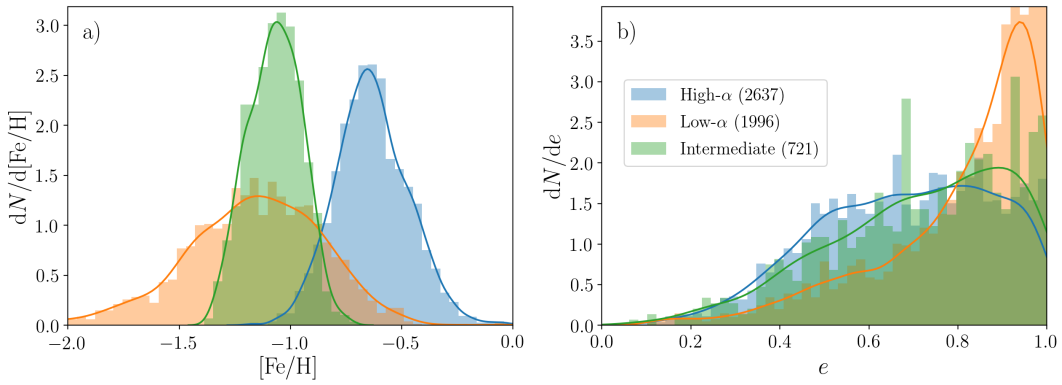

Figure 4.19: Distribution of the iron abundances (panel a) and eccentricities (panel b) of the three hyper-components of the 'high velocity' sample. **Figure Credit:** Paper III.

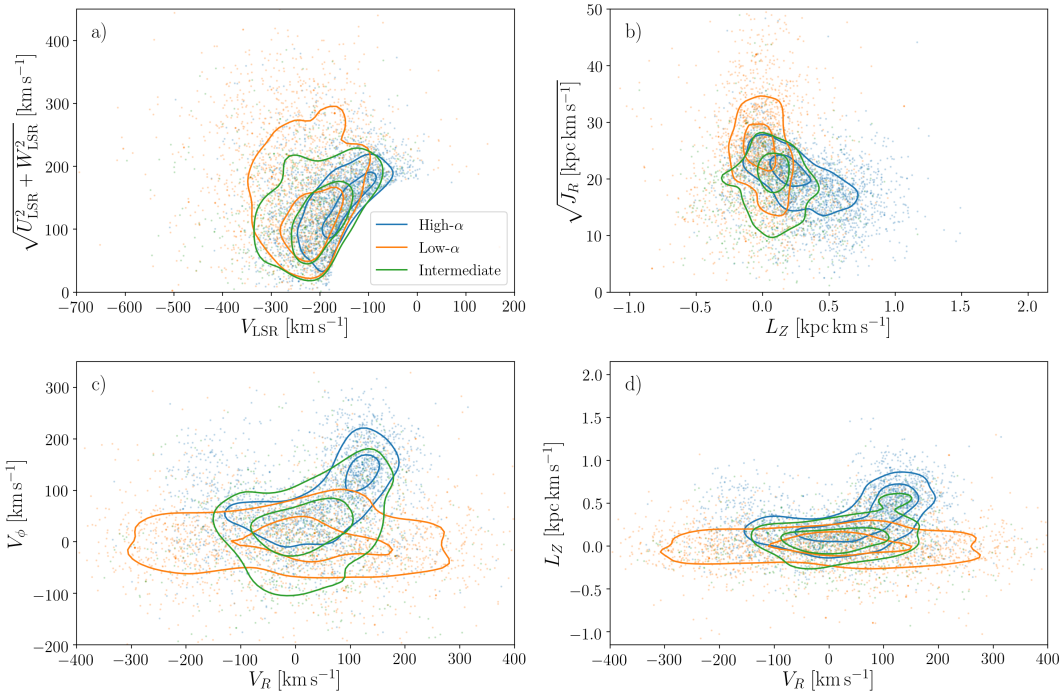

Figure 4.20: Distribution of stars of the three identified hyper-components in the Toomre diagram (panel a), the action plane L_Z vs. $\sqrt{J_R}$ (panel b), Galactocentric velocities V_R vs. V_ϕ (panel c) and V_R vs. L_Z (panel d). Points show individual points and contours indicate the loci of the majority of stars. **Figure Credit:** Paper III.

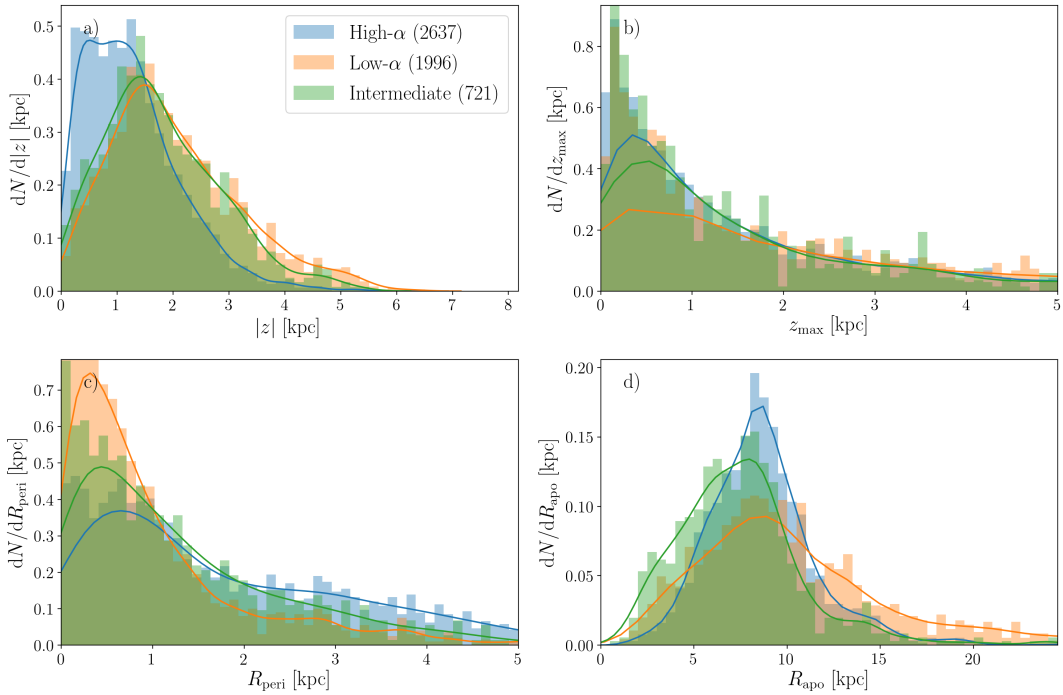

Figure 4.21: Distribution of orbit parameters current absolute vertical height $|z|$ (panel a), maximum absolute vertical height $z_{\rm max}$ (panel b) as well as the pericenter (panel c) and apocenter (panel d) radii for the three hyper-components of the 'high velocity' sample. Points show individual points and contours indicate the loci of the majority of stars. **Figure Credit:** Paper III.

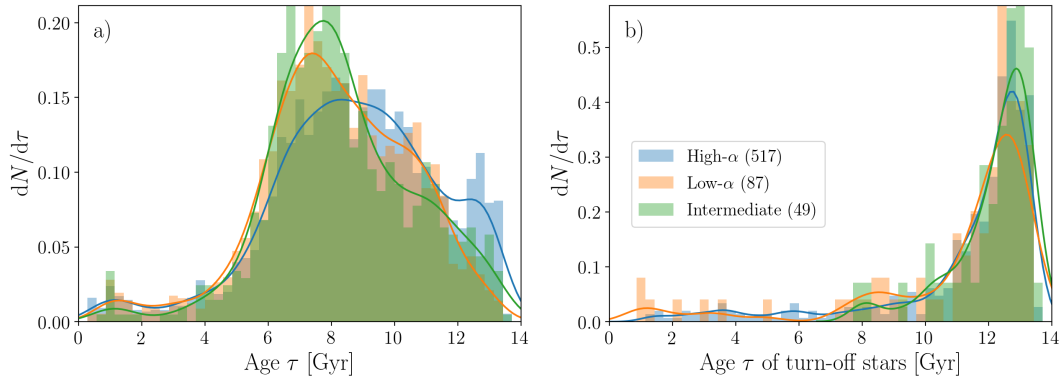

Figure 4.22: Distribution of stellar ages for all stars (panel a) and only turn-off stars (panel b) of the three hyper-components of the 'high velocity' sample. **Figure Credit:** Paper III.

stars are distributed at the edge of the cut-off velocity Toomre diagram at $v_{\rm tot} = 180\,{\rm km/s}$ and their density decreases with increasing $v_{\rm tot}$.

The eccentricities of this component are distributed evenly between 0.4 and 1.0 (see panel b) of Fig. 4.19). From the distribution of apocenter radii (mainly below $R_{\rm apo} < 10\,{\rm kpc}$) in panel d) of Fig. 4.21 it can be seen that these stars mainly stay within inner Galaxy. The distribution of stellar ages is show in Fig. 4.22 shows that the majority of these stars are old ($\tau = 12.3^{+0.7}_{-2.7}\,{\rm Gyr}$) when turn-off stars are used as reliable age tracers. We mention though that the significantly less reliable ages from giant stars would point towards the inclusion also of significantly younger ages ($\tau = 8.8^{+2.7}_{-2.4}\,{\rm Gyr}$) and therefore a significantly longer star formation history.

The low-α hyper-component The abundances of numerous elements of this component, including the α, odd-Z, and the iron-peak elements are lower than the high-α component.We not however, that the neutron capture elements, although only sparsely measured, appear to be rather more enriched than the high-α component. The azimuthal velocities and azimuthal actions of this component are symmetrically distributed around the zero point and show that stars of this component do on average not co-rotate with the disk. Their orbits are however strongly eccentric with $e = 0.87^{+0.09}_{-0.24}$ (see panel b) of Fig. 4.19) and reach further distances from the Galactic center, both in radial and vertical direction (see $R_{\rm apo}$ and $z_{\rm max}$ in panels c) and b) of Fig. 4.21). The stellar ages of this component are mainly distributed above 10 Gyr, that is, $\tau = 12.3^{+0.6}_{-3.6}\,{\rm Gyr}$), when estimated from turn-off stars, but are on average significantly lower ($\tau = 8.1^{+2.6}_{-1.9}\,{\rm Gyr}$) when also using the less reliable ages from giants.

The intermediate hyper-component The main characteristic of this component in the Gaussian Mixture Model input was the narrow distribution of low [Fe/H] ($-1.07^{+0.12}_{-0.14}$) but high [Mg/Fe]. The chemistry of this component thus does match neither the high- nor the low-α-components and we see further differences to these components. All measured α-element abundances are significantly enriched at the same level or above those of the high-α-component and thus more enriched than the low-α component. We note that [O/Fe] is even higher than for the high-α-component. The odd-Z elements Na and Al, as well as the iron peak elements are however less enriched than the high-α component but still more enriched than the low-α component (compare e.g. the abundances of Na in Table 4.3). The dynamical properties of this component are at values between the low- and high-α component, but agree more with the low-α population, as can be appreciated from the overlapping contours of the two components in Fig. 4.20. The only dynamic feature of this component, that does not seem to be intermediate between the low- and high-α component are the apocenter radii, where the intermediate component ($R_{\rm apo} = 7.24^{+2.85}_{-2.97}\,{\rm kpc}$) exhibits smaller values than the high-α ($R_{\rm apo} = 8.46^{+2.56}_{-2.47}\,{\rm kpc}$) and the low-$\alpha$ component ($R_{\rm apo} = 9.47^{+6.47}_{-3.90}\,{\rm kpc}$). The stellar ages of this component ($\tau = 12.7^{0.4}_{-1.5}\,{\rm Gyr}$) are slightly older by $\sim 0.4\,{\rm Gyr}$ than the other components when estimated from turn-off stars, but show similarly younger ages when including the less reliable giants.

4.6 DISCUSSION

In this study, we examine two different samples of data from the GALAH survey with the aim to decompose the stellar composition chemodynamically. The first part of the results were presented for the 'full' sample, which we decomposed simultaneously via chemical and dynamical properties. In the second part of the study, we have analysed the properties of a sample that we first selected dynamically (with $v_{\rm tot} > 180\,{\rm km/s}$) and then decomposed chemically.

In this section, we now discuss our results, by first assessing which chemodynamic properties are the most promising for the dissection of the halo and disk. We then compare the components that we found from the decomposition of the 'full' and 'high velocity' sample with the aim to assess if the dynamically identified 'Sausage' (Belokurov et al., 2018) is correlated with the chemically identified low-α halo population (Nissen & Schuster, 2010). Subsequently we will characterise the stellar halo with a particular discussion of the intersection between of the found high$-\alpha$ disk and accreted halo hyper-components, where we found an intermediate sample of stars with distinct dynamics and chemistry from the aforementioned two hyper-components. Finally, we will discuss the contentious ages of halo stars.

4.6.1 THE TRANSITION BETWEEN DISK AND HALO

With the aim to characterise the MW and its stellar composition, we have explored the chemodynamic data of the 'full' sample. Although the Galaxy is an evolving system with continuously changing parameters, studies of the stellar content of the MW allow to explore, which parameters of the Galaxy show smooth or distinguishable patterns and might even be possible to assign samples of stars to larger groups or stellar populations. For the disk stars, in particular stellar ages and the chemical pattern have shown that stars are likely belonging to at least two different populations, but for the stellar halo, we still need to explore how many populations might exist. We have thus explored different parameter combinations to assess in which ones the transition between disk and halo are smooth or clearly separated. With the analyses presented in Sec. 4.3, we find smooth transitions between disk and halo within the Toomre diagram, but find significant overdensities in the action space ($\sqrt{J_R}$ vs. L_Z) as well as the Galactocentric velocities V_R vs. V_ϕ. As expected from the limited scale heights of the disk, we further find a difference of the stellar composition with vertical height. The most striking differences are however found in the chemical composition. While the [α/Fe] vs. [Fe/H] plane allows to find overdensities with roughly 0.2 dex difference in the α-enhancement, other elements like the odd-Z elements Al and Na as well as the iron-peak elements Mn and Cu show even larger spreads in their abundances. We thus agree with Hawkins et al. (2015), that these elements are the most promising stellar properties to explore the stellar composition of the MW and in particular its halo.

4.6.2 LINKING THE COMPONENTS OF THE CHEMODYNAMICALLY DECOMPOSED SAMPLES

The decomposition of both the 'full' and 'high velocity' sample of our data, yielded significant differences in the dynamical as well as chemical properties of the identified components and hyper-components. We report their dynamical and chemical properties as well as stellar ages independently for the 'full' sample (Secs. 4.4.1 and 4.4.2) and the 'high velocity' sample (Sec. 4.5.3). In this section, we now assess how correlated the identified hyper-components are. Because the 'high velocity' sample is a subset of the 'full' sample, we can do this by comparing the overlap between the two types of hyper-components; the absolute and relative overlap between the samples in Table 4.4. Subsequently we discuss the the properties for the hyper-components having most significant overlap, i.e. the two 'high-α' hyper-components (with 81% overlap) and the 'accreted halo' hyper-components (with 59% overlap). Lastly, we discuss the more inconclusive overlap between the high-velocity 'intermediate' hyper-component (overlapping with both the 'accreted halo' by 46% and the 'metal-poor halo' of the full sample with 36%).

Table 4.4: Overlap of stars from the three hyper-components of the 'high velocity' sample decomposition to the six hyper-components of the 'full' sample decomposition.

'Full' sample hyper-component	'High velocity' hyper-component					
	High-α		Intermediate		low-α	
	2637	(100%)	721	(100%)	1996	(100%)
Low-α disk	21	(1%)	0	(0%)	0	(0%)
Intermediate disk	0	(0%)	0	(0%)	0	(0%)
High-α disk	2145	(81%)	124	(17%)	33	(2%)
Accreted halo	302	(11%)	331	(46%)	1173	(59%)
Metal-poor halo	63	(2%)	257	(36%)	743	(37%)
Outlier	106	(4%)	8	(1%)	47	(2%)

There is effectively no overlap of the 'high velocity' sample with the low-α and intermediate disk Of all the 5354 stars that were used from the 'high velocity' sample, only 21 ($\ll$ 1%) were assigned to the low-α or intermediate disk and only 161 (3%) were assigned to the outliers. The contribution of the low-α disk to the high velocity stars is thus effectively zero.

The high-α disk agrees with the high-α 'high velocity' component The agreement between the two independently identified high-α hyper-components is 81%. When we further compare the chemical and dynamical properties of the two components (compare Table 4.2 with Table 4.3) we find that the median values of the components are however different. The high-α 'high velocity' component is always located at the edges of the high-α disk distribution, that is, its L_Z is for example consistent with the lower end of the 'full' sample component.

With the exception of the eccentricity, a strongly non-Gaussian distribution, the chemical, dynamical, and age distributions are thus always consistent within their 16th and 84 percentiles. This leads us to the conclusion that the high-α 'high velocity' component is consistent with being the old, metal-poor, and dynamically hotter extension of the high-α disk.

The 'Sausage' and the low-α halo component are strongly correlated The overlap between the accreted halo component of the 'full' sample, which was identified similarly to be the 'Sausage' (Belokurov et al., 2018) due to its extension in V_R at $V_\phi \sim 0\,\mathrm{km/s}$, and the low-$\alpha$ component of the 'high velocity' sample is 59% (1173 of the 1996 low-α halo stars). From all the 'high velocity' stars that were overlap with the accreted halo component of the 'full' sample (1806), 65%, that is, a two-thirds majority, are coming from the low-α component of the 'high velocity' stars.

We find further evidence for this correlation in the strikingly similar distributions of dynamical properties. Both components show the same distribution in the L_Z vs. V_ϕ diagram (compare panel g) of Fig. 4.9 with panel d) of Fig. 4.20) and show the same distribution of distinctively high eccentricities (compare panel b) of Fig. 4.11 with panel b) of Fig. 4.19). The studies by Mackereth et al. (2019b) and Schuster et al. (2012) found similar distributions in their analysis of the metal-poor regime of APOGEE DR14 and the sample from Nissen & Schuster (2010), respectively. The most convincing evidence can be found from the α-element pattern, which is different from the disk and in strong agreement between the two accreted components of the 'full' and 'high velocity' sample.

This leads us to the conclusion that the two hyper-components are correlated and the 'Sausage' population found by Belokurov et al. (2018) is basically the low-α population identified by Nissen & Schuster (2010).

It is important to note the large contribution (46%) of the intermediate population of the 'high velocity' sample to the accreted halo component of the 'full' sample and we discuss this in detail subsequently. Furthermore, we see that a non-negligible amount of stars of the low-α component of the 'high velocity' sample has not been assigned to the accreted halo of the 'full' sample, but rather the metal-poor halo (37%). A possible explanation for such a high rate could be, that the metal-poor halo is actually extending all the way up into the regime of the accreted halo with similar [Fe/H] and [α/Fe] than the low-α halo population, but different dynamical properties, for example L_Z or V_R outside of the extended ellipse of the 'Sausage'. An analysis to assess if this high overlap is actually driven by a true chemodynamic superposition of components or contamination driven by errors or shortcomings of the Gaussian Mixture Model analysis is however beyond the scope of this study.

The high α and high odd-Z component with inconclusive dynamics The comparison of the intermediate hyper-component with the high-α disk and accreted hyper-components of the 'high velocity' sample indicates that this component can not be assigned to one of the two components. Its α-enhancement is higher than that of the disk, but its iron abundance is significantly lower than those of the high-α disk. Furthermore several elements like Na, Al, Mn, Ni, and Cu show values between the high-α disk and the accreted halo (see Table 4.3). Its dynamical properties are also distributed between

the two hyper-components, but typically closer to the accreted population (see again Table 4.3 or for example the overlap between the orange and green contours in V_R vs. L_Z in Fig. 4.20). It is thus reasonable, that the chemodynamic decomposition of the 'full' sample (without the use of Na, Al, Mn, Ni, and Cu abundances, but among others V_R and L_Z) suggests a dynamically driven assignment to the accreted halo. We thus plan a more sophisticated chemodynamic decomposition of the 'full' sample, by including abundance measurements of odd-Z elements or iron peak elements.

When we compare our findings with those from Nissen & Schuster (2010), we see that this intermediate component would be assigned to the high-α halo with the cut by Nissen & Schuster (2010), as can be appreciated from the black line in panel a) of Fig. 4.23. This line is the one that Nissen & Schuster (2010) used to separate their sample. When we assess the abundances of the 42 high$-\alpha$ stars from the Nissen & Schuster (2010) sample, we also find a trend of decreasing [Na/Fe] and [Ni/Fe] with iron abundance, that is, the 22 stars of the high$-\alpha$ population from Nissen & Schuster (2010) with [Fe/H] < -0.8 show average [Na/Fe] $\sim 0.0 \pm 0.09$ and [Ni/Fe] $\sim -0.01 \pm 0.03$, whereas those of the high$-\alpha$ population with [Fe/H] ≥ -0.8 show [Na/Fe] $\sim 0.11 \pm 0.03$ and [Ni/Fe] $\sim 0.02 \pm 0.02$. Although the absolute values are different, this trend is in agreement with the intermediate location of our identified intermediate hyper-component in the [Na/Fe] vs. [Ni/Fe] plane (see panel c) of Fig. 4.23.

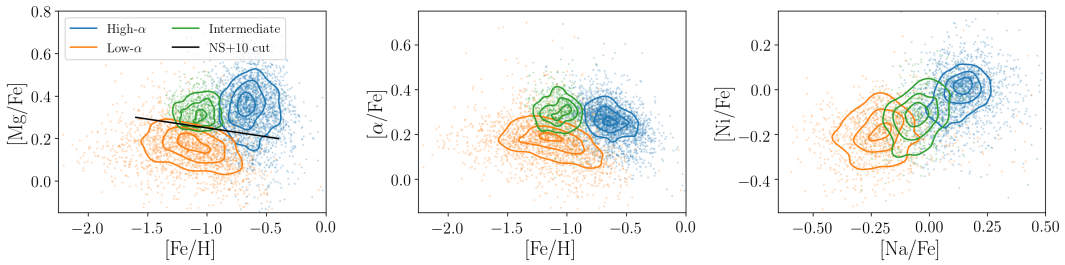

Figure 4.23: Distribution of element abundances [Fe/H] vs. [Mg/Fe] (panel a), [Fe/H] vs. [α/Fe] (panel b), and [Na/Fe] vs. [Ni/Fe] (panel c) for the three hyper-components of the 'high velocity' sample. The three panels show those stars from the greyscale distribution of Figs. 4.14 to 4.16, that have been assigned to the three hyper-component. Points show individual measurements and contours indicate the distribution of the hyper-components in these planes. **Figure Credit: Paper III**.

We note that the location of our identified intermediate component is in good agreement with the stars analysed by Hayes et al. (2018) as 'HMg Pop' with high [Mg/Fe]. Although the authors do not report values with the individual abundances, we see a qualitative agreement of the abundance trends of our intermediate component with their samples. When compared with the low-α population both our 'intermediate' and their 'HMg Pop' components show higher values for [Mg/Fe], [α/Fe], [O/Fe], [Al/Fe], [Ni/Fe] and slightly higher values for [Si/Fe], [K/Fe], [Ca/Fe], [Cr/Fe], [Mn/Fe]. While Hayes et al. (2018) identified distinct differences in the form of the distributions of both populations with Galactocentric Standard of Rest velocities as a function of Galactic longitude l, our sample has a limited coverage across Galactic longitude l.

This intermediate population further will be very interesting to answer the question, if there is an in-situ halo. The same level of high enhancement of α-process elements as the high-α disk suggests both a similar enhancement by SNe II and that SNe Ia did not contribute significantly before the stars of this component formed. The different ratios of odd-Z elements like [Na/Fe] and [Al/Fe] suggests a nucleosynthetic environment with different neutron and/or proton excesses, e.g. because of metallicity dependent SN yields or presence of other polluting sources. Especially the dependence of these enrichment of these elements on the C+N abundances (see e.g. Kobayashi et al., 2006) will be important to test and could help to understand the origin of this component. We thus suggest that Galactic Chemical Evolution models should be used to constrain the chemical pattern of stars of the more metal-poor high-α disk sequence and these could then be compared to those of the intermediate hyper-component.

The blue and red sequences of the 'high velocity' stars are correlated with the halo and high-α disk. Several papers accompanied the publication of *Gaia* DR2 to describe its content. One of the papers that attracted most attention was the description of the observational Hertzsprung-Russell diagram by Gaia Collaboration et al. (2018a), which showed two distinct sequences in the *Gaia* CMD plane, when looking at stars with high total or tangential velocity. With our selection of the 'high velocity' sample, we also identified these two sequences in the spectroscopic version of this plane, the $T_{\rm eff}$ vs. $\log g$ plane (see panel b) of Fig. 4.2).

In Fig. 4.24, we are now plotting the same $T_{\rm eff}$ vs. $\log g$ plane and aim to identify if and which component contributes to the two sequences identified between the main sequence and the giant branch. In each panel, we also show an isochrone with 13 Gyr (similar to the median ages of all components) and [Fe/H] = −0.7 (between the median iron abundances of the high-α component and the other two components). This isochrone helps to conclude that the red sequences (redder colors in the CMD plane or lower $T_{\rm eff}$ at a given $\log g$) is almost exclusively populated by the high-α component, whereas both the intermediate and low-α component populate the blue sequences (with bluer colors in the CMD plane or higher $T_{\rm eff}$ at a given $\log g$).

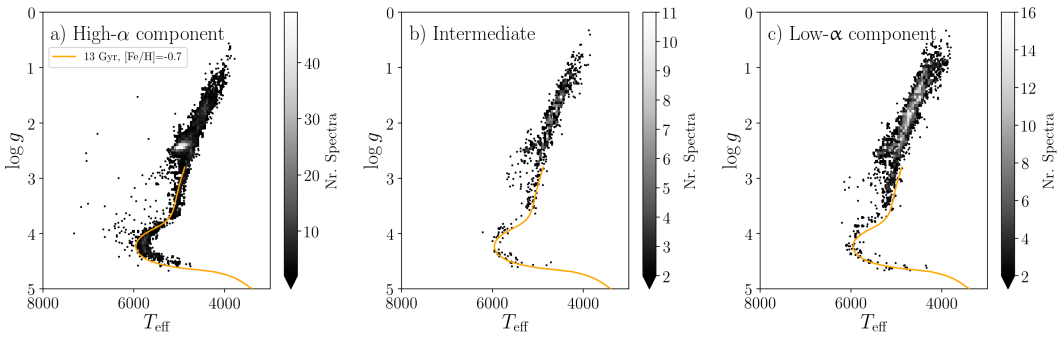

Figure 4.24: Distribution of the three identified hyper-components of the 'high velocity' sample in the $T_{\rm eff}$ vs. $\log g$ plane. An isochrone with 13 Gyr (similar to the median ages of all components) and [Fe/H] = −0.7 (between the median iron abundances of the high-α component and the other two components) is plotted to guide the eye up to the giant branch. **Figure Credit: Paper III**.

4.6.3 A QUESTION OF AGE: THE CONTENTIOUS AGE DISTRIBUTIONS OF THE HALO STARS

As mentioned in the introduction, the literature on the distribution of stellar ages of halo stars, independent of their definition via spatial, chemical or dynamical criteria, is persistently ambiguous and contradictory. Among others, Schuster et al. (2012) used the isochrone fitting technique for TO stars and found that halo stars are typically $10 - 13$ Gyr old and the high-α stars are (the main contributors to the red sequence among high velocity stars) on average $2 - 3$ Gyr older than the low-α ones (those mainly contributing to the blue sequence). They thus propose a scenario in which a first accretion sequence forms the high-α component, before a few major accretion events after these aforementioned $2 - 3$ Gyr produce the low-α halo. Contrary to this, the recent study by Gallart et al. (2019), based on synthetic CMD fitting, estimated that all halo stars are equally old and older than the bulk of the disk stars. For both the red and blue sequence of the high velocity stars (selected with tangential velocities above 200 km/s) they find peak ages of 13.4 Gyr and that more than 50% of the stars are older than 12.3 Gyr. A third possible age distribution was reported by Das et al. (2019), who estimated that the ages of the low-α giants actually point towards younger ages as low as 8 Gyr and an age gradient between 8 and 13 Gyr, suggesting a star formation period of 5 Gyr for the accreted halo stars. Subsequently we aim to assess if the halo and high-α disk components are coeval and if we do not only see differences in their ages but possibly even significant age gradients within a component.

Are the halo and high-α disk components coeval? The comparison of the reliable turn-off star ages of the 'full' sample (see panel a) of Fig. 4.11 and values in Table 4.2) and the 'high velocity' sample (see panel b) of Fig. 4.22 and values in Table 4.3) show that all halo components and the high velocity extension of the high-α component are all old, with median ages above 12.5 Gyr and even higher peak ages. Within these ranges, the distribution of stellar ages is clearly skewed and suggests star formation up to 10 Gyr ago for all components, but negligible star formation (or contamination) after this time.

Under the assumption, that the turn-off star ages are representative of the full sample of stars, their coeval and high ages suggest, that the chemical enrichment of these components happened both on short short timescales (mainly within less than 2 Gyr) and in different environments (due to the significant differences in the α, odd-Z, and iron-peak element patterns). Given that the vast number of high-α disk still formed after this time, that is, between 12 and 10 Gyr ago, it is more complex to bring the accretion of the system that now constitutes the low-α halo in connection with the hiatus of the high-α disk star formation and onset of the low-α disk formation, as suggested by Helmi et al. (2018). This connection would however be possible, if the accreted material did not only bring the accreted stars, but also gas with it, which later settled into the disk and contributed to the birth material of the low-α disk 8 Gyr ago (see also Gallart et al., 2019).

Contrary to Das et al. (2019), who further found an age gradient between 8 to 13 Gyr (see their Fig. 7), with 90% of the stars between 8.8 and 11.8 Gyr with a median age of 10.5 Gyr, we do not see such a gradient, but only a very narrow distribution of turn-off star ages (see panel a) of Fig. 4.25). Our values are in good agreement with the estimates from Gallart et al. (2019), but stand in clear contrast to the estimates from both Schuster et al. (2012) and Das et al. (2019) and we thus aim to assess what might influence the different age estimates.

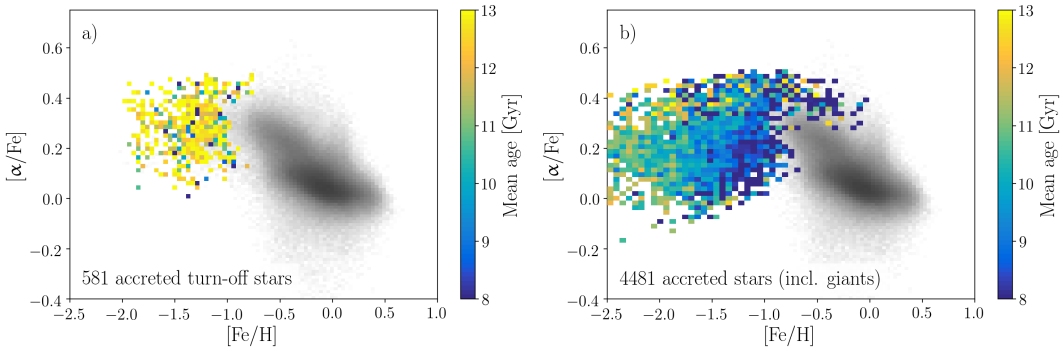

Figure 4.25: Mean stellar ages (color-code) of stars of the accreted halo component in the [Fe/H] vs. [α/Fe] plane for turn-off stars (panel a) and all evolutionary stages (panel b). The density distribution of the 'full' sample is plotted in the background with a greyscale to guide for visualisation. **Figure Credit: Paper III**.

Possible influences of different age estimates Schuster et al. (2012) estimated their age distribution in a similar manner to us via isochrone fitting of turn-off stars. In their study, they also discuss the influences of age estimates extensively, including the influence of gravitational settling into isochrone models (see also Jofré & Weiss, 2011), the correction of spectroscopic to photometric offsets, and the choice of isochrone metallicity (commonly estimated by a combination of iron and α abundances). In addition to these choices, the choice of isochrone models itself is important and different in our case, because Schuster et al. (2012) used Y^2 (see e.g. Demarque et al., 2004) with individually adjusted [α/Fe], whereas we use Parsec (Bressan et al., 2012) isochrones with linear enhancement of [α/Fe] between 0 and 0.4 in the range of $0 <$ [Fe/H] < -1. To estimate the influence of these choices, we propose a reanalysis of our ages or an analysis of the ages of the Schuster et al. (2012) stars in a future study. If the age estimates of our study would change, an additional discussion of the differences with respect to the study by Gallart et al. (2019) would also be necessary.

Another important criterion that might influence the differences of the age estimates is however the sample selection. The study by Das et al. (2019) for example only used giants to estimate their stellar ages and their giant ages are confined to the range of . To allow the comparison with Das et al. (2019), we also plot the age distribution of our giants in the [Fe/H] vs. [α/Fe] plane (see panel b) of Fig. 4.25) and find an age gradient, but with even lower ages than Das et al. (2019). The found gradient for giants however, raises the question, if possibly the age distribution of giants is different from those of

turn-off stars, or actually only the reliability of these measurements. Regarding the latter, we want to stress that Das et al. (2019) use an prior for different component, that is, for thick disk ($\mu_\tau = 10\,\mathrm{Gyr}$, $\sigma_\tau = 2\,\mathrm{Gyr}$) as well as stellar halo ($\mu_\tau = 11\,\mathrm{Gyr}$, $\sigma_\tau = 2\,\mathrm{Gyr}$). We suggest that the use and influence of these priors should be investigated further, given that we have seen that the actual ages of the stars seem to significantly deviate from these values, when measured with other methods and samples. In addition, we suggest to include age estimates from chemical clocks, such as the [C/N] ratio for giant stars (Masseron & Gilmore, 2015; Martig et al., 2015) to further test the found isochrone ages by Das et al. (2019) and compare those with turnoff stars ages.

4.7 Conclusions

In this study, we have explored the chemodynamic composition of the stellar disk and halo with the 'full' GALAH sample and were able to find several properties that show discriminative power.

We have shown that the decomposition of the Milky Way is a powerful approach to study the chemodynamic and temporal composition of the Galaxy. With GMMs we identified six hyper-components via the chemodynamic decomposition and were able to link the identified components to the low- and high-α disk, the accreted halo, that is the 'Sausage' identified by Belokurov et al. (2018), and the metal-poor halo.

By analysing the chemical composition of high velocity stars we have been able to link the 'Sausage' with the low-α halo found by Nissen & Schuster (2010) and furthermore showed that the red sequence of stars (in the CMD and T_{eff} vs. $\log g$ plane) is correlated with the high-α disk, whereas the blue sequence of stars is correlated with the halo.

The intermediate halo population with high [Mg/Fe] and [Al/Fe] as well as [Na/Fe] however continues to be enigmatic, because its dynamic properties are rather similar to the accreted halo, but its chemical properties are distinct from the accreted halo and the high-α disk. Further studies, e.g. via the comparison of Galactic Chemical Evolution models should be able to explain if this population is potentially the metal-poor extension of the high-α disk, as suggested for example by Beers et al. (2002).

The age distribution of the accreted halo also remains contentious, because our age estimates of TO stars suggest this population to be coeval with the metal-poor halo and high-α disk (similar to results obtained via CMD fitting by Gallart et al. (2019)), whereas the age estimates from giant stars by Das et al. (2019) suggest it to be younger and exhibit an age gradient. We suggest further analyses of TO stars or the exploration of other age estimation techniques like ages from the [C/N] ratio (Masseron & Gilmore, 2015; Martig et al., 2015) for the giants.

A component that we have not analysed in more detail yet is the metal-poor halo, mainly because we have not been able to estimate a large variety of element abundances for its stars and were therefore not able to include many metal-poor stars in the the GMMs of the 'high velocity' sample. The low metallicity and the chemical abundances, that were measured for some of its stars, indicate that this component is significantly

different from the in-situ disk. Possibly this component is assembled from many smaller systems that were cannibalised early and their dynamics are now indistinguishable from the rest of the halo. Further tests remain to examine the connection of the metal-poor halo (4481 spectra in our sample) with the accreted halo (3863 spectra in our sample) and metal-poor globular clusters like ωCen.

Chapter 5

Conclusions and outlook

We are living in exciting times for Galactic Archaeology. Until only a few years ago, our understanding of the chemodynamic composition of our Galaxy and thus our means to unravel its formation were based on studies with only hundreds of or in rare cases some thousands of stars. The advent of large stellar surveys has broadened our horizon and the prospects of Galactic archaeology. The observations of more than a billion stars by the *Gaia* satellite have revolutionised our knowledge of the phase space of the stars around us and every day thousands of new stellar spectra are observed by spectroscopic surveys. The combination of these data allows the chemodynamic exploration of our Galaxy with the aim to understand its stellar content and unraveling its formation.

In this Chapter, I highlight my contributions to this chemodynamic exploration by concluding the work of this Thesis in Sec. 5.1. In Sec. 5.2, I look into the future and elaborate on the follow-up of the presented research as well as future prospects of the field of Galactic Archaeology with large stellar surveys.

5.1 Conclusions

The work presented in this Thesis is focussed around the GALAH survey, for which I continue to play a leading role in the spectroscopic analysis. The extraction of chemical information from the GALAH spectra and their combination with the two astrometric releases of the *Gaia* satellite to estimate dynamical information and stellar ages laid the basis for the astronomical exploration of the data (Chapter 2). During my PhD research I have conducted two studies of the Milky Way, that is, the chemodynamic exploration of the stellar disk (Chapter 3) and the chemodynamic exploration of the stellar halo and its interplay with the disk (Chapter 4).

Chapter 2: Estimating chemical, dynamical, and age information for more than 650,000 stars

Over the course of the last four years, I have developed spectroscopic pipelines, which are used by the GALAH consortium to analyse spectra of the HERMES spectrograph. Starting with several pioneering analyses of high-fidelity data sets, these pipelines have

been optimised to deliver chemical abundances for up to 30 elements between Li and Eu from trustworthy spectral windows, thus covering numerous nucleosynthesis channels.

After the publication of astrometric information by the *Gaia* collaboration and asteroseismic information by the K2 and CoRoT collaborations, I have adjusted the spectroscopic pipelines to be able to also include such non-spectroscopic information.The use of this additional information effectively breaks important degeneracies present in the spectroscopic analyses and have thus helped to significantly increase the accuracy of the GALAH survey analysis.

Because of the growing number of observed spectra (currently reaching more than 750,000 for the GALAH survey alone), we need to estimate abundances on an industrial scale. To estimate this information in an efficient way, I have implemented an adapted version of the data-driven analysis tool *The Cannon* (Ness et al., 2015). This tool makes use of the full spectral range of the survey and builds models based on a training set of spectra with known stellar labels in order to predict stellar labels of other spectra, observed in the same manner. Because this approach currently still needs the full label information for each training set spectrum, I have invented a method to bridge this shortcoming. With this method we first estimate the best model to represent the most important stellar labels, that is, stellar parameters. Subsequently, the model is only perturbed with one abundance label at a time (for a training set subset with available abundances), which can only influence the model coefficients in those regions, where lines of the element are situated. With this approach we have already been able to estimate up to 23 abundances for 342,682 stars as part of the second data release of the GALAH collaboration (see **Paper I**).

Currently, the analysis of GALAH DR3 is on-going and includes several major improvements compared to the commonly and previously conducted analyses. Those include the use of astrometric information for all stars, but also a line-by-line analysis of element abundances, which significantly improves the obtained accuracy and precision. (see **Paper IV**). Furthermore, I have estimated stellar ages and dynamic information for all the $\sim 650,000$ stars as part of GALAH DR3, which will be provided to the community as value-added-catalogs accompanying GALAH DR3 and have already been used in this Thesis for the chemodynamic exploration of our Galaxy.

CHAPTER 3: THE OLD, HIGH-α AND THE YOUNG, LOW-α DISK

The first exploration of the data overlapping between GALAH and *Gaia* with reliable chemical, dynamical, and age information, focussed on the chemodynamic composition of the stellar disk. At the time, the overlap consisted of 7066 turn-off stars, that is, ten times more stars than the seminal study by Bensby et al. (2014).

In this study (**Paper II**), we investigate the correlations between stellar age, iron abundance [Fe/H], and mean alpha-enhancement [α/Fe]. We recover the result that stars of the high-α sequence are typically older than stars of the low-α sequence, the latter spanning iron abundances of $-0.7 <$ [Fe/H] $< +0.5$. While these two sequences become indistinguishable in [α/Fe] vs. [Fe/H] at the metal-rich regime, we find that age can be used in combination with [Fe/H] and [α/Fe] to separate stars from the extended high-α

and the low-α sequence even in this regime. Almost all stars on the high-alpha sequence are older than 8 Gyr - the vast majority even older then 10 Gyr. Stars of the low-alpha sequence are younger than 8 Gyr - the vast majority even younger than 8 Gyr (see also Haywood et al., 2013).

When dissecting the sample by stellar age, we find that the old stars (> 8 Gyr) have lower angular momenta L_z than the Sun, which implies that they are on eccentric orbits and originate from the inner disc (see also Anders et al., 2018). Stars of the low-α sequence show a gradient in L_z from low [Fe/H] ($L_z > L_{z,\odot}$) towards higher [Fe/H] ($L_z < L_{z,\odot}$), which implies that the stars at the high-metallicity end of this sequence are likely not originating from the close solar vicinity (see also Haywood, 2008a). This conclusion was already drawn by Hayden et al. (2015) based on spatial information only, but our work added the dynamical aspects, that is, demonstrated that these high-metallicity stars are on eccentric orbits currently visiting the Solar neighborhood.

Contrary to some previous smaller scale studies we find a continuous evolution in the high-α-sequence up to super-solar [Fe/H] rather than a gap, which has been interpreted as a separate 'high-α metal-rich' population. We further find that studies that assign stars to the populations purely via their kinematic properties or the [Fe/H] vs. [α/Fe] plane are systematically biased.

Chapter 3: Chemodynamic decomposition of the GALAH survey and the characterisation of the stellar halo

The overlap of the the second data release of *Gaia* and the latest analysis of GALAH spans an unprecedented number of chemodynamic dimensions. This allows to explore and decompose the chemodynamic content of the stellar disk and halo as seen with GALAH.

In this study (**Paper III**), we first explore this content with the commonly used chemodynamic decomposition tools, that is, the Toomre diagram or the [Fe/H] vs. [α/Fe] plane. When also analysing other combinations of chemodynamic properties, we find properties like azimuthal action L_Z, Galactocentric radial velocity V_R, eccentricity e, and stellar age τ to show similar or even more distinct transitions in their properties between the disk and halo.

Because the analyses of GALAH DR3 are still ongoing, the chemical compositions for the 'full'[1] sample of GALAH stars are limited to [Fe/H] and [α/Fe]. However, chemical abundances for up to 30 elements were estimated for a subset of 17756 'high velocity' stars (4% of the 'full' sample) with total velocities above $v_{\rm tot} > 180\,{\rm km\,s^{-1}}$.

In the study, we first use the combination of the dynamic properties L_Z and V_R with the chemical properties [Fe/H] and [α/Fe] to decompose the 'full' GALAH sample with Gaussian Mixture Models with 24 Gaussian components and recover six hyper-components among them, that is, the low-α and high-α disk and a third component with intermediate disk properties, an accreted halo and a metal-poor halo component, as well as a component of outliers with properties similar to the disk but extreme [α/Fe] values.

[1]This sample was selected from the full GALAH DR3 sample by applying quality cuts and excluding stars with non-trivial selection criteria.

Furthermore, we decompose the dynamically selected 'high velocity' stars with a chemical decomposition with the four abundance ratios [Fe/H], [Mg/Fe], [Na/Fe], and [Mn/Fe], representing the stellar metallicity tracer and three different nucleosynthesis groups. With a Gaussian decomposition we find three hyper-components, that is, a high-α metal-rich component, a low-α component, and a high-α more metal-poor component.

Because the 'high velocity' sample is a subset of the 'full' sample, we are able to compare the overlap of the two different types of identified hyper-components and subsequently link them to one another with several findings. We conclude that there is effectively no overlap of the 'high velocity' sample with the low-α and intermediate disk. The high-α disk agrees with the high-α 'high velocity' component. This component is enhanced in other element ratios, e.g. [Na/Fe] and [Mn/Fe]. The accreted halo population with $L_Z \sim 0\,\mathrm{kpc\,km\,s^{-1}}$ and a large range of V_R, identified as the so-called 'Sausage' by Belokurov et al. (2018), is strongly correlated with the low-α halo component identified chemically by Nissen & Schuster (2010). We find that the component with high α abundances but [Fe/H] below that of the disk also shows high odd-Z abundances (contrary to the low-α population), but overlaps with both other components dynamically. We find that the blue and red sequences of the 'high velocity' stars are correlated with the halo and high-α disk, respectively. When looking at the stellar ages of the identified components, we find that all 'high velocity' components as well as the halo components of the 'full' sample are very old and coeval, which is in agreement with the results by Gallart et al. (2019), but in contrast to the ages differences found by Schuster et al. (2012) and the age gradients found for the accreted halo stars by Das et al. (2019).

5.2 OUTLOOK

This Thesis is written in a vibrant time of the research field of Galactic archaeology. The results and analyses presented in this Thesis are valuable for on-going and upcoming surveys, such as WEAVE, MOONS, 4MOST, SDSS-V, and MSE. With the on-going analyses of large-scale spectroscopic surveys and the chemodynamic exploration of the Galaxy, the research field of Galactic archaeology is currently making excellent progress towards our aim to understand the formation of the MW.

In this section, I highlight aspects that I believe will be important to further improve spectroscopic analyses as well as aspects that will be important to further our understanding of the our Galaxy as the main subject of near-field cosmology, thereby establishing a link between stellar physics and the research of galaxies and cosmology.

IMPROVING LARGE-SCALE SPECTROSCOPIC ANALYSIS

The recent progress in the spectroscopic analysis of stars is immense, but we are still only at the beginning of exploring the stellar content of our Galaxy as we have only observed around $\sim 0.001\%$ of the stars of our Galaxy with high-resolution spectrographs. The upcoming surveys like WEAVE, MOONS, 4MOST, SDSS-V, and MSE will significantly increase this ratio, but will also face several challenges due to the large amount of data and the high precision that that is needed to further our understanding of the Galaxy.

In the introduction (see Sec. 1.3.3.1), I have already outlined those challenges of large-scale spectroscopic analyses that were addressed and partially even met throughout the work of this Thesis. Subsequently I highlight further challenges.

The advantages and drawbacks of data-driven analyses The recent applications of data-driven analyses have shown that these are powerful tools to analyse the spectral content efficiently and precisely. They have, however, also revealed shortcomings in their flexibility and ability to extrapolate.

In the future, we will rely more than ever on the advantages of data-driven analyses to also explore the data beyond our analytical understanding, for example by finding correlations of certain pixels with elements in the infrared or CNO line tracers with stellar age (see e.g. Ness et al., 2016; Ho et al., 2017a; Hawkins et al., 2018), which can then be validated from astrophysical considerations.

One has to be careful, however, to blindly trust the outcome of these analyses, because they might sense correlations that are not motivated via astrophysics, for example the similar trends of telluric lines with α-element lines, found for the GALAH survey selection. Important steps are already made to only allow data-driven methods to explore truly astrophysical correlations, but should be developed further to use as much spectral information as possible. Additional important improvements include the use of more flexible models (Ting et al., 2018b) and the treatment of incomplete data (Leung & Bovy, 2019).

We have to explore the influence of the training set composition for data-driven methods further. Until now, we have not yet found a reliable way to construct the best training set, but rather combine those spectra with highest quality with those that sample the parameter space. It is therefore vital to further test the need of a homogeneous representation of parameters and the dominance of outliers.

Fully consistent chemical compositions Up until now, almost all spectroscopic analyses analyse elements individually by assuming the abundance of all other elements to be scaled-solar. Brewer et al. (2015) however showed that significantly higher accuracy and precision can be reached, if all elements are fitted simultaneously or at least consistently within an iterative process. Being consistent in terms of chemical composition is also important in the generation of the atmosphere and the synthetic spectrum. In particular, a decrease in the abundance of a main electron donor, such as Mg, leads to a lower number of free electrons available to form H^- ions, which is the dominant source of continuous opacity in cool stellar atmospheres and therefore influences the line strength also of other species (see e.g. Mucciarelli et al., 2012). Ting et al. (2018a) have shown that such conserving internal consistency can also enable the measurement of element abundances from low-resolution spectra and/or elements without any detectable spectral features, but with an indirect influence on lines of other species via the atomic-molecular equilibrium.

The reliability of 1D LTE approaches and the challenges of 3D non-LTE The possibly hardest challenge that we will have to face is the implementation of accurate modelling of stellar atmospheres. This topic was addressed throughout this Thesis, but deserves to be highlighted again in this outlook, as we still have a lot of progress to make

in this field and the use or non-use of 3D non-LTE can significantly change our scientific conclusions. A recent example by Amarsi et al. (2019b) shows that abundance trends under different atmosphere assumptions vary strongly. Using 3D non-LTE, Amarsi et al. (2019b) showed that the trends of [C/O] among metal-poor halo stars change their sign, thus not needing an additional nucleosynthesis of the first stars or other explanations. Furthermore, they showed that metal-poor stars with previously believed metal-poor stars extreme enrichment in [C/Fe] from 1D LTE analyses, so called CEMP, might actually be carbon-normal when analysed with 3D non-LTE. Advances in the 3D non-LTE analyses are thus vital for our exploration of the metal-poor Galaxy and in particular the halo, but we want to stress that the use of 1D non-LTE is already a preferable intermediate step.

UNRAVELING THE EVOLUTION OF OUR GALAXY

To unravel the formation history of the MW, several aspects seem to be the most promising. From an observational point of view, the estimation of reliable, that is, both accurate and precise, stellar ages seems to be the most promising field, as it would directly place stars and Galactic components onto the evolutionary scale of the Universe. The results of the analysis conducted in this Thesis, however, point towards quite similar ages of several Galactic components, making it hard to assign major events or changes in the Galactic structure to one or the other component. Thus, the comparison with the continually improving simulations, that is, both in the cosmological and the chemical evolutionary context, seems to be most promising to favour er even rule out certain formation scenarios of the MW. If chemical tagging actually works and we find the building blocks of our Galaxy for a large part of the currently observed field stars, we might be able to further understand both the big and detailed picture of the build-up of our Galaxy. To make this become true, we will however heavily rely on our ability to cross-correlate surveys to both expand the number of observed stars for the pool of chemical tagging, but also the number of observed elements and nucleosynthesis channels.

The contentious ages of stars and the role of mergers in the formation of the disk Throughout this Thesis, stellar ages have been proven to have a significant discriminative power and will be key to further understand if the high-α and low-α sequences of the disk might actually have formed stars at the same time (between 8 and 10 Gyr ago) or if their star formation is completely separated. The latter would hint towards a significant event like a major merger, which stopped the star formation around 10 Gyr ago and mixing the birth material of the young low-α stars to show their distinct chemical composition from the oldest high-α disk stars.

Several open question also remain regarding the importance of the accreted halo for the shape of our Galaxy. Was the material that we see now as the accreted halo part of a minor or major merger? Is the accreted halo responsible for the hiatus in star formation of the high-α disk and the onset of the low-α disk formation? Did it bring the new gas that would be needed for the two-infall model (Chiappini et al., 1997) to change the chemical composition of the birth material of the low-α disk? Or is the formation proposed by Clarke et al. (2019) more reasonable, that is, the formation of the high-α disk in the course of clump formation at early times?

The estimates by Kruijssen et al. (2018) suggest that no major mergers happened since $z \sim 4$ (corresponding to $\tau \sim 12$ Gyr). An old accreted halo component like the 'Sausage' (Belokurov et al., 2018; Helmi et al., 2018) with the ages estimated by our analysis (**Paper III**) are therefore consistent with a major merger before $z \sim 4$. However, if the merger would be that massive, we would expect a remnant core cluster. The search among known clusters in our Galaxy, most notably ωCen (see e.g. Myeong et al., 2018a,b) or dwarf spheroidals (see e.g. Hayes et al., 2018) seems most promising. We thus strongly rely on the progress of the exploration of both new globular clusters (possibly in or beyond the densest regions of the Galactic center) as well as the further characterisation of dwarf spheroidal galaxies (see e.g. Koch et al., 2006).

Improving the reliability of stellar ages estimates will help to significantly narrow down the possible formation scenarios of the MW. Such improvements are needed both from the model perspective (e.g. for isochrone fitting techniques), but also from the observational perspective. In the future, we expect more age estimates from chemical clocks, like the [C/N] ratio in giants (Masseron & Gilmore, 2015; Martig et al., 2015; Ness et al., 2016), [Y/Mg] ratios in dwarfs (Nissen, 2015; Spina et al., 2016). We note however, that also the observations of the Kepler, K2, CoRoT missions have lead to reliable estimates of masses, which can be used together with chemical compositions to estimate stellar masses. The on-going observations of the TESS satellite (Ricker et al., 2015) as well as the upcoming PLATO mission (Rauer et al., 2014; Miglio et al., 2017) are promising mass estimates with 10% uncertainties and reliable age estimates.

Linking observations and simulations In addition to the growing number of observations of stars in our Galaxy, the number and quality of simulations to compare the observations to has grown. These simulations come in different flavours and include stellar population synthesis models of the Galaxy (e.g. Sharma et al., 2011) as well as chemical evolution models and simulations in a cosmological context.

With the help of cosmological simulations, such as EAGLE (Crain et al., 2015; Schaye et al., 2015), NIHAO (Wang et al., 2015), AURIGA (Grand et al., 2017) or IllustrisTNG (Pillepich et al., 2018), which are able to form MW equivalents, we can now compare detailed observed and simulated properties (see e.g. Mackereth et al., 2019b) in order to favour certain formation scenarios of Galactic components (see e.g. Grand et al., 2018; Clarke et al., 2019; Buck et al., 2019).

The chemodynamic decomposition presented in this Thesis is promising in order to dissect the building blocks of the Galaxy. Once the full set of abundances are estimated, a new decomposition with the additional use of odd-Z elements would likely bring more clarity to the chemodynamic properties of different components of our Galaxy. In addition to the comparison with cosmological simulations, especially the comparison with galactic chemical evolution models and simulations (see e.g. Kobayashi et al., 2006; Kobayashi & Nakasato, 2011) will help to pin down the important nucleosynthesis sites of each component and will also help to improve the shortcomings of current chemical evolution models, in particular for the metal-poor regime with the most metal-poor and first stars.

Chemical tagging The chemical tagging of stars as proposed by Freeman & Bland-Hawthorn (2002) still remains an important and long-term goal of the field of Galactic archaeology. With the progress achieved throughout this Thesis and expected in the future, it will still take some time to figure out if we can trace back stars that were born together via their chemical composition. We have already outlined the particular challenges in the practicalities of chemical tagging in the introduction, but if we would be able to trace back field stars to their origin, we would be able to understand the formation of the Galaxy also in its smallest building blocks. Advances in chemical tagging will also be vital to estimate the fraction of stars that may have escaped from globular clusters (see e.g. Lind et al., 2015) and thus the fraction of Galactic halo that stems from disrupted clusters, which is currently estimated to be very low (Koch et al., 2019). The stellar halo with all its streams and valuable substructure thus remains one of the most promising tracers of Galactic history.

Cross-correlating surveys An undeniable challenge of Galactic archaeology is that even large-scale surveys are and will not be able to observe all stars of the MW. If we want to increase the number of stars that can be used for chemodynamic studies, it is inevitable to combine survey information while making sure that the information of different surveys is on the same scale. However, star-by-star comparisons of surveys (see e.g. Kunder et al., 2017) have shown deficits in the accuracy of surveys. To meet this challenge, several approaches are conceivable (on top of the intrinsic improvement of each survey analysis): The same analysis method could be applied for two different surveys (see e.g. the use of the *Gaia*-ESO code BACCHUS onto APOGEE spectra by Hawkins et al., 2016). Another approach makes use of data-driven methods based on stars observed by two surveys. As pointed above, the training of such methods relies on provided stellar labels (see Eq. 1.25). However, these do not have to be estimated by the survey or data-driven method itself, but can come from literature values. By using stellar labels from one survey (A), Ho et al. (2017b,a); Casey et al. (2017) showed for example that it is possible to train a spectral model for another survey (B) simply based on the overlap of stars between survey A (with known stellar labels) and B (with the corresponding spectra).

To show the power of combining surveys, we plot the spatial distribution of mean stellar ages from the observations of the GALAH survey (**Paper IV**), APOGEE (Ness et al., 2016), and LAMOST (Ho et al., 2017a) in Fig. 5.1, which already by eye shows clear gradients on a Galactic scale with younger stars in the mid-plane and old stars far away from the Galactic plane as well as towards its center.

Bringing all conducted spectroscopic surveys on the same scale will be a milestone for the study of the MW as a compilation of stars (see Eq. 1.2), as we envisioned in the beginning of the introduction in Sec. 1 based on the review by Rix & Bovy (2013).

This Thesis has highlighted several of the challenges involved in reducing the errors introduced by different spectroscopic analysis techniques and those must first be overcome. Ultimately, we envision that the accuracy of extracted parameters and abundances should be limited by the observational quality of spectra only, not by deficiencies in the modelling or in the extraction methods. I conclude this Thesis with the promise

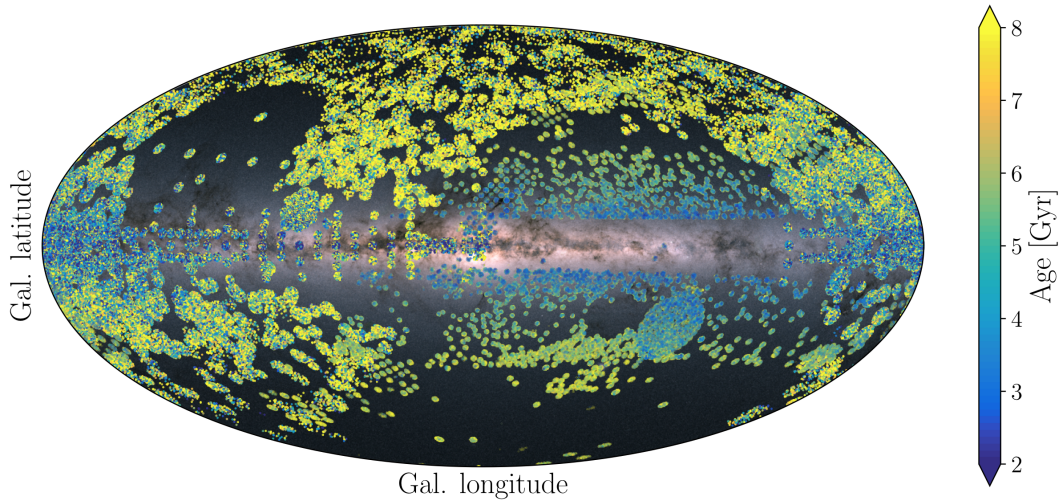

Figure 5.1: Spatial distribution of stellar ages of stars observed by GALAH (**Paper IV**), APOGEE (Ness et al., 2016), and LAMOST (Ho et al., 2017a). The stellar flux map of *Gaia* DR2 (Gaia Collaboration et al., 2018b) is plotted in the background to guide the eye.

that stellar spectroscopy and Galactic archaeology with million-star surveys will continue to flourish in the coming decades.

ACRONYMS

2MASS **Two Micron All-Sky Survey**

4MOST **4-metre Multi-Object Spectroscopic Telescope**

AGB Asymptotic Giant Branch

APOGEE **Apache Point Observatory Galactic Evolution Experiment**

CCD Charge-Coupled Device

CMD Color-Magnitude Diagram

Cspace *C*-spaceChemical space

DESI **Dark Energy Spectroscopic Instrument**

DF stellar Distribution Function

DR Data Release

G Gaia satellite G-band magnitude

***Gaia* RVS** ***Gaia* Radial Velocity Spectrometer**

GALAH Galactic Archaeology with HERMES

GBS *Gaia* FGK benchmark stars

G_{BP} Gaia satellite blue photometer magnitude

GCS **Geneva-Copenhagen Survey**

GMMs Gaussian Mixture Models

G_{RP} Gaia satellite red photometer magnitude

HERMES High Efficiency and Resolution Multi-Element Spectrograph

HIPPARCOS **High Precision Parallax Collecting Satellite**

HRD Hertzsprung-Russell Diagram

IRFM Infrared Flux Method

LAMOST **Large Sky Area Multi-Object Fiber Spectroscopic Telesope**

LSR Local Standard of Rest

LTE Local Thermodynamic Equilibrium

non-LTE Non-Local Thermodynamic equilibrium

MOONS **Multi-Object Optical and Near-infrared Spectrograph**

MS Main Sequence

MSE **Maunakea Spectroscopic Explorer**

MW Milky Way

Paper I Buder et al. (2018)

Paper II Buder et al. (2019)

Paper III Buder et al. (in prep. a)

Paper IV Buder et al. (in prep. b)

PFS **Subaru Prime Focus Spectrograph**

PMS Pre-Main Sequence

RAVE **Radial Velocity Experiment**

RC Red Clump

RGB Red Giant Branch

SDSS **Sloan Digitial Sky Survey**

SEGUE **Sloan Extension for Galactic Understanding and Exploration**

SNe Supernova(e)

SNe Ia Supernovae type Ia

SNe II core-collapse Supernovae type II

TESS Transiting Exoplanet Survey Satellite

TGAS Tycho-*Gaia* Astrometric solution

TO Turn-off

WD White Dwarf

WEAVE **William Herschel Telescope Enhanced Area Velocity Explorer**

First Author Publications of S. Buder

Buder, S., et al. (in prep. b). The GALAH Survey: third data release. *MNRAS*.
This publication was used in this thesis.

Buder, S., et al. (in prep. a). The GALAH Survey: Confirming the Milky Way Halo Duality in Chemical Space. *MNRAS*.
This publication was used in this thesis.

Buder, S., Lind, K., Ness, M. K., et al. (2019). The GALAH survey: An abundance, age, and kinematic inventory of the solar neighbourhood made with TGAS. *A&A*, 629:A19.
This publication was used in this thesis.

Buder, S., Asplund, M., Duong, L., et al. (2018), The GALAH Survey: second data release. *MNRAS*, 478:4513-4552.
This publication was used in this thesis.

CO-AUTHORED PUBLICATIONS

Sharma, S., Stello, D., Bland-Hawthorn, J., Hayden, M.R., **et al.** (2019). The K2-HERMES Survey: Age and Metallicity of the Thick Disc. *ArXiv e-prints*.

Lin, J., Asplund, M., Casagrande, L., **Buder, S.**, et al. (2019). The GALAH Survey: Temporal Chemical Enrichment of the Galactic Disk. *MNRAS submitted*.

Čotar, K., Zwitter, T., Traven, G., **et al.** (2019b). The GALAH survey: unresolved triple Sun-like stars discovered by the Gaia mission. *ArXiv e-prints*.

Khanna, S., Sharma, S., Tepper-Garcia, T., **et al.** (2019b). The GALAH survey and Gaia DR2: Linking ridges, arches and vertical waves in the kinematics of the Milky Way. *ArXiv e-prints*.

Hayden, M., Bland-Hawthorn, J., Sharma, S., **et al.** (2019). The GALAH Survey: Chemodynamics of the Solar Neighbourhood. *ArXiv e-prints*.

Kos, J., Bland-Hawthorn, J., Asplund, M., **Buder, S.**, et al. (2019). Discovery of a 21 Myr old stellar population in the Orion complex. *ArXiv e-prints*.

Žerjal, M., Ireland, M. J., Nordlander, T., Lin, J. **et al.** (2019). The GALAH Survey: Lithium-strong KM dwarfs. *ArXiv e-prints*.

Bland-Hawthorn, J., Sharma, S., Tepper-Garcia, T., Binney, J., **et al.** (2019). The GALAH survey and Gaia DR2: dissecting the stellar disc's phase space by age, action, chemistry and location. *ArXiv e-prints*.

Čotar, K., Zwitter, T., Kos, T., Munari, U., **et al.** (2019a). The GALAH survey: a catalogue of carbon-enhanced stars and CEMP candidates. *MNRAS*, 483:3196.

Simpson, J. D., Martell, S. L., Da Costa, G., **et al.** (2019). The GALAH survey: Co-orbiting stars and chemical tagging. *MNRAS*, 482:5302.

Khanna, S., Sharma, S. Bland-Hawthorn, J., **et al.** (2019a). The GALAH Survey: Velocity fluctuations in the Milky Way using red clump giants. *MNRAS*, 482:4215.

Gao, X., Lind, K., Amarsi, A. M., **Buder, S.**, et al. (2018). The GALAH Survey: Verifying abundance trends in the open cluster M67 using non-LTE spectroscopy. *MNRAS*, 481:2666.

Zwitter, T., Kos, J., Chiavassa, A., **Buder, S.** (2018). The GALAH Survey: Accurate Radial Velocities and Library of Observed Stellar Template Spectra. *MNRAS*, 581:645.

Kos, J., Bland-Hawthorn, J. Betters, C. H., **et al.** (2018). Holistic spectroscopy: Complete reconstruction of a wide-field, multi-object spectroscopic image using a photonic comb. *MNRAS*, 480:5475.

Kos, J., de Silva, G., **Buder, S.**, et al. (2018). The GALAH Survey and *Gaia* DR2: (Non)existence of five sparse high-latitude open clusters. *MNRAS*, 480:5242.

Simpson, J. D., Stello, D. Sharma, D., **et al.** (2018). The GALAH and TESS-HERMES surveys: high-resolution spectroscopy of luminous supergiants in the Magellanic Clouds and Bridge. *ArXiv e-prints*.

Quillen, A. C., De Silva, G. M., Sharma, S., **et al.** (2018). The GALAH Survey: Stellar streams and how stellar velocity distributions vary with Galactic longitude, hemisphere and metallicity. *MNRAS*, 478:228.

Duong, L., Freeman, K. C., Asplund, M., **et al.** (2018). The GALAH survey: properties of the Galactic disk(s) in the solar neigbourhood. *MNRAS*, 476:5216.

Kos, J., Bland-Hawthorn, J., Freeman, K., **Buder, S.**, et al. (2018). The GALAH Survey: Chemical Tagging of Star Clusters and New Members in the Pleiades. *MNRAS*, 473:4612.

Wittenmyer, R. A., Sharma, S., Stello, D., **Buder, S.**, et al. (2018). The K2-HERMES Survey. I. Planet Candidate Properties from K2 Campaigns 1-3. *AJ*, 155:84.

Sharma, S., Stello, D., **Buder, S.**, et al. (2018). The TESS-HERMES survey Data Release 1: high-resolution spectroscopy of the TESS southern continuous viewing zone. *MNRAS*, 473:2004.

Przybilla, N., Aschenbrenner, P., **Buder, S.** (2017). Candidate exoplanet host HD131399A: a nascent Am star. *A&A*, 604:9.

Jofré, P.; Heiter, U., **Buder, S.** (2017). Gaia FGK benchmark stars: a bridge between spectroscopic surveys. *ASInC*, 14:37.

Jofré, P., Heiter, U., Worley, C. C.; **et al.** (2017). *Gaia* FGK Benchmark stars: Opening the black box of stellar element abundance determination. *A&A*, 601:38.

Martell, S. L. and Sharma, S. and Buder, S. and Duong, L. and Schlesinger, K. J. and Simpson, J. and Lind, K. and Ness, M. and Marshall, J. P. and Asplund, M. and Bland-Hawthorn, J. and Casey, A. R. and De Silva, G. and Freeman, K. C. and Kos, J. and Lin, J. and Zucker, D. B. and Zwitter, T. and Anguiano, B. and Bacigalupo, C. and Carollo, D. and Casagrande, L. and Da Costa, G. S. and Horner, J. and Huber, D. and Hyde, E. A. and Kafle, P. R. and Lewis, G. F. and Nataf, D. and Navin, C. A. and Stello, D. and Tinney, C. G. and Watson, F. G. and Wittenmyer, R. (2017). The GALAH survey: observational overview and Gaia DR1 companion. *MNRAS*, 465:3203-3219.

Mugrauer, M., **Buder, S.**, Reum, F., Birth, A. (2017). The Großschwabhausen binary survey. *AN*, 338:61.

Ginski, C., Mugrauer, M., Seeliger, M., **Buder, S.**, et al. (2016). A lucky imaging multiplicity study of exoplanet host stars - II. *MNRAS*, 457:2173.

Schmidt, T. O. B., Neuhäuser, R., Briceño, C, **et al.** (2016). Direct Imaging discovery of a second planet candidate around the possibly transiting planet host CVSO 30. *A&A*, 593:75.

Fritzewski, D. J., Kitze, M., Mugrauer, M., **et al.** (2016). Long-term photometry of IC 348 with the Young Exoplanet Transit Initiative network. *MNRAS*, 462:2396.

Raetz, St., Schmidt, T. O. B.;,Czesla, S., **et al.** (2016). YETI observations of the young transiting planet candidate CVSO 30 b. *MNRAS*, 460:2834.

Garai, Z., Pribulla, T., Hambálek, Ľ., **et al.** (2016). Search for transiting exoplanets and variable stars in the open cluster NGC 7243. *AN*, 337:261.

Seeliger, M., Kitze, M., Errmann, R., **et al.** (2015). Ground-based transit observations of the HAT-P-18, HAT-P-19, HAT-P-27/WASP40 and WASP-21 systems. *MNRAS*, 451:4060.

BIBLIOGRAPHY

Abadi, M. G., Navarro, J. F., & Steinmetz, M. 2006, MNRAS, 365, 747

Abadi, M. G., Navarro, J. F., Steinmetz, M., & Eke, V. R. 2003, ApJ, 597, 21

Abolfathi, B., Aguado, D. S., Aguilar, G., et al. 2018, ApJS, 235, 42

Abuter, R., Amorim, A., Bauboeck, M., et al. 2019, arXiv e-prints, arXiv:1904.05721

Adibekyan, V. Z., Santos, N. C., Sousa, S. G., & Israelian, G. 2011, A&A, 535, L11

Adibekyan, V. Z., Sousa, S. G., Santos, N. C., et al. 2012, A&A, 545, A32

Ahn, C. P., Alexandroff, R., Allende Prieto, C., et al. 2012, ApJS, 203, 21

Albareti, F. D., Allende Prieto, C., Almeida, A., et al. 2017, ApJS, 233, 25

Aleo, P. D., Sobotka, A. C., & Ramírez, I. 2017, ApJ, 846, 24

Allende Prieto, C., Majewski, S. R., Schiavon, R., et al. 2008, Astronomische Nachrichten, 329, 1018

Alonso, A., Arribas, S., & Martinez-Roger, C. 1995, A&A, 297, 197

Amarsi, A. M., & Asplund, M. 2017, MNRAS, 464, 264

Amarsi, A. M., Asplund, M., Collet, R., & Leenaarts, J. 2015, MNRAS, 454, L11

—. 2016a, MNRAS, 455, 3735

Amarsi, A. M., Barklem, P. S., Collet, R., Grevesse, N., & Asplund, M. 2019a, arXiv e-prints, arXiv:1903.08838 [astro-ph.SR]

Amarsi, A. M., Lind, K., Asplund, M., Barklem, P. S., & Collet, R. 2016b, MNRAS, 463, 1518

Amarsi, A. M., Nissen, P. E., Asplund, M., Lind, K., & Barklem, P. S. 2019b, A&A, 622, L4

Amarsi, A. M., Nordlander, T., Barklem, P. S., et al. 2018, A&A, 615, A139

An, D., Pinsonneault, M. H., Terndrup, D. M., & Chung, C. 2019, arXiv e-prints, arXiv:1904.00122 [astro-ph.SR]

Anders, F., Chiappini, C., Santiago, B. X., et al. 2018, A&A, 619, A125

Armillotta, L., Krumholz, M. R., & Fujimoto, Y. 2018, MNRAS, 481, 5000

Arnould, M., Goriely, S., & Takahashi, K. 2007, Phys. Rep., 450, 97

Arnould, M., & Norgaard, H. 1975, A&A, 42, 55

Asplund, M. 2005, ARA&A, 43, 481

Asplund, M., Grevesse, N., Sauval, A. J., & Scott, P. 2009, ARA&A, 47, 481

Asplund, M., Nordlund, Å., Trampedach, R., Allende Prieto, C., & Stein, R. F. 2000, A&A, 359, 729

Astraatmadja, T. L., & Bailer-Jones, C. A. L. 2016, ApJ, 833, 119
Astropy Collaboration, Robitaille, T. P., Tollerud, E. J., et al. 2013, A&A, 558, A33
Bailer-Jones, C. A. L., Rybizki, J., Fouesneau, M., Mantelet, G., & Andrae, R. 2018, AJ, 156, 58
Barden, S. C., Jones, D. J., Barnes, S. I., et al. 2010, in Proc. SPIE, Vol. 7735, Ground-based and Airborne Instrumentation for Astronomy III, 773509
Bastian, N., & Lardo, C. 2018, ARA&A, 56, 83
Battistini, C., & Bensby, T. 2015, A&A, 577, A9
—. 2016, A&A, 586, A49
Baumgardt, H., & Kroupa, P. 2007, MNRAS, 380, 1589
Bedding, T. R., Huber, D., Stello, D., et al. 2010, ApJ, 713, L176
Beers, T. C., Drilling, J. S., Rossi, S., et al. 2002, AJ, 124, 931
Bell, E. F., Zucker, D. B., Belokurov, V., et al. 2008, ApJ, 680, 295
Belokurov, V., Erkal, D., Evans, N. W., Koposov, S. E., & Deason, A. J. 2018, MNRAS, 478, 611
Belokurov, V., Zucker, D. B., Evans, N. W., et al. 2006, ApJ, 642, L137
Bensby, T., Feltzing, S., & Lundström, I. 2003, in Astronomical Society of the Pacific Conference Series, Vol. 304, CNO in the Universe, ed. C. Charbonnel, D. Schaerer, & G. Meynet, 175
Bensby, T., Feltzing, S., & Oey, M. S. 2014, A&A, 562, A71
Bensby, T., & Lind, K. 2018, ArXiv e-prints, arXiv:1804.00033
Bensby, T., Yee, J. C., Feltzing, S., et al. 2013, A&A, 549, A147
Bensby, T., Feltzing, S., Gould, A., et al. 2017, A&A, 605, A89
Bergemann, M. 2011, MNRAS, 413, 2184
Bergemann, M., & Gehren, T. 2008, A&A, 492, 823
Bergemann, M., Pickering, J. C., & Gehren, T. 2010, MNRAS, 401, 1334
Bergemann, M., Ruchti, G. R., Serenelli, A., et al. 2014, A&A, 565, A89
Bergemann, M., Huber, D., Adibekyan, V., et al. 2019, arXiv e-prints, arXiv:1903.03157 [astro-ph.SR]
Bergh, S. V. D. 1980, Philosophical Transactions of the Royal Society of London Series A, 296, 319
Bertelli Motta, C., Salaris, M., Pasquali, A., & Grebel, E. K. 2017, MNRAS, 466, 2161
Bessell, M. S. 1990, PASP, 102, 1181
Bica, E., Dutra, C. M., Soares, J., & Barbuy, B. 2003, A&A, 404, 223
Binney, J. 2012, MNRAS, 426, 1324
—. 2013, New A Rev., 57, 29
Binney, J., & McMillan, P. 2011, MNRAS, 413, 1889
Binney, J., & Tremaine, S. 2008, Galactic Dynamics: Second Edition (Princeton University Press)
Bird, J. C., Kazantzidis, S., Weinberg, D. H., et al. 2013, ApJ, 773, 43
Blanco-Cuaresma, S., & Fraix-Burnet, D. 2018, A&A, 618, A65

Blanco-Cuaresma, S., Soubiran, C., Heiter, U., et al. 2015, A&A, 577, A47
Bland-Hawthorn, J., & Freeman, K. C. 2004, PASA, 21, 110
Bland-Hawthorn, J., & Gerhard, O. 2016, ARA&A, 54, 529
Bland-Hawthorn, J., Kos, J., Betters, C. H., et al. 2017, Optics Express, 25, 15614
Bland-Hawthorn, J., Krumholz, M. R., & Freeman, K. 2010, ApJ, 713, 166
Bland-Hawthorn, J., Sharma, S., Tepper-Garcia, T., et al. 2019, MNRAS, 486, 1167
Böhm-Vitense, E. 1958, ZAp, 46, 108
Bonaca, A., Conroy, C., Wetzel, A., Hopkins, P. F., & Kereš, D. 2017, ApJ, 845, 101
Borissova, J., Bonatto, C., Kurtev, R., et al. 2011, A&A, 532, A131
Bournaud, F., Elmegreen, B. G., & Martig, M. 2009, ApJ, 707, L1
Bovy, J. 2015, ApJS, 216, 29
Bovy, J., & Rix, H.-W. 2013, ApJ, 779, 115
Bovy, J., Rix, H.-W., & Hogg, D. W. 2012a, ApJ, 751, 131
Bovy, J., Rix, H.-W., Liu, C., et al. 2012b, ApJ, 753, 148
Bovy, J., Rix, H.-W., Schlafly, E. F., et al. 2016, ApJ, 823, 30
Bovy, J., Nidever, D. L., Rix, H.-W., et al. 2014, ApJ, 790, 127
Boyajian, T. S., von Braun, K., van Belle, G., et al. 2013, ApJ, 771, 40
Bressan, A., Marigo, P., Girardi, L., et al. 2012, MNRAS, 427, 127
Brewer, J. M., Fischer, D. A., Basu, S., Valenti, J. A., & Piskunov, N. 2015, ApJ, 805, 126
Brown, A. G. A., Vallenari, A., Prusti, T., et al. 2016, Astronomy & Astrophysics, 595, A2
Brzeski, J., Case, S., & Gers, L. 2011, Proc.SPIE, 8125, 812504
Buck, T., Ness, M., Obreja, A., Macciò, A. V., & Dutton, A. A. 2019, ApJ, 874, 67
Buder, S., Asplund, M., Duong, L., et al. 2018, MNRAS, 478, 4513
Buder, S., Lind, K., Ness, M. K., et al. 2019, A&A, 624, A19
Burbidge, E. M., Burbidge, G. R., Fowler, W. A., & Hoyle, F. 1957, Reviews of Modern Physics, 29, 547
Cannon, A. J., & Pickering, E. C. 1901, Annals of Harvard College Observatory, 28, 129
—. 1918a, Annals of Harvard College Observatory, 92
—. 1918b, Annals of Harvard College Observatory, 91, 1
—. 1919a, Annals of Harvard College Observatory, 93
—. 1919b, Annals of Harvard College Observatory, 94
—. 1920, Annals of Harvard College Observatory, 95
—. 1921, Annals of Harvard College Observatory, 96
—. 1922, Annals of Harvard College Observatory, 97
—. 1923, Annals of Harvard College Observatory, 98
—. 1924, Annals of Harvard College Observatory, 99
Carlos, M., Nissen, P. E., & Meléndez, J. 2016, A&A, 587, A100
Carney, B. W., Aguilar, L., Latham, D. W., & Laird, J. B. 1990, AJ, 99, 201
Carollo, D., Beers, T. C., Lee, Y. S., et al. 2007, Nature, 450, 1020

Carollo, D., Beers, T. C., Chiba, M., et al. 2010, ApJ, 712, 692
Carollo, D., Chiba, M., Ishigaki, M., et al. 2019, arXiv e-prints, arXiv:1904.04881
Carpenter, J. M. 2000, AJ, 120, 3139
—. 2001, AJ, 121, 2851
Carretta, E., Bragaglia, A., Gratton, R. G., et al. 2010a, A&A, 516, A55
—. 2009, A&A, 505, 117
—. 2010b, ApJ, 714, L7
Casagrande, L., Ramírez, I., Meléndez, J., Bessell, M., & Asplund, M. 2010, A&A, 512, A54
Casagrande, L., Schönrich, R., Asplund, M., et al. 2011, A&A, 530, A138
Casagrande, L., & VandenBerg, D. A. 2014, MNRAS, 444, 392
Casagrande, L., Wolf, C., Mackey, A. D., et al. 2019, MNRAS, 482, 2770
Casagrande, L., Portinari, L., Glass, I. S., et al. 2014, MNRAS, 439, 2060
Casey, A. R., Hogg, D. W., Ness, M., et al. 2016, ArXiv e-prints, arXiv:1603.03040 [astro-ph.SR]
Casey, A. R., Hawkins, K., Hogg, D. W., et al. 2017, ApJ, 840, 59
Casey, A. R., Ho, A. Y. Q., Ness, M., et al. 2019, arXiv e-prints, arXiv:1902.04102
Castelli, F., & Kurucz, R. L. 2003, in IAU Symposium, Vol. 210, Modelling of Stellar Atmospheres, ed. N. Piskunov, W. W. Weiss, & D. F. Gray, A20
Chambers, K. C., Magnier, E. A., Metcalfe, N., et al. 2016, ArXiv e-prints, arXiv:1612.05560 [astro-ph.IM]
Chaplin, W. J., & Miglio, A. 2013, ARA&A, 51, 353
Chen, Y., Bressan, A., Girardi, L., et al. 2015, MNRAS, 452, 1068
Chen, Y., Girardi, L., Bressan, A., et al. 2014, MNRAS, 444, 2525
Chen, Y. Q., Zhao, G., Xue, X. X., et al. 2019, ApJ, 871, 216
Chiappini, C., Matteucci, F., & Gratton, R. 1997, ApJ, 477, 765
Chiappini, C., Matteucci, F., & Romano, D. 2001, ApJ, 554, 1044
Chiappini, C., Anders, F., Rodrigues, T. S., et al. 2015, A&A, 576, L12
Cirasuolo, M., Afonso, J., Carollo, M., et al. 2014, in Proc. SPIE, Vol. 9147, Ground-based and Airborne Instrumentation for Astronomy V, 91470N
Clarke, A. J., Debattista, V. P., Nidever, D. L., et al. 2019, MNRAS, 484, 3476
Clarke, C. J., Bonnell, I. A., & Hillenbrand, L. A. 2000, Protostars and Planets IV, 151
Clayton, D. 1983, Principles of Stellar Evolution and Nucleosynthesis, Astronomy / Astrophysics (University of Chicago Press)
Cooper, A. P., Parry, O. H., Lowing, B., Cole, S., & Frenk, C. 2015, MNRAS, 454, 3185
Côté, B., Eichler, M., Arcones, A., et al. 2018a, arXiv e-prints, arXiv:1809.03525 [astro-ph.HE]
Côté, B., Fryer, C. L., Belczynski, K., et al. 2018b, ApJ, 855, 99
Cottrell, P. L., & Da Costa, G. S. 1981, ApJ, 245, L79
Crain, R. A., Schaye, J., Bower, R. G., et al. 2015, MNRAS, 450, 1937
Cropper, M., Katz, D., Sartoretti, P., et al. 2018, A&A, 616, A5

Cui, X.-Q., Zhao, Y.-H., Chu, Y.-Q., et al. 2012, Research in Astronomy and Astrophysics, 12, 1197
Cunha, K., Frinchaboy, P. M., Souto, D., et al. 2016, Astronomische Nachrichten, 337, 922
Cutri, R. M., Skrutskie, M. F., van Dyk, S., et al. 2003, VizieR Online Data Catalog, 2246
Dalton, G., Trager, S., Abrams, D. C., et al. 2014, in Proc. SPIE, Vol. 9147, Ground-based and Airborne Instrumentation for Astronomy V, 91470L
Dalton, G., Trager, S., Abrams, D. C., et al. 2016, in Proc. SPIE, Vol. 9908, Ground-based and Airborne Instrumentation for Astronomy VI, 99081G
Das, P., Hawkins, K., & Jofre, P. 2019, arXiv e-prints, arXiv:1903.09320
de Jong, R. S., Barden, S., Bellido-Tirado, O., et al. 2014, in Proc. SPIE, Vol. 9147, Ground-based and Airborne Instrumentation for Astronomy V, 91470M
de Jong, R. S., Agertz, O., Agudo Berbel, A., et al. 2019, arXiv e-prints, arXiv:1903.02464 [astro-ph.IM]
De Laverny, P., Recio-Blanco, A., Worley, C. C., & Plez, B. 2012, A&A, 544, A126
De Ridder, J., Barban, C., Baudin, F., et al. 2009, Nature, 459, 398
De Silva, G. M., Freeman, K. C., & Bland-Hawthorn, J. 2009, PASA, 26, 11
De Silva, G. M., Freeman, K. C., Bland-Hawthorn, J., et al. 2015, MNRAS, 449, 2604
Delgado Mena, E., Tsantaki, M., Adibekyan, V. Z., et al. 2017, A&A, 606, A94
Demarque, P., Woo, J.-H., Kim, Y.-C., & Yi, S. K. 2004, ApJS, 155, 667
DESI Collaboration, Aghamousa, A., Aguilar, J., et al. 2016, arXiv e-prints, arXiv:1611.00036 [astro-ph.IM]
Di Matteo, P., Haywood, M., Lehnert, M. D., et al. 2018, arXiv e-prints, arXiv:1812.08232
Dias, W. S., Alessi, B. S., Moitinho, A., & Lépine, J. R. D. 2002, A&A, 389, 871
D'Orazi, V., Magrini, L., Randich, S., et al. 2009, ApJ, 693, L31
Dotter, A. 2016, ApJS, 222, 8
Dotter, A., Chaboyer, B., Jevremović, D., et al. 2008, ApJS, 178, 89
Dotter, A., Conroy, C., Cargile, P., & Asplund, M. 2017, ApJ, 840, 99
D'Souza, R., & Rix, H.-W. 2013, MNRAS, 429, 1887
Duong, L., Asplund, M., Nataf, D. M., et al. 2019, arXiv e-prints, arXiv:1903.09706
Duong, L., Freeman, K. C., Asplund, M., et al. 2018, MNRAS, 476, 5216
Edvardsson, B., Andersen, J., Gustafsson, B., et al. 1993, A&A, 275, 101
Eggen, O. J. 1974, PASP, 86, 162
Eggen, O. J., Lynden-Bell, D., & Sandage, A. R. 1962, ApJ, 136, 748
Eilers, A.-C., Hogg, D. W., Rix, H.-W., & Ness, M. K. 2019, ApJ, 871, 120
El-Badry, K., Rix, H.-W., Ting, Y.-S., et al. 2018a, MNRAS, 473, 5043
El-Badry, K., Ting, Y.-S., Rix, H.-W., et al. 2018b, MNRAS, 476, 528
Epstein, C. R., Elsworth, Y. P., Johnson, J. A., et al. 2014, ApJ, 785, L28

ESA, ed. 1997, ESA Special Publication, Vol. 1200, The HIPPARCOS and TYCHO catalogues. Astrometric and photometric star catalogues derived from the ESA HIPPARCOS Space Astrometry Mission

Ester, M., Kriegel, H.-p., Jorg, S., & Xu, X. 1996, in Proceedings of 2nd International Conference on KDD, 226

Evans, D. W., Riello, M., De Angeli, F., et al. 2018, ArXiv e-prints, arXiv:1804.09368 [astro-ph.IM]

Fabbro, S., Venn, K. A., O'Briain, T., et al. 2018, MNRAS, 475, 2978

Fall, S. M., Krumholz, M. R., & Matzner, C. D. 2010, ApJ, 710, L142

Farrell, T. J., Birchall, M. N., Heald, R. W., et al. 2014, in Proc. SPIE, Vol. 9152, Software and Cyberinfrastructure for Astronomy III, 915223

Feltzing, S., Howes, L. M., McMillan, P. J., & Stonkutė, E. 2017, MNRAS, 465, L109

Fernández-Alvar, E., Fernández-Trincado, J. G., Moreno, E., et al. 2018, ArXiv e-prints, arXiv:1807.07269

Feuillet, D. K., Bovy, J., Holtzman, J., et al. 2016, ApJ, 817, 40

—. 2018, MNRAS, 477, 2326

Font, A. S., McCarthy, I. G., Crain, R. A., et al. 2011, MNRAS, 416, 2802

Forbes, D. A., & Bridges, T. 2010, MNRAS, 404, 1203

Foreman-Mackey, D., Hogg, D. W., Lang, D., & Goodman, J. 2013, PASP, 125, 306

Frankel, N., Rix, H.-W., Ting, Y.-S., Ness, M., & Hogg, D. W. 2018, ApJ, 865, 96

Fraunhofer, J. 1823, Annalen der Physik, 74, 337

Freeman, K., & Bland-Hawthorn, J. 2002, ARA&A, 40, 487

Freeman, K. C. 1987, ARA&A, 25, 603

Freytag, B., Steffen, M., Ludwig, H.-G., et al. 2012, Journal of Computational Physics, 231, 919

Friel, E. D. 1995, ARA&A, 33, 381

Fu, X., Bressan, A., Marigo, P., et al. 2018, MNRAS, 476, 496

Fuhrmann, K. 1998, A&A, 338, 161

—. 2004, Astronomische Nachrichten, 325, 3

—. 2011, MNRAS, 414, 2893

Fuhrmann, K., Chini, R., Kaderhandt, L., & Chen, Z. 2017, ApJ, 836, 139

Gaia Collaboration, Prusti, T., de Bruijne, J. H. J., et al. 2016, A&A, 595, A1

Gaia Collaboration, Babusiaux, C., van Leeuwen, F., et al. 2018a, ArXiv e-prints, arXiv:1804.09378 [astro-ph.SR]

Gaia Collaboration, Brown, A. G. A., Vallenari, A., et al. 2018b, A&A, 616, A1

Gallart, C., Bernard, E. J., Brook, C. B., et al. 2019, arXiv e-prints, arXiv:1901.02900

Gandhi, S. S., & Ness, M. K. 2019, arXiv e-prints, arXiv:1903.04030

Gao, X., Lind, K., Amarsi, A. M., et al. 2018, MNRAS, 481, 2666

García Pérez, A. E., Allende Prieto, C., Holtzman, J. A., et al. 2016, AJ, 151, 144

Garz, T. 1973, A&A, 26, 471, (GARZ)

Gezari, D., Pitts, P., & Schmitz, M. 2000, Catalog of Infrared Observations (Version 5.1), available: http://ircatalog.gsfc.nasa.gov/cio_homepage.html [27-Mar.-2015], NASA/Goddard Space Flight Center, Greenbelt, MD
Gilmore, G., & Reid, N. 1983, MNRAS, 202, 1025
Gilmore, G., Wyse, R. F. G., & Kuijken, K. 1989, ARA&A, 27, 555
Gilmore, G., Randich, S., Asplund, M., et al. 2012, The Messenger, 147, 25
Gonzalez, O. A., & Gadotti, D. 2016, in Astrophysics and Space Science Library, Vol. 418, Galactic Bulges, ed. E. Laurikainen, R. Peletier, & D. Gadotti, 199
Grand, R. J. J., Gómez, F. A., Marinacci, F., et al. 2017, MNRAS, 467, 179
Grand, R. J. J., Bustamante, S., Gómez, F. A., et al. 2018, MNRAS, 474, 3629
Gray, D. F. 2008, The Observation and Analysis of Stellar Photospheres (Cambridge University Press)
Grenon, M. 1999, Ap&SS, 265, 331
Grevesse, N., Asplund, M., & Sauval, A. J. 2007, Space Sci. Rev., 130, 105
Grundahl, F., Briley, M., Nissen, P. E., & Feltzing, S. 2002, A&A, 385, L14
Guedes, J., Mayer, L., Carollo, M., & Madau, P. 2013, ApJ, 772, 36
Gustafsson, B. 2018, A&A, 620, A53
Gustafsson, B., Edvardsson, B., Eriksson, K., et al. 2008, A&A, 486, 951
Hampel, M., Stancliffe, R. J., Lugaro, M., & Meyer, B. S. 2016, ApJ, 831, 171
Hansen, C. J., Primas, F., Hartman, H., et al. 2012, A&A, 545, A31
Harris, W. E. 1996, AJ, 112, 1487
Hawkins, K., Jofré, P., Gilmore, G., & Masseron, T. 2014, MNRAS, 445, 2575
Hawkins, K., Jofré, P., Masseron, T., & Gilmore, G. 2015, MNRAS, 453, 758
Hawkins, K., Masseron, T., Jofré, P., et al. 2016, A&A, 594, A43
Hawkins, K., Ting, Y.-S., & Walter-Rix, H. 2018, ApJ, 853, 20
Hayden, M. R., Recio-Blanco, A., de Laverny, P., Mikolaitis, S., & Worley, C. C. 2017, A&A, 608, L1
Hayden, M. R., Bovy, J., Holtzman, J. A., et al. 2015, ApJ, 808, 132
Hayes, C. R., Majewski, S. R., Shetrone, M., et al. 2018, ApJ, 852, 49
Haywood, M. 2008a, A&A, 482, 673
—. 2008b, MNRAS, 388, 1175
Haywood, M., Di Matteo, P., Lehnert, M., et al. 2018, ArXiv e-prints, arXiv:1802.09887
Haywood, M., Di Matteo, P., Lehnert, M. D., Katz, D., & Gómez, A. 2013, A&A, 560, A109
Haywood, M., Snaith, O. N., Lehnert, M. D., Di Matteo, P., & Khoperskov, S. 2019, arXiv e-prints, arXiv:1903.03188
Heijmans, J., Asplund, M., Barden, S., et al. 2012, in Proc. SPIE, Vol. 8446, Ground-based and Airborne Instrumentation for Astronomy IV, 84460W
Heiter, U., Jofré, P., Gustafsson, B., et al. 2015a, A&A, 582, A49
Heiter, U., Lind, K., Asplund, M., et al. 2015b, Phys. Scr, 90, 054010
Helmi, A. 2008, A&A Rev., 15, 145

Helmi, A., Babusiaux, C., Koppelman, H. H., et al. 2018, Nature, 563, 85
Henden, A. A., Templeton, M., Terrell, D., et al. 2016, VizieR Online Data Catalog, 2336
Herwig, F. 2005, ARA&A, 43, 435
Hinkel, N. R., Timmes, F. X., Young, P. A., Pagano, M. D., & Turnbull, M. C. 2014, AJ, 148, 54
Hinkle, K., Wallace, L., Valenti, J., & Harmer, D. 2000, Visible and Near Infrared Atlas of the Arcturus Spectrum 3727-9300 A (ASP)
Ho, A. Y. Q., Rix, H.-W., Ness, M. K., et al. 2017a, ApJ, 841, 40
Ho, A. Y. Q., Ness, M. K., Hogg, D. W., et al. 2017b, ApJ, 836, 5
Høg, E., Fabricius, C., Makarov, V. V., et al. 2000, A&A, 355, L27
Hogg, D. W., Casey, A. R., Ness, M., et al. 2016, ApJ, 833, 262
Holtzman, J. A., Hasselquist, S., Shetrone, M., et al. 2018, AJ, 156, 125
Huber, D., Zinn, J., Bojsen-Hansen, M., et al. 2017, ApJ, 844, 102
Hunter, J. D. 2007, Computing In Science & Engineering, 9, 90
Ibata, R., Irwin, M., Lewis, G., Ferguson, A. M. N., & Tanvir, N. 2001, Nature, 412, 49
Ibata, R. A., Gilmore, G., & Irwin, M. J. 1995, MNRAS, 277, 781
Iben, Jr., I. 1965, ApJ, 142, 1447
Ivanova, D. V., & Shimanskiĭ, V. V. 2000, Astronomy Reports, 44, 376
Ivezić, Ž., Beers, T. C., & Jurić, M. 2012, ARA&A, 50, 251
Ivezić, Ž., Sesar, B., Jurić, M., et al. 2008, ApJ, 684, 287
Iwamoto, K., Brachwitz, F., Nomoto, K., et al. 1999, ApJS, 125, 439
Jofré, P., Heiter, U., & Soubiran, C. 2018, ArXiv e-prints, arXiv:1811.08041 [astro-ph.SR]
Jofre, P., Heiter, U., Tucci Maia, M., et al. 2018, ArXiv e-prints, arXiv:1808.09778 [astro-ph.SR]
Jofré, P., Panter, B., Hansen, C. J., & Weiss, A. 2010, A&A, 517, A57
Jofré, P., & Weiss, A. 2011, A&A, 533, A59
Jofré, P., Heiter, U., Soubiran, C., et al. 2014, A&A, 564, A133
—. 2015, A&A, 582, A81
Jofré, P., Heiter, U., Worley, C. C., et al. 2017, A&A, 601, A38
Johnson, C. I., & Pilachowski, C. A. 2010, ApJ, 722, 1373
Jurić, M., Ivezić, Ž., Brooks, A., et al. 2008, ApJ, 673, 864
Karakas, A. I., García-Hernández, D. A., & Lugaro, M. 2012, ApJ, 751, 8
Karakas, A. I., & Lattanzio, J. C. 2014, PASA, 31, e030
Karovicova, I., White, T. R., Nordlander, T., et al. 2018, MNRAS, 475, L81
Katz, D., Sartoretti, P., Cropper, M., et al. 2019, A&A, 622, A205
Kausch, W., Noll, S., Smette, A., et al. 2015, A&A, 576, A78
Keller, S. C., Schmidt, B. P., Bessell, M. S., et al. 2007, PASA, 24, 1
Kharchenko, N. V., Piskunov, A. E., Schilbach, E., Röser, S., & Scholz, R.-D. 2013, A&A, 558, A53
King, C. R., Da Costa, G. S., & Demarque, P. 1985, ApJ, 299, 674

King, I. 1958, AJ, 63, 109
Kirby, E. N., Guhathakurta, P., Bolte, M., Sneden, C., & Geha, M. C. 2009, ApJ, 705, 328
Kirchhoff, G., & Bunsen, R. 1860, Annalen der Physik, 186, 161
Kjeldsen, H., & Bedding, T. R. 1995, Astronomy & Astrophysics, 293, 87
Kobayashi, C., Karakas, A. I., & Umeda, H. 2011, MNRAS, 414, 3231
Kobayashi, C., & Nakasato, N. 2011, ApJ, 729, 16
Kobayashi, C., Umeda, H., Nomoto, K., Tominaga, N., & Ohkubo, T. 2006, ApJ, 653, 1145
Koch, A., Grebel, E. K., & Martell, S. L. 2019, arXiv e-prints, arXiv:1904.02146
Koch, A., Grebel, E. K., Wyse, R. F. G., et al. 2006, AJ, 131, 895
Koch, A., Rich, R. M., Reitzel, D. B., et al. 2008, ApJ, 689, 958
Kollmeier, J. A., Zasowski, G., Rix, H.-W., et al. 2017, ArXiv e-prints, arXiv:1711.03234
Koposov, S. E., Glushkova, E. V., & Zolotukhin, I. Y. 2008, A&A, 486, 771
Kormendy, J., & Kennicutt, Jr., R. C. 2004, ARA&A, 42, 603
Kos, J., & Zwitter, T. 2013, ApJ, 774, 72
Kos, J., Lin, J., Zwitter, T., et al. 2017, MNRAS, 464, 1259
Kos, J., Bland-Hawthorn, J., Freeman, K., et al. 2018, MNRAS, 473, 4612
Kroupa, P., & Boily, C. M. 2002, MNRAS, 336, 1188
Kruijssen, J. M. D. 2012, MNRAS, 426, 3008
Kruijssen, J. M. D., Pfeffer, J. L., Reina-Campos, M., Crain, R. A., & Bastian, N. 2018, MNRAS, arXiv:1806.05680
Krumholz, M. R., Bate, M. R., Arce, H. G., et al. 2014, Protostars and Planets VI, 243
Kumar, Y. B., Reddy, B. E., & Lambert, D. L. 2011, ApJ, 730, L12
Kunder, A., Kordopatis, G., Steinmetz, M., et al. 2017, AJ, 153, 75
Kurucz, R. L. 2007, Robert L. Kurucz on-line database of observed and predicted atomic transitions
Lada, C. J. 2006, ApJ, 640, L63
Lada, C. J., & Lada, E. A. 2003, ARA&A, 41, 57
Lee, Y. S., Beers, T. C., An, D., et al. 2011, ApJ, 738, 187
Letarte, B., Hill, V., Tolstoy, E., et al. 2010, A&A, 523, A17
Leung, H. W., & Bovy, J. 2019, MNRAS, 483, 3255
Lewis, I. J., Cannon, R. D., Taylor, K., et al. 2002, MNRAS, 333, 279
Lin, J., Dotter, A., Ting, Y.-S., & Asplund, M. 2018, MNRAS
Lin, J., Asplund, M., Ting, Y.-S., et al. 2019, The GALAH Survey: Temporal Chemical Enrichment of the Galactic Disk, MNRAS
Lind, K., Asplund, M., & Barklem, P. S. 2009, A&A, 503, 541
Lind, K., Asplund, M., Barklem, P. S., & Belyaev, A. K. 2011, A&A, 528, A103
Lind, K., Bergemann, M., & Asplund, M. 2012, MNRAS, 427, 50
Lind, K., Koposov, S. E., Battistini, C., et al. 2015, A&A, 575, L12

Lindegren, L. 2018, GAIA-C3-TN-LU-LL-124-01: Re-normalising the astrometric chi-square in Gaia DR2

Lindegren, L., & Feltzing, S. 2013, A&A, 553, A94

Lindegren, L., Lammers, U., Bastian, U., et al. 2016, A&A, 595, A4

Lindegren, L., Hernandez, J., Bombrun, A., et al. 2018, ArXiv e-prints, arXiv:1804.09366 [astro-ph.IM]

Lineweaver, C. H. 1999, Science, 284, 1503

Liu, F., Asplund, M., Yong, D., et al. 2019, arXiv e-prints, arXiv:1902.11008 [astro-ph.SR]

Liu, S., Du, C., Newberg, H. J., et al. 2018, ArXiv e-prints, arXiv:1806.10315

Lodders, K., Palme, H., & Gail, H.-P. 2009, Landolt Börnstein, 712

Loebman, S. R., Roškar, R., Debattista, V. P., et al. 2011, ApJ, 737, 8

Luo, A.-L., Zhao, Y.-H., Zhao, G., et al. 2015, Research in Astronomy and Astrophysics, 15, 1095

Mackereth, J. T., Bovy, J., Schiavon, R. P., et al. 2017, MNRAS, 471, 3057

Mackereth, J. T., Bovy, J., Leung, H. W., et al. 2019a, arXiv e-prints, arXiv:1901.04502

Mackereth, J. T., Schiavon, R. P., Pfeffer, J., et al. 2019b, MNRAS, 482, 3426

Magic, Z., Collet, R., Asplund, M., et al. 2013, A&A, 557, A26

Maiorca, E., Randich, S., Busso, M., Magrini, L., & Palmerini, S. 2011, ApJ, 736, 120

Majewski, S. R. 1993, ARA&A, 31, 575

Majewski, S. R., APOGEE Team, & APOGEE-2 Team. 2016, Astronomische Nachrichten, 337, 863

Majewski, S. R., Zasowski, G., & Nidever, D. L. 2011, ApJ, 739, 25

Majewski, S. R., Schiavon, R. P., Frinchaboy, P. M., et al. 2017, AJ, 154, 94

Maoz, D., Mannucci, F., & Brandt, T. D. 2012, MNRAS, 426, 3282

Maoz, D., Sharon, K., & Gal-Yam, A. 2010, ApJ, 722, 1879

Marigo, P., Girardi, L., Bressan, A., et al. 2017, ApJ, 835, 77

Marino, A. F., Villanova, S., Piotto, G., et al. 2008, A&A, 490, 625

Marino, A. F., Sneden, C., Kraft, R. P., et al. 2011, A&A, 532, A8

Martell, S. L., Shetrone, M. D., Lucatello, S., et al. 2016, ApJ, 825, 146

Martell, S. L., Sharma, S., Buder, S., et al. 2017, MNRAS, 465, 3203

Martig, M., Minchev, I., & Flynn, C. 2014, MNRAS, 442, 2474

Martig, M., Rix, H.-W., Silva Aguirre, V., et al. 2015, MNRAS, 451, 2230

Martig, M., Fouesneau, M., Rix, H.-W., et al. 2016, MNRAS, 456, 3655

Masseron, T., & Gilmore, G. 2015, MNRAS, 453, 1855

Matsuno, T., Aoki, W., & Suda, T. 2019, arXiv e-prints, arXiv:1903.09456

Matteucci, F., & Francois, P. 1989, MNRAS, 239, 885

McCarthy, I. G., Font, A. S., Crain, R. A., et al. 2012, MNRAS, 420, 2245

Mckinney, W. 2011, in Python High Performance Science Computer

McMillan, P. J. 2011, MNRAS, 414, 2446

McMillan, P. J., & Binney, J. J. 2008, MNRAS, 390, 429

McWilliam, A. 1997, ARA&A, 35, 503
McWilliam, A., Wallerstein, G., & Mottini, M. 2013, ApJ, 778, 149
Michalik, D., Lindegren, L., & Hobbs, D. 2015, A&A, 574, A115
Miglio, A., Chiappini, C., Mosser, B., et al. 2017, Astronomische Nachrichten, 338, 644
Mikolaitis, Š., de Laverny, P., Recio-Blanco, A., et al. 2017, A&A, 600, A22
Milone, A. P., Piotto, G., Renzini, A., et al. 2017, MNRAS, 464, 3636
Minchev, I., Chiappini, C., & Martig, M. 2013, A&A, 558, A9
Minchev, I., & Famaey, B. 2010, ApJ, 722, 112
Minchev, I., Martig, M., Streich, D., et al. 2015, ApJ, 804, L9
Mints, A., & Hekker, S. 2018, UniDAM: Unified tool to estimate Distances, Ages, and Masses, Astrophysics Source Code Library, ascl:1804.022
Miszalski, B., Shortridge, K., Saunders, W., Parker, Q. A., & Croom, S. M. 2006, MNRAS, 371, 1537
Mitschang, A. W., De Silva, G., Sharma, S., & Zucker, D. B. 2013, MNRAS, 428, 2321
Mitschang, A. W., De Silva, G., Zucker, D. B., et al. 2014, MNRAS, 438, 2753
Miyamoto, M., & Nagai, R. 1975, PASJ, 27, 533
Morrison, H. L. 1993, AJ, 106, 578
Morrison, H. L., Flynn, C., & Freeman, K. C. 1990, AJ, 100, 1191
Mucciarelli, A., Bellazzini, M., Ibata, R., et al. 2012, MNRAS, 426, 2889
Murray, N., Quataert, E., & Thompson, T. A. 2010, ApJ, 709, 191
Myeong, G. C., Evans, N. W., Belokurov, V., Sanders, J. L., & Koposov, S. E. 2018a, MNRAS, 478, 5449
—. 2018b, ApJ, 863, L28
Nataf, D. M., Gonzalez, O. A., Casagrande, L., et al. 2016, MNRAS, 456, 2692
Navarro, J. F., Frenk, C. S., & White, S. D. M. 1997, ApJ, 490, 493
Ness, M., Hogg, D. W., Rix, H.-W., Ho, A. Y. Q., & Zasowski, G. 2015, ApJ, 808, 16
Ness, M., Hogg, D. W., Rix, H.-W., et al. 2016, ApJ, 823, 114
Ness, M., Freeman, K., Athanassoula, E., et al. 2013, MNRAS, 430, 836
Ness, M., Rix, H.-W., Hogg, D. W., et al. 2018, ApJ, 853, 198
Neves, V., Santos, N. C., Sousa, S. G., Correia, A. C. M., & Israelian, G. 2009, A&A, 497, 563
Nissen, P. E. 2015, A&A, 579, A52
Nissen, P. E., Chen, Y. Q., Carigi, L., Schuster, W. J., & Zhao, G. 2014, A&A, 568, A25
Nissen, P. E., & Gustafsson, B. 2018, A&A Rev., 26, 6
Nissen, P. E., Hoeg, E., & Schuster, W. J. 1997, in ESA Special Publication, Vol. 402, Hipparcos - Venice '97, ed. R. M. Bonnet, E. Høg, P. L. Bernacca, L. Emiliani, A. Blaauw, C. Turon, J. Kovalevsky, L. Lindegren, H. Hassan, M. Bouffard, B. Strim, D. Heger, M. A. C. Perryman, & L. Woltjer, 225
Nissen, P. E., & Schuster, W. J. 2010, A&A, 511, L10
—. 2011, A&A, 530, A15
—. 2012, A&A, 543, A28

Noguchi, M. 1999, ApJ, 514, 77
Nomoto, K. 1984, ApJ, 277, 791
Nomoto, K., Kobayashi, C., & Tominaga, N. 2013, Annual Review of Astronomy and Astrophysics, 51, 457
Nordlander, T., & Lind, K. 2017, A&A, 607, A75
Nordström, B., Mayor, M., Andersen, J., et al. 2004, A&A, 418, 989
O'brian, T. R., & Lawler, J. E. 1991, Phys. Rev. A, 44, 7134, (BL)
Oke, J. B. 1990, AJ, 99, 1621
Önehag, A., Gustafsson, B., & Korn, A. 2014, A&A, 562, A102
Osorio, Y., & Barklem, P. S. 2016, A&A, 586, A120
Osorio, Y., Barklem, P. S., Lind, K., et al. 2015, A&A, 579, A53
Osorio, Y., Lind, K., Barklem, P. S., Allende Prieto, C., & Zatsarinny, O. 2019, A&A, 623, A103
Pancino, E., Lardo, C., Altavilla, G., et al. 2017, A&A, 598, A5
Pasetto, S., Grebel, E. K., Zwitter, T., et al. 2012, A&A, 547, A70
Pedregosa, F., Varoquaux, G., Gramfort, A., et al. 2011, Journal of Machine Learning Research, 12, 2825
Peebles, P. 1971, Physical Cosmology, Princeton series in physics (Princeton University Press)
Pérez, F., & Granger, B. E. 2007, Computing in Science and Engineering, 9, 21
Perryman, M. A. C., Lindegren, L., Kovalevsky, J., et al. 1997, Astronomy & Astrophysics, 323, L49
Perryman, M. A. C., de Boer, K. S., Gilmore, G., et al. 2001, A&A, 369, 339
Pian, E., D'Avanzo, P., Benetti, S., et al. 2017, Nature, 551, 67
Pillepich, A., Madau, P., & Mayer, L. 2015, ApJ, 799, 184
Pillepich, A., Springel, V., Nelson, D., et al. 2018, MNRAS, 473, 4077
Pinsonneault, M. 1997, ARA&A, 35, 557
Pinsonneault, M. H., Elsworth, Y., Epstein, C., et al. 2014, ApJS, 215, 19
Pinsonneault, M. H., Elsworth, Y. P., Tayar, J., et al. 2018, ApJS, 239, 32
Piskunov, N., & Valenti, J. A. 2017, A&A, 597, A16
Pitrou, C., Coc, A., Uzan, J.-P., & Vangioni, E. 2018, Phys. Rep., 754, 1
Popper, D. M. 1947, ApJ, 105, 204
Porras, A., Christopher, M., Allen, L., et al. 2003, AJ, 126, 1916
Prantzos, N. 2012, A&A, 542, A67
Prantzos, N., Abia, C., Limongi, M., Chieffi, A., & Cristallo, S. 2018, MNRAS, 476, 3432
Prantzos, N., de Laverny, P., Guiglion, G., Recio-Blanco, A., & Worley, C. C. 2017, A&A, 606, A132
Press, W. H., & Schechter, P. 1974, ApJ, 187, 425
Price-Jones, N., & Bovy, J. 2019, arXiv e-prints, arXiv:1902.08201
Prša, A., Harmanec, P., Torres, G., et al. 2016, The Astronomical Journal, 152, 41

Quillen, A. C., De Silva, G., Sharma, S., et al. 2018, MNRAS, 478, 228
Quinn, P. J., Hernquist, L., & Fullagar, D. P. 1993, ApJ, 403, 74
Ramírez, I., Fish, J. R., Lambert, D. L., & Allende Prieto, C. 2012, ApJ, 756, 46
Randich, S., Gilmore, G., & Gaia-ESO Consortium. 2013, The Messenger, 154, 47
Randich, S., Tognelli, E., Jackson, R., et al. 2018, A&A, 612, A99
Rauer, H., Catala, C., Aerts, C., et al. 2014, Experimental Astronomy, 38, 249
Recio-Blanco, A., Bijaoui, A., & de Laverny, P. 2006, MNRAS, 370, 141
Recio-Blanco, A., de Laverny, P., Kordopatis, G., et al. 2014, A&A, 567, A5
Reddy, B. E., Lambert, D. L., & Allende Prieto, C. 2006, MNRAS, 367, 1329
Reddy, B. E., Tomkin, J., Lambert, D. L., & Allende Prieto, C. 2003, MNRAS, 340, 304
Reeves, H., Fowler, W. A., & Hoyle, F. 1970, Nature, 226, 727
Reggiani, H., Amarsi, A. M., Lind, K., et al. subm., A Non-LTE model of K I
Reggiani, H., Meléndez, J., Kobayashi, C., Karakas, A., & Placco, V. 2017, A&A, 608, A46
Ricker, G. R., Winn, J. N., Vanderspek, R., et al. 2015, Journal of Astronomical Telescopes, Instruments, and Systems, 1, 014003
Rix, H.-W., & Bovy, J. 2013, A&A Rev., 21, 61
Rix, H.-W., Ting, Y.-S., Conroy, C., & Hogg, D. W. 2016, ApJ, 826, L25
Roederer, I. U., Schatz, H., Lawler, J. E., et al. 2014, ApJ, 791, 32
Ruchti, G. R., Fulbright, J. P., Wyse, R. F. G., et al. 2011, ApJ, 743, 107
Rutten, R. J. 2003, in Astronomical Society of the Pacific Conference Series, Vol. 288, Stellar Atmosphere Modeling, ed. I. Hubeny, D. Mihalas, & K. Werner, 99
Sackmann, I.-J., & Boothroyd, A. I. 1992, ApJ, 392, L71
—. 1999, ApJ, 510, 217
Sadavoy, S. I., & Stahler, S. W. 2017, MNRAS, 469, 3881
Saito, R. K., Minniti, D., Dias, B., et al. 2012, A&A, 544, A147
Salaris, M., & Cassisi, S. 2005, Evolution of stars and stellar populations (J. Wiley)
Salaris, M., Weiss, A., & Percival, S. M. 2004, A&A, 414, 163
Samland, M. 1998, ApJ, 496, 155
Sanders, J. L., & Binney, J. 2015, MNRAS, 449, 3479
—. 2016, MNRAS, 457, 2107
Sanders, J. L., & Das, P. 2018, ArXiv e-prints, arXiv:1806.02324
Savage, B. D., & Mathis, J. S. 1979, ARA&A, 17, 73
Schaye, J., Crain, R. A., Bower, R. G., et al. 2015, MNRAS, 446, 521
Schiavon, R. P., Zamora, O., Carrera, R., et al. 2017, MNRAS, 465, 501
Schlegel, D. J., Finkbeiner, D. P., & Davis, M. 1998, ApJ, 500, 525
Schlesinger, K. J., Johnson, J. A., Rockosi, C. M., et al. 2012, ApJ, 761, 160
Schönrich, R., Asplund, M., & Casagrande, L. 2011, MNRAS, 415, 3807
Schönrich, R., & Bergemann, M. 2014, MNRAS, 443, 698
Schönrich, R., & Binney, J. 2009, MNRAS, 399, 1145
Schönrich, R., Binney, J., & Dehnen, W. 2010, MNRAS, 403, 1829

Schuster, W. J., Moitinho, A., Márquez, A., Parrao, L., & Covarrubias, E. 2006, A&A, 445, 939
Schuster, W. J., Moreno, E., Nissen, P. E., & Pichardo, B. 2012, A&A, 538, A21
Searle, L., & Zinn, R. 1978, ApJ, 225, 357
Seitenzahl, I. R., Ciaraldi-Schoolmann, F., Röpke, F. K., et al. 2013, MNRAS, 429, 1156
Sellwood, J. A., & Binney, J. J. 2002, MNRAS, 336, 785
Sharma, S., Bland-Hawthorn, J., Johnston, K. V., & Binney, J. 2011, ApJ, 730, 3
Sharma, S., Stello, D., Bland-Hawthorn, J., Huber, D., & Bedding, T. R. 2016, ApJ, 822, 15
Sharma, S., Stello, D., Buder, S., et al. 2018, MNRAS, 473, 2004
Sheinis, A., Anguiano, B., Asplund, M., et al. 2015, Journal of Astronomical Telescopes, Instruments, and Systems, 1, 035002
Shetrone, M., Venn, K. A., Tolstoy, E., et al. 2003, AJ, 125, 684
Shetrone, M. D., Côté, P., & Sargent, W. L. W. 2001, ApJ, 548, 592
Silva Aguirre, V., Bojsen-Hansen, M., Slumstrup, D., et al. 2018, MNRAS, 475, 5487
Simpson, J. D., De Silva, G. M., Martell, S. L., et al. 2017, MNRAS, 471, 4087
Skrutskie, M. F., Cutri, R. M., Stiening, R., et al. 2006, The Astronomical Journal, 131, 1163
Skúladóttir, Á., Tolstoy, E., Salvadori, S., Hill, V., & Pettini, M. 2017, A&A, 606, A71
Slumstrup, D., Grundahl, F., Brogaard, K., et al. 2017, A&A, 604, L8
Smette, A., Sana, H., Noll, S., et al. 2015, A&A, 576, A77
Smiljanic, R., & Gaia-ESO Survey Consortium. 2018, in IAU Symposium, Vol. 334, Rediscovering Our Galaxy, ed. C. Chiappini, I. Minchev, E. Starkenburg, & M. Valentini, 128
Smiljanic, R., Korn, A. J., Bergemann, M., et al. 2014, A&A, 570, A122
Soderblom, D. R. 2010, ARA&A, 48, 581
Sousa, S. G., Santos, N. C., Israelian, G., Mayor, M., & Udry, S. 2011, A&A, 533, A141
Souto, D., Cunha, K., Smith, V. V., et al. 2018, ApJ, 857, 14
Spina, L., Meléndez, J., Karakas, A. I., et al. 2016, A&A, 593, A125
Spite, F., & Spite, M. 1982, A&A, 115, 357
Spitoni, E., Silva Aguirre, V., Matteucci, F., Calura, F., & Grisoni, V. 2018, ArXiv e-prints, arXiv:1809.00914
Steinmetz, M., Zwitter, T., Siebert, A., et al. 2006, AJ, 132, 1645
Stello, D., Huber, D., Sharma, S., et al. 2015, ApJ, 809, L3
Stello, D., Zinn, J., Elsworth, Y., et al. 2017, ApJ, 835, 83
Takada, M., Ellis, R. S., Chiba, M., et al. 2014, PASJ, 66, R1
Talon, S., & Charbonnel, C. 1998, A&A, 335, 959
—. 2004, A&A, 418, 1051
Tang, J., Bressan, A., Rosenfield, P., et al. 2014, MNRAS, 445, 4287
Taylor, M. B. 2005, in Astronomical Society of the Pacific Conference Series, Vol. 347, Astronomical Data Analysis Software and Systems XIV, ed. P. Shopbell, M. Britton,

& R. Ebert, 29
The Astropy Collaboration, Price-Whelan, A. M., Sipőcz, B. M., et al. 2018, ArXiv e-prints, arXiv:1801.02634 [astro-ph.IM]
Tian, H.-J., Liu, C., Carlin, J. L., et al. 2015, ApJ, 809, 145
Ting, Y.-S., Conroy, C., & Goodman, A. 2015, ApJ, 807, 104
Ting, Y.-S., Conroy, C., & Rix, H.-W. 2016, ApJ, 816, 10
Ting, Y.-S., Conroy, C., Rix, H.-W., & Asplund, M. 2018a, ApJ, 860, 159
Ting, Y.-S., Conroy, C., Rix, H.-W., & Cargile, P. 2017, ApJ, 843, 32
—. 2018b, arXiv e-prints, arXiv:1804.01530 [astro-ph.SR]
Ting, Y.-S., Freeman, K. C., Kobayashi, C., De Silva, G. M., & Bland-Hawthorn, J. 2012, MNRAS, 421, 1231
Tissera, P. B., Scannapieco, C., Beers, T. C., & Carollo, D. 2013, MNRAS, 432, 3391
Tody, D. 1986, in Proc. SPIE, Vol. 627, Instrumentation in astronomy VI, ed. D. L. Crawford, 733
Tody, D. 1993, in Astronomical Society of the Pacific Conference Series, Vol. 52, Astronomical Data Analysis Software and Systems II, ed. R. J. Hanisch, R. J. V. Brissenden, & J. Barnes, 173
Tolstoy, E., Hill, V., & Tosi, M. 2009, ARA&A, 47, 371
Travaglio, C., Gallino, R., Arnone, E., et al. 2004, ApJ, 601, 864
Traven, G., Matijevič, G., Zwitter, T., et al. 2017, ApJS, 228, 24
Trick, W. H., Coronado, J., & Rix, H.-W. 2019, MNRAS, 484, 3291
Ulyanov, D. 2016, Multicore-TSNE, `https://github.com/DmitryUlyanov/Multicore-TSNE`
Čotar, K., Zwitter, T., Traven, G., et al. 2019, arXiv e-prints, arXiv:1904.04841 [astro-ph.SR]
Valenti, J. A., & Piskunov, N. 1996, A&AS, 118, 595
van der Maaten, L., & Hinton, G. 2008, Journal of Machine Learning Research, 9, 2579
Van Dokkum, P. G. 2001, PASP, 113, 1420
van Leeuwen, F. 2007, A&A, 474, 653
Venn, K. A., Irwin, M., Shetrone, M. D., et al. 2004, AJ, 128, 1177
Viani, L. S., Basu, S., Chaplin, W. J., Davies, G. R., & Elsworth, Y. 2017, ApJ, 843, 11
Villalobos, Á., & Helmi, A. 2008, MNRAS, 391, 1806
Walt, S. v. d., Colbert, S. C., & Varoquaux, G. 2011, Computing in Science and Engg., 13, 22
Wang, L., Dutton, A. A., Stinson, G. S., et al. 2015, MNRAS, 454, 83
White, S. D. M., & Rees, M. J. 1978, MNRAS, 183, 341
Wittenmyer, R. A., Sharma, S., Stello, D., et al. 2018, AJ, 155, 84
Wojno, J., Kordopatis, G., Piffl, T., et al. 2017, MNRAS, 468, 3368
Wolf, C., Onken, C. A., Luvaul, L. C., et al. 2018, PASA, 35, e010
Woosley, S. E., & Weaver, T. A. 1995, ApJS, 101, 181
Xiang, M., Shi, J., Liu, X., et al. 2018, ApJS, 237, 33

Yanny, B., Rockosi, C., Newberg, H. J., et al. 2009, AJ, 137, 4377
Yong, D., Lambert, D. L., Allende Prieto, C., & Paulson, D. B. 2004, ApJ, 603, 697
Yoshii, Y. 1982, PASJ, 34, 365
Zacharias, N., Finch, C., & Frouard, J. 2017, AJ, 153, 166
Zacharias, N., Finch, C. T., Girard, T. M., et al. 2013, AJ, 145, 44
Zasowski, G., Johnson, J. A., Frinchaboy, P. M., et al. 2013, AJ, 146, 81
Zhang, H. W., & Zhao, G. 2005, Monthly Notices of the Royal Astronomical Society, 364, 712
Zhao, G., Mashonkina, L., Yan, H. L., et al. 2016, ApJ, 833, 225

ACKNOWLEDGEMENTS

Before I start the usual listing of names let me say: If you think this thesis is important enough to look at these pages you deserve a great thank you. **THANK YOU!**

Finishing this Thesis and the work related with it is a tremendous professional and personal accomplishment for me. Reaching this point was not possible without the support of so many people: family, friends and colleagues.

Above all, I like to thank my supervisors, Karin Lind and Melissa Ness. You have both contributed this Thesis and me growing up scientifically so much, that the following words can only capture a small part of my gratitude of your positive influences.

Karin, du har varit den bästa handledaren jag kunnat önska mig - tillmötesgående, kunnig, snäll, motiverande och alltid öppen för att svara på alla slags frågor. Jag är tacksam att du gett mig chansen att komma i kontakt med olika typer av forskning och att arbeta med observationsprojekt och kollegor över hela världen. Tack vare dig har jag fått resa jorden runt; träffat så många intressanta och inspirerande människor och kunnat bygga ett relevant nätverk. Tusen, tusen tack!

Melissa, I am grateful to have had you as a supervisor and constant source of happiness and motivation. Your never-ending enthusiasm has always helped me to continue to like the work I do. I have to admit that during harder times I caught myself printing a plot and walk to your office to catch a bit of your excitement and happily walk back to my office. You have helped me to start narrowing down the questions one should ask in science and for my research. Thank you!

I further like to thank Andreas Koch, Hans-Walter Rix, and Johanna Stachel for accepting the extra work of being part of my thesis panel as well as Norbert Christlieb for helping me to stay on track as part of my Thesis committee throughout the years.

During my PhD I had the opportunity to work with many great people who contributed in one way or another to this thesis. I like to list some of them here:

Martin Asplund Thank you for being a great survey working group head and for hosting and supervising me during my visits to Stromlo - I have obviously been seriously impressed and not only by your 'academic cheerleading'. Thank you also for giving me the chance to come to ANU and continue working in the field of Galactic archaeology.

I am looking forward to learning more from you and together with you in the coming years!

Thomas Nordlander I am looking forward to hanging out together in Canberra. I am always surprised how you manage to hide (or decorate?) all your scientific knowledge behind some of the funniest (worst?) phrases I ever heard. Es war eine Ehre, dein Chauffeur sein zu dürfen - unsere gemeinsamen Autofahrten bis jetzt waren unglaublich witzig - ich bin schon sehr gespannt, wohin uns der Niveau Limbo demnächst bringt.

The GALAH survey collaboration Thank you, Joss and Ken, for envisioning this great project and a great thank you to the steering group members and builders for making it become reality.

Hans-Walter Rix Thank you for always being a great help to keep the bigger picture in mind and having advice when I was stuck with the huge amount of data that we have just started to explore. It was a pleasure to be a satellite of your Milky Way group for the last four years.

The (core) Lind group: Anish, Ása, Diane, Karin, and Xudong Thanks for being a great group of colleagues to work together and always helpful with great advice. Sorry (but actually not sorry) for forcing all the social activities and conversations on you.

I consider myself incredibly lucky to have been able to work at the MPIA with the most encouraging working environment I experienced. A big thanks goes also to the people that have helped me every now and then with scientific advice, including David Hogg, Morgan Fouesneau, Wilma Trick, Johanna Coronado, Paula Jofré, Ulrike Heiter, Chiara Battistini, Andy Gallagher, Camilla Juul Hansen, and many more.

While all of the aforementioned researchers have helped me scientifically, I would not have reached this point in life without the help of so many other people:

Mama und Papa Danke, dass ihr mich in all den 27 Jahren so großartig unterstützt habt. Ich bin euch unglaublich dankbar für all den Rückhalt und die Freiräume, die ihr mir gegeben habt. Dank euch habe ich gelernt immer das Beste zu geben und ihr wart so stark mich nach Afra zu lassen. Danke für alles!

Marcel, Anna, Wilhelm, und Alma Marcel, du warst immer mein größtes Vorbild und ich bin so froh einen so tollen Bruder zu haben, der immer für mich da ist. Danke! Anna, Wilhelm, und Alma: Danke dass ihr ein Teil meines Lebens seid. Es ist immer großartig euch in Schweden zu besuchen und von der Arbeit abzuschalten um Zeit mit meiner 'schwedischen' Familie zu genießen.

Meine Großeltern Auch wenn ihr nicht alle den Abschluss meiner Doktorarbeit am gleichen Ort erlebt, bin ich mir sicher, dass ihr alle ein bisschen Stolz darauf seid und ich bin euch dankbar für all eure Unterstützung.

Robert Junge, Junge, Junge! Bald haben wir es beide geschafft. Wer hätte gedacht, dass wir beide mal nen Doktor bekommen? Ich bin so froh, dass wir uns damals in der Straßenbahn begegnet sind. Ich verdanke dir echt ne ganze Menge, aber bevor das hier zu nem Tagebucheintrag ausartet nur so viel: Ich bin echt froh, dass wir immer noch

so viel Kontakt haben, und dass du mich mental unterstützt. Danke, dass du mich für's Rennradfahren, unsere Challenges und Sport generell so begeistert hast.

Tobias Buck Du bist der beste Heidelberger Freund, den ich mir vorstellen konnte und der beste Büronachbar sowieso - jajaja, genau. Es hat unglaublich viel Spaß gemacht mit dir zusammen Sachen zu organisieren, egal ob Königstuhl Bars oder GC Retreat Quizzes. Dabei stell ich mir noch heute immer die Frage: Wie heißt eigentlich die Mutter von Nicki Lauda?

Die Jenaer Chris, Tim, Lukas, Malte und Co. Zusammen haben wir es durch's Studium geschafft und obendrein noch ne geile Zeit gehabt. Was will man mehr? Ein Dank auch an die Sternwarten-Mitarbeiter, mit denen ich zusammen zahlreiche Nächte beobachtet habe. Danke auch an meine Suppenkasper, insbesondere János und Manni, für die zahlreichen kulinarischen Köstlichkeiten, die wir während dieser Zeit zusammen ausprobiert haben. Jula: Wir haben uns zwar erst später richtig kennen gelernt, aber deine Sportlichkeit hat mich immer motiviert, noch einen drauf zu setzen - ohne dich hätten wir nie beim Getting Tough mitgemacht.

Lexy und Georgie Danke für deine/eure Unterstützung während des Studiums und dass ihr immer den Rückhalt gegeben habt, den ich brauchte, aber auch den Ausblick wie ich ein besserer Mensch werden kann.

Christina Eilers and Johannes Esser. Zusammen mit Tobi seid ihr mein engerer Kreis von Freunden in Heidelberg geworden und habt mir dabei geholfen mich zurecht zu finden und mich immer wieder auf den Boden der Tatsachen züruck gebracht, wenn nötig.

Office 217 This office made all my working days enjoyable. Many thanks to Tobias Buck (again), Hans, Hector, Arianna, Martin, Sassa, and Paolo. Martin, a special thanks to you for the crazy sports trips - I mean who would not love to swim in Neckar in November right?

My fellow boulder enthusiasts, especially Morgan, Allison, Rebecca, and Alina. Thanks for bringing me back to this sport and solving so many non-scientific problems.

My fellow pub quizzers, thanks for the knowledge and fun you brought to the table and most important: Don't panic!

I most probably forgot to thank many people who contributed to my success. If you read this, I probably have to thank you. Sorry for missing you. So, thanks a lot!

Finally I like to acknowledge support from the Alexander von Humboldt Foundation in the framework of the Sofja Kovalevskaja Award endowed by the Federal Ministry of Education and Research.

Some of my collaboration travels were supported from Universities Australia and Deutsche Akademische Austauschdienst, the Hunstead Fund for Astrophysics at the University of Sydney and the National Science Foundation under Grant No. PHY-1430152 (JINA Center for the Evolution of the Elements).

The GALAH survey data used for this Thesis is based on data acquired through the Australian Astronomical Observatory, under programmes: A/2013B/13 (The GALAH pilot survey); A/2014A/25, A/2015A/19, A2017A/18 (The GALAH survey phase 1),

A2018 A/18 (Open clusters with HERMES), A2019A/1 (Hierarchical star formation in Ori OB1), A2019A/15 (The GALAH survey phase 2), A/2015B/19, A/2016A/22, A/2016B/10, A/2017B/16, A/2018B/15 (The HERMES-TESS program), and A/2015A/3, A/2015B/1, A/2015B/19, A/2016A/22, A/2016B/12, A/2017A/14, (The HERMES K2-follow-up program). We acknowledge the traditional owners of the land on which the AAT stands, the Gamilaraay people, and pay our respects to elders past and present.

Parts of the computations were performed on resources provided by the Swedish National Infrastructure for Computing (SNIC) at UPPMAX under project 2015/1-309 and 2016/1-400 as well as the AVATAR cluster at the Research School of Astronomy and Astrophysics of the Australian National University in Canberra.

Parts of this Thesis work were also carried out at the *Gaia* Sprints, hosted by the Center for Computational Astrophysics at the Simons Foundation in New York City and the Max-Planck-Institut für Astronomie, Heidelberg.

This work has made use of data from the European Space Agency (ESA) mission *Gaia* (http://www.cosmos.esa.int/gaia), processed by the *Gaia* Data Processing and Analysis Consortium (DPAC, http://www.cosmos.esa.int/web/gaia/dpac/consortium). Funding for the DPAC has been provided by national institutions, in particular the institutions participating in the *Gaia* Multilateral Agreement.

The following software and programming languages made this research possible: IRAF (Tody, 1986, 1993), CONFIGURE (Miszalski et al., 2006), TOPCAT (version 4.4; Taylor, 2005); Python (version 2.7) and its packages ASTROPY (version 2.0; Astropy Collaboration et al., 2013; The Astropy Collaboration et al., 2018), MATPLOTLIB (Hunter, 2007), PANDAS (version 0.20.2; Mckinney, 2011), NUMPY (Walt et al., 2011), IPYTHON (Pérez & Granger, 2007), and GALPY (version 1.3; Bovy, 2015). This research has made use of the VizieR catalogue access tool, CDS, Strasbourg, France. The original description of the VizieR service was published in A&AS 143, 23. This research mad use of the TOPCAT tool, described in Taylor (2005). This publication makes use of data products from the Two Micron All Sky Survey, which is a joint project of the University of Massachusetts and the Infrared Processing and Analysis Center/California Institute of Technology, funded by the National Aeronautics and Space Administration and the National Science Foundation.

STATEMENT

This thesis is my own work and I have only used the sources indicated. Where the work of others has been quoted or reproduced, the source is always given.

Heidelberg, 9th May 2019 .....